RIGA TECHNICAL UNIVERSITY

Faculty of Civil Engineering

Institute of Materials and Structures

Rims Janeliukstis

Doctoral Student of the Study Program „Civil Engineering"

STRUCTURAL DAMAGE IDENTIFICATION BASED ON MODE SHAPE TRANSFORMATIONS AND SUPERVISED LEARNING

Doctoral thesis

Scientific supervisors
Senior researcher *Dr. sc. ing.*
SANDRIS RUČEVSKIS

Professor *Dr. sc. ing.*
ANDRIS CHATE

Riga 2019

A DOCTORAL THESIS SUBMITTED TO RIGA TECHNICAL UNIVERSITY IN FULFILLMENT OF THE REQUIREMENTS FOR THE DEGREE OF DOCTOR OF SCIENCE IN ENGINEERING

The current doctoral thesis for the scientific degree of Doctor of Engineering to be granted has been submitted for the defence at the open meeting of RTU Promotion Council on May 17th of year 2019 at the Laboratory house of Riga Technical University, Paula Valdena street 1, auditorium 101.

OFFICIAL REVIEWERS

Associate Professor *Dr. habil. sc. ing.* Andrzej Katunin
Silesian University of Technology, Institute of Fundamentals of Machinery Design, Poland

Assistant Professor *PhD* Manuel Chiachio Ruano
University of Granada, Department of Structural Mechanics and Hydraulics Engineering, Spain

Leading researcher *Dr. sc. ing.* Janis Andersons
University of Latvia, Institute of Mechanics of Materials, Latvia

CONFIRMATION

I confirm that the current doctoral thesis submitted for a doctoral degree in engineering to be granted in Riga Technical University, is my own work. The doctoral thesis has not been submitted to any other university for consideration of a PhD title for the author.

Rims Janeliukstis ……………………………. (signature)
Date: ………………………

The doctoral thesis has been written in English. It comprises of introduction, 6 chapters, conclusion, bibliography, 102 figures, 57 equations and 26 tables. The total number of pages is 172. The bibliography contains 216 entries.

ABSTRACT

The present thesis is devoted to development of structural damage localization methods in 1D (beams) and 2D (plates) metal and composite structural elements, as well as damage characterization in pre-stressed railway concrete sleepers.

The first part is based on mode shape transformation methods, such as continuous wavelet transform and mode shape curvature squares. The rationale behind using structural mode shapes is that they provide spatial information about the structure of interest. Mode shapes are measured using non-contact scanning laser vibrometer system. The scanning points serve as sensors in classical experimental modal analysis, hence the user has an advantage to easily adjust the resolution of mode shape by varying a density of the scanning grid. The extracted mode shapes of damaged structures are processed using the aforementioned transform techniques to reveal the location of damage. A new algorithm based on variance of normalized wavelet scalogram is developed for beam structures. This method provides the advantage over the conventional continuous wavelet transform in terms of not needing to select the most appropriate wavelet function and scale parameter for optimum damage localization performance. This part of the thesis is conducted under the framework of the Latvia State Research Program under grant agreement "Innovative Materials and Smart Technologies for Environmental Safety, IMATEH".

The second part of the thesis is devoted to development of methods for structural defect localization based on supervised learning models. Studies involve the localization of pseudo-defect on a cantilevered carbon composite laminate plate and separation of acoustic emission sources in pre-stressed railway concrete sleepers under flexural loading.

The first step for the composite plate involves the extraction of resonant frequencies of the plate using experimental and numerical modal analyses. The extracted resonant frequencies are used as driving frequencies for harmonic excitation of the plate for inducing mechanical strains. A point mass is added on several zones of the plate and mechanical strains are recorded via strain sensors. The point mass serves as a pseudo-defect locally modifying mass of the structure and thus providing changes to structural response. The features sensitive to the position of added mass are extracted from strain time series and used to train classifiers based on k-NN and linear discriminant techniques. Trained classifiers are validated on unknown query points in terms of classifying the points as to belong to one of zones of the plate.

Acoustic emission parameters of the railway concrete sleepers are analysed and post-processed to be employed as damage-sensitive features for classification algorithms based on decision trees. Peak frequencies of acoustic emissions are also studied and a shift in these frequencies is observed with increasing distance from the largest density of cracking in the sleepers.

ANOTĀCIJA

Promocijas darbs ir veltīts bojājumu lokalizācijas metožu izstrādei 1D (siju) un 2D (plātņu) metāla un kompozītmateriāla konstrukcijas elementos, kā arī bojājumu rakturošanai iepriekš sasspriegtos dzelzceļa betona gulšņos.

Pirmā daļa ir balstīta uz konstrukciju pašsvārstību formu transformācijas metodēm, piemēram, nepārtraukto telpisko veivletu transformāciju un pašsvārstību formu liekuma kvadrātu. Pašsvārstību formu izmantošana pamatota ar to, ka tās nodrošina telpisko informāciju par interesējošo konstrukciju. Pašsvārstības formas tika mērītas, izmantojot bezkontakta skenēšanas lāzera vibrometru. Skenēšanas punkti var tikt uzskatīti par sensoriem klasiskajā eksperimentālajā modālajā analīzē. Līdz ar to, salīdzinot ar klasisko modālo analīzi, lietotājam ir priekšrocība viegli pielāgot izmērāmo pašsvārstības formu izšķirtspēju, mainot skenēšanas režģa blīvumu. Bojāto konstrukciju pašsvārstības formas tiek apstrādātas, izmantojot iepriekšminētās transformācijas metodes, lai atklātu bojājuma atrašanās vietu. Izstrādāts algoritms, kas balstīts uz normalizētās veivletu mēroggrammas dispersiju bojājumu lokalizēšanai siju konstrukcijās. Šis algoritms dod priekšrocības salīdzinājumā ar parasto nepārtraukto veivletu transformāciju, jo nav nepieciešams izvēlēties vispiemērotāko veivletu funkciju un mēroga parametru optimālai bojājuma lokalizācijai. Šī darba daļa tiek veikta Latvijas Valsts pētniecības programmas ietvaros saskaņā ar granta līgumu "Inovatīvie materiāli un viedās tehnoloģijas vides drošumam, IMATEH".

Promocijas darba otrā daļa ir veltīta konstrukciju bojājumu lokalizācijas metožu, balstītām uz uzraudzītās mašīnmācīšanās modeļiem, izstrādi. Pētījumi ir veikti pseidoefektu lokalizācijai uz oglekļa lamināta kompozītmateriāla konsolplātnes, kā arī akustisko emisiju avotu atdalīšanai iepriekšsasspriegtos dzelzceļa betona gulšņos lieces slodzē.

Pirmais solis oglekļa kompozīta plātnes gadījumā ietver plātes rezonanses frekvenču identifikāciju, izmantojot eksperimentālo un skaitlisko modālo analīzi. Identificētās rezonanses frekvences tiek izmantotas kā nesējfrekvences plāksnes harmoniskai ierosmei. Plāte tiek sadalīta vienādās zonās, katrā zonā tiek pielikta punktveida masa, un mehāniskās deformācijas tiek reģistrētas ar deformāciju mērītājiem. Punktveida masa kalpo kā pseidoefekts, lokāli modificējot konstrukcijas masu, tādējādi nodrošinot izmaiņas konstrukcijas dinamiskajā atbildē uz ierosmi. Bojājumjutīgie parametri, kas ir atkarīgi no pieliktās masas atrašanās vietas uz plātnes, tiek iegūti no izmērītajām deformāciju laikrindām, un tie tiek izmantoti klasifikācijas modeļu apmācībai, pamatojoties uz tuvāko kaimiņu un lineārās diskriminācijas metodēm. Apmācītie klasifikatori ir pārbaudīti uz vairākiem jauniem masas pielikšanas punktiem to klasificēšanai kā piederīgus vienai no plātnes zonām.

Dzelzceļa betona gulšņu akustiskās emisijas parametri tiek analizēti un pēcapstrādāti to tālākai izmantošanai par bojājumtīgiem parametriem klasifikācijas algoritmos, kas balstās uz lēmumu pieņemšanas kokiem. Tika pētītas arī akustisko emisiju pīķa frekvences, un šo frekvenču nobīde tiek novērota, palielinoties attālumam no apgabala ar lielāko plaisu koncentrāciju gulšņos.

ACKNOWLEDGEMENTS

TABLE OF CONTENTS

NOMENCLATURE AND ABBREVIATIONS

AE – Acoustic Emission

CFRP – Carbon Fibre Reinforced Plastic

CM – Condition Monitoring

CWT – Continuous Wavelet Transform

DER – Damage Estimate Reliability

DOF – Degree of Freedom

DI – Damage Index

FEM – Finite Element Method

FFT – Fast Fourier Transform

k-NN – k-nearest neighbours

MSCS – Mode Shape Curvature Square

NWS – Normalized Wavelet Scalogram

SDI – Standardized Damage Index

SDIg – Standardized Damage Index with a threshold $g = 1.28$, 2 or 3

SHM – Structural Health Monitoring

SLV – Scanning Laser Vibrometer

SR – Success Rate

TVNWS – Thresholded Variance of Normalized Wavelet Scalogram

WS – Wavelet Scalogram

WT – Wavelet Transform

E – modulus of elasticity in MPa

Fi – Fourier approximation function with order $i = 1, 2, 3, ..., 8$

FP – false-positive damage ratio

G – modulus of rigidity in MPa

I – second moment of inertia in m^4

M – bending moment in N $\cdot$ m

p – denominator for mode shape DOF number (integer)

s – scale factor of wavelets

T – universal threshold

Z – fractional thresholded variance of normalized wavelet scalogram

δ – noise level in %

ε – mechanical strain in microstrain $\mu\epsilon$

κ – mode shape curvature in m^{-2}

κ_x – reconstructed mode shape curvature in x direction in m^{-2}

κ_y – reconstructed mode shape curvature in y direction in m^{-2}

ν – Poisson's ratio

ρ – mass density in kg/m^3

ρ_{xy} – correlation ceoficient between signals x and y

ψ – wavelet function

INTRODUCTION

Motivation and scope

Demands for structural integrity of different civil and engineering structures have grown over the years. This can be mainly attributed to the increasing complexity and size of such structures as civil buildings, skyscrapers, bridges, dams, stadiums, tunnels, and industrial facilities, naval and aerial transport. Also, these structures need to maintain structural integrity and functionality throughout the entire service life under constantly changing environmental conditions. In some cases, these structures may have to operate in aggressive environments. The consequences of a structural failure are often tragic and involve serious financial investments. The failure of some objects endangering a considerable amount of people is shown in Fig. 1.1. On July 30, 2011 the Boeing 737-800 carrying 168 passengers crashed in Guyana and broke in two pieces. Luckily, nobody died, but they all were taken to hospital [1]. "Iranian media says at least 50 people have reportedly been killed on January 19, 2017, including over 30 firefighters, in the collapse of a burning high-rise Plasco building in Tehran. At least 75 people, including 45 firefighters, were injured as the 17-storey tower collapsed in an event one witness described as like a "scene from a horror movie"" [2].

In order to prevent these catastrophes, safety inspections have to be carried out on a regular basis. However, these inspections are often time consuming and costly and, as a result, non-destructive Structural Health Monitoring (SHM) has emerged as a new field in engineering community. SHM has gained significance in the era of complex and massive structures and vehicles in domains of civil, mechanical and aerospace engineering communities. Lightweight structures, such as airplanes are also increasingly exploiting the benefits of SHM. SHM technologies are based on sensors (usually piezoelectric or optical fibre) which are mounted directly on the structure or, in case of layered composite structures, embedded within the structure. In conjunction with control units these sensors are used to signal any changes in internal state of the structure in response to environmental loads (temperature, pressure) or direct damage. Systems equipped with such technologies have the obvious benefits over conventional structures of preventing disastrous structural collapses, extending infrastructure life time, and reducing maintenance costs and helping design of composite materials [3].

Fig. 1.1. Failure of structures endangering peoples' lives. Left: A jet with a fuselage broken in two pieces – a crash in Guyana [1], right: high-rise building collapsed in Tehran killing 50 people [2].

Aims of the thesis

Although numerous SHM solutions particularly targeted at composites structures already exist, some factors hinder their potential implementation in practice. This is due to complex nature of composites themselves, in particular, anisotropy. Moreover, different possible failure modes in composite structures may require sophisticated tailoring of SHM methods. Also, high demands for structural safety are imposing high standards to SHM in terms of reliability, robustness and safety. Therefore, the aim of this PhD thesis is to develop damage identification methods for one-dimensional and two-dimensional structures using mode shape transformation methods, as well as classification framework for damage interrogation in railway sleepers and condition monitoring of two-dimensional structural members.

Tasks of the thesis

In order to accomplish the aim, the following tasks are set:
1) To review the relevant scientific literature on various vibration-based and machine learning-based SHM techniques;
2) To develop methods for structural damage localization in one-dimensional and two-dimensional structures by using structural deflection shape transformations based on novel modifications of continuous spatial wavelet transform and mode shape curvature squares methods;
3) To develop methods for damage identification in full-scale pre-stressed railway concrete sleepers using advanced signal processing techniques based on supervised learning of acoustic emission signals;
4) To develop a method for condition monitoring of massively produced two-dimensional structural parts with an added benefit of structural defect localization using supervised learning algorithms.
5) To validate the developed methods in experimental studies.

Scientific novelty

A novel structural damage localisation algorithm for beam structures based on variance of normalized scalogram of spatial continuous wavelet transform is developed. The benefits of this algorithm include the use of all wavelet functions so that there is no need to select the most appropriate function. The second advantage of this method is that no particular scale parameter has to be chosen. This novel method is compared with conventional spatial continuous wavelet transform and mode shape curvature squares techniques and its advantages are highlighted.

Smoothing techniques for mode shape data is proposed in order to simulate mode shapes of healthy structure using exclusively the mode shape data of damaged structure. Hence, there is no need for modal information of a healthy structure which is often impossible to obtain.

Acoustic emission source separation technique for pre-stressed railway concrete sleepers based on supervised learning algorithms is developed. By separating these sources, a unique signature of each source in a form of frequency content can be studied further. Peak frequency

shifts with a distance from the largest concentration of cracks which, in turn, are acoustic emission sources, is studied and a correlation law is established.

Practical significance of the thesis

Methods for structural damage localization in beam and plate structures are developed allowing to locate damage in structural members using deflection shape data of the damaged structure. Hence there is no need to obtain the baseline deflection shape information of the healthy structure. The developed methods can, up to a point, be effectively used on deflection shapes contaminated with noise of varying degree (at least 4 %) and different sensor densities or resolutions of deflection shapes.

Method for acoustic emission source separation in full-scale pre-stressed railway concrete sleepers is developed which might be used to gain fundamental insights in peak frequency contents of acoustic emission from cracking concrete during service life after processing the signals obtained from acoustic emission sensors mounted on sleepers which lie in the most critical locations of railway track, namely, turnouts. These contents than, in turn, can be correlated with relevant operational failure modes of the sleepers under dynamic loading from passing railway stock.

Supervised machine learning schemes are effective in interrogating structural changes, such as changes in mass or stiffness. This approach developed for two-dimensional mass-produced structural elements (wind turbine blades, aircraft wings, etc.) can be effectively applied in aerospace industry in order to detect and localize and potentially determine the severity of damage in aircraft elements equipped with sensor network of reasonable density.

Methodology of the research

- Deflection shape measurements were carried out using non-contact laser scanning vibrometer *Polytec*[TM] PSV-400-B.
- Deflection shape signals were post-processed and all the calculations were performed using mathematical package *Matlab*[TM].
- Numerical models of the structures, as well as numerical modal analysis was conducted using commercial finite element package *Ansys*[TM].
- Impact damage was implemented using low-velocity impact drop tower *Instron*[TM] Dynatup 9250 HV.
- Railway concrete sleepers were subjected to three-point bending according to the European standard BS EN 13230.
- Acoustic emission signals in railway concrete sleepers under flexural loading were recorded using a 4-channel DAQ AE system from Physical Acoustics Corporation (PAC, now *Mistras*). The data acquisition was performed using AE-Win software.
- Mechanical strains in the CFRP plate were measured using two 350 Ω strain gauges and dynamic excitation of the plate was conducted by employing *MFC*[TM] (Macro Fibre Composites) actuator. *Agilent* 3322A 20 MHz Waveform generator was used for generating

harmonic signal with a driving frequency equal to resonant frequency. *Spider 8* acquisition system was used for strain signal acquisition and *Catman* software was used for visualization.

- Statistics theory was used for data post-processing.

Applicability limitations of the developed methods

- The developed methods for structural damage localization are applicable to beam (one dimension) and plate (two dimensions) structural elements only.
- Deflection shape signals of the damaged structure must be readily available for the implementation of the algorithms of damage localization. Chances of successful damage localization improve with increasing number of deflection shape signals as with fewer signals at hand there is a higher possibility that zero amplitude of the signal coincides with a location of damage.
- All available wavelet functions at different scale parameters and Fourier approximation functions must be tested in order to select the one with the best performance as this information is not available a priori.
- No damage at the edges of the structures can be localized using the developed algorithms due to edge effects.
- Only limited number of acoustic emission sensors can be mounted on railway sleepers on field. For higher feasibility, it is advised to mount the sensors only on sleepers in the most critical locations of the railway track.
- The high sensitivity to noise of the acoustic emission approach suggests that a reasonable cracking severity has to be reached in order for the developed method to provide early warning of damage in the case of sleeper operation on an actual railway track.

The arguments for defence of the thesis

1. Methods for structural damage localization in one-dimensional and two-dimensional structures by using structural deflection shape transformations based on novel modifications of continuous spatial wavelet transform and mode shape curvature squares methods are developed.
2. Methods for damage identification in full-scale pre-stressed railway concrete sleepers using advanced signal processing techniques based on supervised learning of acoustic emission signals are developed.
3. Method for condition monitoring of massively produced two-dimensional structural parts with an added benefit of defect localization using supervised learning algorithms is developed.
4. The developed methods are experimentally validated and suggest that structural damage can be effectively localized.

Structure of the thesis

The overview of the study part of the thesis is shown in Fig. 1.2 and described below.

PART I-------------------------- Mode Shape Transformations (CWT, MSCS, TVNWS)

Mode shapes measured in

1D **Al beam 1d**
1D **Al beam 2d** — **mill-cut damage**
2D **Al plate**

1D 2D **CFRP beam** — **impact damage**

PART II -------------------------- Classification-based damage identification

pseudo-defect localization — 2-D structural parts — **Condition Monitoring**

separation of cracking sources — Pre-stressed railway concrete sleepers — **passive SHM (acoustic emission)**

Fig. 1.2. Schematic outline of structural damage identification methodology.

Chapter 1: Overview of problems of structural inspection.

Chapter 2: Description of developed damage localization algorithms.

PART I – Mode shape transformation

Chapter 3: Damage localization in beam structures using developed structural damage localization methods.

Chapter 4: Damage localization in plate structures using developed structural damage localization methods.

PART II – Classification of damage-sensitive features

Chapter 5: Condition monitoring with defect localization in a two-dimensional structures based on supervised multiclass classification of strain features.

Chapter 6: Characterization of acoustic emission sources in pre-stressed railway concrete sleepers using classification algorithms.

Conclusions.

1. TRENDS IN STRUCTURAL DAMAGE ASSESSMENT

Currently 27% of an average aircraft's life cycle cost is spent on inspection and repair. The aerospace industry is increasingly using composite materials to take advantage of their excellent specific strength and stiffness properties, fatigue performance, as well their ability to reduce radar detection [4]. CFRP has an ultimate strength more than 5 times that of steel and is less than 60 % of the weight of aluminium. Therefore, the increase in load is small when it is used. In addition, it can provide effective waterproofing to damaged concrete and help prevent the corrosion of steel on account of its good chemical and water resistance [5]. Unfortunately, composites are also subjected to deterioration and such crack damage will appear during their service due to aging, chemical corruption, mechanical vibration, shocks etc. [6]. Hence, sophisticated SHM methods are of great importance for safe operation of composite structures and vehicles.

1.1. Failure modes in polymeric composite structures and pre-stressed concrete sleepers

The common damages in composites are fibre breakage, matrix cracking, fibre-matrix de-bonding and delamination between plies, most of which occur beneath the top surfaces and are barely visible [3]. These failure modes are illustrated in Fig. 1.3.
In [8-10] it is reported that the main fracture mode that has an effect on the residual strength of composite materials is delamination. Mode I, mode II, and the combination of these pure modes are usually present in many real conditions of the delamination damage of laminated composites. Loading conditions and layup types are among the effective factors in the delamination behaviour.

Although composite materials are promising substitutes for metals, ceramics and polymers in many applications due to such qualities as high specific strength, stiffness, corrosion resistance and tailorable properties, they are vulnerable to various failure modes, such as matrix cracking, debonding, and delamination. The studies of low-velocity impact are important in case of composite materials because impact is one of the main failure modes of composites in through-thickness direction [11].
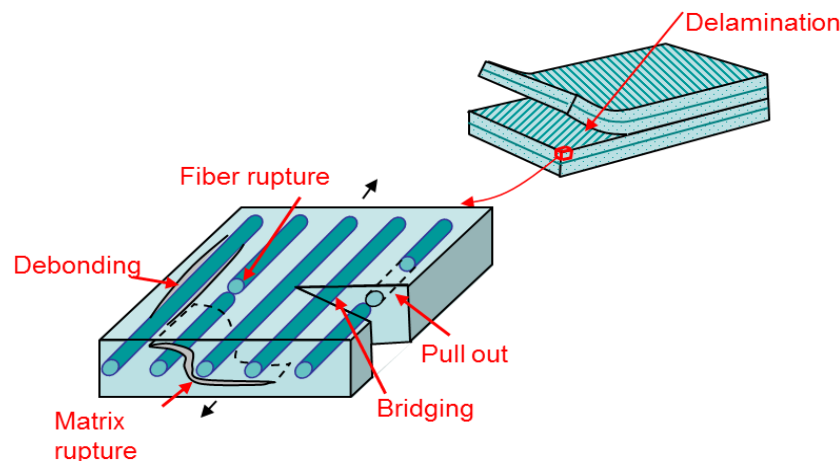
Fig. 1.3. Common failure modes in composite materials [7].

Numerous studies have been conducted on the effect of impact on composite materials [12-15]. Stelldinger et al. [12] found that existence of rubber layers between plies in carbon/epoxy laminate decreases the impact damage, while Topac et al. [13] used high-speed camera to record the evolution of impact fracture in CFRP laminate beam. Toivola et al. [14] observed that a combination of epoxy with a curing agent tetreglycidyl-4`-4 diaminodiphenylmethane with diethylenetriamine produces fluorescence phenomena when an epoxy resin system is subjected to impact, thus revealing even barely visible damage. Li et al. [15] detected presence of impact in CFRP structure using infrared thermography.

Nowadays, the development of advanced micro-mechanics of composite damage has provided the feasibility to express tiny damage in the dynamic model of various composite structures, and many micro-mechanics models of composite damage have been developed, such as the damage model of tensor inner-variables, the damage model of generalized elasticity, the meso-scale damage model, and models of micro-crack damage and crack extension [6].

Matrix cracks perpendicular to the fibre and parallel with the fibre are two kinds of the most salient damage in laminated composite structures. According to the micromechanics damage theory of composites, when multiple cracks occur in some area of a composite plate, there will be variation of the local elastic stiffness. Generally, the matrix crack damage will cause reduction of the elastic moduli in the composite plate, and the smaller the crack number and size, the less the effect on the change of mechanical characteristics of the composite plate [6].

Railway concrete sleepers and bearers are a safety-critical component of the railway system. Despite the fact that there are more than 1 billion concrete sleepers and bearers around the world, their SHM systems have not fully been developed. The key technical barriers to the development include the complexity and the scale of ballasted railway track networks. Railway concrete sleepers are a common term (so-called 'crosstie' in North American) for the cross beams supporting running rails in open plain tracks. They are designed to transfer the load from the rails into the ballast and substructure below and to secure track gauge during train traffics. Another duty of the sleepers is to prevent track movement in longitudinal and lateral directions so that gauge width, track geometry and alignments are maintained for high quality ride comfort. During construction phase, they also act as a platform to construct an accurate line and level of the rail. It is important to note that the sleepers supporting switches and crossings are called 'bearers' in practice since the bearers are designed to structurally support more than just running rails. The duties, design and performance of both sleepers and bearers are thus similar.

In general, railway concrete sleepers are vulnerable to various modes of damage when a railway system possesses unpredictable defects such as wheel flats, rail squats, rolling contact fatigues, and voided ballast beds [16-17]. In railway switches and crossings, the bearers are exposed to inevitable high-intensity impact loadings from the train wheels travelling over crossing nose or changing direction. It is estimated that a sleeper is subjected to around 80 million load cycles or more in a life span, which are inflicted by the presence of defects [18-21]. Using pre-stressing technique improves the loading capacity and fracture characteristics of the concrete [22]. However, a sleeper can fail in several ways during its operational lifetime, including

- flexural cracking;
- longitudinal splitting;
- breakage due to derailment;
- cutting cracks.

The main causes of failure of railway concrete sleepers in North America and worldwide are depicted in Fig. 1.4.

Two main failure mechanisms are the tensile cracking and compressive crushing of the concrete [22]. In [24], for both hard and soft tracks it was flexural cracking that occurred first. Static loading study in [25] also supports this, with flexural cracking occurring first and being the cause of failure at the ultimate capacity load (Fig. 1.5).

Longitudinal fractures relate to the steel tendons, occurring when bonding between the concrete and steel fails. The sudden release of tension in the steel produces stress waves along the interface, splitting the concrete. The sleepers are designed structurally to satisfy the maximum positive moment occurred at the rail seat and the maximum negative bending moment at the mid span, provided that the ballast evenly distributes the load. However, it is often the case that the ballast is not uniform, so these conditions can vary. Literature indicates that flexural cracking at the mid span (or called 'centre-bound crack') is one of the principal failure modes [24, 26, 27] (Fig. 1.6).
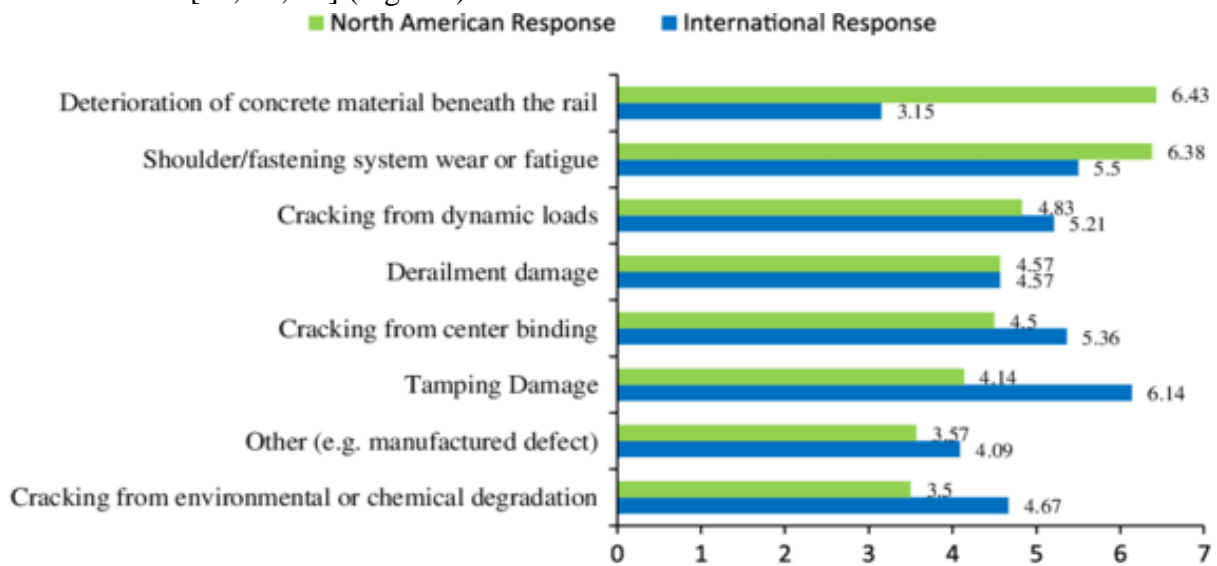
Fig. 1.4. The most critical failures for railway concrete sleepers [23].

17

Fig. 1.5. Failure of railway concrete sleeper due to tensile fracture [23].

(*a*)　　　　　　　　　　　　　　　(*b*)

Fig. 1.6. Cracks in concrete sleepers due to impact loading: (*a*) cracks at the centre of the sleepers; (*b*) cracks near the rail seats [23].

In a flexural static loading simulation and experiments of pre-stressed concrete sleepers in [24], it was demonstrated that after the initiation stage of the crack at the centre of the sleeper it bifurcates and grows horizontally in later stages. With increased loading, numerous cracks initiate around the central crack and propagate vertically. When the central crack is approaching a critical length of failure, it propagates in random directions. Further to these factors, hostile environmental conditions also promote sleeper failure. Pre-stressed concrete structures are also vulnerable to corrosion damage [28]. Steel tendon corrosion will reduce the tensile capacity so the sleeper is more susceptible to dynamic and quasi-static loads. It has been statistically analysed that 1.2% of manufactured sleepers carry defects from which 0.3% are used in secondary lines and the remaining 0.9% are rejected [29].

1.2. Structural Health Monitoring

Terms Structural Health Monitoring (SHM), Non-destructive Testing (NDT) and Condition Monitoring (CM) should not be used interchangeably. According to [30], NDT methods are

used during manufacture process of a part or structure, so that potential flaws are removed at this early stage rather than being repaired later. CM is employed when the component is already in use and its performance needs to be assessed. SHM, on the other hand, uses the information gathered at manufacturing stage when flaws within some tolerance limits were detected by NDT. The ongoing data generated by CM is also taken into consideration for SHM. In this concept (Fig. 1.7), SHM is the overall aim, using NDT for initial evaluation and CM for ongoing assessment. The comparison between Non-Destructive Testing and Structural Health Monitoring is depicted in Table 1.1.

As the damage position is not known a priori, the sensor network must cover the whole structure. Minimum weight and size, connectivity, durability/robustness/repairability and embeddability into the host structural material are critical issue [31].

SHM systems employ the use of sensor network. Depending on structural behaviour and other considerations, actuators may also be used. Based on this distinction, the SHM methods are classified into active and passive (Fig. 1.8).

Fig. 1.7. Relationship between SHM, CM and NDT [30].

Table 1.1

Comparison of NDT and SHM [31]

NDT	SHM
Inspection is done by external probes and equipment	Sensors are permanently attached at fixed locations in the structure
Off-line monitoring, parts need to be disassembled for inspection	On-line monitoring, aircraft inspection may be done in flight or during overnight stops
Time-based maintenance, checks must be regularly spaced	Condition-based maintenance, disassembly only when repairs are required.
Labour intensive	Evaluation done without human intervention
Mature technologies are available	Still under development for real structures

The mostly employed SHM methods for interrogation of composite structures along with their efficiency to detect various failure modes are shown in Table 1.2 with legends E-enabled, D-disabled. These methods are Lamb waves, Electromechanical Impedance (EMI), active

vibration-based, strain-based and acoustic emission. It can be seen that all of these methods are able to detect cracks and delamination and also de-bonding, except for acoustic emission. On the other hand, only acoustic emission is capable to detect impact damages.
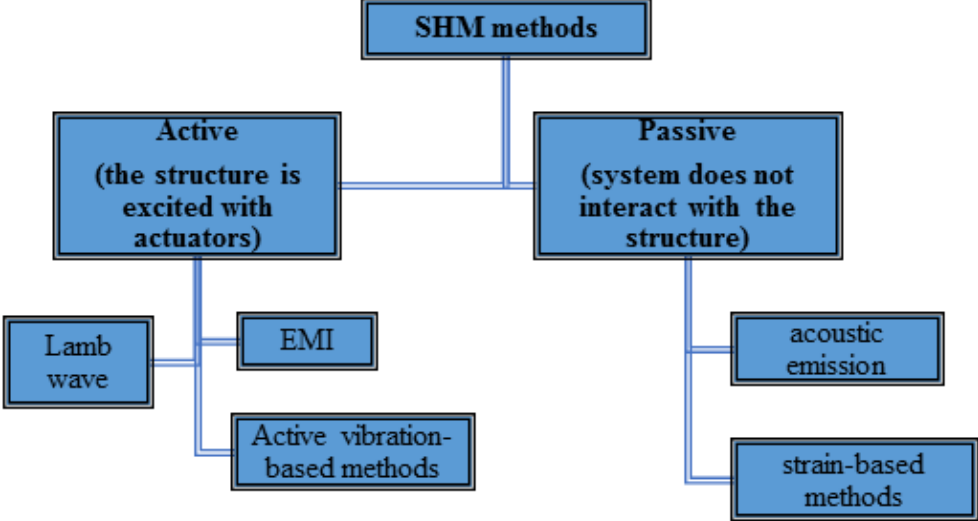
Fig. 1.8. Active and passive SHM methods [3].

Table 1.2

Typical SHM methods for composites [3]

Methods	Sensors	Strain	Impact	De-bonding	Delamination	Crack	Characteristics
Lamb waves	Piezoelectric	D	D	E	E	E	Global monitoring, high sensitivity, on-line and off-line
	Fibre optic sensor	D	D	E	E	E	Global monitoring, requires PZT actuators, limited by high-frequency modulation
EMI	Piezoelectric	D	D	E	E	E	Local monitoring, off-line
Active vibration-based	Piezoelectric & accelerometer	E	D	E	E	E	On-line & off-line, medium and high frequency vibration and acceleration monitoring
	Fibre optic sensor	E	D	E	E	E	On-line & off-line, low frequency (< 1 kHz) vibration monitoring
Strain-based	Resistance strain gauge	E	D	E	E	E	On-line, relying on loads
	Fibre optic sensor	E	D	E	E	E	Distribution measurement, on-line, rely on loads
Acoustic emission	Piezoelectric & Acoustic emission sensor	D	E	D	E	E	On-line

1.2.1. Active SHM

Active vibration-based SHM methods are based on a fact that structural dynamic characteristics are functions of the physical properties, such as mass, stiffness and damping. Therefore, damages, arising with physical property changes, can cause detectable differences in vibration responses. The dynamic characteristic parameters commonly used in the method include frequency, mode shape, power spectrum, mode curvature, frequency response function (FRF), mode flexibility matrix, energy transfer rate, etc. [3]. A typical SHM system based on active vibrations is shown in Fig. 1.9.

An array of PZT are bonded to the structure, one of them is submitted to electric burst, the others capture the elastic waves produced; all the combinations are done, and the response signals are stored. The process is repeated again and again, any damage at the path between two sensors (either direct path or after reflections) will change the received signal; in this way the damage occurrence is detected, and approximately located [31].

The most prominent active SHM methods include Lamb waves and electromechanical impedance spectroscopy. Lamb waves are elastic waves that can propagate in a thin solid plate with wavelengths of the same order of magnitude as the thickness of the plate with free boundaries [3, 4, 32]. Lamb waves are usually excited and received by PZT wafers [3, 4] and sometimes by Fibre Optic Sensors (FOS) [3, 33] and PVDF. There are 2 groups of Lamb waves, symmetric (S) and anti-symmetric (A) [4]. The propagation of Lamb waves on the surface of material is described using dispersion curves which plot the phase and group velocities versus the product of excitation frequency and thickness. The dispersive nature of waves means that the different frequency components of the Lamb waves travel at different speeds and that the shape of the wave packet changes as it propagates through solid media [32, 34]. Derivation of the dispersion curves begins with solution of the wave equation (to find the phase velocity of a wave) which require the information on elastic material properties. This dispersion curve is used to determine a frequency range where only the fundamental modes S_0 and A_0 propagate and to find any non-dispersive regions. After the excitation of the Lamb waves, the time of flight in an oscilloscope between two sensors of known separation is measured. This information can then be used to locate damaged areas along a specimen, without using any analytical models, by observing the disturbed wave between the sensor and actuator. Lamb waves can be transmitted over long distances and they possess high sensitivity to both the surface and the internal defects [3].
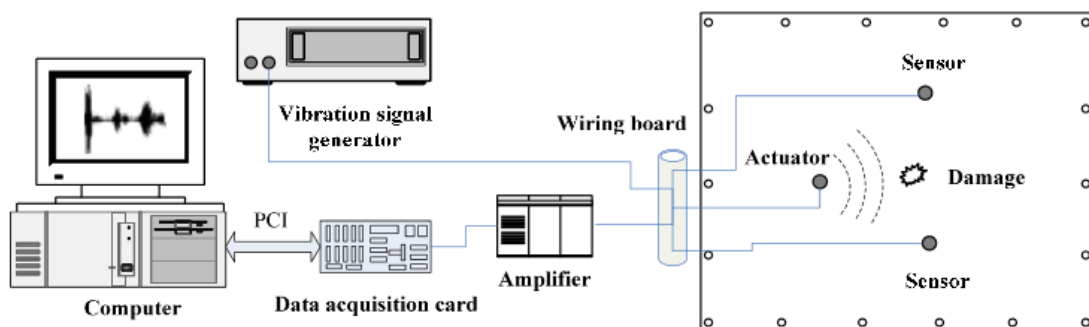
Fig. 1.9. A typical active vibration-based SHM system [3].

Electromechanical impedance (EMI) method is very simple to implement and uses low-cost, small and lightweight piezoelectric sensors and actuators. These sensors consist of adhesive tapes bonded to the host structure that are minimally invasive and can be used in real time and in in-situ SHM systems [35]. To apply PZT as an actuator-sensor simultaneously, a PZT patch bonded to a structure is driven by a fixed alternating electric field. A surface charge is generated in response to an applied mechanical stress (direct piezoelectric effect), and conversely, a mechanical strain is produced in response to an applied electric field (converse piezoelectric effect). The EMI defined as the ratio of the applied voltage and the resulting current can then be measured by a commercially available impedance analyser [36]. The frequency range must be high enough for the signal wavelength to be significantly smaller than the defect size [37]. In general, the EMI is measured at high frequencies in the range of 30–400 kHz. Under this high-frequency range, the wavelength of the excitation is small and sensitive enough to detect minor changes in the structural integrity [36]. Due to the high frequency of excitation used in EMI technique, the monitoring range of effective sensitivity of the PZT transducer is limited to its near vicinity. It has been estimated that the sensing area of a single PZT can vary anywhere from 0.4 m (sensing radius) on composite structures to 2 m on simple metal beams. This localized nature of the sensing region provides an advantage in that the impedance sensor is less sensitive to boundary condition changes or any operational vibrations. On the other hand, this characteristic of limited sensing range usually demands an active sensing network system for real world applications [36].

1.2.2. Passive SHM

Strain measurement

Strain-based method is an effective passive SHM method, because the presence of damage in the structure under normal operational loads can alter the local strain distribution due to the changing load path. It is also useful to know the load state on the structure, which is needed for fatigue life management programs, currently implemented in all the military aircrafts fleets. From local strain measurements damage initiation cannot be detected, except in the very strange coincidence that the sensor position matches the position of the crack. Local cracks do not change the overall strain field, they change only the near field, a few centimetres around the crack [31].

In practical applications, the strain-based method can be performed in two ways. In one way, the strain distribution of the intact structure is measured as the baseline in advance. Damage can be then detected when the current strain measurement significantly diverges from the baseline. In the other way, a theoretical model for the structure is established and analysed to acquire the strain data corresponding to various structural states. Comparing the data to the actually acquired ones directly or with criterions, the structural integrity is evaluated. The key issue lies in this methodology is how to make the model exact enough especially for the complex real-life structure [3].

Acoustic emission

AE technique is based on the detection of elastic surface stress waves caused by the dissipation of elastic energy due to the opening of a crack or plastic deformation [8]. The micro-motion of the tip of the crack excites elastic waves which are acquired by sensors on the surface of the material. Generally, AE waves propagate in the ultrasonic range. The number of recorded signals during loading is connected to the number of active sources within the material [38].

AE is an effective method of imperfection analysis. This mechanical vibration generated by material defects such as matrix micro cracking, fibre-matrix de-bonding, localized delamination, or fibre pull-out and breakage. The stress waves that result from these types of defects spread out concentrically from their origin and are detected by an array of highly sensitive piezoelectric devices. Acoustic emission technique is different from most other NDE techniques in two aspects. The first difference is the origin of the signal. Instead of supplying energy to the object, this method listens to the "sound" generated by energy released in the object. The second difference is the method that AE deals with dynamic processes in a material [39]. The schematic of AE is shown in Fig. 1.10.

Advantages [39]:

- The ability to discern between developing and stagnant defects.
- High sensitivity.
- Fast and global inspection using multiple sensors.
- Permanent sensor mounting for process control.
- No need to disassemble and clean a specimen.
- Very useful in detecting many different damage types (fatigue cracks, fibre fractures, matrix micro-cracks, fibre-matrix de-bonding, and delamination) caused by fatigue loading.

Disadvantages [39]:

- Complex data analysis to correlate acoustic emission data to specific types of damage mechanisms.
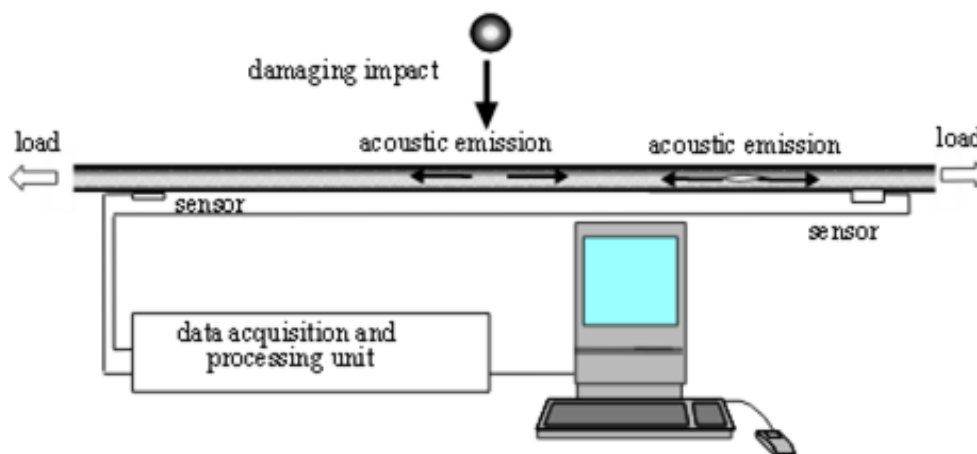
Fig. 1.10. Principal scheme of AE testing [40].

In order to identify the type of damage in composites, which involves fibre failure, the transverse failure and delamination, the acoustic emission (AE) technique is a promising technique [8]. During the past few decades, many successful research works have shown the

23

remarkable capability of AE for early damage detection of composite materials. However, there is a significant challenge for a reliable AE based SHM system for composite structures due to the anisotropic nature of the materials and complicated design and usage. Much research has been undertaken to create more reliable quantitative AE for the SHM of composite structures. A recent study proved *modal acoustic emission* (*MAE*) to be the preferred method for source location detection and failure characterization as it gives more accurate results than traditional AE has been shown to give. This concept fully utilizes the theory of wave propagation in solid media (e.g. beam, thin plates etc.) and signal processing such as spectral analysis and time - frequency analysis. Besides the Lamb's wave analysis, MAE also requires the signal's time-frequency information. For this particular purpose, CWT provides better accuracy for both time and frequency information compared with the STFT method. Several researchers interested in MAE have successfully used CWT, either for source location or for failure characterization [41]. The energy criteria at each wavelet decomposition level can be used to identify the dominant fracture mechanism in an order [8]. Three dominant damage mechanisms (matrix cracking, fibre–matrix de-bonding, and fibre breakage) take place during delamination, while these different damage mechanisms generate different AE parameters. Additionally, the achieved results specified that higher frequencies and amplitudes emerging in the tests were related to fibre breakage, while lower ranges contributed to matrix cracking and fibre–matrix de-bonding damages [9].

If AE transducers are not placed at the appropriate distance from the source, the strength of the extensional waves might be attenuated and lost along their way to the sensors, thus losing the information. Research work on the optimal distance of the transducer from the crack is an essential requirement for the development of an AE based damage detection system [41].

Time of arrival (*TOA*) is another method which is frequently used for AE source location. It uses 2 AE sensors to locate an AE source in a linear direction and 3 sensors for a 2D plate [41].

In [8] standard double cantilevered composite beams were loaded and acoustic emission was recorded. In Fig. 1.10, a load-time plot and its relationship with AE event energy for one specimen is shown. The overlay of acoustic emission activity and loading is used to correlate the occurrence of cracking with high energy acoustic emission and to eventually trace the moment of cracking. In the Fig. 1.11 near the maximum load some AE events are detected and crack is being propagated.

With regards to railway concrete sleepers, crack initiation and propagation detected by acoustic emission (AE) technique are derived from the stress source of deformation within the sleepers. When a load is applied by trains, instigating crack growth, an acoustic signal is emitted from the tip of the crack, identifying its location and growth rate. Authors in [42] showed the feasibility of using AE monitoring applied to concrete structures. The changes of AE parameters reflect structural degradation, such as cracking, ultimately leading to failure. Currently there is a lack of insight into the use of non-destructive technologies (NDTs) within the rail industry and increasing traffic demands placed on track structures have pressed the need for an adequate monitoring system, especially for remote critical assets such as switches and crossings or railway bridges. The integration of NDTs and rail infrastructure for the

development of 'smart tracks' will reduce the risks imposed by any damage to the structure. Therefore, it is valuable to conduct a thorough investigation into SHM systems for practical applications in the future.

   AE sensing is particularly useful in circumstances that require long-term health observation. Once the AE technology has been installed, it can be left to perform SHM without physical maintenance. In 2012, repair works to the Hammersmith flyover in London used over 400 AE sensors for the detection of tendon failure [43]. The sensor network was only partially effective because they were installed decades after the initial construction, so the already defected structure was taken as the baseline condition [44]. Implementation on railway structures would have the same flaw, as damage to the sleepers can only be identified just after the sensor installation. However, the data is still valuable as the sleepers with the most progressive cracking can be identified and classified for track maintenance.
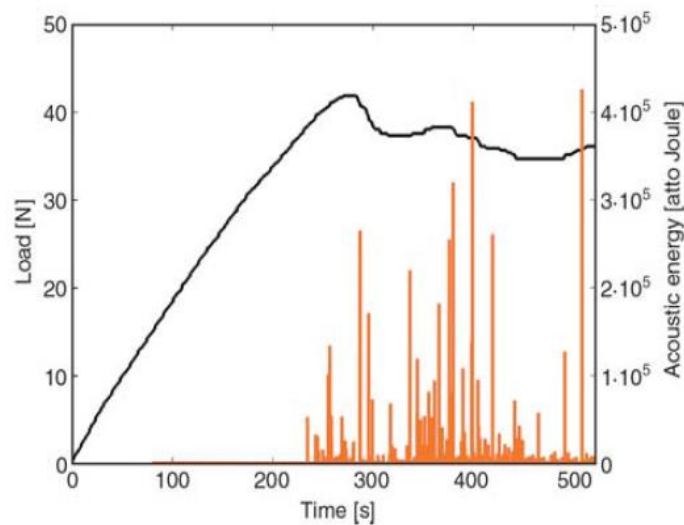
Fig. 1.11. Delamination load and AE signal energy vs. time [8].

1.3. Vibration-based damage identification

   One of the most popular classes of SHM methods is based on structural vibrations. These methods rely on the fact that dynamic characteristics, namely, resonant frequencies, mode shapes and damping are influenced by the stiffness of the structure. Extensive literature reviews on this topic can be found in [45, 46]. Several studies [47-49] have shown that mode shape transformations have been proved to be highly sensitive to damage and could be used for damage detection and quantification. The most serious shortcoming of those methods, however, is a necessity for a baseline data of a healthy structure, which in most cases are difficult or even impossible to obtain. This issue can be solved either by employing Gapped Smoothing Techniques to simulate a healthy structure by generation of a smoothed surface of mode shape curvature or using Wavelet Transform (WT) technique. According to [50] damage detection methods can be classified into 4 levels:

- Level 1. Sensing the presence of damage in the structure;
   The underlying idea of global vibration-based damage identification methods is that dynamic characteristics, for example, resonant frequencies, mode shapes and damping, of the

structure are influenced by the presence of damage [51]. These methods employ mostly the damage induced *resonant frequency shifts* in frequency response spectra and EMI spectroscopy.

- Level 2. Localizing the damage in the structure;

  It is of crucial importance not only to detect presence of damage, but also to determine its location. Among many damage identification methods of SHM, those that are the most widely used, are based on dynamic response of the structure. The underlying idea behind these methods is that the stiffness of the structure decreases locally in the region of damage. The dynamic parameters, mostly resonance frequencies and deflection shapes of the structure are extracted and subjected to some transformation in order to either detect damage or, taking an one step further, localize it. Methods that fall into this cathegory are *Wavelet Transform, Mode Shape Curvature, Modal Flexibility* and *Modal Strain Energy*.

- Level 3. Quantifying the extent of damage;
- Level 4. Predicting the remaining service life of the structure.

1.3.1. Modal methods

Various damage identification methods that are based on mode shapes and their derivatives gained a wide popularity due to ability to assess the structure on a local level [10, 52, 53-56]. These level 2 methods, for example, are: Modal Curvature (MC) [10, 54, 56-58], Modal Flexibility (MF) [56, 59] and Modal Strain Energy (MSE) [59, 60] methods. In MC-based approach, one calculates the 2nd derivative of mode shape and calculates its distribution over length of a beam or surface of a plate. Highest peaks indicate the location of damage. The moment – curvature equation for an isotropic beam is given by [61]

$$\kappa(x) = \frac{M(x)}{EI} \tag{1.1}$$

where $M(x)$ – bending moment, N · m;

x – coordinate in the longitudinal direction of a beam, m;

E – modulus of elasticity, MPa;

I – area moment of inertia, m^4.

If a de-bonding or other damage is present in a structure, it reduces the flexural stiffness EI of the structure at the damaged region, which increases the magnitude of the curvature of the structure at that section. These changes in curvature are local in nature.

MF and MSE methods are based on the fact that presence of damage alters the structural parameters of flexibility (decreases) and strain energy, when structure deforms in its deflection shapes, respectively. The drawback of MC, MF and MSE methods is that there is a necessity in reference data of undamaged structure to which the data obtained from a damaged structure is compared and their difference or ratio is expressed as a damage index.

Mode shape curvature square (MSCS) method, which is based on modal strain energy [62] or modal stiffness [63] comparison between healthy and damaged structure. The need for the modal data of a healthy structure (baseline modal data) is one of the most significant drawbacks

of those methods, as baseline modal data is sometimes difficult or even impossible to obtain. This issue is usually solved by employing Gapped Smoothing Techniques to generate a smoothed surface of mode shape curvature, thus simulating a healthy state of the structure [10].

Many studies [48, 49, 53, 64-81] confirm that mode shapes and corresponding mode shape curvatures are highly sensitive to damage and can be used for detection and quantification of the damage. Maia et al. in [68] performed extensive numerical simulations on a beam structure to compare damage identification sensitivity within different methods, based on the changes of mode shape, mode shape slope, mode shape curvature and mode shape curvature square, respectively. These methods were also tested experimentally on a steel beam with free-free boundary conditions. The authors found that MSCS method performed better in both numerical and experimental cases.

Fu et al. in [70] exploited a damage identification approach based on local reduction of Young's modulus in a structure by performing numerical simulations of forced vibration response under external force in a cantilevered steel plate. The authors studied single as well as multiple damage scenarios with different levels of noise contamination and measurement point reduction. The researchers concluded that the algorithm is effective and robust for both single and multiple sites of damage. Multiple crack scenarios were also studied by Khiem et al. in [49]. The authors derived a simplified expression of resonant vibration modes of a beam with an arbitrary number of cracks, which, in combination with a regularization method, allows for estimation of both location and size of multiple cracks. Results indicated that the proposed algorithm was successful at damage identification even at sparse and noisy data conditions. Perez et al. in [71] conducted a series of experiments on low-velocity impact damage according to ASTM standards in numerous composite laminated plates. The damage identification procedure consisted of rigorous study of the following damage indicators – frequency shift, mode shape changes and curvature of mode shape changes – all due to damage. The authors concluded that it was hard to make a general conclusion on whether these damage indicators are effectively applicable to all composite structures because the results are highly dependent on the number of measured degrees of freedom and modes. Hammad et al. [72] proposed to treat the undamaged zones of the beam as linear elastic, whereas the zones containing multiple cracks are assigned a nonlinear behaviour, thus improving an existing crack model. Results showed that sensitivity of changes in vibration characteristics were proportional to stiffness of a beam support; however, as damage severity increased, the respective change of non-linearity did not follow the monotonic trend; therefore, it cannot be used for damage detection. Hsu et al. [73] suggested a local flexibility method built on a pseudo-local virtual force action on the structure to identify local changes in stiffness in hyperstatic beams. Damage detection studies employed variation of a number of mode shapes. Results showed that only few modes are sufficient in order to identify the damage. Modal strain energy changes in damage identification were exploited by numerous of researchers. Shih et al. in [74] showed that damage can be assessed through changes of resonant frequencies, modal flexibility and modal strain energy. The approach was tested on a full scale slab-on-girder bridge with different damage scenarios. Researchers found that resonant frequency differences were dependent on location and severity of damage, however Beskhyroun et al. in [75] employed operational deflection shapes (ODS)

from the entire frequency range of interest instead of just resonant frequencies. Their studies showed that damage had an influence not only on resonant frequencies, but on other frequencies as well and in some cases the effect of damage on structure was more pronounced at these other frequencies. In [81] the authors claimed that the location of damage could be found from the peaks in the changes of modal flexibility and modal strain energy. Ooijevaar et al. in [76] used a modal strain energy damage index and later standardization of this index according to statistical hypothesis approach, as well as mode shape curvatures, obtained in vibration measurements, to identify impact damage in two advanced skin stiffener composite structures (in 1D and 2D). Results indicated that this method is capable of detecting, localizing and also roughly quantifying the size of barely visible impact damage, although the methodology is affected by design of the structure and position of the damage and it is crucial to understand the failure mechanisms. Several visual methods are also incorporated in damage detection. Alves et al. in [77] proposed a pattern recognition technique to identify the damage – the main features of the undamaged system are set as reference, while the corresponding features of the damaged structure are extracted and compared to the reference. Any significant deviation is considered to be a signature of damage. The researchers considered a simply supported steel beam excited with a hammer and shaker with 5 different damage scenarios. The authors concluded that this algorithm is successful, although the data obtained from impact testing was classified with higher accuracy than that obtained with a shaker. Dworakowski et al. in [78] used a digital image correlation to build a deflection curve of a cantilevered beam. After the introduction of damage these curves were fitted to 2 line segments and an angle between segments was taken as a damage index. The authors argued that this methodology utilizes a global damage detection approach using the whole deflection curve at once, therefore giving a noise-free result representation. This approach is capable of detecting small cracks that are not visible to the naked eye. Mosalam et al. in [79] used scanning laser stations to visualize and assess the damage of various structures in laboratory conditions, as well as in post-earthquake fields. The researchers justified their approach stating that it is possible to make 3D deformation pattern scans of real objects with high accuracy, post-processing of the obtained graphical images, the method permits a convenient access to the object by scanning from a distance, however it is possible to acquire data only form visible surfaces. Dincal et al. in [80, 81] proposed a damage detection procedure for beam structures, employing Euler-Bernoulli beam theory. This procedure is based on the assumption that internal stresses in a structure are invariant before and after the application of damage. The damage index was taken as the ratio of the flexural stiffness of the damaged and healthy structure and it reveals singularities in a curvature profile of a beam structure. The algorithm was validated in an experiment using a cantilevered beam capturing the location, extent and severity of the damage with no significant errors. The same team of authors in [78] attempted to evaluate their own damage identification mechanism [77] by using field measurements – modal data from the Interstate 40 bridge, where four incremental damage sites were introduced via torch cuts in the web and flange of the girder of the bridge. The researchers used the modal flexibility matrix, which was used to approximate the transverse displacements of structure. They argued that each row of the modal flexibility matrix can be interpreted as the deformed shape of a structure because of a unit load applied at the

corresponding degree of freedom. Results showed that damage was successfully localized and its severity estimated. In most of these papers the absolute difference in the mode shape data between the healthy and the damaged state of structure is defined as damage index, and the maximum value typically indicates the location of damage.

1.3.2. Continuous wavelet transform

In the case of Fourier transform, the signal is deconstructed into sine and cosine waves that are infinitely long, giving large resolution in frequency, while having large uncertainty in time. Fourier transform cannot find the instantaneous frequency of a signal, that is, the exact frequency of a signal at an exact moment in time [82]. *Wavelets* $\psi(t)$, on the other hand, are special functions with small oscillations, so that they have zero mean as opposed to harmonic periodic sine and cosine functions. Some examples of wavelets in time domain are shown in Fig. 1.12.

When a signal is deconstructed into wavelets being added together, it is called wavelet transform. Wavelets are limited in time and frequency. As wavelets are limited in time, it also provides more resolution in time domain as a finite wave can be translated along the time axis. To provide the desired resolution in time, wavelets can be either compressed (for high frequencies) or expanded (for low frequencies) by altering scale or dilation parameter [82]. Example of wavelet at different scale and position in time is depicted in Fig. 1.13.
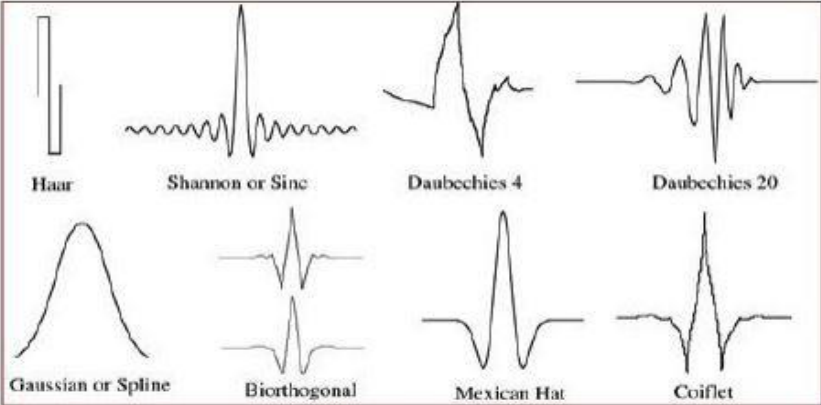
Fig. 1.12. Common wavelet functions [82].
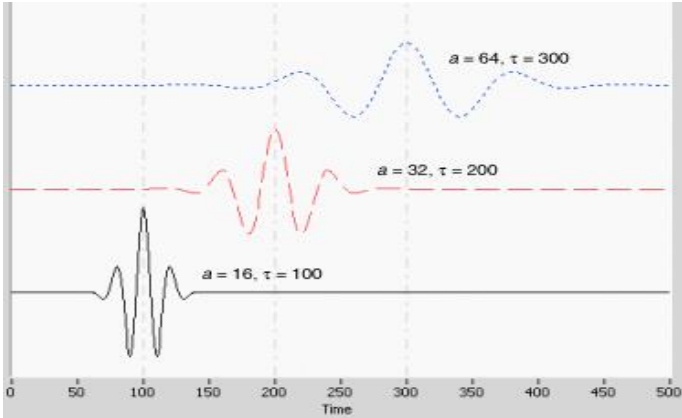
Fig. 1.13. Wavelet at different scales and moments in time [82].

By applying the wavelet transform, a signal is deconstructed using the same wavelet at different scales [82]. The procedure of wavelet transform is as follows [83]:

- Pick a wavelet and compare it to the first section of the signal and calculate the correlation coefficient (Fig. 1.14 (*a*));
- Shift the wavelet to the right and repeat the step 1 until the whole signal is covered (Fig. 1.14 (*b*));
- Scale the wavelet and repeat the steps 1 through 2 (Fig. 1.14 (*c*));
- Repeat steps 1 through 3 for all scales.
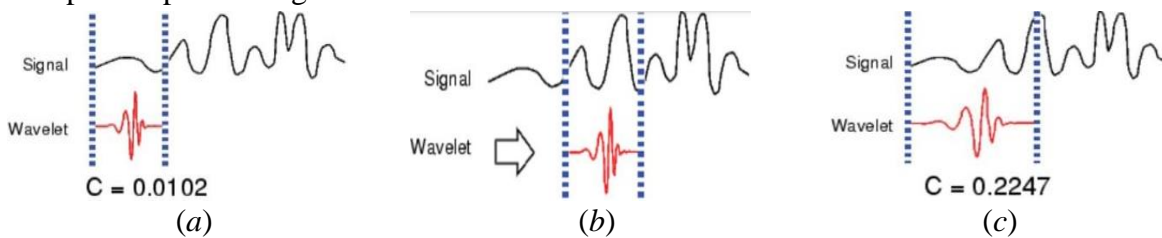
Fig. 1.14. Illustration of wavelet transform [83].

Continuous wavelet transform (CWT) is a signal processing technique gaining popularity in civil, electric, aerospace, mechanical and other engineering communities. Wavelet theory has been developed since the beginning of the 20th century by Haar, but it did not result in a unified theory. A current wavelet analysis as we-know-it was introduced by Grossman and Morlet in 1984. Later, in 1989 Mallat founded wavelet theory for signal decomposition [84]. Wavelet transform technique originated in the 1990's and was mainly used for signal singularity detection [84], image compression [85], noise removal from signals [86-90], pathology detection in medicine [91] and structural damage detection. The first study of damage detection based on wavelet-transformed vibration data of buildings caused by underground trains and road traffic was carried out by Newland in 1990's [84, 92, 93].

Identification of faults is one of top priorities in the field of machinery – one-dimensional wavelet transform with different modifications supplemented with auxiliary algorithms has been used to detect flaws in bearings [94-99], gears [100] and gearboxes [101]. Fei et al. in [94] calculated relative energies of 4th layer wavelet decomposition coefficients of vibration signals obtained from a damaged bearing. This data was later used as a diagnostic feature of a damage fault. Yan et al. in [95] proposed a wavelet function selection procedure for Wavelet Packet Transform technique to assess the damage. Combet et al. [100] proposed an integrated modulus of wavelet bicoherence based on Morlet wavelet to extract the tooth damage features from a vibration signal of a faulty gear.

Numerous studies have exploited one-dimensional wavelet transform for damage identification in beam structures with single damage [102-112] and multiple damages [113-114]. Gokdag et al. in [107] combined both, CWT and Discrete Wavelet Transform (DWT) to extract the damage features form vibration modes of a beam. Authors used the symlet wavelets of different orders to test the Modal Assurance Criterion involving damaged and healthy modes. Xu et al. in [105] performed a CWT technique to detect crack tips in beams with horizontally embedded cracks using Gaussian wavelets of orders 2 and 3. Montanari et al. in [103] applied a padding method to reduce the edge effects of measured vibration modes of a beam. This

method was based on a definition of extension functions to fit the original noisy data applying the least squares algorithm and afterwards a CWT was used to detect the damage using this modified data. Interesting studies in [93] proposed to classify wavelet-based methods for damage detection into 3 groups: 1) variation of wavelet coefficients [109, 115], 2) local perturbation of wavelet coefficients in space domain, 3) reflected wave caused by local damage. The first of these methods is used to find the existence and severity of damage and is based on the fact that variation of wavelet transform coefficients is caused by change of modal parameters of the structure. The second method is used to localize the damage in structures by detection of irregularity of wavelet transform coefficients near the damage site. The third method is used to measure the severity as well as location of the damage. It is based on the analysis of the wave reflected from local damage in the structure. Work similar to the third method was done in [116]. Authors suggested wavelet transform technique for signal processing to distinguish between the changes in wave propagation, caused by local discontinuities and cracks in beams and rods. In [111] Janeliukstis et al. performed a CWT on aluminium beams subjected to clamped-clamped and free-free boundary conditions, while in [112] researchers used this procedure on polymer composite beams. In both cases CWT algorithm showed promising damage identification results, however a suitable wavelet function had to be chosen based on damage estimate reliability versus wavelet scale analysis.

Apart from the damage localization methods stated above, lately the most attention is directed to the Wavelet Transform (WT) method and its different modifications, which mainly include Continuous WT, Discrete WT and also Wavelet Packet Transform (WPT) methods. This attention is justified by the fact that the WT methods do not require a reference information on a healthy structure and one can localize damage using data exclusively from a damaged structure. Large number of studies are devoted to damage localization in beam and plate structures using WT. Particular interest lies in damage localization in composite plates as those are widely used in advanced structures and vehicles. Vast studies on this subject have been conducted by Katunin et al. [117-121]. In [117], a crack damage was identified in a CFRP laminate rotor blade with complex nonlinear geometry using different variations of 2-D WT. The conclusion was that the Discrete WT using B-spline wavelet function provided the best damage identification results. In [118] and [119], laminated polymer composite plates with an artificial damage were considered and their mode shapes were used in damage localization using two-dimensional WT applying fractional B-spline wavelets with continuous parametric optimization. Study [121] was devoted to low-velocity impact damage localization in composite plates. Mode shapes were measured and used as an input data in the Discrete WT. Results suggested that quincux nonseparable wavelets were able to detect even damage of low energy (different diameter impactors were used). These results were also supported with ultrasonic C-scans. In [120] honeycomb sandwich composite plates were subjected to typical composite damage, such as delaminations, cracks of a core and sheets and impact damages that occur most frequently in a manufacturing and service process of a structure. Two-dimensional Discrete WT was performed on experimentally measured mode shapes of the plates and damage was successfully localized using fractional B-spline wavelets. Damage localization in composite plates was also conducted in [48], where 2-D Continuous WT was compared with

2-D Strain Energy and 2-D Gapped Smoothing methods and proved to be superior in terms of immunity to noise and reduced sensor data. Huang et al. [122] performed 2-D Continuous WT of a strain data of a loaded simply supported plate with integrated sensor network. Conclusion was that the method was not only able to locate damage, but also to assess its severity. Yan et al. [6] investigated the possibility to detect damage in epoxy/glass fiber composite laminate plate with embedded piezoelectric actuator and sensors. Structural response was decomposed using WPT and damage was successfully detected. Quiao et al. in [123] applied a 2D CWT algorithm on numerically simulated mode shapes of a plate with different failure modes. They also compared this method to other techniques, such as 2D Gapped Smoothing method and 2D Strain Energy method and found that 2D CWT outperformed other algorithms in terms of robustness to noise and sensor spacing. A two-dimensional version of CWT has been applied to plate structures [124, 125].

WT has been also applied in case of real industrial objects, such as wind turbines [52, 126]. A fusion of wavelet transform and modal curvature methods is presented in [102] to detect multiple damage sites in CFRP beams. As in [127, 124], a scanning laser vibrometer was used as automated and reliable means to measure deflection shapes with an option to tailor the signal size of deflection shapes and frequency response function. Choi et al. in [128] employed a laser to visualize ultrasonic wave propagation in metal welding. They wavelet-transformed the images of wave propagation and exploited the wavelet scalogram to enhance the visibility of damage by focusing on the frequency, that is characteristic to damage-inducing waves.

Detection of failure in concrete members poses significant challenges, in particular, due to anisotropy of the material and complexity of structure in case of reinforcement. Nevertheless, some studies are conducted on this matter. Kaewunruen et. al in [129, 130] has been studying health condition of railway concrete sleepers by conducting dynamic analysis under various boundary conditions and comparing modal parameters (resonant frequencies and damping ratios) of sleepers at healthy state and after subjection to different severities of impact loading. Other researchers have attempted to localize the damage in concrete structures by applying wavelet analysis [131-134]. In [131] wavelet packet transform with Morlet wavelet was used on vibration signals of concrete plates with embedded steel bars. Energy and relative entropy distributions were calculated for different lengths of de-bonding between steel bars and concrete matrix. Results suggest that these wavelet techniques are sensitive to this mode of damage. In [132] Complex Morlet wavelet was used in CWT to conduct time-frequency analysis of bridge concrete column subjected to seismic loading. Changes of resonant frequencies due to damage were detected. Researchers in [133] exploited feasibility of wavelet packet transform to detect de-bonding between concrete and steel in a steel tube filled with concrete. Energy of a wavelet packet-decomposed vibration signal, collected with PZT sensors, was computed and compared to another damage index, based on root-square mean deviation of signal energy features. In [134] researchers presented a finite element model based on polynomial wavelets which are a linear combination of Legendre polynomials. These were used to characterize hybrid-mixed stresses in L-shaped concrete plate. Melhem et. al in [135] compared the performance of wavelet and Fourier transforms to detect damage in Portland cement concrete pavements and simply supported concrete beams subjected to fatigue loading.

1.4. Supervised learning using extraction of damage-sensitive features

The vast exploitation of mass-produced structural components, such as wind turbine blades, aircraft wings, bearings in rotating machinery and the like, has raised demands for advanced Condition Monitoring (CM) methods [136]. Damage in these structural parts causes a significant downtime and is associated with considerable repair costs and oftentimes requires direct access to the structure in question [137, 138]. Moreover, damage may oftentimes not be visible to the naked eye – it may lie hidden between interfaces of the structure [139]. Effective methods will be able to detect damage in components of interest thus alarming that the particular component has to be replaced.

CM is a multidisciplinary field spanning mechanical, aerospace, computer and civil engineering sectors. With the development of machine learning concepts, the methodologies from regression and classification were transferred to the domain of structural damage identification where they have been successfully applied to capture the damage. Different classifier models exist for such purposes. Those models can be either simple linear or complex non-linear ones depending on the decision boundaries between classes. The common examples of linear classifiers include linear discriminant, decision trees and Naïve Bayes. The typical non-linear methods are neural networks, k-nearest neighbours (k-NN) among others. These learning methods can also be divided into supervised methods where data is grouped based on class labels or unsupervised methods, such as clustering where no data labels are assigned [140, 141].

Data classification algorithms, such as decision trees, k-nearest neighbours, Naïve Bayes, support vector machines and other hold a potential to be applied in damage detection methodologies based on relevant feature extraction from vibration signals of monitored structures. Decision trees along with the k-nearest neighbour methods are one of the most widely used classification techniques. Numerous examples of successful fault detection of rotating members in automotive and electrical engineering industry can be found in literature [142-146]. In [143] the vibration signals were collected from machining tools and subjected to statistical feature extraction using principle component analysis and decision trees for service life prediction. k-nearest neighbours were applied to vibration signals of bearings in electric traction motors to detect and classify the type of degradation [145] and the problem of fault detection in induction motors employing a pattern recognition of current and voltage signatures by k-nearest neighbours was tackled in [146].

So far, classification algorithms in structural damage identification have been successfully applied in either binary classification problems, for example, to classify whether the structure is healthy or not or multiclass classification distinguishing between different states of structural health [147-163]. In [151] authors applied a two-stage classification scheme to classify the health of joints bonding between skin and spar of composite plate by collecting amplitude-modulated ultrasonic wave signals. The first stage was to classify if the bonding is healthy or not and the second stage attempted at classifying various levels of dis-bonding. In [152] the dimensionality of acceleration signals acquired from multi-story steel frame structures with varying stiffness was reduced with principal component analysis and Sammon mapping

technique. *k*-NN classifier and linear vector quantization were used to classify the damage severity. It was shown that the Mahalanobis distance proved superior over the traditional Euclidean distance. Decision trees classifier was applied to classify if elastic strains exceed some threshold value in a cross-section of a particle/fiber filled composite material under uniaxial tension in [153]. In [154, 155] the feasibility of damage identification in carbon polymer composite plate instrumented with piezoelectric transducers using *k*-NN algorithm was studied. Structural response time series were recorded through sensors. Sensor fusion approach was used and different options of *k*-NN classifiers available in *Matlab*™ Classification application were studied and it was concluded that fine and weighted *k*-NN options provided the best damage classification results distinguishing between healthy plate and different damage scenarios. Points of large pressure measured with optical FBG sensors on an aluminium sandwich structure were successfully localized with distance discriminant in [156]. In [157] researchers used Gaussian discriminant analysis to classify whether a delamination or matrix cracking occurred in cyclically loaded carbon composite laminates of different lay-up instrumented with piezoelectric actuators and sensors. Results showed that a misclassification rate of 21 % was achieved. Damage severity was classified in an aircraft grade aluminium plate by inducing Lamb waves in [158]. Various classifiers were compared, including *k*-NN and variations of linear and quadratic classifiers. The highest classification accuracies were obtained with quadratic discriminant classifier reaching 80.7 %. Linear discriminant classifier was employed to classify impact damage severity of composite plates in [159]. Wavelet packet coefficients were used as damage sensitive feature and it was demonstrated that the classification accuracy increased when using higher numbers of wavelet packets. *k*-NN, quadratic discriminant, decision trees and artificial neural networks were used to classify delamination area in composite wind turbine blades in [160]. It was found that artificial neural networks classifier performed the best, followed by weighted *k*-NN, decision trees and quadratic discriminant as the least performing. In [161] a defect classification framework of composite laminate panels subjected to heat pulse was developed. Temperature decay was approximated by exponential model distinguishing between homogeneous and defective parts of the plate. The defective part hosting various defects was examined for classification of defect type, namely, internal, surface or no defects. Out of the classifiers tested (decision trees, decision forests and *k*-NN (with and without distance weighting)), decision forests proved to be superior with classification accuracy of 99.47 %. Principal component analysis has been applied to classify different delamination states in smart composites [162] and damage severities by incrementing added mass in [163]. In [164] k-NN was successfully adopted on numerically simulated data for classifying healthy, damaged and noisy patterns (up to 20 % noise) of time-delayed signals gathered from sensors installed on an aircraft wing stabilizer structure. In [165] strain pattern recognition using nearest neighbours combined with 2D principal component analysis was carried out on a simply supported plate with different hole sizes.

Different classification schemes are applied to concrete structures for distinguishing between different aspects of structural conditions. For example, the classification of fracture modes [166-172] where a decision on type of the fracture is based on a marginal separating

points in RA value/average frequency plane. Points above this margin refer to tensile cracking, while the ones below – to shear cracks. In [170] the AE technique was applied to cylindrical concrete pipes and it was shown that corrosion and macro cracks-induced damage can be distinguished by applying Kernel Density Estimation Function (KDFE). Researchers in [172] proposed to couple AE monitoring with Digital Image Correlation (DIC) technique to assess the various damage-induced structural features, such as crack length and profile of horizontal displacement in the cross-section of structural concrete. In [173, 174], a Gaussian mixture modelling (GMM) was employed to enhance the classification of cracks. Gaussian mixture is essentially a superposition of Gaussian functions leading to a kind of multivariate probabilistic analysis that allows to group large quantity of data into several clusters. In [175] the AE events in a reinforced concrete block specimens were localized in 3-D and clustered into 4 clusters depending on the amplitudes and angles of the emitted acoustic P-waves. Clusters were formed by inverting a relative moment tensor. In [176] the visual images of wooden sleepers were used in a structural condition classification scheme based on support vector machines and multi-layer perceptron. The scheme classified sleepers to belong to either "good" or "bad" category with a classification rate of 90 %. Researchers in [177] used the mutual relationship between calm ratio and load ratio of AE signals to classify damage in reinforced concrete slabs into categories, such as "minor damage", "intermediate damage" and "heavy damage".

Pattern recognition techniques are widely applied to key structural elements mostly to classify either the failure modes or the nature of damage itself. There are two types of pattern recognition approaches. When the type of damage mechanism is known the supervised pattern recognition is used. On the other hand, the unsupervised pattern recognition is used to select damage sensitive features when no information on damage is available [178]. In the following studies wavelet transform is used as an aid in the extracted AE data processing. In [179], various damage mechanisms in glass/epoxy composite laminates were classified with the aid of fuzzy-c means clustering enhanced with principal component analysis (PCA) coupled with wavelet packet transform (WPT). Separated clusters included matrix cracking and fibre-matrix de-bonding. These damage modes were also verified by SEM images. In [180], researchers used wavelet de-noising of acquired AE waveform data of corroded stainless steel specimens and applied a Random Forest (RF) and k-Nearest Neighbour (k-NN) classifiers to classify the data. A new decision rule, called security voting has been applied to enhance the decision rate of the classic majority voting rule.

1.4.1. Classification algorithms - k-nearest neighbours

The nearest-neighbour method was first used by statisticians in early 1950's. In 1960's it was adopted as a classification scheme and since then has been widely used in pattern recognition [181]. *k-nearest-neighbour algorithm* is a form of learning where training instances are stored and each new instance is tested on resemblance to the existing instances through the means of a distance metric. This new instance is labelled as one of the classes of instances based on the closest distance to an instance (nearest neighbour) of the same class. If more than one nearest neighbour is used, then the majority class of the closest k neighbours is assigned to the

new instance [181]. It is imperative to apply the distance weights in case if several points lie near the decision boundary. Points farher from the query point (point to be classified) are assigned smaller weights than closer points due to respectively, smaller and larger likelihood of the query point to belong to the class of these data points.

The decision boundaries of nonlinear methods like k-NN are locally linear segments, but in general have a complex shape that is not equivalent to a line in two dimensions or a hyperplane in higher dimensions. These boundaries are also variable. If a problem is nonlinear and its class boundaries cannot be approximated well with linear hyperplanes, then nonlinear classifiers are often more accurate than linear classifiers [182]. It is usually desirable to have as much training data as possible in machine learning, but in k-NN large training sets come with a severe efficiency penalty in classification [182].

1.4.2. Classification algorithms – Linear discriminant

Linear classifier is a classifier that decides class membership by comparing a linear combination of the features to a threshold [182]. In two dimensions, a linear classifier is a line with the functional form

$$w_1 x_1 + w_2 x_2 = b \tag{1.2}$$

where $(x_1 \quad x_2)^T$ – two-dimensional vector of the data;

$\quad (w_1 \quad w_2)^T$ – the parameter vector that defines (together with b) the decision boundary.

The rule of classification is to assign the data point a class A if $w_1 x_1 + w_2 x_2 > b$ or class B if $w_1 x_1 + w_2 x_2 \leq b$.

Linear methods can only model one type of class boundary, a linear hyperplane [182]. Discriminant classification models assume that different classes y generate data x based on different Gaussian distributions. The space of x values divides into regions where a classification y is a particular value. For linear discriminant analysis the regions are separated by straight lines. Classification based on linear discriminant involves the following steps:

- Classifier training – the fitting function estimates the parameters of a Gaussian distribution for each class:
  - o the sample mean

$$\hat{\mu} = \frac{\sum_{n=1}^{N} M_{nk} x_n}{\sum_{n=1}^{N} M_{nk}} \tag{1.3}$$

where $M_{nk} - N \times K$ class membership matrix with the property

$$M_{nk} = \begin{cases} 1 \text{ if observation } n \text{ is from class } k \\ \quad 0 \text{ otherwise} \end{cases} \tag{1.4}$$

  - o the sample covariance is calculated by first subtracting the sample mean of each class from the observations of that class, and taking the empirical covariance matrix of the result

$$\hat{\Sigma} = \frac{\sum_{n=1}^{N} \sum_{k=1}^{K} M_{nk} (x_n - \hat{\mu}_k)(x_n - \hat{\mu}_k)^T}{N - K} \tag{1.5}$$

(the model has the same covariance matrix for each class, only the means vary).

- Prediction of the new data – the trained classifier finds the class with the smallest misclassification cost

$$\hat{y} = \underset{y=1,\dots,K}{\operatorname{argmin}} \sum_{k=1}^{K} \hat{P}(k|x)C(y|k) \tag{1.6}$$

where $\hat{y}$ – the predicted classification;

K – the number of classes;

$\hat{P}(k|x)$ – the posterior probability of class k for observation x.

Posterior probability is a product of prior probability (either with uniform or empirical distribution) and a likelihood function (which is usually of multivariate normal density). $C(y|k)$ is the cost of classifying an observation as y when its true class is k.

Linear discriminant classifiers have the option of regularization – finding an optimum set of parameters γ and ϵ that lead to an effective predictive model. The amount of regularization γ is responsible for regularizing the covariance and correlation matrices of data X as

$$\widetilde{\boldsymbol{\Sigma}} = (1 - \gamma)\boldsymbol{\Sigma} + \gamma \operatorname{diag}(\hat{X}^T * \hat{X}) \tag{1.7}$$

and

$$\widetilde{\boldsymbol{C}} = (1 - \gamma)\boldsymbol{C} + \gamma \boldsymbol{I} \tag{1.8}$$

where $\boldsymbol{\Sigma}$ – non-regularized covariance matrix of data X;

$\hat{X}$ – centred version of data X;

$\boldsymbol{C}$ – non-regularized correlation matrix of X;

$\boldsymbol{I}$ – identity matrix.

The linear term in regularized discriminant classifier for a data point x from a vector X is

$$(x - \mu_0)^T \widetilde{\boldsymbol{\Sigma}}^{-1}(\mu_k - \mu_0) \tag{1.9}$$
$$= \left[(x - \mu_0)^T \left(\operatorname{diag}(\hat{X}^T * \hat{X}) \right)^{-1/2} \right] \left[\widetilde{\boldsymbol{C}}^{-1} \left(\operatorname{diag}(\hat{X}^T * \hat{X}) \right)^{-1/2} (\mu_k - \mu_0) \right]$$

where μ_k – mean vector of elements from class k in a vector X;

μ_0 – vector of means of rows of vector X.

Regularization parameter ϵ (not to be confused with)is a threshold applied to the last term in square brackets in Eq. (1.9) as

$$\left| \widetilde{\boldsymbol{C}}^{-1} \left(\operatorname{diag}(\hat{X}^T * \hat{X}) \right)^{-1/2} (\mu_k - \mu_0) \right| \leq \epsilon \tag{1.10}$$

If Eq. (1.10) holds true, each component of the vector $\left[\widetilde{\boldsymbol{C}}^{-1} \left(\operatorname{diag}(\hat{X}^T * \hat{X}) \right)^{-1/2} (\mu_k - \mu_0) \right]$ is set to zero. For class k, if component j is thresholded to zero, component j of x does not enter into the evaluation of the posterior probability.

1.4.3. Classification algorithms – Decision trees

Nodes in a *decision tree* involve testing a particular attribute; usually this attribute is compared with a constant. Leaf nodes give a classification that applies to all instances that reach

the leaf. To classify an unknown instance, it is routed down the tree according to the values of the attributes tested in successive nodes and when a leaf is reached the instance is classified according to the class of a leaf.

If the attribute that is tested at the node is numeric, this test determines whether its values is greater or less than some constant, giving a 2-way split (*binary trees*). Each leave contains a numeric value that is the average of all the training set values to which the leaf applies. Decision trees that predict numeric quantities are called *regression trees* [181]. An example of a decision tree used in classification of damage in terms of severity is shown in Fig. 1.15.

Decision trees have been widely used in damage prediction for civil engineering applications, such as reinforced concrete buildings [183] exposed to seismic risk where the statistical damage classification is necessary to discern the buildings in need for retrofitting [184]. Mechbal et al. in [185] proposed to use multiclass support vector machines in conjunction with decision tree technique to obtain posterior probabilities of existence, as well as a location of damage in composite plate. Artificial damage of different severities was simulated and applied in different positions of the plate. The proposed method proved to successfully locate the damage in most cases.
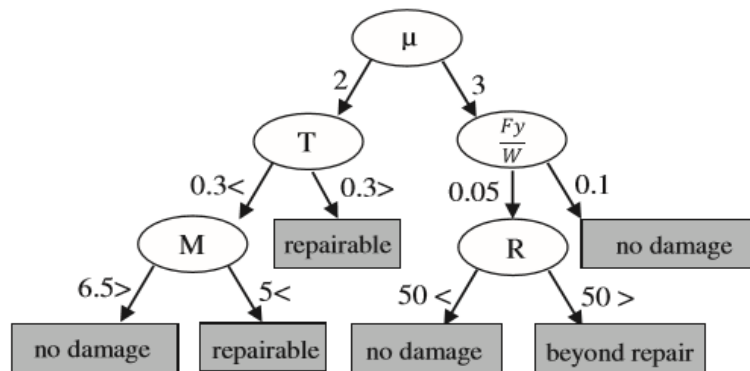
Figure 1.15. Example of a decision tree [183].

1.4.4. Data partitioning

Generally, the whole dataset can be divided into 3 parts [181]:

- *Training data* which is used to build classifiers;
- *Validation data* to optimize parameters of classifier;
- *Testing data* (not used in the formation of the classifier) is used to calculate the error rate of the final, optimized model to predict the performance of the classifier on a new data.

Various validation schems exist. In K-fold *cross-validation* one decides on a fixed number of folds to partition the data in. For K number of folds, the data is split into K approximately equal partitions and each in turn is used for testing while the remainder is used for training. The whole procedure is repeated K times so that every instance has been used exactly once for testing.

In general, the larger the training sample, the better the classifier, although the returns begin to decrease once a certain amount of data is exceeded. Also, the larger the test sample, the more accurate the error estimate.

1.4.5. Performance optimization and evaluation

Important feature to assess the performance of any classifier is the loss function. The larger the losses, the poorer the classification model, hence more inaccurate results of classification.

Cross-validation loss is an average loss for observations not used for training. In K-fold cross validation for every fold K, a classification loss for in-fold observations using a model trained on out-of-fold observations is computed. In *Matlab*™ environment, each observation j from a data sample of size n is assigned weights w_j. The observation weights are normalized to unity

$$\sum_{j=1}^{\eta} w_j = 1 \tag{1.11}$$

so that they sum to the corresponding prior class probability. The weighted fraction of misclassification for the observed class label y_j is

$$L = \sum_{j=1}^{\eta} w_j \boldsymbol{I}\{\hat{y}_j \neq y_j\} \tag{1.12}$$

where $\hat{y}_j$ – class label corresponding to the class with the maximal posterior probability;

$\boldsymbol{I}\{x\}$ – indicator function.

A total of four classification outcomes are possible:
- *true positives* (TP) – data is correctly classified as positive;
- *true negatives* (TN) – data is correctly classified as negative;
- *false positives* (FP) – outcome is incorrectly classified as positive when it is negative;
- *false negatives* (FN) – outcome is incorrectly classified as negative when it is positive;

TP and FP are correct classifications, while classifications FP and FN are incorrect. Overall *success rate* (SR) is computed as

$$SR = \frac{TP + TN}{TP + TN + FP + FN} \tag{1.13}$$

Optimization of these parameters is imperative for successful classification of data.

In multiclass prediction, the result in a test set is displayed as a *confusion matrix* with a row and column for each class. Each matrix element shows the number of test samples for which the actual class is the row and predicted class is the column. Good results correspond to large numbers down the main diagonal and, ideally zero, off-diagonal elements [181]. Fig. 1.16 shows a confusion matrix of data with 4 classes, marked as NOT (no damage), DMG1 (damage 1), DMG2 (damage 2) and DMG3 (damage 3). Figure to the left shows unsatisfactory classification results with a lot of misclassifications, while that to the right shows the best possible classification.
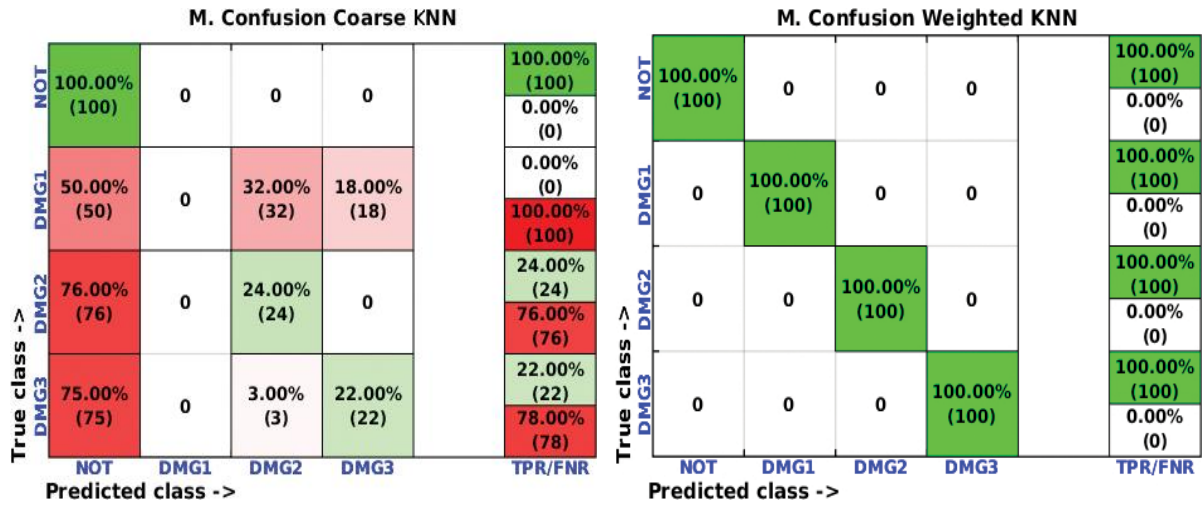
Fig. 1.16. Confusion matrices for a damage detection problem [186].

2. DAMAGE LOCALIZATION ALGORITHMS

This chapter introduces damage localization algorithms developed in this thesis. These algorithms are based on Continuous Wavelet Transform (CWT), Mode Shape Curvature Square (MSCS), a new algorithm based on normalized wavelet scalogram (TVNWS) and classification algorithms, such as *k*-nearest neighbours, decision trees and linear discriminant. MSCS and CWT with a spatial variable are widely used in damage detection and localization in beam and plate structures. The drawback of MSCS method − a need for the data of the healthy structure − is solved using an interpolation technique with a Fourier series approximation, simulating smooth mode shape curvature curve of the healthy beams and polynomial smoothing technique for plate structures.

2.1 Continuous spatial wavelet transform

Wavelets $\psi(t)$ are special functions with small oscillations, so that they have zero mean. Wavelets possess several distinctive properties, such as
- support width;
- may be orthogonal/biorthogonal;
- may be symmetric/asymmetric;
- the majority of wavelets are grouped in families, for example, Mexican Hat (mexh, esmexh, gabmexh), Derivative of Gaussian (dog, dog2, dog3), Morlet (morl, isomorl, esmorl, rmorl), etc.;
- isotropic or orthotropic in dependence on that how their properties depend on rotational angle in a plane.

If $\psi(x)$ (1-D) or $\psi(x, y)$ (2-D) is a *wavelet mother function*, then the set of wavelet family functions $\psi_{s,a}(x)$ (1-D) or $\psi_{s,a,b}(x, y)$ (2-D) is created by translating over x or/and y axes (respective parameters a and b) and dilating (parameter s) the $\psi_{s,a}(x)$ (1-D) or $\psi_{s,a,b}(x, y)$ (2-D) [86, 109, 187]:

$$\psi_{s,a}(x) = \frac{1}{\sqrt{|s|}} \psi\left(\frac{x - a}{s}\right) \tag{2.1}$$

$$\psi_{s,a,b}(x, y) = \frac{1}{\sqrt{s^2}} \psi\left(\frac{x - a}{s}, \frac{x - b}{s}\right) \tag{2.2}$$

WT is a digital signal processing technique, capable of managing analysis of continuous as well as transient signals in time domain. WT is used to transform the original signal into a different domain where additional data analysis becomes possible. Wavelet analysis is usually performed in time-frequency domain, indicating that wavelets have a period and a frequency. This wavelet frequency is called central frequency of wavelet and it can be imagined as a frequency that wavelet would have if it has sinusoidal nature. Wavelet pseudo frequencies are obtained by dividing the central frequency with a scale parameter s. The scale parameter, also known as dilation parameter, is a real positive number, that depicts a compression $(0 < s < 1)$, when window function is very narrow, therefore it is appropriate for high-frequency components. On the other hand, a tension $(s > 1)$ of wavelet function along abscissa axis gives

rise to the very wide windows that are suitable for the low-frequency components of the signal [187, 188]. This concept is based on *Heisenberg uncertainty principle*, which states that it is not possible to obtain high resolution in frequency and time simultaneously [93]. WT can adopt a flexible time-frequency window, thus this method exceeds different Fourier transform sub techniques [109]. Spatial wavelet analysis is performed, as the name implies, in spatial domain, simply replacing time with coordinate, giving rise to wavelet function (in 2-D) $\psi(x, y)$ [92, 113].

In its nature, WT is a convolution of analysed signal $f(x, y)$ with a wavelet function $\psi(x, y)$ [105] and measures actually a correlation between $f(x, y)$ and $\psi(x, y)$ [121]. For a given value of s, $\psi(x, y)$ translates along x and y axes and convolves with every segment of signal $f(x, y)$. Large magnitude transform coefficients indicate places with high degree of correlation and vice versa.

In SHM this technique is employed to reveal damage-affected signal portion. In the damage identification procedure, large WT coefficients appear as spikes in WT plots of y versus x. The coordinates that correspond to these spikes contain the location of damage because damage can be imagined as a discontinuity of a signal.

The 1-D and 2-D CWT for a two-dimensional signal and isotropic wavelets is given by [86]

$$W_{s,a} = \frac{1}{\sqrt{|s|}} \int f(x)\psi^* \left(\frac{x-a}{s}\right) dx = \int f(x)\psi^*_{s,a}(x) dx \qquad (2.3)$$

$$W_{s,a,b} = \frac{1}{\sqrt{s^2}} \iint f(x,y) \cdot \psi^* \left(\frac{x-a}{s}, \frac{y-b}{s}\right) dxdy = \iint f(x,y) \cdot \psi^*_{s,a,b}(x,y) dxdy \qquad (2.4)$$

where asterisk denotes complex conjugation. These wavelet transform coefficients are extremely sensitive to any discontinuities and singularities of signal $f(x, y)$ therefore damage due to a sudden loss of stiffness can be detected in mode shapes that have large amplitude wavelet coefficients. It is a damaged location.

Damage index for each of mode shapes is depicted as follows

$$DI^n_{i,s} = W^n_{i,s} = \int_L w^n_i \psi^*_{s,a}(x) dx \qquad (2.5)$$

$$DI^n_{i,j,s} = W^n_{i,j,s} = \iint_S w^n_{i,j} \psi^*_{s,a,b}(x,y) dxdy \qquad (2.6)$$

where w^n – the measured transverse displacement of the structure;

$\quad n$ – mode number;

$\quad i$ – number of grid points in x direction;

$\quad j$ – number of grid points in y direction;

$\quad L$ – length of a beam, m;

$\quad S$ – surface of a plate, m^2.

However, mode shapes, measured in experimental conditions, are always contaminated by measurement noise, which may lead to false peaks in damage index profiles, thus misleading data interpretation. In order to overcome this problem, it is proposed to summarize the results

for all modes. The summarized damage index is then defined as the average summation of damage indices for all modes and normalized with respect to the largest value of each mode

$$DI_{i,s} = \frac{1}{N} \sum_{n=1}^{N} \frac{DI_{i,s}^n}{\max(DI_{i,s}^n)} \quad (2.7)$$

$$DI_{i,j,s} = \frac{1}{N} \sum_{n=1}^{N} \frac{DI_{i,j,s}^n}{\max(DI_{i,j,s}^n)} \quad (2.8)$$

where N – total number of modes.

According to [60, 189], these damage indices are then standardized and a concept of statistical hypothesis testing is applied to classify damaged and healthy elements and to localize damage depending on the pre-defined damage threshold value. In order to test the hypothesis, the normalized damage index, given in Eq. (2.7) and Eq. (2.8), is standardized yielding *standardized damage index*

$$SDI_{i,s} = \frac{DI_{i,s} - \mu_s}{\sigma_s} \quad (2.9)$$

$$SDI_{i,j,s} = \frac{DI_{i,j,s} - \mu_s}{\sigma_s} \quad (2.10)$$

where μ_s – scale-dependent mean value of damage indices $DI_{i,s}$ and $DI_{i,j,s}$;

σ_s – scale-dependent standard deviation of damage indices $DI_{i,s}$ and $DI_{i,j,s}$.

The decision for the localization of damage is established based on the level of significance used in the hypothesis test, which can be determined from a pre-assigned classification criterion:

a) choose null-hypothesis H_0 (element i of the structure is healthy) if $SDI_{i,s} < C_r$ ($SDI_{i,j,s} < C_r$);

b) choose alternate hypothesis H_1 (element i of the structure is damaged) if $SDI_{i,s} \geq C_r$ ($SDI_{i,j,s} \geq C_r$),

where C_r is a threshold value. Tipical C_r values, widely used in literature are 1.28, 2 and 3 for 90 %, 95 % and 99 % confidence levels for the presence of damage.

A new damage metric, called *damage estimate reliability* is introduced in an attempt to quantify the performance of each of wavelet functions in terms of the reliability of damage localization. For a one-dimensional problem DER is calculated by splitting the whole length of an object (beam in our case) into 2 parts:

a) – the zone of damage:

b) – the rest of the object.

These two zones are identified based on a priori knowledge about the exact location of damage. In each of these parts standardized damage indices are summed up and divided by the number of sample points yielding an average standardized damage index $\overline{SDI_{i,s}}$ ($\overline{SDI_{i,j,s}}$) in a respective part. DER is a ratio of an average SDI in part a) divided by an average SDI in all parts combined and expressed in percentage as:

$$DER_s = 100\% \cdot \frac{\alpha^{-1} \sum_{i=1}^{\alpha} SDI_{i,s}}{A^{-1} \sum_{i=1}^{A} SDI_{i,s}} = 100\% \cdot \frac{\overline{(SDI_{i,s})}_a}{\overline{(SDI_{i,s})}_b} \qquad (2.11)$$

$$DER_s = 100\% \cdot \frac{(\alpha\beta)^{-1} \sum_{j=1}^{\beta} \sum_{i=1}^{\alpha} SDI_{i,j,s}}{(AB)^{-1} \sum_{j=1}^{B} \sum_{i=1}^{A} SDI_{i,j,s}} = 100\% \cdot \frac{\overline{(SDI_{i,J,s})}_a}{\overline{(SDI_{i,J,s})}_b} \qquad (2.12)$$

where α – number of SDI DOFs in the zone of damage in x direction;

β – number of SDI DOFs in the zone of damage in y direction;

A – total number of SDI DOFs along the x direction;

B – total number of SDI DOFs along the x direction.

For 1-D case, SDI distributions are calculated for all 78 wavelets, each at 128 scale parameters (aluminium beams and CFRP beam) and for 16 wavelets in 2-D case, each at 16 scale parameters (CFRP beam with deflection shapes measured in 2-D). A DER value corresponding to each scale is calculated.

A large variety of different wavelet functions is present in wavelet analysis. These functions are grouped in families, for example, daubechies, symlet, coiflet, biothogonal wavelets and more. Members of each family are distinguished by an order of the wavelet function. These orders may range from 1 to 10 or larger. Taking this into account, there are many possibilities for WT. Unfortunately, not all of these functions perform equally well in damage detection.

In practice, one cannot predict the optimum wavelet function for damage identification, therefore all different wavelet functions available in $Matlab^{TM}$ Wavelet Toolbox are tested. A number given next to the wavelet name indicates the order (number of vanishing moments) of the wavelet (refer to Table 2.1).

Table 2.1

Short-hand labels of wavelet functions, found in $Matlab^{TM}$ Toolbox

Daubechies	Coiflet	Symlet	Gaus	Bi-orthogonal	Reverse bi-orthogonal	Complex gaus	Complex morlet	Shannon
db2	coif1	sym1	gaus1	bior1.1	rbio1.1	cgau1	cmor 1-1	shan1-1
db3	coif2	sym2	gaus2	bior1.3	rbio1.3	cgau2	cmor 1-1.5	shan1-1.5
db4	coif3	sym3	gaus3	bior1.5	rbio1.5	cgau3	cmor 1-0.1	shan1-0.1
db5	coif4	sym4	gaus4	bior2.2	rbio2.2	cgau4	cmor 1-0.5	shan1-0.5
db6	coif5	sym5	gaus5	bior2.4	rbio2.4	cgau5		shan2-3
db7		sym6	gaus6	bior2.6	rbio2.6			
db8		sym7	gaus7	bior2.8	rbio2.8			
db9		sym8	gaus8	bior3.1	rbio3.1			
db10				bior3.3	rbio3.3			
				bior3.5	rbio3.5			
				bior3.7	rbio3.7			
				bior3.9	rbio3.9			
				bior4.4	rbio4.4			
				bior5.5	rbio5.5			
				bior6.8	rbio6.8			

2.2 Thresholded variance of normalized wavelet scalogram

Detection of the most energetic features in the signal at different scale and time or space is of particular interest in damage identification. Such three-dimensional plots of coefficients of CWT are known as *wavelet scalograms* [190, 191]. More beneficial, however is a *normalized wavelet scalogram* (NWS). Regions of maxima in NWS are called wavelet transform ridges – these are used for determination of instantaneous frequency of a signal [191]. These ridges also correspond to time or, in case of spatial WT, - a coordinate with the most energetic features of the signal. It is well known that zones of damage attain large values of WT coefficients, therefore ridges in a NWS denote the location of damage for a spatial CWT.

In most cases, the presence of damage modifies the vibration signal in a way that the portion of signal affected by damage has relatively larger energy than other parts of this signal. Hence, detection of these energetic portions of a signal can reveal the location of damage. One of the most effective techniques is the construction of wavelet scalograms which are 3-D plots consisting of coefficients of CWT with respect to wavelet scale and dimension of the structure. *Wavelet scalogram* is essentially a squared magnitude of WT coefficients.

$$WS_{s,a(i)} = \left|W_{s,a(i)}\right|^2 \tag{2.13}$$

More beneficial in localization of a fault, however is a *normalized wavelet scalogram* (NWS), where WT coefficients are first normalized with respect to scale parameter

$$NWS_{s,a(i)} = \left|\frac{W_{s,a(i)}}{s}\right|^2 \tag{2.14}$$

In this work, damage metric is defined as a *variance of a normalized wavelet scalogram* with respect to scale parameter and expressed as follows

$$S_{a(i)} = \sigma^2\left(NWS_{s,a(i)}, s\right) \tag{2.15}$$

Eq. (2.15) is used to calculate variance distributions for all 78 wavelet functions (Table 2.1). The reason for testing such a large number of wavelets lies in the fact that the performance of each individual wavelet function is not known prior to actually testing it. The shape of analysed signal is different in every situation; thus it is recommended to test all available wavelets.

Universal threshold is applied to variance distribution for every wavelet function to filter out the insignificant values of $S_{a(i)}$. Universal threshold is defined as

$$T = \sigma\sqrt{2\ln(A)} = \frac{MAD}{0.6745}\sqrt{2\ln(A)} = \frac{\text{Median}\left|S_{a(i)} - \text{Median}\left(S_{a(i)}\right)\right|}{0.6745}\sqrt{2\ln(A)} \tag{2.16}$$

where σ – the standard deviation of noise of $S_{a(i)}$;

A – number of DOFs in a mode shape signal;

MAD – Median Absolute Deviation.

MAD is the median value of the absolute difference between every sample of the signal and it`s median. The value of 0.6745 in the denominator makes the estimate unbiased for the normal distribution.

Originally, this threshold was adapted in image noise reduction routine by using wavelets [192-194]. The $S_{a(i)}$ values that do not pass the threshold value T, are assigned a value of zero,

otherwise these value are assigned a value of 1, giving *thresholded variance of normalized wavelet scalogram*

$$\text{if}(S_{a(i)} \geq T) \rightarrow TS_{a(i)} = 1$$
$$\text{else} \rightarrow TS_{a(i)} = 0 \tag{2.17}$$

Values of $TS_{a(i)}$ are summed up over all 78 wavelet functions for each i, yielding *summarized thresholded variance of normalized wavelet scalogram*

$$\Lambda_{a(i)} = \sum_{j=1}^{78} TS_{a(i),j} \tag{2.18}$$

All i values of $\Lambda_{a(i)}$ are summed together to yield *total thresholded variance of normalized wavelet scalogram*

$$\Theta = \sum_{i=1}^{A} \sum_{j=1}^{78} TS_{a(i),j} = \sum_{i=1}^{A} \Lambda_{a(i)} \tag{2.19}$$

$\Lambda_{a(i)}$ is expressed in percent of Θ for each i, giving *fractional thresholded variance of normalized wavelet scalogram*

$$Z_{a(i)} = 100 \cdot \Lambda_{a(i)} / \Theta \tag{2.20}$$

The universal threshold (T_2 to distinguish from threshold applied to $S_{a(i)}$) is applied to $Z_{a(i)}$ so just the most significant peaks remain and the logical decision as the one stated in Eq. (2.17) is applied once more

$$\text{if}(Z_{a(i)} \geq T_2) \rightarrow TZ_{a(i)} = 1$$
$$\text{else} \rightarrow TZ_{a(i)} = 0 \tag{2.21}$$

The final decision on the location of damage is based on those coordinates x (related to i) that correspond to $Z_{a(i)}$ values that have passed the universal threshold T_2.

2.3. Mode shape curvature square

The majority of various damage detection methods based on mode shape transformations require the baseline data of the healthy structure as a reference for comparison with any future damage-induced changes of dynamic parameters. In real life, this data is rarely available, especially for structures that are already in exploitation.

This thesis provides means to estimate a state of a healthy structure through an interpolation technique applying a Fourier series approximation on a mode shape curvature data of the damaged structure, thus generating smooth mode shape curvature curves.

The Fourier series is used to describe a periodic signal by splitting it in a harmonic series comprising of sine and cosine terms. The trigonometric form of Fourier series is

$$\kappa(x) = a_0 + \sum_{i=1}^{u} a_i \cos(u\omega x) + b_i \sin(u\omega x) \tag{2.22}$$

where a_0 – constant (intercept) term in the data and is associated with the $i = 0$ cosine term;

ω – the fundamental frequency of the signal;

u – the number of harmonics or order of a series.

In this study, the mode shape curvature data of beams is approximated with Fourier series functions of orders 1-8. The obtained coefficient values a_0, a_i, b_i and ω are used to reconstruct the approximation of mode shape curvature data using Eq. (2.22). The damage index DI is defined as the absolute difference between the measured curvature of the damaged structure and reconstruction of the mode shape curvature approximation with Fourier series representing the healthy structure. The locations of abrupt large amplitude DI increase are attributed a location of damage according to the algorithm. The damage index for all deflection shapes at a grid point i is expressed as follows

$$DI_i^n = \left| \left(\frac{\partial^2 w^n}{\partial x^2} \right)_{(i)}^2 - \kappa_x^{n\,2}{}_{(i)} \right| \tag{2.23}$$

where κ_x^n is a reconstructed mode shape curvature data in one dimension (x direction), m^{-2}.

It must be noted that the value of the calculated mode shape curvature as well as approximation reconstruction at grid point are normalized with respect to the largest value of each component. The calculation of mode shape curvatures is performed by the central difference approximation of mode shapes at grid point i as:

$$\left(\frac{\partial^2 w^n}{\partial x^2} \right)_{(i)} = \frac{w_{i+1}^n - 2w_i^n + w_{i-1}^n}{h^2} \tag{2.24}$$

where h – the distance between two successive nodes or measured points, m.

For more than one deflection shape used, the damage index is calculated using Eq. (2.7). Afterwards, this damage index is also standardized (refer to Eq. (2.9.)), leading to SDI. DER values are also obtained.

Damage localization algorithm is extended to two dimensions to tackle the problem in plate-type structures.

The mode shape curvature of a healthy structure has a smooth surface and is obtained by a polynomial approximation. This procedure is carried out using a mode shape curvature of a damaged structure and applying a least-squares fitting technique with the following steps at each data point [195]:

- Regression weights are calculated using a tri-cube function:

$$w_i = \left(1 - \left| \frac{x - x_i}{\mathrm{d}(x)} \right|^3 \right)^3 \tag{2.25}$$

where x – the predictor value associated with the response value to be smoothed;

$\quad x_i$ – the nearest neighbours of x as defined by the span;

$\quad \mathrm{d}(x)$ – the distance along the abscissa from x to the most distant predictor value within the span.

These weights possess the following properties:

- o The data point to be smoothed has the largest weight and the most influence on the least-squares fit.

- o   Data points outside the span have no weight and no influence on the fit.
- A weighted linear least-squares regression is carried out.
- The smoothed value is given by the weighted regression at the predictor value.

Two-dimensional MSCS method is adopted with a following relation for a damage index for n^{th} mode at a grid point (i, j):

$$DI_{i,j}^n = \left| \left(\frac{\partial^2 w^n}{\partial x^2} \right)^2_{(i,j)} - \kappa_x^{n2}{}_{(i,j)} \right| + \left| \left(\frac{\partial^2 w^n}{\partial y^2} \right)^2_{(i,j)} - \kappa_y^{n2}{}_{(i,j)} \right| \tag{2.26}$$

where κ_x^n – smoothed mode shape curvature surface in x direction, m^{-2};

κ_y^n – smoothed mode shape curvature surface in y direction, m^{-2}.

The mode shape curvatures are calculated from the mode shapes by the central difference approximation at grid point (i, j) as:

$$\begin{aligned}
\left(\frac{\partial^2 w^n}{\partial x^2} \right)_{(i,j)} &= \frac{w_{i+1,j}^n - 2w_{i,j}^n + w_{i-1,j}^n}{h^2} \\
\left(\frac{\partial^2 w^n}{\partial y^2} \right)_{(i,j)} &= \frac{w_{i,j+1}^n - 2w_{i,j}^n + w_{i,j-1}^n}{h^2}
\end{aligned} \tag{2.27}$$

2.4. Data classification

The problem of Condition Monitoring (CM) of structural elements is addressed from a machine learning point of view. Machine learning algorithms, such as one-class kernel classifier [196] have proven to be an effective tool in pinpointing the location of damage in real structural elements – steel frames. However, the damage has to be close to one of the sensors. The proposed algorithm enhances the traditional CM approach by taking it one step further – besides providing the information on whether or not the damage is present, damage localization scheme is adopted as in [185, 197]. Current study serves as a continuation of the study in [198]. This method is developed specifically for two-dimensional structural elements, such as wind turbine blades, airplane wings or hull elements that are scheduled for regular structural inspection to pinpoint the location of damage. The realization of the algorithm is implemented through the following steps:

1.   Harmonic analysis of a structural part is carried out to identify the resonant frequencies.
2.   Structural part equipped with an actuator is partitioned into arbitrary number of zones (which serve as class labels) and a point mass is applied in each zone an arbitrary number of times.
3.   At each event of application of point mass, the real and imaginary values of strain corresponding to the maximum amplitude of the harmonic strain response (at each frequency from step 2) due to applied harmonic force from the actuator are extracted and strain magnitude is computed according to

$$|\varepsilon| = \sqrt{\left(\mathrm{Re}(\varepsilon) \right)^2 + \left(\mathrm{Im}(\varepsilon) \right)^2} \tag{2.28}$$

where $\mathrm{Re}(\varepsilon)$ – real part of the complex strain response;

$\text{Im}(\varepsilon)$ – imaginary part of the complex strain response.

It is known that the application of mass will cause a shift of resonant frequency peaks of the structure with respect to the healthy state. Amplitudes of strain readings will decrease in correlation with the magnitude of this frequency shift. With small enough frequency shift it is possible for strain sensors to capture strain readings from a particular frequency peak at a lower amplitude than the peak value (healthy state) but still within peak limits, hence signalizing damage. According to [199], strain response provides more useful information regarding damage assessment and monitoring than conventional acceleration measurements.

4. These extracted strain data is organized into separate matrices for each of the identified resonant frequencies

$$1^{\text{st}} \text{ frequency} \qquad\qquad\qquad \text{last frequency} \qquad\qquad (2.29)$$

$$\begin{pmatrix} \{1\}_{m\times1} & \{|\varepsilon_1|\}_{m\times1} & \{|\varepsilon_2|\}_{m\times1} \\ ... & ... & ... \\ \{n\}_{m\times1} & \{|\varepsilon_1|\}_{m\times1} & \{|\varepsilon_2|\}_{m\times1} \end{pmatrix}_{n\times k+1} \begin{pmatrix} \{1\}_{m\times1} & \{|\varepsilon_1|\}_{m\times1} & \{|\varepsilon_2|\}_{m\times1} \\ ... & ... & ... \\ \{n\}_{m\times1} & \{|\varepsilon_1|\}_{m\times1} & \{|\varepsilon_2|\}_{m\times1} \end{pmatrix}_{n\times k+1}$$

where m – number of points per each class;

n – number of zones the part is partitioned into;

k – number of strain sensors on the part.

The curvy braces denote vector entities. By using finite element modelling, all of the simulated damage scenarios can be compiled into a sort of catalogue for the particular structural component. Then, by observing response data of a real damaged structure measured by real sensors, conclusions on damage location and severity can be drawn and adequate actions taken.

5. Two different supervised learning algorithms – linear discriminant and non-linear k-NN are used to build classifiers from the acquired strain data for each of the resonant frequencies separately. The justification behind choosing these classifiers is that the linear discriminant is a simple one with few hyperparameters to optimize, while k-NN is a simple, though non-linear algorithm.

6. K-fold cross-validation scheme is adopted to tune the parameters of classifiers and avoid overfitting.

7. Unknown query points are introduced in different locations of the plate and this data is passed to the built classifiers to predict the labels (zones) for these points. These query points are then localized by seeking the smallest difference between their strain signatures and strains from built classification models. Also, the issue of proximity of defect to the sensor is avoided in this case.

8. The final results of the methodology are displayed in terms of distributions of prediction probability along every zone of the structure for each of query points and both classifiers.

PART I – MODE SHAPE TRANSFORMATIONS

3. DAMAGE LOCALIZATION IN 1-D STRUCTURES

This chapter aims at numerically and experimentally demonstrating applicability and effectiveness of three mode shape transform methods – Thresholded Variance of Normalized Wavelet scalogram (TVNWS), Mode Shape Curvature Square (MSCS), Continuous Wavelet Transform (CWT) with a spatial variable – for damage localization in aluminium beams containing one and two mill-cut damage sites, as well as a CFRP beam with an impact damage, all subjected to clamped-clamped boundary conditions.

3.1. Case study 1: Aluminium beams with a mill-cut damage

3.1.1. Numerical model

Commercial finite element program *Ansys*^{TM} is used to build numerical models of all structures considered in this thesis.

Geometrical configuration of aluminium beams is shown in Fig. 3.1. One beam with one site of mill-cut damage and one beam with two mill-cut damages are considered with dimensions matching the ones for experimental study. FE model of aluminium beams consists of 2D beam elements. Each node has 3 degrees of freedom, namely translations along the X and Y axes and rotation along the Z axis. Beams are constructed by means of 148 equal length elements ($i = 149$ nodes). The elastic material properties are taken as follows: $E = 69$ GPa, $\nu = 0.31$, $\rho = 2708$ kg/m^3. The damage is modelled by reducing the flexural stiffness EI of the selected elements, which is achieved by decreasing the thickness of elements in the damaged region of the beam.

In order to compare the sensitivity of the damage identification algorithm to noisy experimental data, a uniformly distributed random noise was added to the numerically simulated mode shapes

$$w^n = \widetilde{w}^n \times \left(1 + \delta(2r - 1)\right) \tag{3.1}$$

where $\widetilde{w}^n$ – noise free transverse displacement of the structure;

r – the uniformly distributed random values in the interval $(0, 1)$;

δ – the noise level, %.
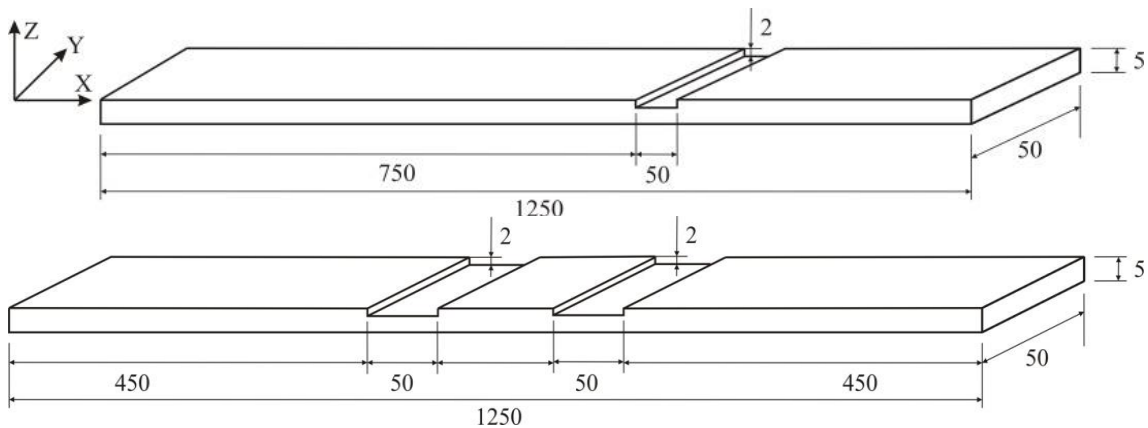
Fig. 3.1. Geometry of aluminium beams (in mm).

It is often not possible to equip the structure with a dense grid of sensors. Therefore an additional study was conducted where numerical mode shape data was divided by integer numbers $p = 1, 2, 3, 4, 5, 6$.

Damage localization procedure employing all 3 algorithms (CWT, MSCS and TVNWS) is carried out using numerically simulated mode shapes contaminated with noise with the levels of $\delta = 0.5\ \%$, $1\ \%$, $2\ \%$ and $4\ \%$. The application of noise implies variation in damage localization results as mode shape vectors themselves are varied. Hence, for a rigorous treatment of such a variability a statistical analysis is carried out where damage localization procedure is run 100 times for every combination of noise level and sensor density. These combinations are depicted in Table 3.1.

The reason why no runs are carried out at noise levels 1 % and 2 % for all sensor densities, except $p = 1$ is that the largest sensitivity to parameter variations is observed for the largest sensor density. As for coarser sensor grids, only the lowest and highest limits of variability ($\delta = 0.5\ \%, 4\ \%$) are of interest in this work.

For each of these 100 runs, the best (largest) DER values for CWT and MSCS methods and a single value of DER* for TVNWS are recorded along with respective standardized damage index profiles. These best values are characterized by an average value over 100 runs and a confidence interval implying the confidence level of 95 % according to Eq. (3.2)

$$x = \bar{x} \pm z^* \frac{\sigma}{\sqrt{\eta}} \qquad (3.2)$$

where x – SDI and DER value;

z^* – number of standard deviations from standardized normal (Z-distribution);

σ – standard deviation;

η – sample size.

In case of 95 % confidence level $z^* = 1.96$. ($\eta = 100$ for 100 runs from Table 3.1).

Table 3.1

Parametric study combinations with number of runs shown for aluminium beams

$\delta(\%)/p$	1	2	3	4	5	6
0.5	x100	x100	x100	x100	x100	x100
1	x100	-	-	-	-	-
2	x100	-	-	-	-	-
4	x100	x100	x100	x100	x100	x100

3.1.2. Dynamic vibration test

Specimens under test are two aluminium beams labelled as Al beam 1d (1 damage site) and Al beam 2d (2 damage sites) (Fig. 3.2) with the same dimensions and locations of damage as in a numerical model in Fig. 3.1.
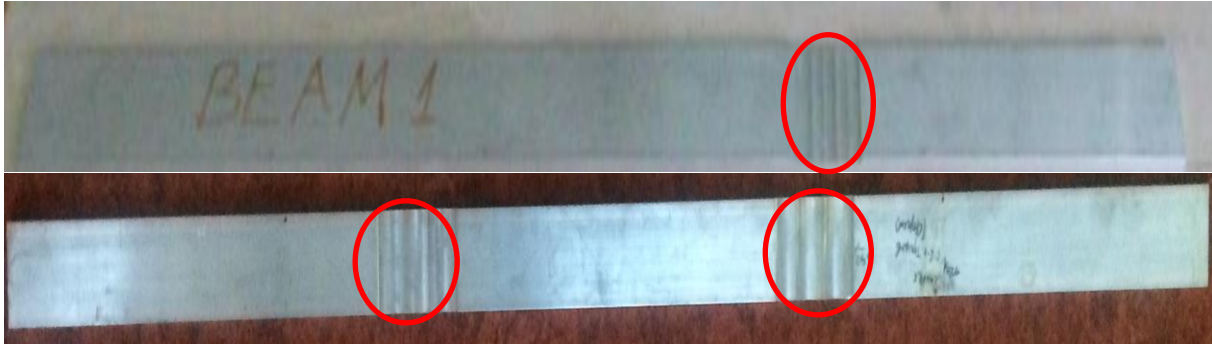
Fig. 3.2. Tested aluminium beams with the regions of mill-cut damage.

Before the damage is introduced into the beams, these beams are subjected to the dynamic vibration test in order to store their deflection shapes for further comparison purposes.

The resonance frequencies and corresponding deflection shapes of the beams are measured using a *Polytec*[TM] PSV-400-B scanning laser vibrometer. *Polytec*[TM] system consists of a PSV-I-400 LR optical scanning head equipped with a sensitive vibrometer sensor (OFV-505), OFV-5000 controller, PSV-E-400 junction box, a Bruel & Kjaer type 2732 amplifier, and a computer system with a data acquisition board and PSV software (Fig. 3.3).

The following procedure is required for a PSV acquisition system:

- Define the outer edges of a testing object;
- Depending on the geometry of an object set up a scanning grid consisting of points in one or two dimensions to uniformly cover the testing object. The density of points in either direction can be varied. Vibrations of a structure are measured in these points, in normal direction to the surface of the structure.

Both ends of aluminium beams are fixed (clamped) (10 mm from both sides) using two vices with a clamping torque of 20 Nm. A periodic chirp signal generated by internal function generator is sent to a piezoelectric element which is used as an actuator to excite the beams, while CFRP plate was excited using loudspeaker and aluminium plate was excited with a vibration shaker. After the measurement has been performed in one point, the vibrometer automatically moves the laser beam to a successive point of the scan grid, measures the response using the Doppler principle and validates the measurement with the signal-to-noise ratio. During the measurement the photo-detector (highly sensitive digital decoder VD-07), measures the time dependant vibration velocity. After the measurements have been performed at each point, the averaged time response is transformed to the frequency domain using Fast Fourier Transform giving as a result – frequency spectrum. Further post-processing of the data (e.g. integration) gives the displacement deflection shapes. More details about the proper arrangement of the experimental set-up can be found in [200-202].

After the frequency spectrum and resonant frequencies have been obtained, the beams are excited by a periodic sine wave signal which is tuned to a frequency corresponding to each of the resonant frequencies. This is done in order to obtain the deflection shapes. The size of deflection shape signal and set-up parameters used for frequency spectra measurements are shown in Table 3.2 where letters "d" and "h" stand for damaged and healthy specimens.

Table 3.2

Vibrational scanning parameters for aluminium beams

Scan parameter	Bandwidth (Hz)	Resolution (mHz)	FFT lines	Sample frequency (Hz)	Signal amplitude (V)	Size of a deflection shape signal
Al Beam 1d	0-1600	500	3200	4096	6	1×149
Al Beam 1h	0-1600	250	6400	4096	7	1×149
Al Beam 2d	0.25-1600	250	6400	4096	6	1×149
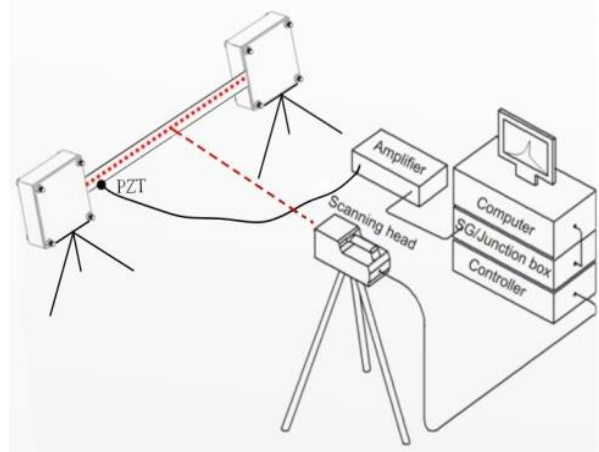
Fig. 3.3. Experimental set – up for modal analysis employing scanning laser vibrometer.

The respective frequency spectra are depicted in Fig. 3.4. It must be noted that the bandwidth in which vibration test is performed is set to 1600 Hz for both beams. In this frequency region 14 deflection shapes are identified for Al beam 1d. The extracted resonant frequencies for both aluminium beams at their healthy and damaged state are shown in Table 3.3. Two deflection shapes corresponding to healthy and damaged states of Al beam 1d are shown in Fig. 3.5.
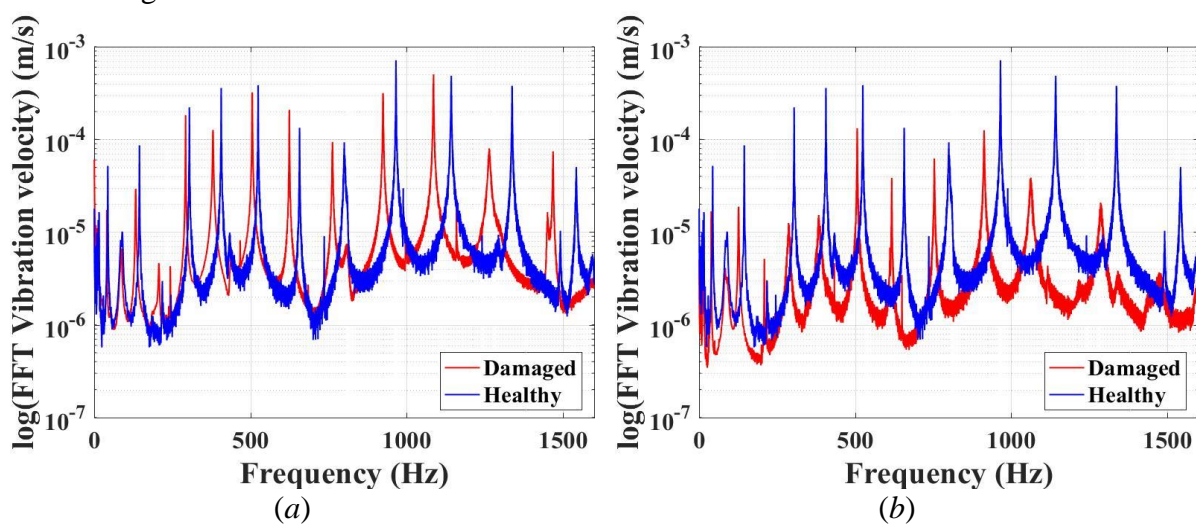
Fig. 3.4. Frequency spectra of aluminium beams: (*a*) Al beam 1d; (*b*) Al beam 2d.

Table 3.3

Resonant frequencies (Hz), extracted for clamped-clamped aluminium beams from a vibration test and finite element simulation

No.	Beam 1d damaged		Beam 1d healthy		Beam 2d	
	Experiment	FEM	Experiment	FEM	Experiment	FEM
1	15.25	15.99	15.75	16.60	15.25	15.62
2	40.50	43.52	43.75	45.76	38.75	40.67
3	87.50	89.03	85.00	89.71	83.75	88.49
4	133.00	138.56	144.75	148.28	126.50	129.89
5	207.00	217.80	-	221.49	209.25	213.05
6	292.50	301.21	304.50	309.33	286.75	295.63
7	380.00	395.04	406.50	411.80	383.50	375.88
8	505.50	523.08	524.50	528.88	506.50	517.23
9	624.50	638.52	657.00	660.57	617.25	621.43
10	762.50	787.51	800.25	806.85	753.75	764.25
11	924.00	948.32	965.50	967.72	913.00	931.76
12	1086.00	1112.38	1142.50	1143.16	1063.00	1082.08
13	1264.00	1302.45	1337.00	1333.17	1286.25	1272.72
14	1468.50	1501.64	1491.50	1537.72	1473.25	1465.46

As one can see from Fig. 3.5, there exists a non-zero displacement at edges of Al beam 1d. This effect is due to the fact that the first and last points of scanning grid for dynamic vibration test is set-up symmetrically at a distance of 5 mm from both clamping vices of the beam.
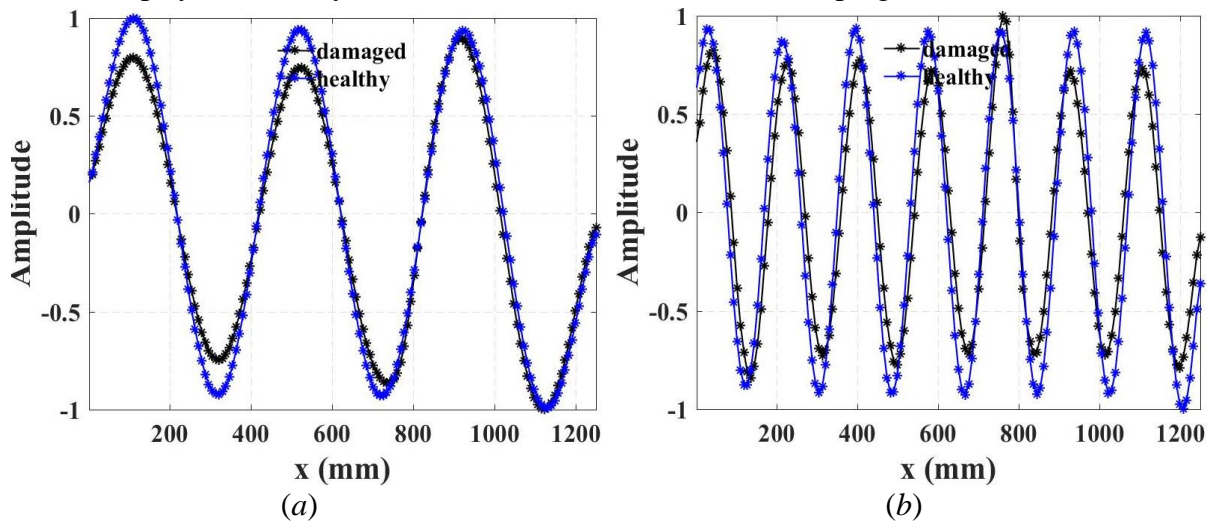

Fig. 3.5. Deflection shapes for Al beam 1d at healthy and damaged state at $p = 1$: (*a*) shape 6; (*b*) shape 14.

3.1.3. Damage detection performance assessment

SDI distributions are calculated for all 78 wavelets, each at 128 scale parameters. Fourier series approximations F1-F8 are used to calculate DER values of SDI for MSCS method. A DER value corresponding to each scale is calculated. As for MSCS method, the same SDI arrays are calculated for each of Fourier series approximation functions. For both methods, only function with highest DER value is selected and applied for further analysis.

DER versus scale plots for both aluminium beams (experimental results) are shown in Fig. 3.6. This behaviour is shown only for sensor densities $p = 1, 3, 6$. With increasing p, smoothness of DER curves decreases. There is clearly a smooth region of DER at scales $s <$ 60. For coarser sensor grids, perturbations in DER profiles are introduced, smoothness decreases and DER dependence on scale becomes more chaotic, resembling noise. Also, one can see that a DER maximum is located in this smooth region of DER corresponding to smaller scales in accordance with [60].

It is worth noting that scale parameter, corresponding to DER maximum, shifts to smaller values as sensor density decreases. These results for simulation case at noise levels of 0 % and 4 % at sensor densities $p = 1, 3, 6$ are depicted in Fig. 3.7 and 3.8 for Al beam 1d and 2d cases, respectively. It can be seen that DER values exhibit some slight differences between no-noise and 4 % noise cases, but mainly at some scale intervals. Also, smoothness of DER curves decreases with increasing sensor density.
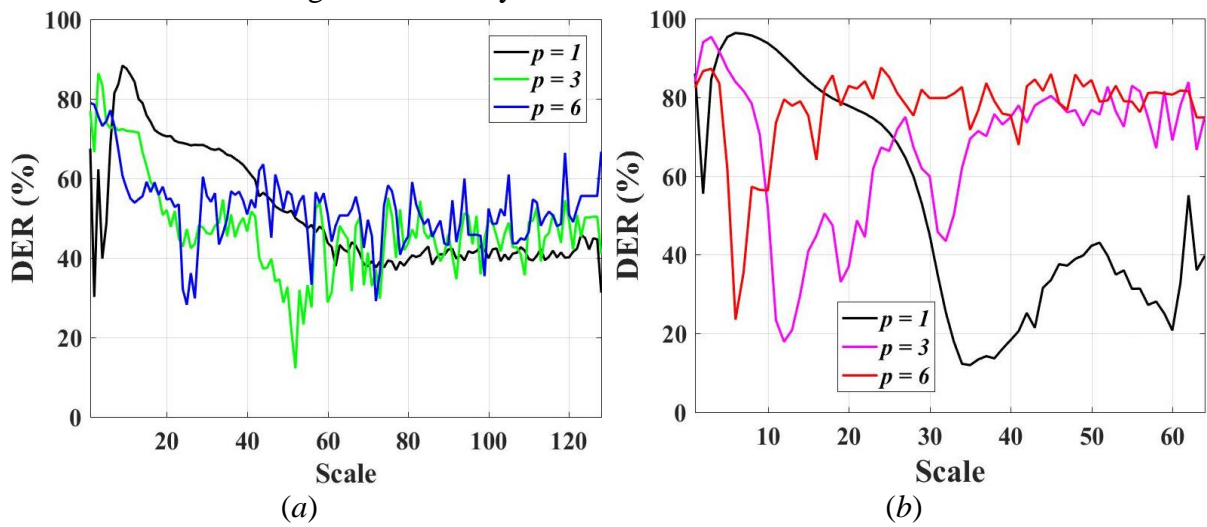
Fig. 3.6. DER vs scale plots at p = 1, 3, 6 (experiment): (*a*) Al beam 1d; (*b*) Al beam 2d.
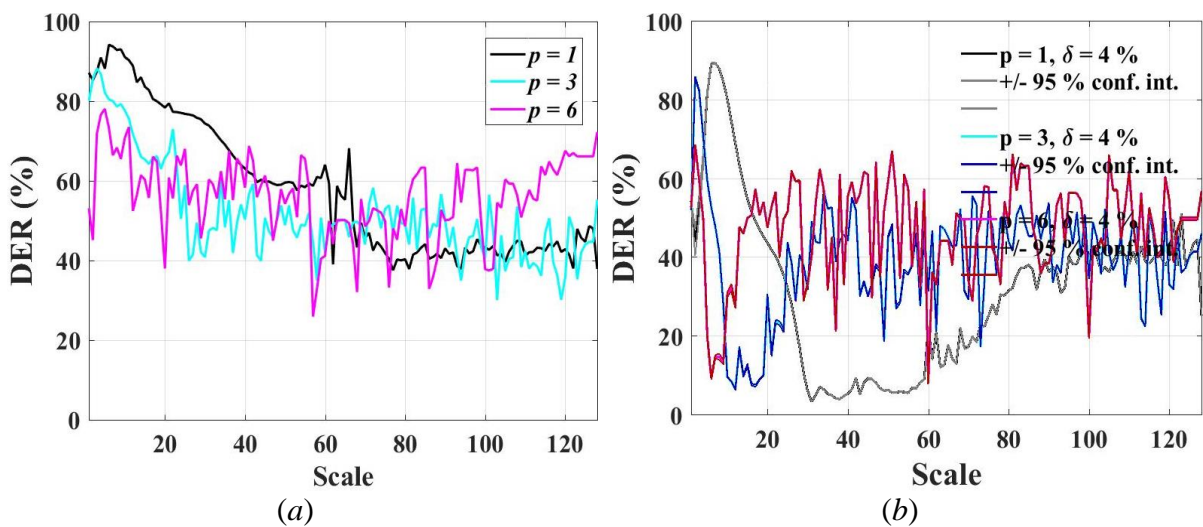
Fig. 3.7. DER vs scale plots at p = 1, 3, 6 (Al beam 1d): (*a*) $\delta = 0$ %; (*b*) $\delta = 4$ %.

Also, 78 wavelet functions are tested in terms of DER values for Al beam with 2 damage sites. Out of these wavelets a complex morlet wavelet of order 1-1 (cmor1-1) is selected for the

damage identification as it yields the best DER value of 97.71 % at scale 6. An analysis of cmor1-1 wavelet performance in terms of scale parameter (or scales) is carried out. In total, 64 scales are included in the study. It is notable that damage identification is effective for scales below 10 (refer to Fig. 3.8). DER vs scale plots are smooth till scale value of about 32. Therefore, only minor deviations of scale at which cmor1-1 wavelet attains maximum DER values are observed.

DER values for MSCS method calculated for every approximation function for both beams are shown in Fig. 3.9.
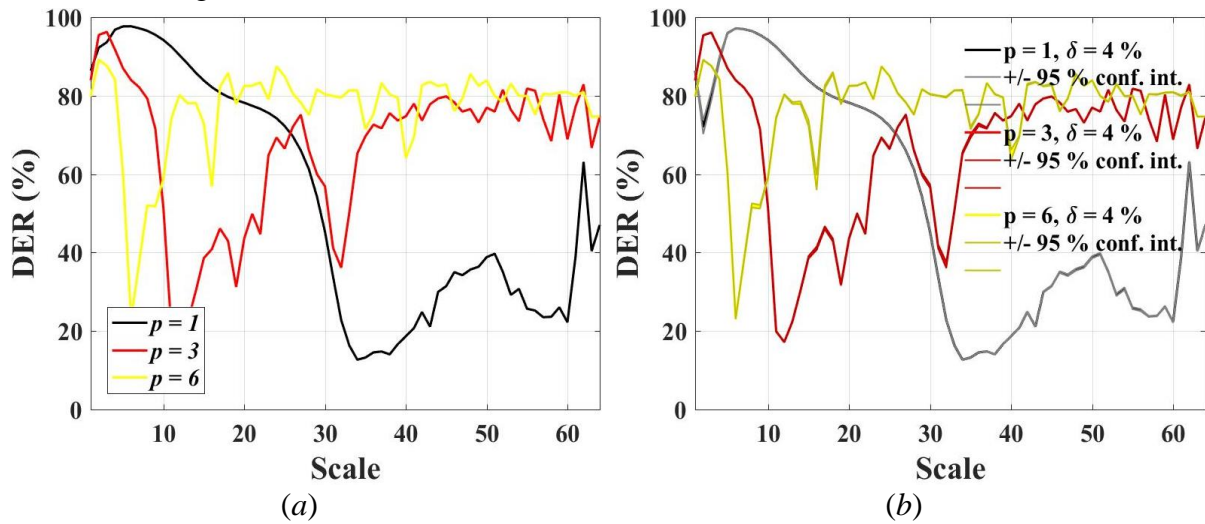
Fig. 3.8. DER vs scale plots at $p = 1, 3, 6$ (Al beam 2d): (*a*) $\delta = 0$ %; (*b*) $\delta = 4$ %.
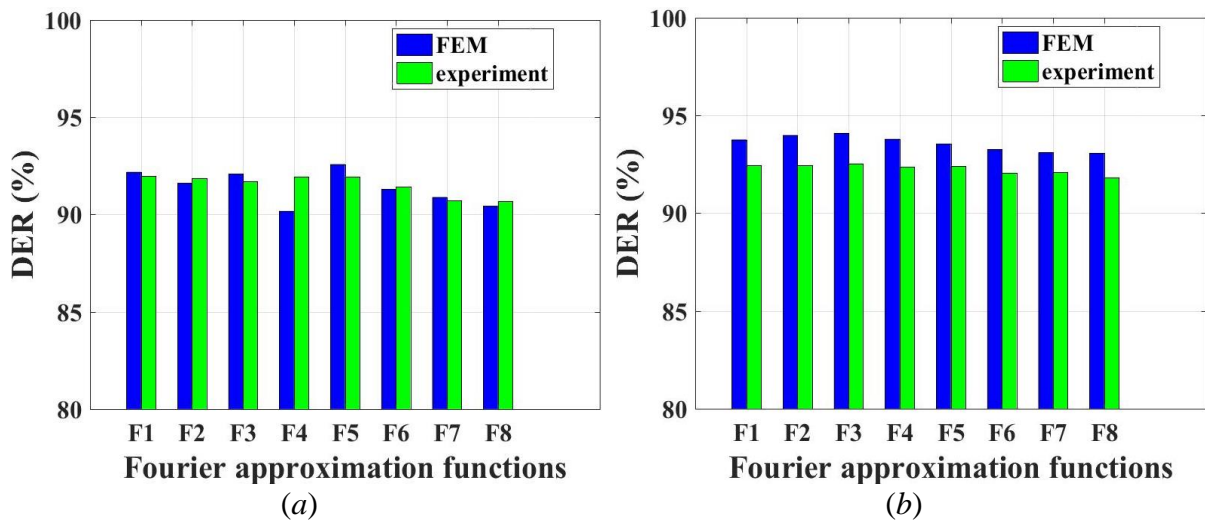
Fig. 3.9. DER for all Fourier functions: (*a*) Al beam 1d; (*b*) Al beam 2d.

For comparison purposes, the range of DER is selected to be equal for both beams and such that the lowest DER and highest DER are inside the range. Overall DER values are lower than those for numerical simulations. This is expected due to measurement noise. As in numerical simulations, the best performing wavelet turns out to be complex morlet of order 1-1 for both beams.

Information on the best functions used for damage localization for both beams are shown in Table 3.4. and Table 3.5. Two points, namely, one point at each end of the beam, are excluded

from the computation in MSCS method as compared to CWT because in order to perform the difference algorithm (refer to Eq. (2.24)) two neighbouring points are required.

Table 3.4

Damage localization parameters for Al beam 1d with the highest maximum DER

Method	p						Experiment	FEM
	1	2	3	4	5	6		
CWT	149	75	50	38	30	25	cmor1-1/9	cmor1-1/6
MSCS	147	73	48	36	28	23	F5	F5
TVNWS	149	75	50	38	30	25	-	-
DOFs							Wavelet/scale or approximation function	

Table 3.5

Damage localization parameters for Al beam 2d with the highest maximum DER

Method	p						Experiment	FEM
	1	2	3	4	5	6		
CWT	149	75	50	38	30	25	cmor1-1/6	cmor1-1/6
MSCS	147	73	48	36	28	23	F3	F3
TVNWS	149	75	50	38	30	25	-	-
DOFs							Wavelet/scale or approximation function	

Mode shape curvatures of healthy and damaged structures and those obtained by an interpolation procedure are shown in Fig. 3.10. for both aluminium beams.
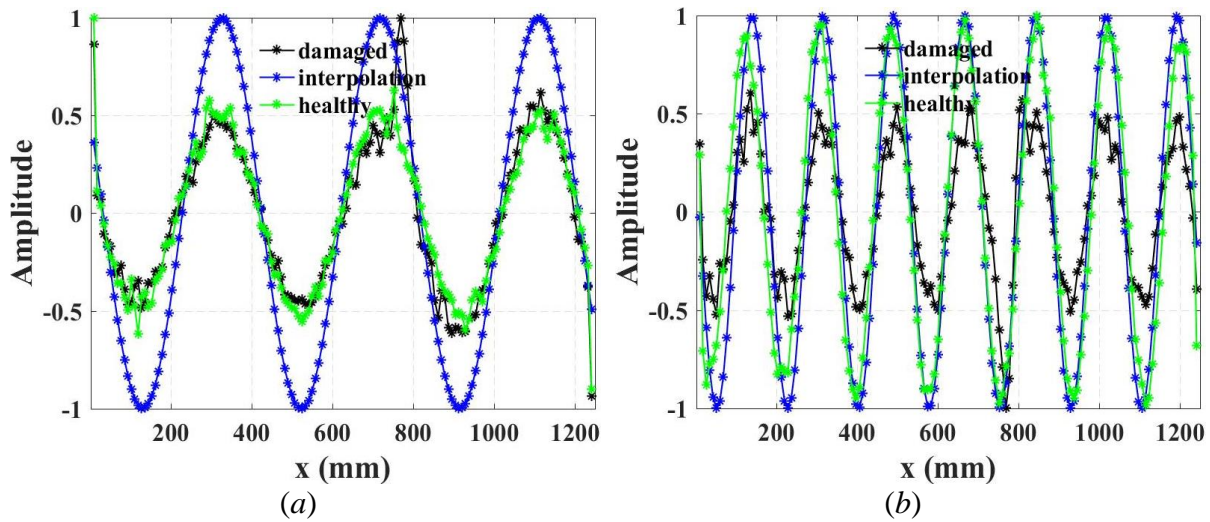
Fig. 3.10. Experimental mode shape curvatures obtained through interpolation and those of healthy and damaged Al beam 1d at $p = 1$: (*a*) shape 6; (*b*) shape 14.

These responses are normalized with respect to a maximum value of that particular curvature, which is the reason why the amplitudes for healthy state and interpolation do not match. It can bee seen that the largest value for a damaged structure corresponds to the location of damage.

3.1.4. Damage localization

The SDI distributions corresponding to scales with the highest DER are shown in Fig. 3.11 (*a*). The highest peak is located in the actual zone of damage between two vertical dashed lines, thus damage is located. Large amplitude SDI value is also found at the left end of Al beam 1d. The respective results for simulation case with 0 % and 4 % noise are shown in Fig. 3.11 (*b*) and (*c*). In addition, it was found that the operational noise of a laser vibrometer is around 0.5 %. Thus, SDI profile, corresponding to this noise level is shown in Fig. 3.11 (*d*).
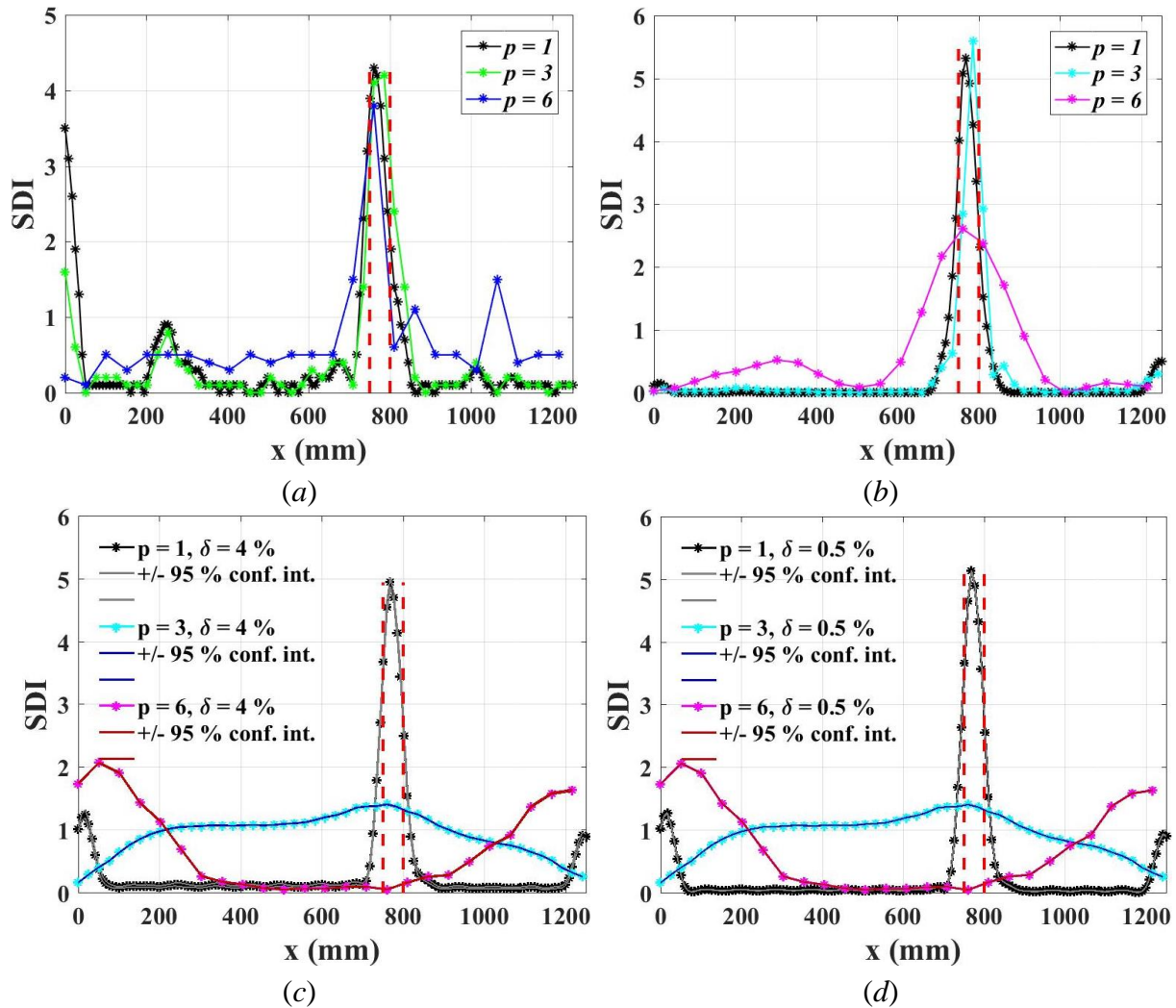
Fig. 3.11. SDI profiles at $p = 1, 3, 6$ (CWT): (*a*) experiment at $s = 9$; (*b*) FEM $- \delta = 0$ % at best scale for each p; (*c*) FEM $- \delta = 4$ % at $s = 6$; (*d*) FEM $- \delta = 0.5$ % at $s = 6$.

For simulation case, SDI peaks with the highest amplitude are located between two vertical lines for sensor densities $p = 1$ and 3, indicating a successful localization of damage. As for case with $p = 6$, highest peak is still in the zone of damage, although the whole SDI profile is wide, thus decreasing the accuracy of damage localization. As with DER vs scale plots, no major differences between noiseless and 4 % noise SDI profiles are observed, indicating that the CWT technique is resistant to noise.

SDI distribution for MSCS method (experimental case) for Al beam 1d is shown in Fig. 3.12 (*a*). While damage identification algorithm clearly manages to locate the damage, it is

rather surprising to discover that the finest sensor grid does not necessarily yield the best results (comparing cases for $p = 1$). Also large amplitude SDI values reside at the ends of the beam. This characteristic is specific to the largest sensor density for $p = 1$. In analogy to the CWT method, SDI calculation results are shown for noiseless, experimental operational noise level (0.5 %) and maximum noise level (4 %) cases in Fig. 3.12 (*b*)-(*d*).
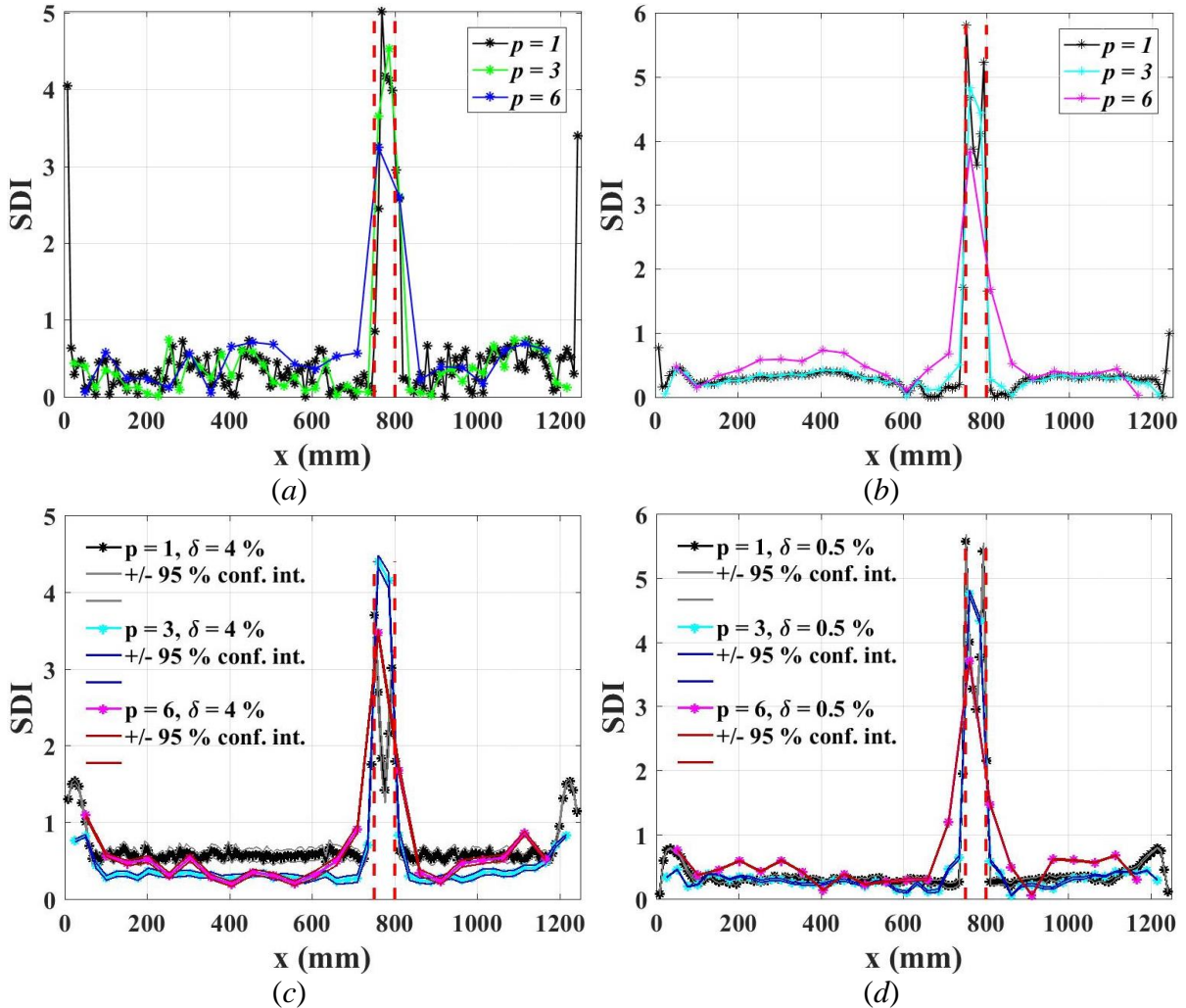
Fig. 3.12. SDI profiles at $p = 1, 3, 6$ (MSCS): (*a*) experiment; (*b*) FEM $- \delta = 0$ %; (*c*) FEM $- \delta = 4$ %; (*d*) FEM $- \delta = 0.5$ %.

One can quickly notice the difference between CWT method here – while the noiseless SDI profiles manage to localize the damage at all sensor densities, SDI profiles at the densest sensor grid and maximum noise are more susceptible to noise as indicated by wider confidence interval. It is worth noting that these SDI profiles with noise are averaged over 100 runs. The individual SDI profiles are characterized by rather smeared values at the highest noise level. On the other hand, SDI profiles for CWT case have to be recalculated for every sensor density – Fig. 3.11 (*c*) and (*d*) show that damage is not localized using the same scale as in Fig. 3.11 (*a*).

For experimental case, as the results suggest, the largest amplitude SDI peaks are associated with the zone of damage. Nevertheless, considerable values also occurred at the boundaries of beams. This effect, known as boundary distortion, is attributed to the fact that operational

deflection shapes are not continuous at the ends of a structure due to boundary conditions. Commonly, this issue is addressed by either generating additional mode shape data beyond the boundary using a cubic spline extrapolation technique or applying some padding (zero, linear, symmetric) methods [103].

   Plots of SDI distributions for Al beam with 2 damage sites using MSCS method are shown in Fig. 3.13 and using CWT method − in Fig. 3.14. For the CWT method, the respective SDI distributions are all shown at scale = 6, set as a reference, since highest DER value is attained at this scale, at original sensor density. At $p = 1$ the highest SDI peaks are convincingly located between two red vertical lines that indicate the zones of damage. At $p = 3$, however SDI are widely spread across the coordinate of the beam, clearly not revealing the damage (at scale = 6). Nevertheless, scale = 3 is the best for this case as indicated by a respective DER vs p plot − one can see that once again two peaks with the largest amplitude are located in the zones of damage. Scale = 6 fails to indicate damage also at the most coarse sensor grid, while scale = 2 is the best for this case. However, both peaks are a bit shifted out of the damage zones.
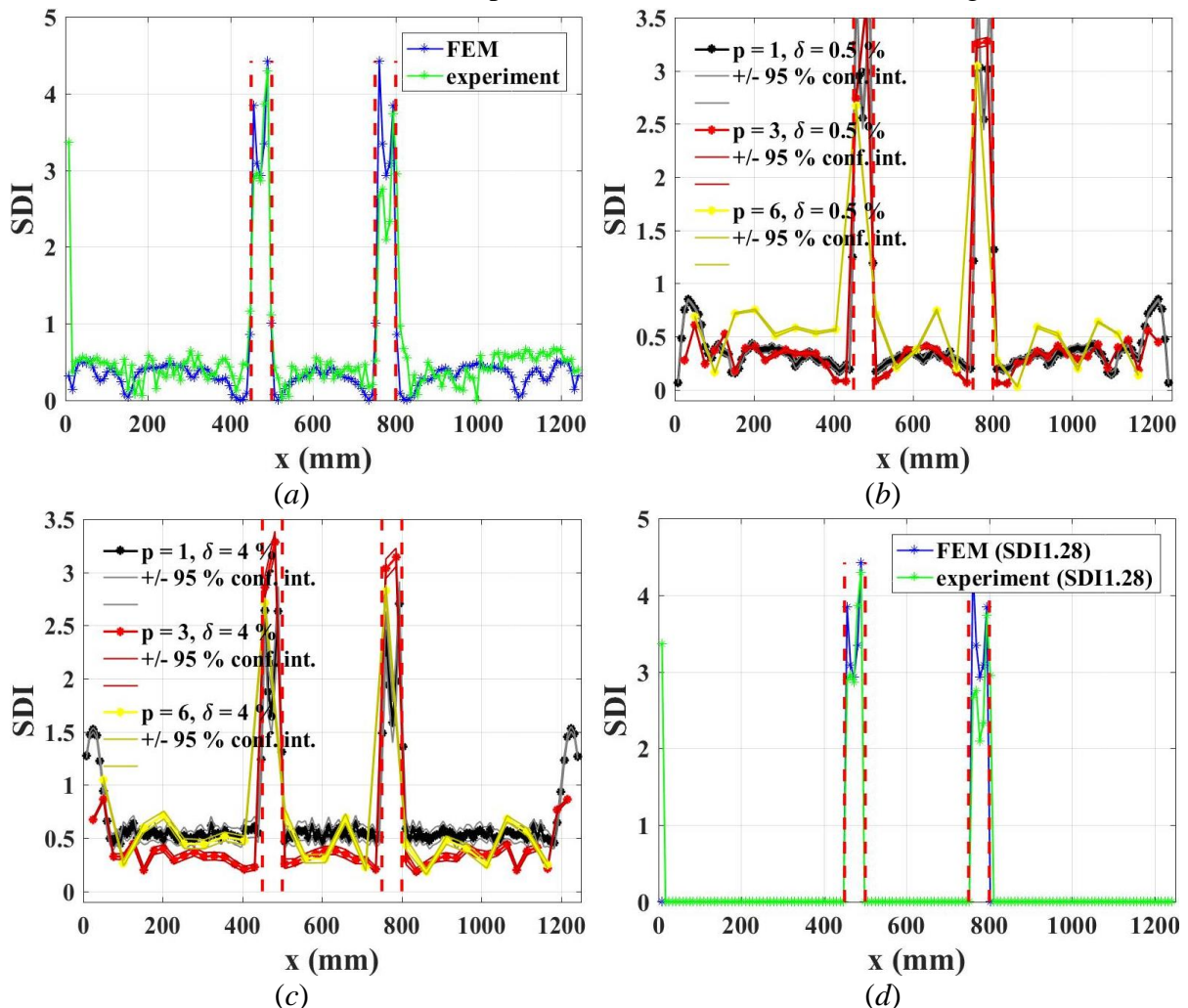
Fig. 3.13. Standardized damage indices for MSCS method for Al beam 2d: (*a*) experiment and FEM (no threshold); (*b*) FEM with $\delta = 0.5$ %; (*c*) FEM with $\delta = 4$ %; (*d*) experiment and FEM (thresholded).
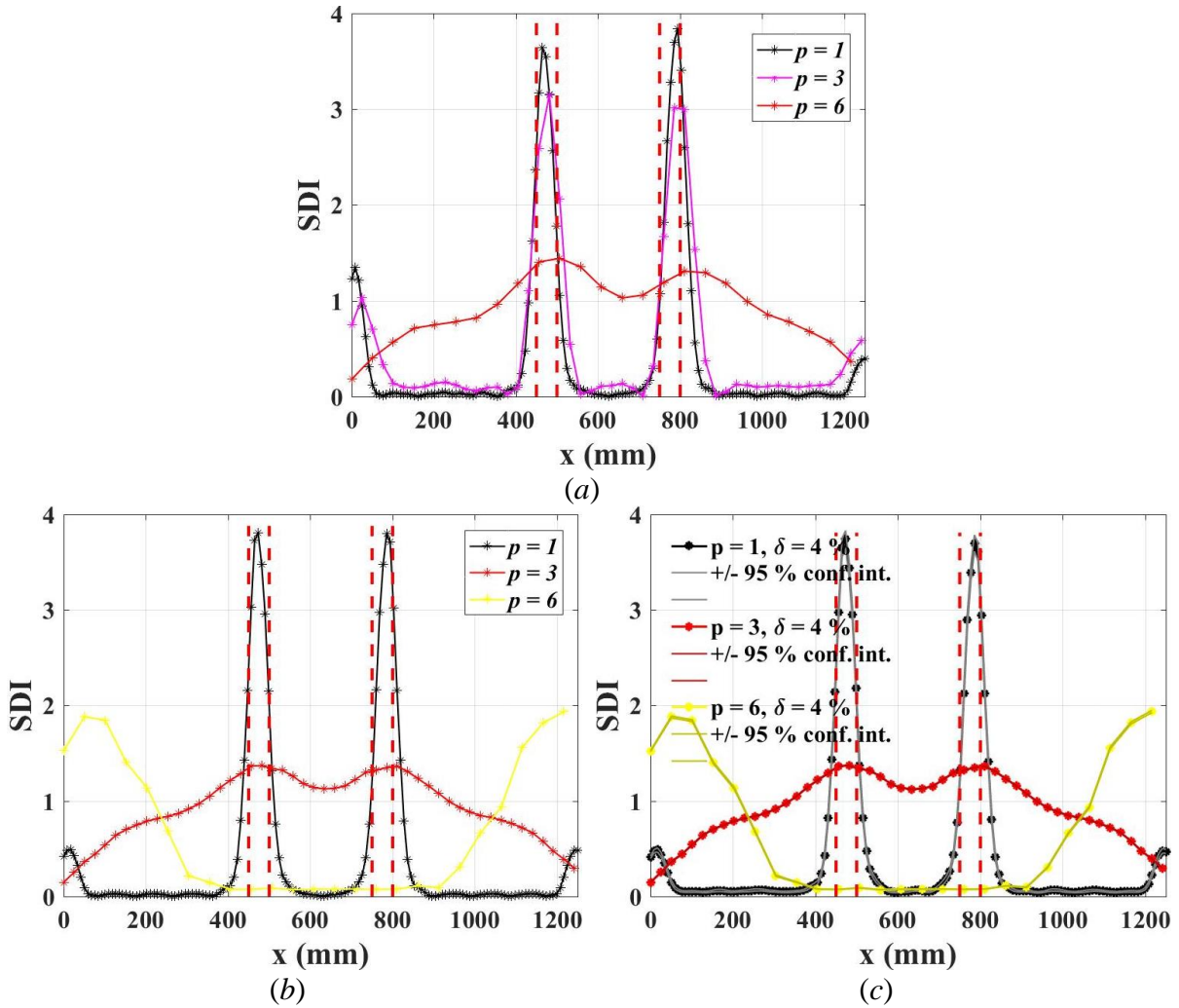
Fig. 3.14. SDI profiles for Al beam 2d (CWT) at scale = 6: (*a*) experiment; (*b*) FEM − δ = 0 %; (*c*) FEM − δ = 4 %.

In this study, by application of statistical hypothesis with damage localization confidence level of 99 %, SDI values lower than a threshold value of 3 are assigned a zero value. Thresholds for SDI are applied to filter out smaller peaks that do not contribute to damage. Although this approach significantly improves damage identification results, large amplitude peaks at the edges of both Al beams (MSCS) and at the left edge of Al beam 1d (CWT) are still present. Thresholded SDI profiles are illustrated in Fig. 3.15 (a) for CWT and MSCS methods and corresponding DER values are also provided. A threshold values of 3 (SDI3), corresponding to 99 % damage assessment confidence was applied to all cases for CWT and MSCS methods. Thresholded SDI profile for Al beam with 2 damage sites using CWT method is shown in Fig. 3.15 (*b*). A clear 100 % DER value is achieved.
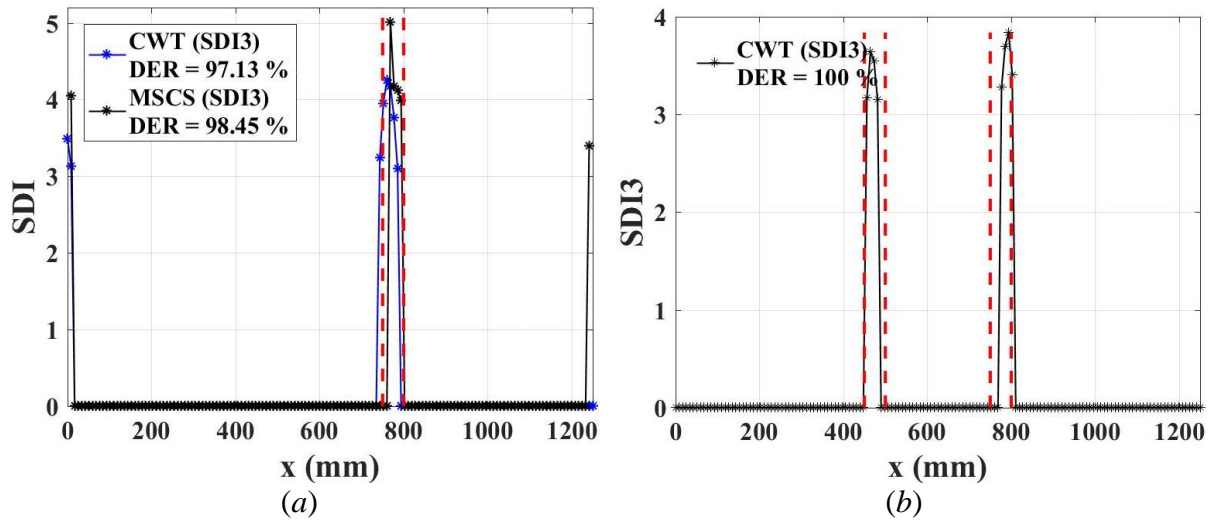
Fig. 3.15. SDI with a threshold value of 3 profiles (experiment) at $p = 1$: (*a*) Al beam 1d; (*b*) Al beam 2d.

As one can see, MSCS method yields slightly better damage identification results than CWT method. For simulated Al beam with 2 damage sites the SDI threshold of 90 % confidence is selected to achieve 100 % DER value. It can be seen, that damage identification algorithm managed to capture the location of damage as highest peaks appear between 2 red vertical lines (depicting the predetermined area of damage).

Scalograms and normalized scalograms for one of the wavelets used in the computation of TVNWS algorithm (Haar wavelet) alongside with a scalogram counterpart of the best performance wavelet from CWT method (complex morlet 1-1) are shown in Fig. 3.16 and Fig. 3.18 for Al beam 1d and Al beam 2d. The zone between the two vertical lines depict the true locations of damage. As one can see, the largest magnitudes are at smaller scales and correctly lie in the zone of damage. However, this response is smeared out over the coordinate of beams with the increasing scales. The importance of scalogram normalization is that the largest magnitudes are neatly concentrated in the zone of damage and the aforementioned smearing effect is neutralized.

Damage localization results using TVNWS method are shown in Fig. 3.17 for Al beam 1d and Fig. 3.19 for Al beam 2d. The fractionalized wavelet scalograms show that the largest amplitude of variance of normalized wavelet scalogram is between vertical lines – in the zone of damage. By applying the universal threshold the second time (T_2) these values are filtered and the ones passing this threshold are depicted in small inlet plots. A separate DER values is calculated for these inlet plots and results are shown. For the cases of $p = 1$, $\delta = 0$ % these DER are 81.4 % for Al beam 1d and 79.6 % for Al beam 2d. The experimental results are shown in green color. Large amplitude is associated with the left edge of the Al beam 1d thus reducing the DER value to just 18.34 %. As for the Al beam 2d, the experimental case outperforms the simulation results with DER equal to 82.53 % and 79.62 %, respectively. By applying the same noise levels and varying sensor densities as for CWT and MSCS methods damage index profiles are calculated and shown in Fig. 3.17 (*b*)-(*c*) and Fig. 3.19 (*b*)-(*c*).
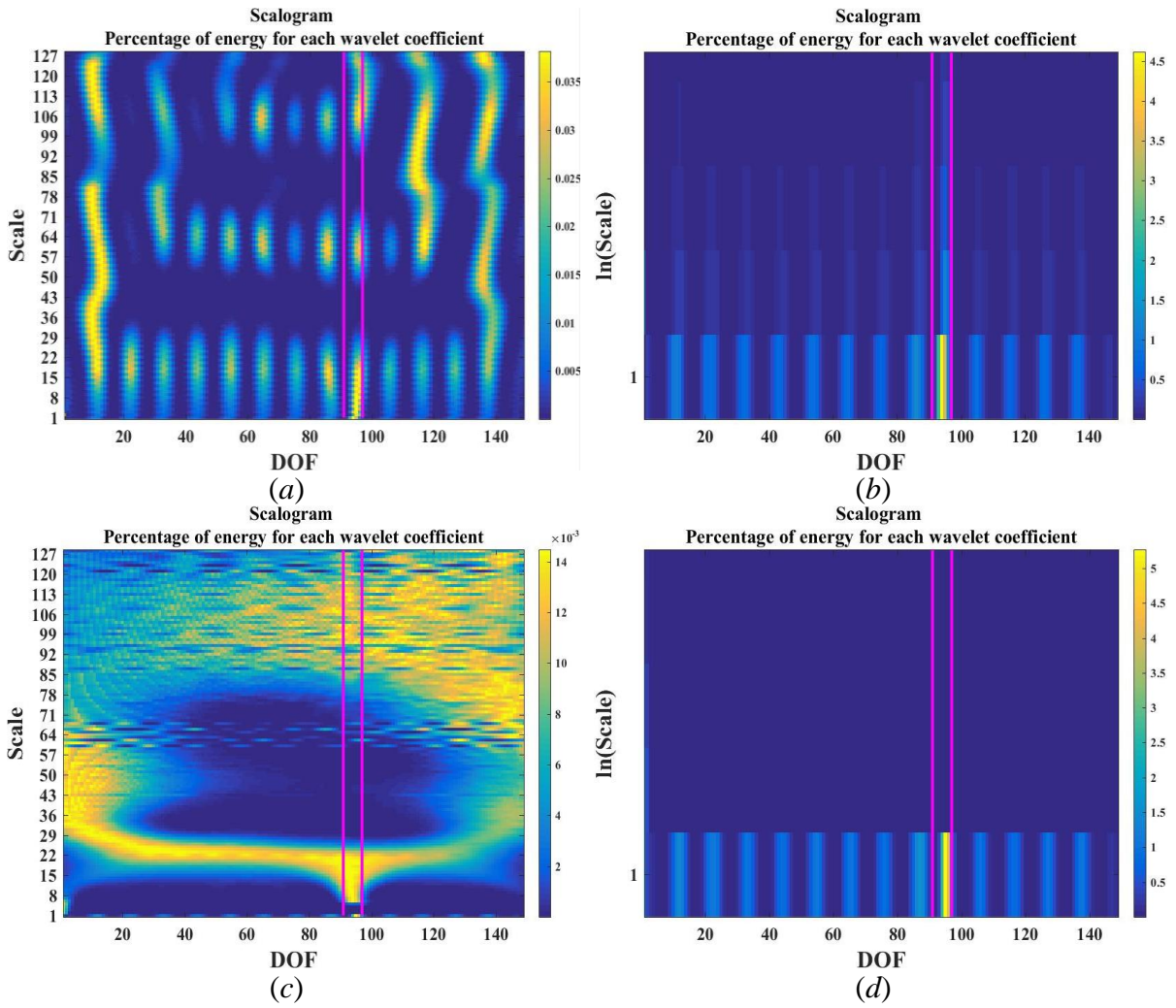
Fig. 3.16. Wavelet scalograms for Al beam 1d at $p = 1$ (experiment): (*a*) scalogram for Haar wavelet; (*b*) normalized scalogram for Haar wavelet; (*c*) best performance scalogram for complex morlet 1-1 wavelet; (*d*) best performance normalized scalogram for complex morlet 1-1 wavelet.

(*a*)

(*b*)   (*c*)
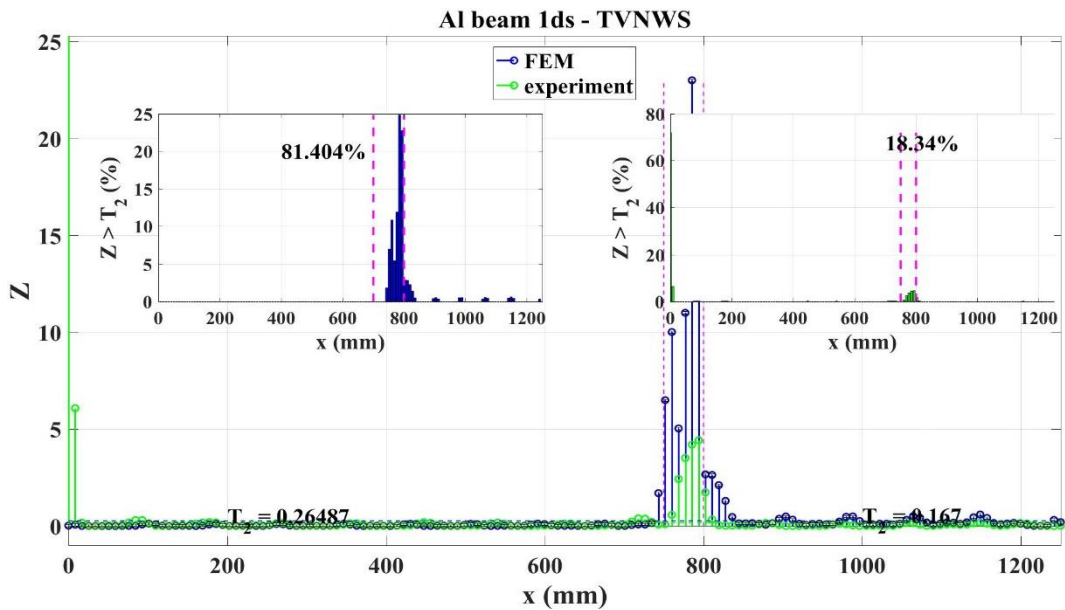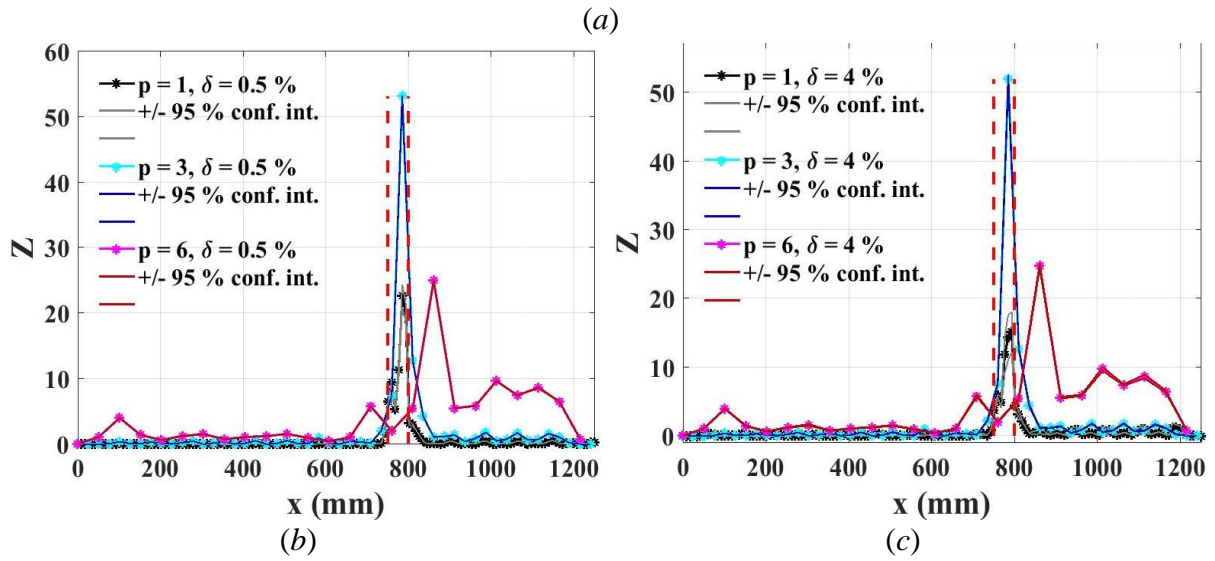
Fig. 3.17. Damage indices for TVNWS method for Al beam 1d: (*a*) fractional wavelet scalogram with second threshold and filtered values; (*b*) FEM with $\delta = 0.5$ %; (*c*) FEM with $\delta = 4$ %.

(*a*)   (*b*)

(*c*)   (*d*)
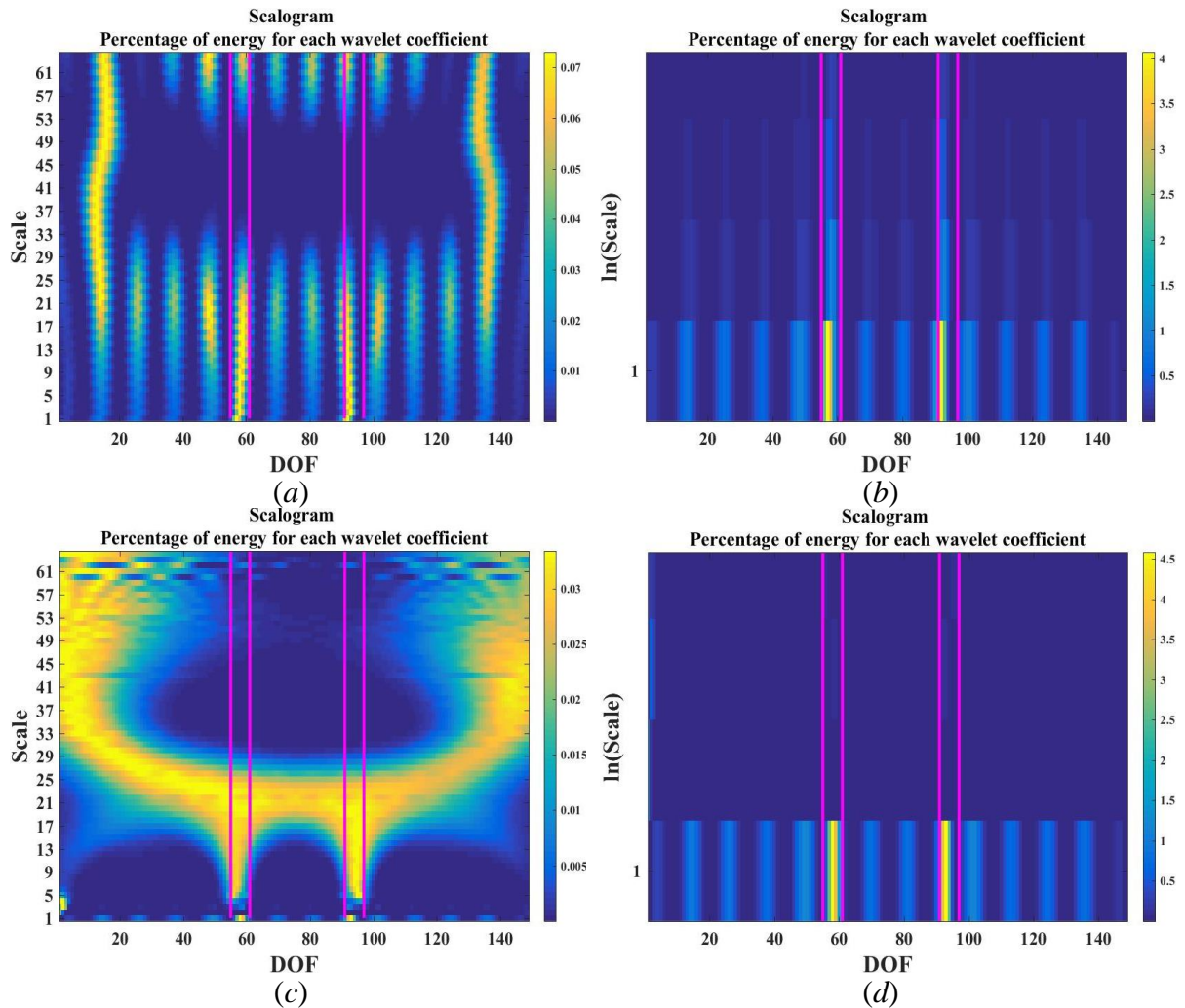
Fig. 3.18. Wavelet scalograms for Al beam 2d at $p = 1$ (experiment): (*a*) scalogram for Haar wavelet; (*b*) normalized scalogram for Haar wavelet; (*c*) best performance scalogram for

65

complex morlet 1-1 wavelet; (*d*) best performance normalized scalogram for complex morlet 1-1 wavelet.

(*a*)

(*b*)

(*c*)
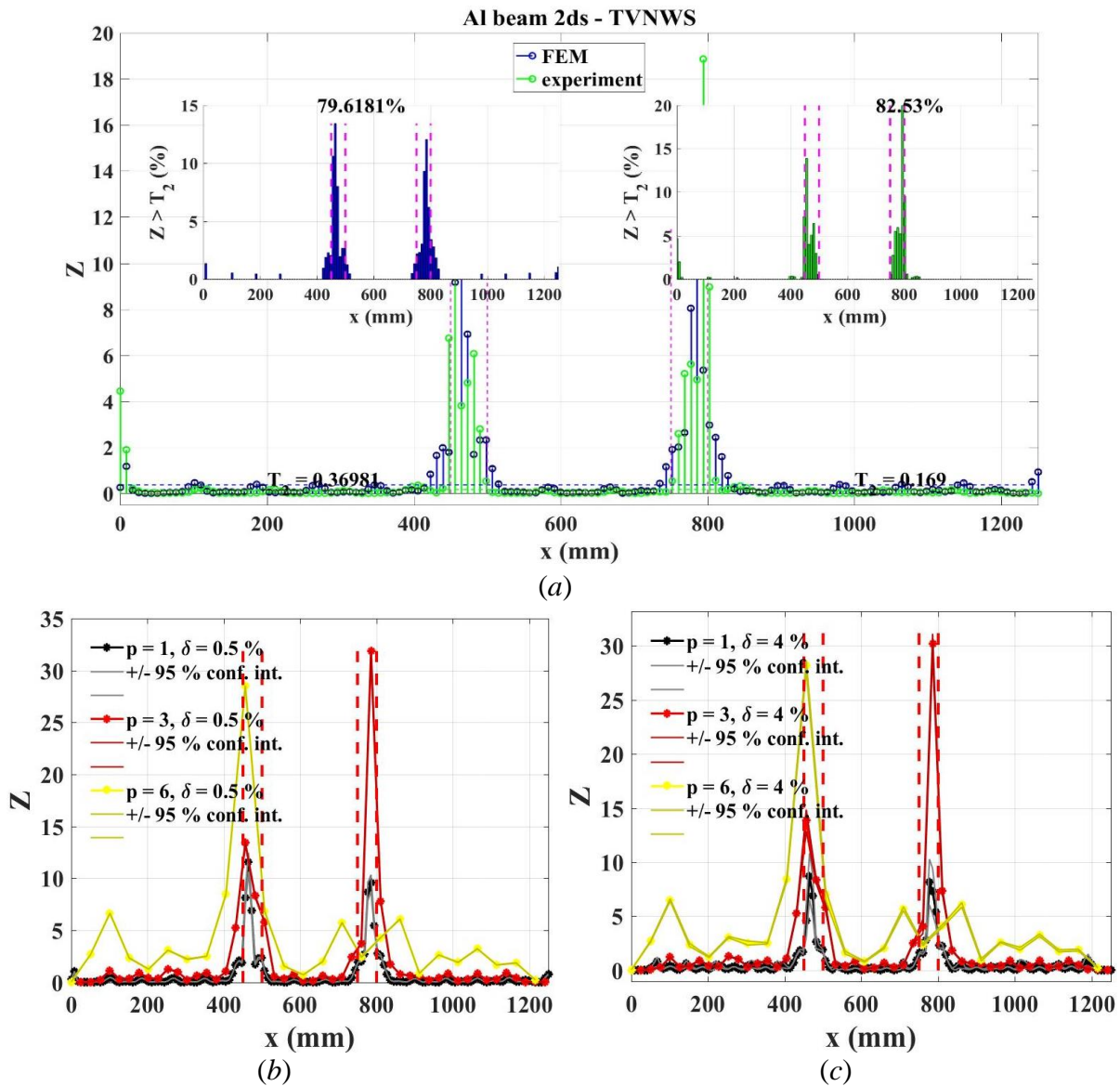
Fig. 3.19. Damage indices for TVNWS method for Al beam 2ds: (*a*) fractional wavelet scalogram with second threshold and filtered values; (*b*) FEM with $\delta = 0.5$ %; (*c*) FEM with $\delta = 4$ %.

It can be seen that the largest peaks are in the zone of damage, except for the smallest sensor density at $p = 6$ where the largest peak is slightly shifted outside the zone of damage for Al beam 1d and only one of two damage sites is localized well for Al beam 2d.

3.1.5. The effect of sensor density and noise

The effect of varying sensor density on damage localization is studied for both aluminium beams and for all 3 methods in the experimental study. The corresponding results are illustrated in Fig. 3.20. In general, performance of MSCS method is superior to that of CWT. First of all, DER variations for MSCS method between the largest and smallest sensor densities are smaller

and therefore more stable than those for CWT. Secondly, DER values themselves are higher for all sensor densities. A predictable trend is obtained in a sense that the performance of the algorithms decreases with decreasing DOFs of mode shape signal. The performance of TVNWS method is the worst among all 3 methods. The variations of DER values are fitted to linear function starting from $p = 2$. The coefficient of determination R^2 indicates a reasonable choice for a fit, especially for Al beam 2d case. The more drastic negative slope of the fit for TVNWS method suggests rather significant susceptibility to mode shape resolution. An interesting fact is that the best results in all cases are obtained not at the maximum number of mode shape DOFs ($p = 1$), but rather at $p = 2$ suggesting that an optimum number of DOFs exists in the case of damage localization.

(a)

(b)
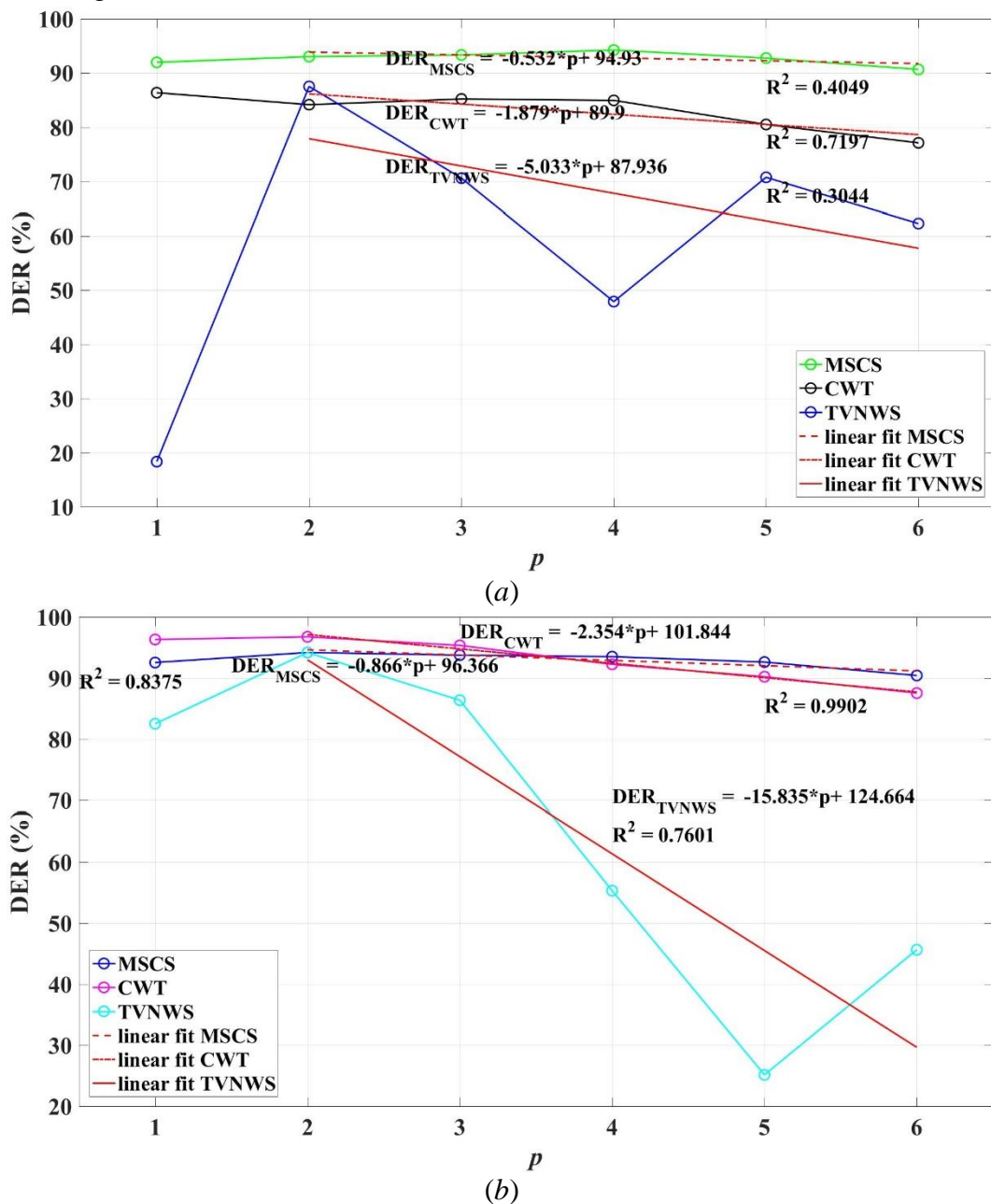
Fig. 3.20. Maximum of DER values versus sensor density (experiment): (a) Al beam 1d; (b) Al beam 2d.

In order to characterize the damage for different sensor density p and noise level cases δ simultaneously, damage estimate reliability diagrams depicting DER values at different noise levels and sensor densities are constructed. The average values over 100 runs along with 95 % confidence interval for both aluminium beams are shown in Fig. 3.21 and Fig. 3.22 using all 3 methods. Blue boxes depict an interval between 25 % and 75 % percentiles with a red horizontal line showing median and black star showing mean value. Black dotted lines with caps depict range of values.

(a)

(b)
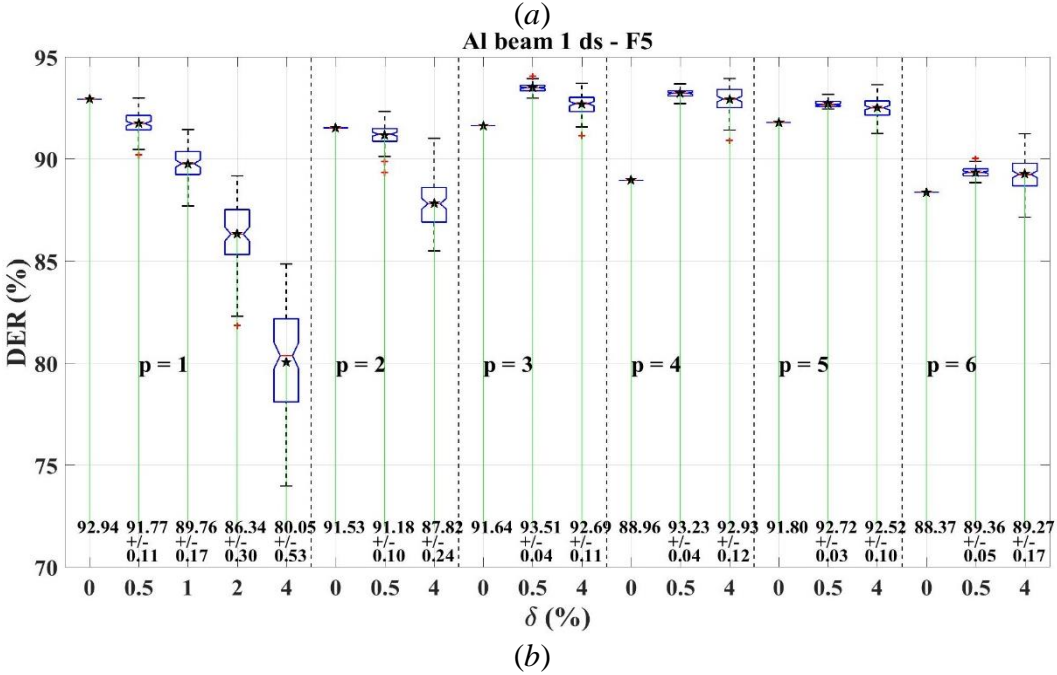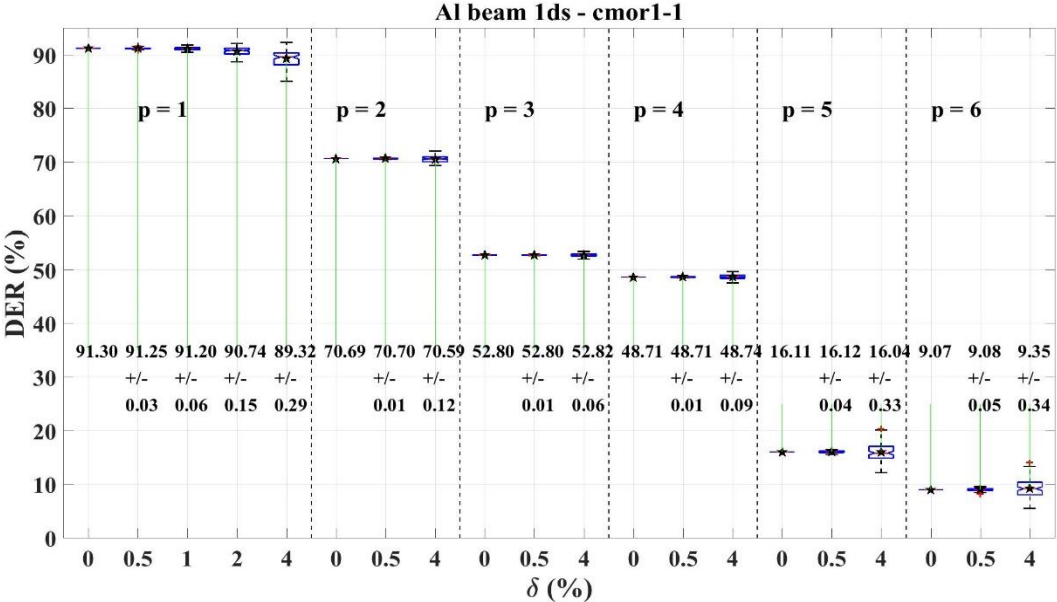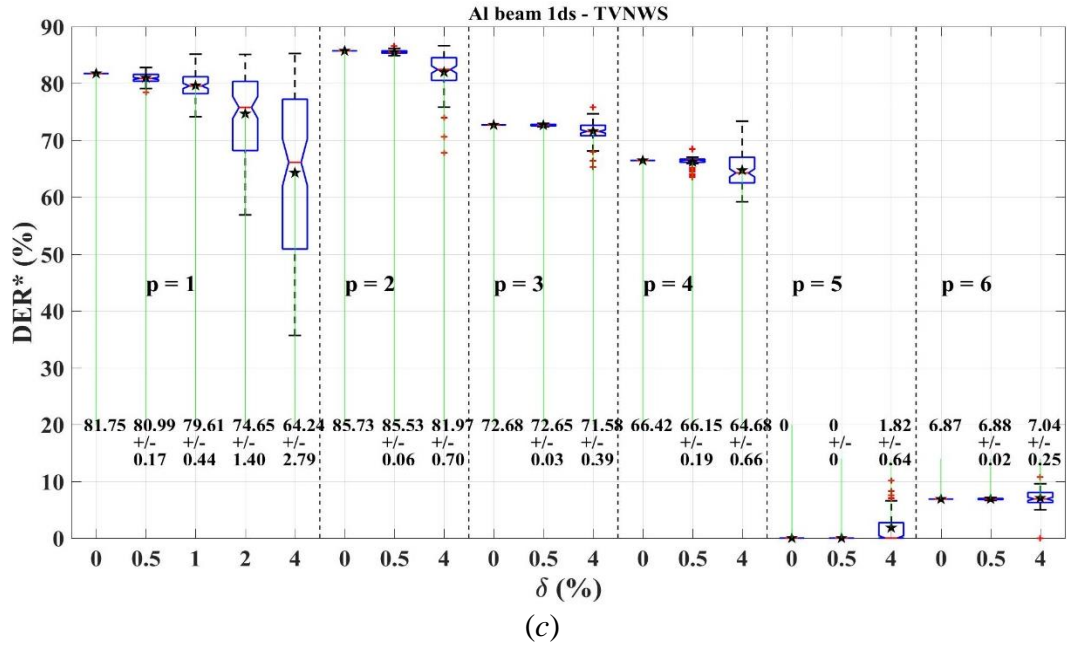
Fig. 3.21. Effect of sensor density and noise on DER variability for Al beam 1d: (*a*) CWT; (*b*) MSCS; (*c*) TVNWS.

Al beam 2 ds - F3

	p = 1				p = 2		p = 3			p = 4			p = 5			p = 6		
94.11	93.31	92.20	90.25	86.52	94.22	93.99	91.95	93.72	93.51	92.69	93.23	93.23	92.93	92.67	92.72	92.52	89.25	89.36	89.27
	+/-	+/-	+/-	+/-		+/-	+/-		+/-	+/-		+/-	+/-		+/-	+/-		+/-	+/-
	0.07	0.10	0.17	0.34		0.05	0.15		0.04	0.11		0.04	0.12		0.03	0.10		0.05	0.17

(b)

Al beam 2ds - TVNWS

	p = 1				p = 2		p = 3			p = 4			p = 5			p = 6		
79.62	81.51	82.22	78.21	68.73	83.55	83.10	84.30	80.86	80.89	80.93	71.59	71.59	71.59	67.28	67.25	67.75	64.20	63.39	66.96
	+/-	+/-	+/-	+/-		+/-	+/-		+/-	+/-		+/-	+/-		+/-	+/-		+/-	+/-
	0,29	0,45	1,20	2,62		0,10	0,56		0,07	0,59		0,02	0,02		0,05	0,53		0,31	1,06
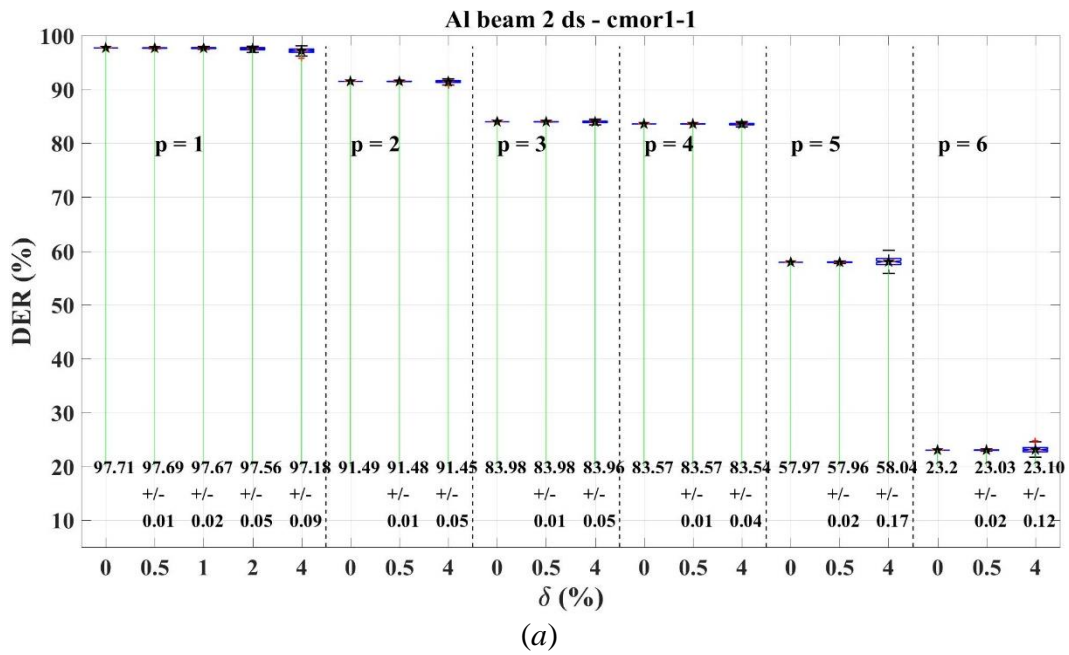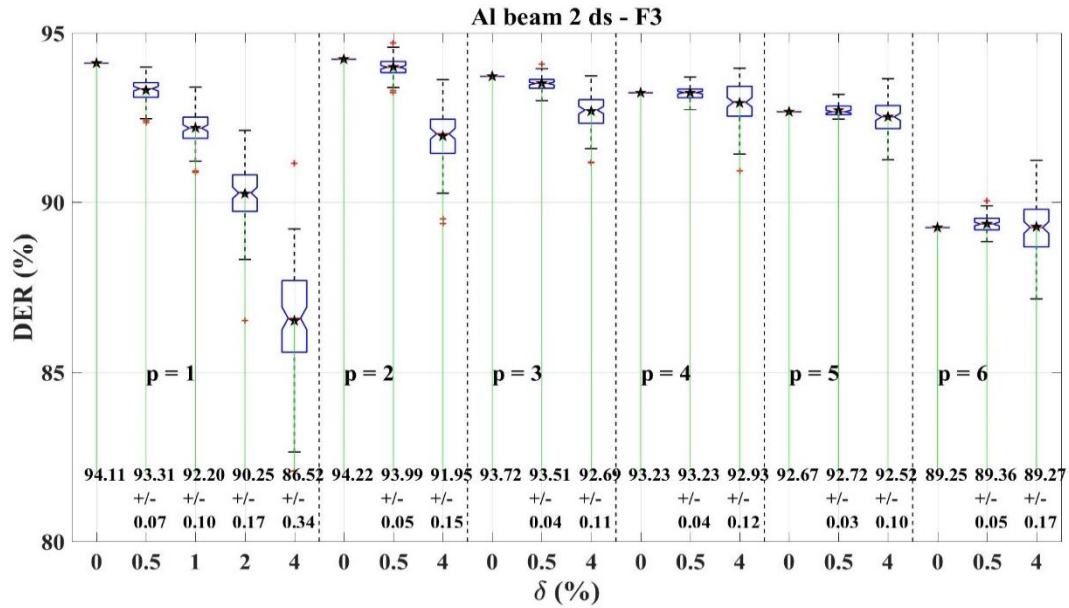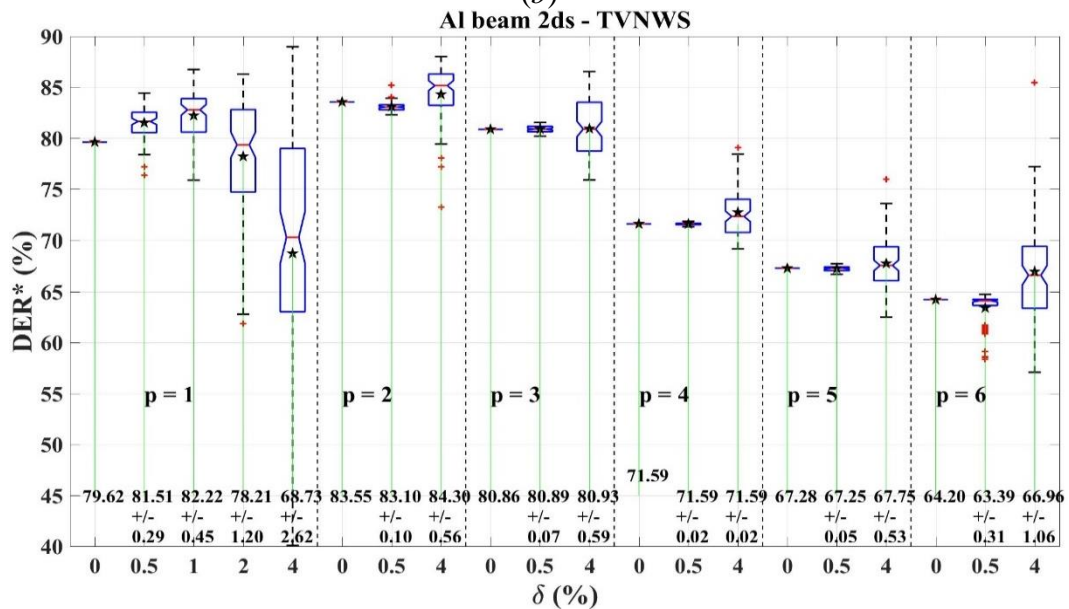
(c)

Fig. 3.22. Effect of sensor density and noise on DER variability for Al beam 2d: (a) CWT; (b) MSCS; (c) TVNWS.

The general trend for CWT method is that DER values drop gradually with increasing p values (decreasing sensor density) for both beams. This drop is not significant in case of Al beam 2ds up until $p = 5$ when DER decrease becomes significant (around 20 %) and at $p = 6$ this difference reaches around 35 % with respect to $p = 5$. Also, increasing noise levels do not have a significant impact on DER.

The effect of noise is more pronounced for MSCS method with higher spread at larger noise levels. The most severe dependency on noise is observed at $p = 1$ with significant DER drop of around 13 % for Al beam 1d and almost 18 % for Al beam 2d. As opposed to CWT method, MSCS method does not exhibit significant DER decrease with increasing p value making MSCS a robust method for damage interrogation in case of limited sensor data (up to a degree).

The most dramatic effect of sensor density on DER is observed for TVNWS method – the difference in DER values is about 75 % by decreasing sensor density from $p = 1$ to $p = 6$ for Al beam 1d, but only about 15 % for Al beam 2d. The harmful effect of noise is pronounced only at $p = 1$ for both beams and is more stable for smaller sensor densities.

As one can see, the overall performance of TVNWS method is the worst among all 3 methods. However, a compromise has to be made between diminished performance and the advantages presented by this method.

3.1.6. The effect of damage depth

Sensitivity of the proposed damage localization methods is tested with respect to various damage depths. Numerically simulated mode shapes of Al beam 1d are used for this parametric study. Damage depths ranging from 0.5 mm to 4.5 mm are considered with an increment of 0.5 mm for this beam with 5 mm thickness. The global reduction of flexural stiffness due to damage can be assessed considering the well-known expression and integrating it along a length of the beam. The integral can be approximately substituted with summation over n elements

$$EI = \int_0^L EI(x)\mathrm{d}x \approx \sum_{i=1}^n EI_i = E \sum_{i=1}^n \frac{b_i h_i^3}{12} \tag{3.3}$$

where b_i – width of an element, m;

$\quad h_i$ – height of an element, m.

The local reduction of stiffness relative to original stiffness is assessed by considering a decrease of thickness in the zone of damage only as other terms in Eq. (3.3) are constant.

$$100 \text{ \%} \times \left(\frac{h_h^3 - h_d^3}{h_h^3} \right) \tag{3.4}$$

where h_h – depth of a healthy structure, m;

$\quad h_d$ – depth of a damaged structure, m.

The relative flexural stiffness reduction with varying damage depths is shown in Fig. 3.23. As one can see, the relationship is cubic with around 73 % reduction of flexural stiffness at damage depth of 4.5 mm.
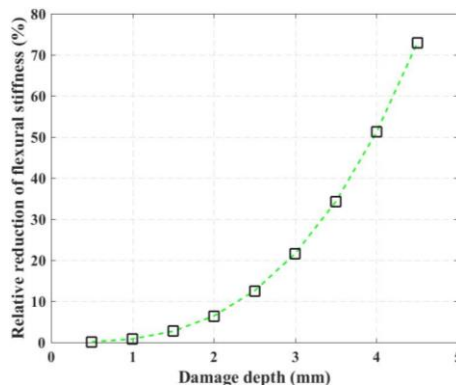
Fig. 3.23. Reduction of relative flexural stiffness with increasing damage depth for a beam with 5 mm thickness.

A simultaneous analysis of the effect of changing sensor density (p) is carried out. DER values for every damage case are recorded and shown in Fig. 3.24. The most stable results are obtained with MSCS method with DER in the range of 83 % to 93 % in all cases. The most unstable performance is achieved, again, with TVNWS. On one hand, high DER values are reached in case of deep damage and high sensor densities. For case $p = 2$ performance of TVNWS method even surpasses the performance of CWT and MSCS methods. On the other hand, this method is extremely sensitive to sensor density and damage depth with dramatic drop of performance. The CWT method is similar to MSCS method in this regard. However, it shows a higher instability with varying damage depth for lower sensor densities.
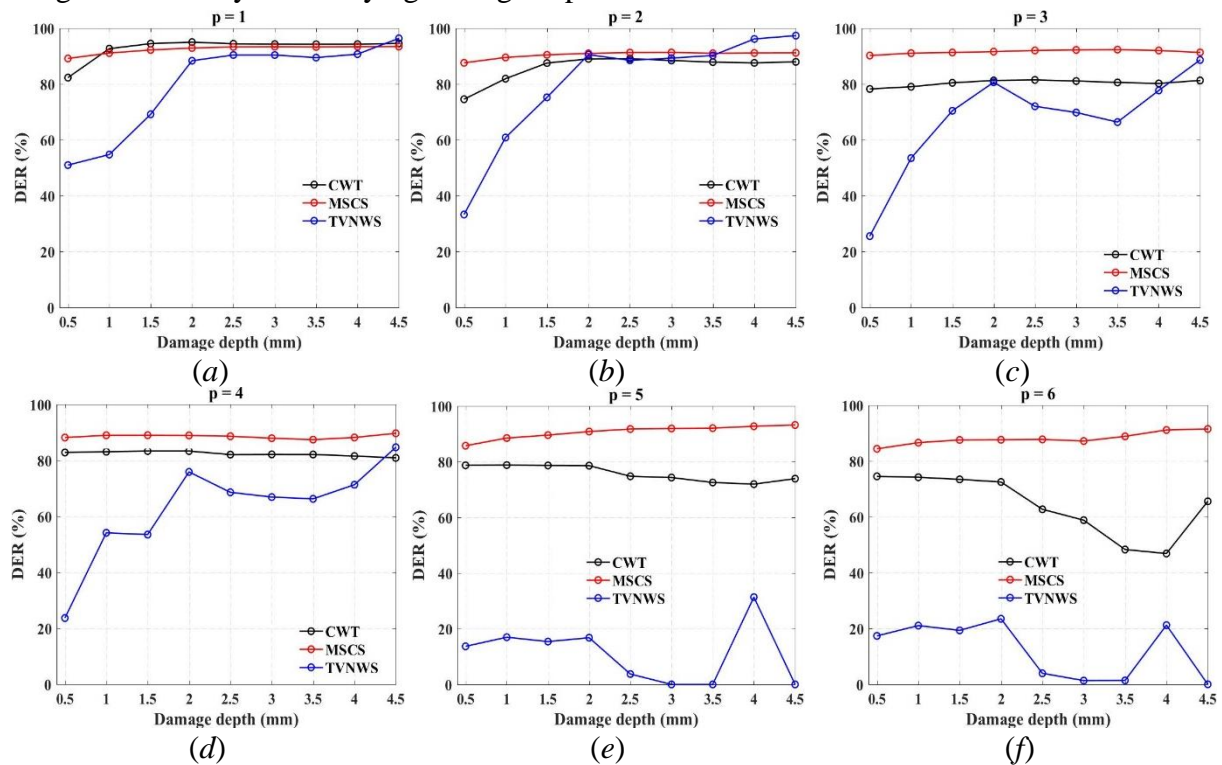
Fig. 3.24. Effect of damage depth and sensor density on DER variability for Al beam 1d for the developed damage localization methods (FEM): (*a*) $p = 1$; (*b*) $p = 2$; (*c*) $p = 3$; (*d*) $p = 4$; (*e*) $p = 5$; (*f*) $p = 6$.

Damage index profiles with damage depths of 0.5 mm, 2.5 mm and 4.5 mm for comparison are shown in Fig. 3.25 for all three methods. The most pronounced effect of damage depth on amplitude of the highest peak is attributed to TVNWS method. It can be noted that amplitude of the highest peak depends on damage depth. However, the largest amplitude is not attained at the deepest damage – 2.5 mm damage scenario is characterized with the largest amplitude peaks for all three methods even if the differences are relatively small for CWT and MSCS. Considerable edge effect is observed for CWT and MSCS methods at the smallest damage depth.

Overall, one can conclude that the proposed methods, except for TVNWS, are adequate for damage localization even in the cases of relatively shallow cuts with flexural stiffness changes below 1 % even with relatively sparse sensor network for mode shape interrogation.
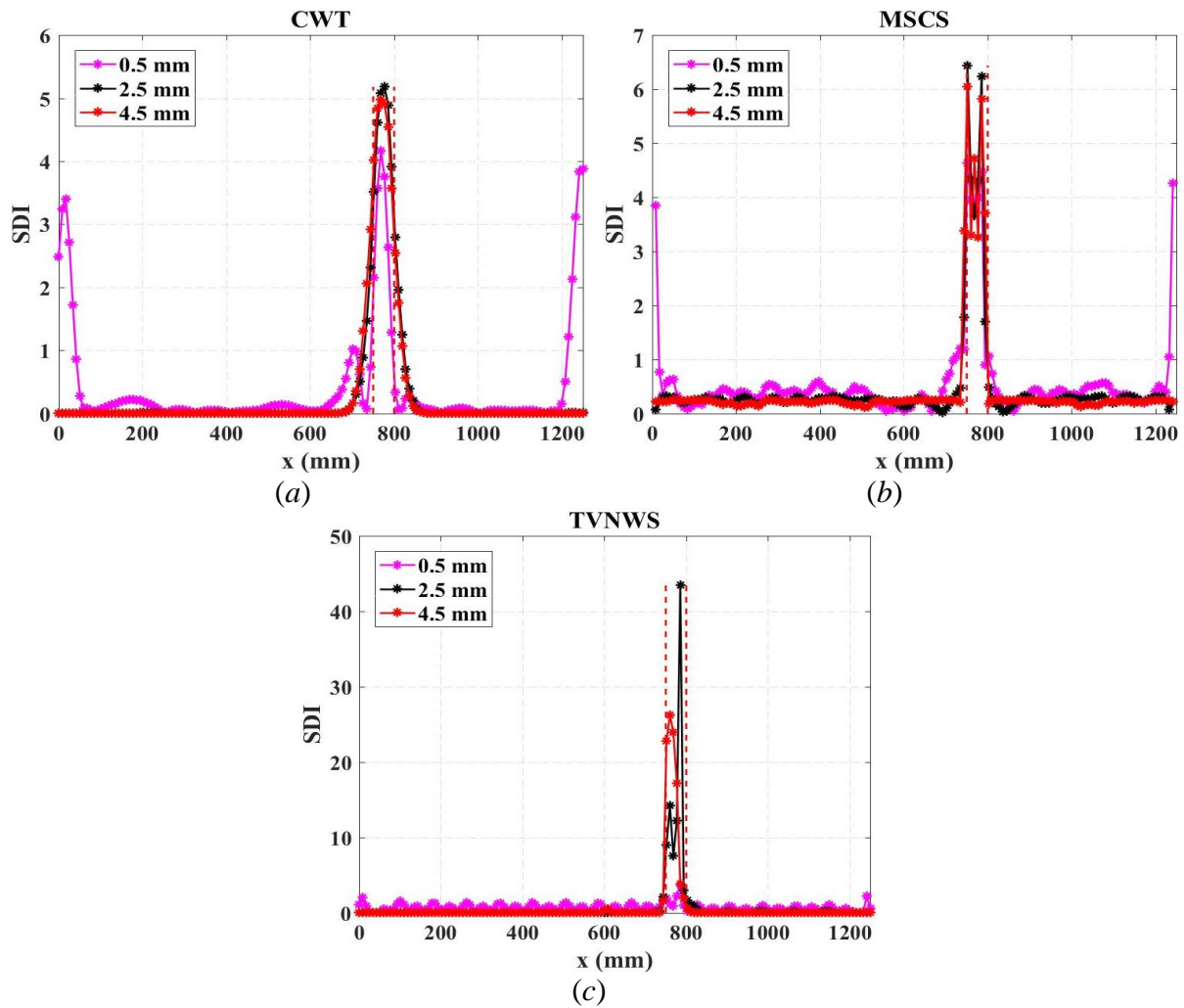
Fig. 3.25. Effect of damage depth on damage index profiles for Al beam 1d for the developed damage localization methods (FEM): (*a*) CWT; (*b*) MSCS; (*c*) TVNWS.

Additional study is carried out in regard to sensitivity of resonant frequency shift with increasing damage. Relative frequency changes were calculated in a similar manner to relative flexural stiffness changes in Eq. (3.4) only without the cubic terms. A total of 15 mode shapes are simulated for this purpose. A slope of frequency shift with varying damage depth is also calculated and all results are shown in Fig. 3.26. The largest slope is attributed to mode shape no. 5 with a value over 8.5 %/mm meaning that the relative frequency shift for this particular mode shape is more than 8.5 % with every millimetre of increasing damage depth. The smallest slope is attributed to mode shape no. 9 with a value of around 1.4 %/mm. By examining the Fig. 3.26, one can see that the most sensitive mode shape to damage in this case are mode shapes no. 5 and no. 1 with a total frequency shift in the range between 35 % and 40 %, while the least sensitive mode shapes are no. 9, no. 11 and no. 12 with a total frequency shift in the range between 7 % and 13 %.
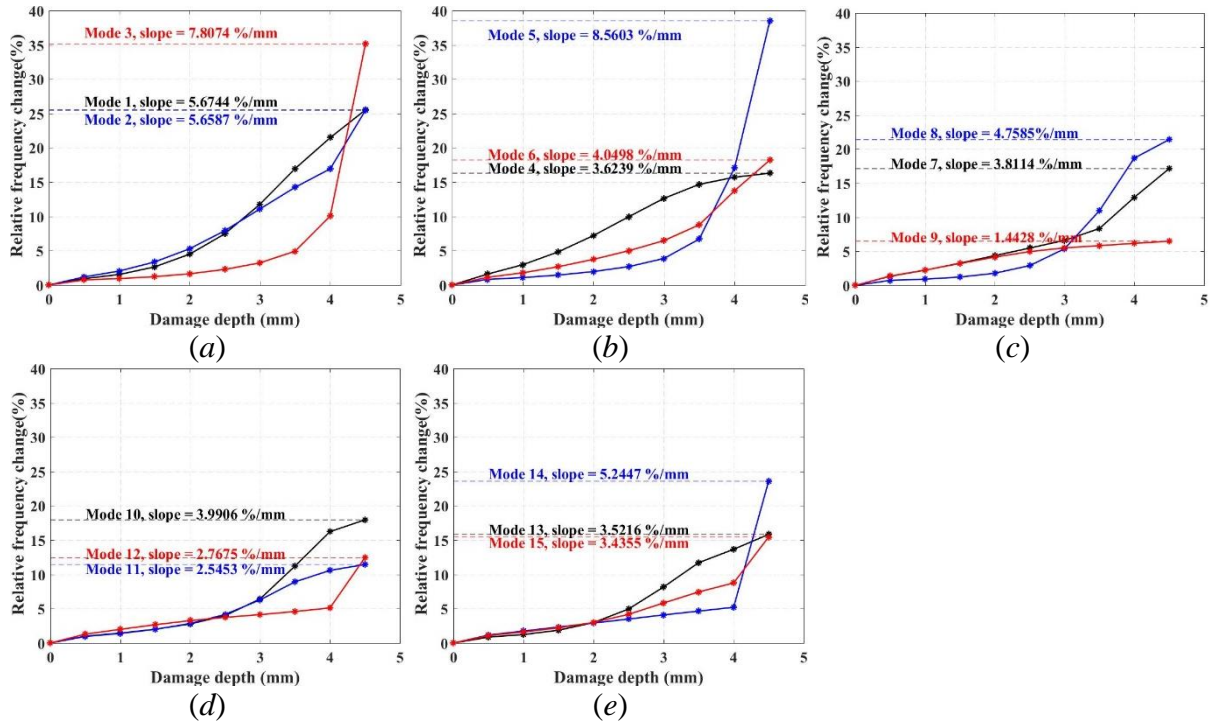
Fig. 3.26. Relative frequency shifts with increasing damage depth for flexural mode shapes of Al beam 1d (FEM): (*a*) mode shapes no. 1, 2 and 3; (*b*) mode shapes no. 4, 5 and 6; (*c*) mode shapes no. 7, 8 and 9; (*d*) mode shapes no. 10, 11 and 12; (*e*) mode shapes no. 13, 14 and 15.

3.2. Case study 2: Composite laminate beam with an impact damage

3.2.1. Numerical model

Laminated carbon/epoxy composite beam depicted in Fig. 3.27 is considered. The zone with dashed lines shows the location of damage based on the outer boundaries of ultrasonic C-scan (subsection 3.2.2). The laminate lay-up is $[0/90/+45/-45]_s$ with a ply thickness of 0.3 mm, thus total thickness of the plate is 2.4 mm. FE element model also consists of 2D beam elements. The beam is assembled of 55 elements ($i = 56$ nodes). The elastic material properties determined from an experiment are as follows: $E_x = 54.5$ GPa, $E_y = 31.04$ GPa, $G_{xy} = 7.09$ GPa, $G_{yz} = 6.5$ GPa, $v_{xy} = 0.3$, $\rho = 1364.9$ kg/m^3. Reduction of stiffness is achieved by decreasing the elastic modulus of elements in the damaged region of the beam.
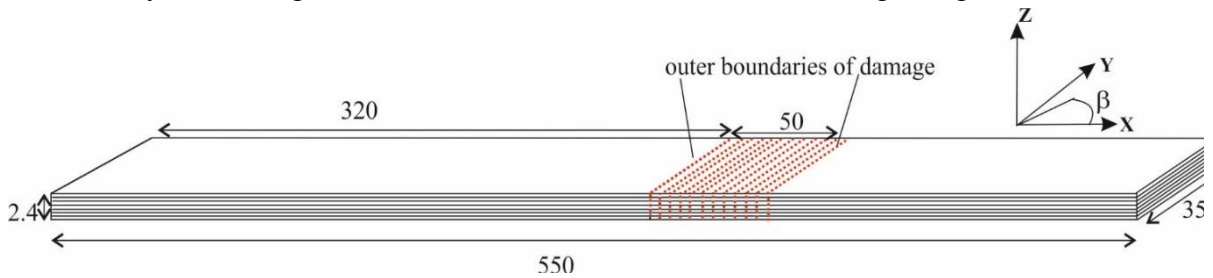
Fig. 3.27. Geometry of a damaged CFRP beam model (in mm).

3.2.2. Low-velocity impact and dynamic vibration testing

Low-velocity impact tests were conducted using INSTRON Dynatup 9250 HV drop tower (Fig. 3.28). The potential energy of the impactor at maximum height is transferred to a sample in the process of an impact. The impactor with hemispherical nose, a diameter of 20 cm and a mass of 2.25 kg was used in the tests. The CFRP beam was fixed by using pneumatic clamps. The impact energy of 15 J was selected, location of impact is set at the distance $L_i = 345$ mm. The photo of the damaged CFRP beam is shown in Fig. 3.29.

In order to assess location and through-thickness depth of damage, a pulse-echo ultrasonic imaging technique is used. The pulse-echo technique consists in generation of a short impulse of the ultrasonic wave by a transmitting transducer. After reflection from the limiting surface the impulses are recorded by a receiving transducer. If there is damage in the test material, some part of the ultrasonic wave is reflected from this damage, returns to the receiving transducer, and is recorded as the echo of the damage. Another part of the wave passes by the damage, reaches the opposite wall of the tested material, reflects from it, and returns to the receiver with some delay as the back-wall echo. The depth of the damage is determined based on the time-of-flight, i.e., the relation between the travel time of an impulse and the ultrasonic wave velocity. Ultrasonic C-scan images were recorded with a resolution step of 0.25 mm. Results of ultrasonic inspection are presented in Fig. 3.30.

(*a*)　　　　　　　　　　　　　　　　　　(*b*)
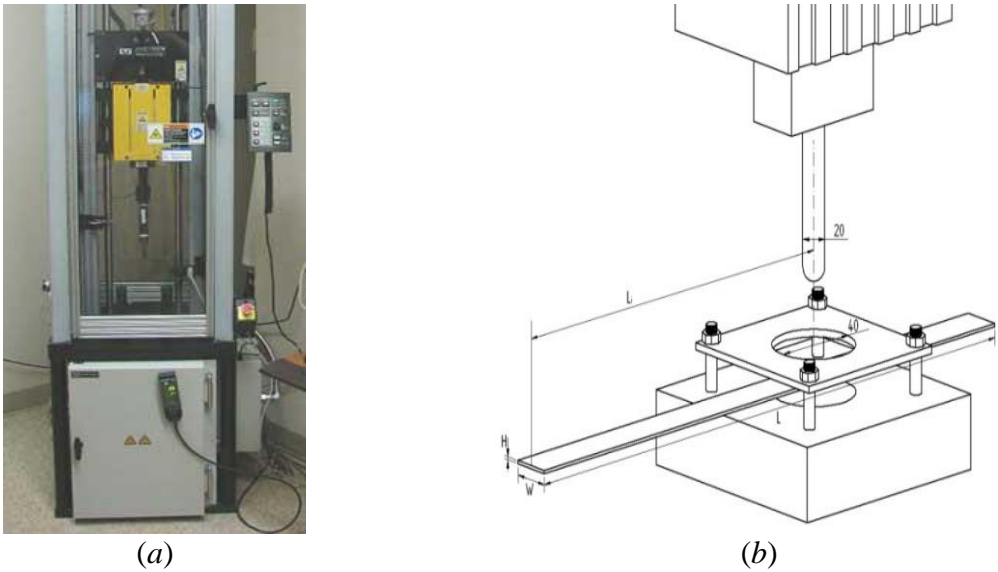
Fig. 3.28. Low-velocity impact testing: (*a*) impact drop tower; (*b*) impact setup.
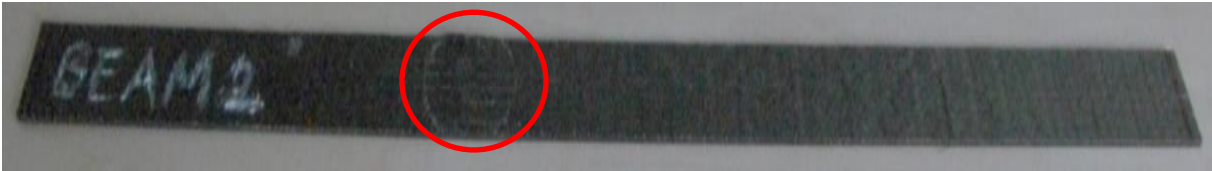
Fig. 3.29. Photograph of the actual composite beam with the region of impact damage.
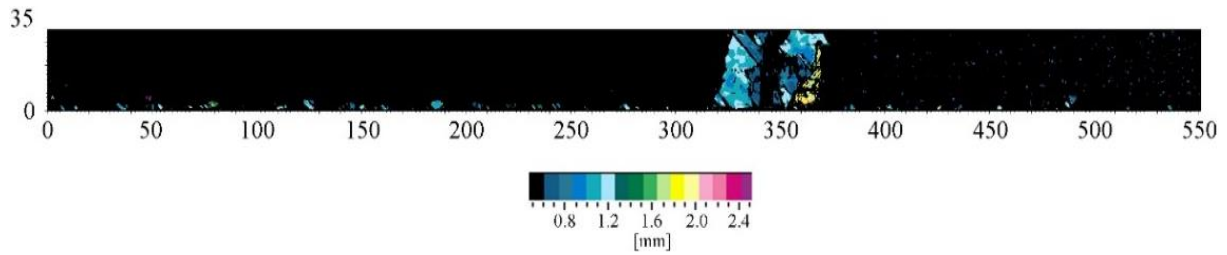
Fig. 3.30. Image of ultrasonic C-scanning for CFRP beam.

Based on the ultrasonic C-scan images for the DER calculations it is assumed that the starting position of damage is 320 mm while the ending position is 370 mm.

The dynamic vibration test was performed using scanning laser vibrometer with the setup parameters as provided in Table 3.6.

Table 3.6

Vibration experiment set-up parameters for CFRP beams

	Bandwidth (Hz)	Resolution (mHz)	FFT lines	Sample frequency (Hz)	Signal amplitude (V)	Size of a deflection shape signal
CFRP Beam d	0-3200	500	6400	8192	8	1×53
CFRP Beam h	0.25-3200	250	12800	8192	8	1×53

The extracted resonant frequencies of the experimental measurements and numerical simulations are depicted in Table 3.7 for the healthy and damaged CFRP beam.

Table 3.7

Resonant frequencies (Hz), extracted for clamped-clamped CFRP beam from a vibration test and finite element simulation

No.	CFRP beam damaged		CFRP beam healthy	
	Experiment	FEM	Experiment	FEM
1	-	47.09	-	51.55
2	136.25	128.14	141.25	142.10
3	263.00	270.06	275.75	278.57
4	413.75	410.32	408.50	460.46
5	656.25	643.29	697.00	687.80
6	891.25	889.37	959.00	960.56
7	1215.25	1189.74	1265.25	1278.74
8	1392.75	1491.38	1608.50	1642.30
9	1807.00	1917.79	1961.75	2051.24
10	2407.00	2320.88	2308.75	2505.52
11	2839.00	2747.38	3035.75	3005.13
12	-	3328.85	3194.75	3550.06
13	-	3814.89	-	4140.29
14	-	4416.80	-	4775.84
15	-	5023.82	-	5456.70

The plot of measured spectra for the CFRP beam is shown in Fig. 3.31.
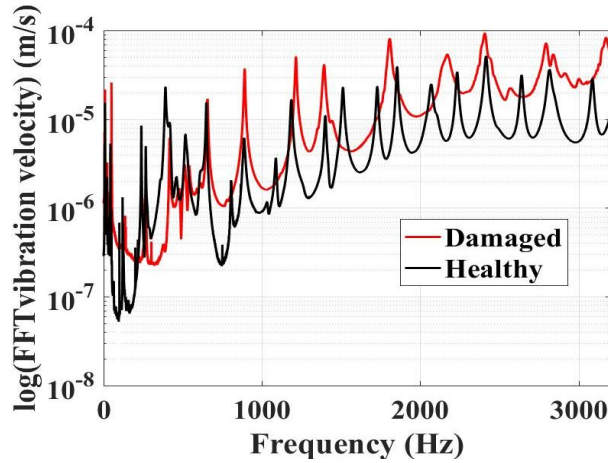
Fig. 3.31. Frequency spectra for CFRP beam.

3.2.3. Damage performance assessment

SDI values were calculated for scales from 1 to 128 for all 78 wavelet functions. Fourier series approximations for the MSCS method are depicted with F1-F8. These results for a CFRP beam are summarized in Table 3.8.

It is necessary to compute DER versus scale plot in order to determine the value of scale parameter at which damage identification was the most successful. As one can see in Fig. 3.32, DER peak values correspond to regions of smaller scale values. After the first peak the rest of the DER(s) pattern is unpredictable – it resembles a noisy signal. Nevertheless, these plots DER(s) are unique to each wavelet and are influenced by boundary conditions, and specimens under test. Only results for wavelets with highest maximum DER values are shown. The best wavelet function turned out to be complex Gaus of order 5 in experimental case. As for simulation cases, the reverse biorthogonal wavelet of order 3.1 showed the best performance. As for MSCS method, Fourier function of order 4 (F4) was the best. The effect of noise is not significant as indicated by relatively narrow confidence interval.

Table 3.8

Damage localization parameters for CFRP beam with the highest maximum DER

Method	p		Experiment	FEM
	1	2		
CWT	53	26	complex Gaus 5/2	reverse biorthogonal 3.1/9
MSCS	51	25	F4	F4
TVNWS	53	26	-	-
	DOFs		Wavelet/scale or approximation function	
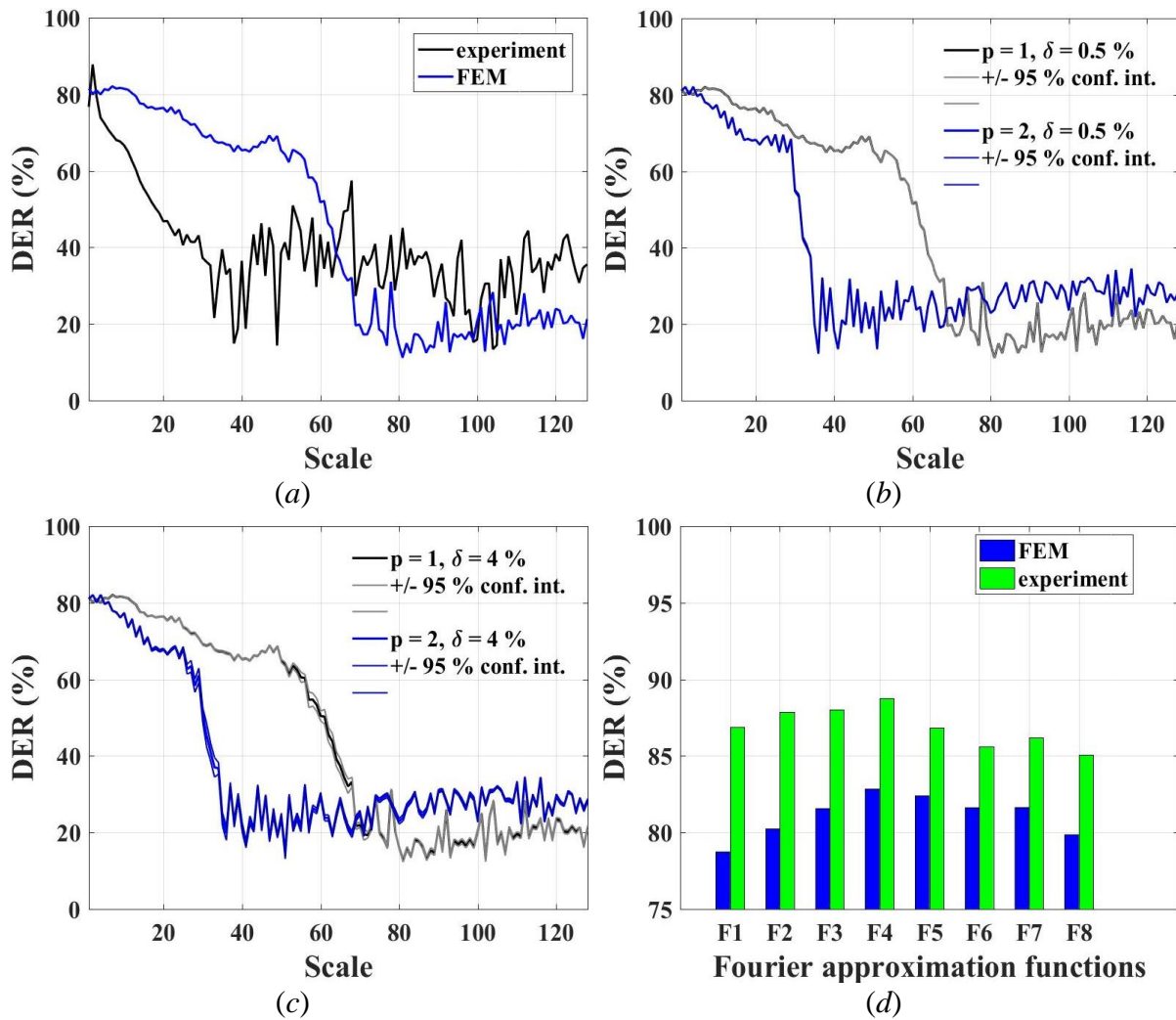
Fig. 3.32. Performance check for CFRP beam: (*a*) DER versus scale for CWT method (experiment, FEM); (*b*) DER versus scale for $\delta = 0.5$ %; (*c*) DER versus scale for $\delta = 4$ %; (*d*) DER for all approximation functions for MSCS method.

3.2.4. Damage localization

Damage identification results for both methods (CWT and MSCS) are shown in Fig. 3.33. and Fig. 3.34, respectively. As one can see, the location of damage, which is indicated between two red dashed lines, is successfully identified by both methods. There are some smaller peaks present in these plots that are later filtered out using SDI thresholds. After the application of threshold DER values in all cases increased by roughly 10 %.

Both algorithms manage to localize the damage even by decreasing sensor density from $p = 1$ to $p = 2$ and introducing noise. The case with noise level of $\delta = 4$ % displays more variability in SDI profile shown by confidence intervals proving that MSCS method is rather susceptible to noise.
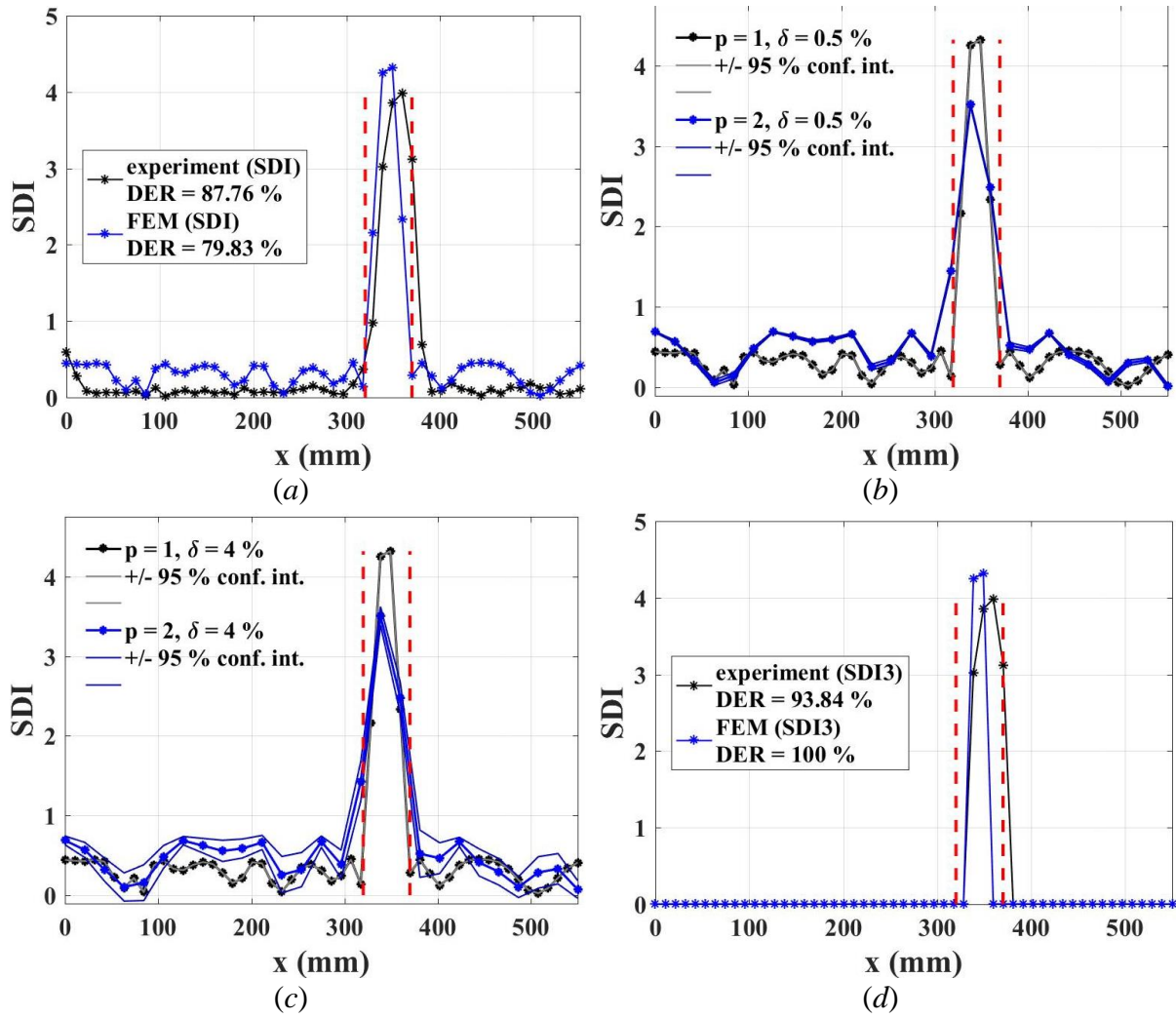
Fig. 3.33. Standardized damage indices for CWT method: (*a*) experiment and FEM (no threshold); (*b*) FEM with $\delta = 0.5$ %; (*c*) FEM with $\delta = 4$ %; (*d*) experiment and FEM (thresholded).
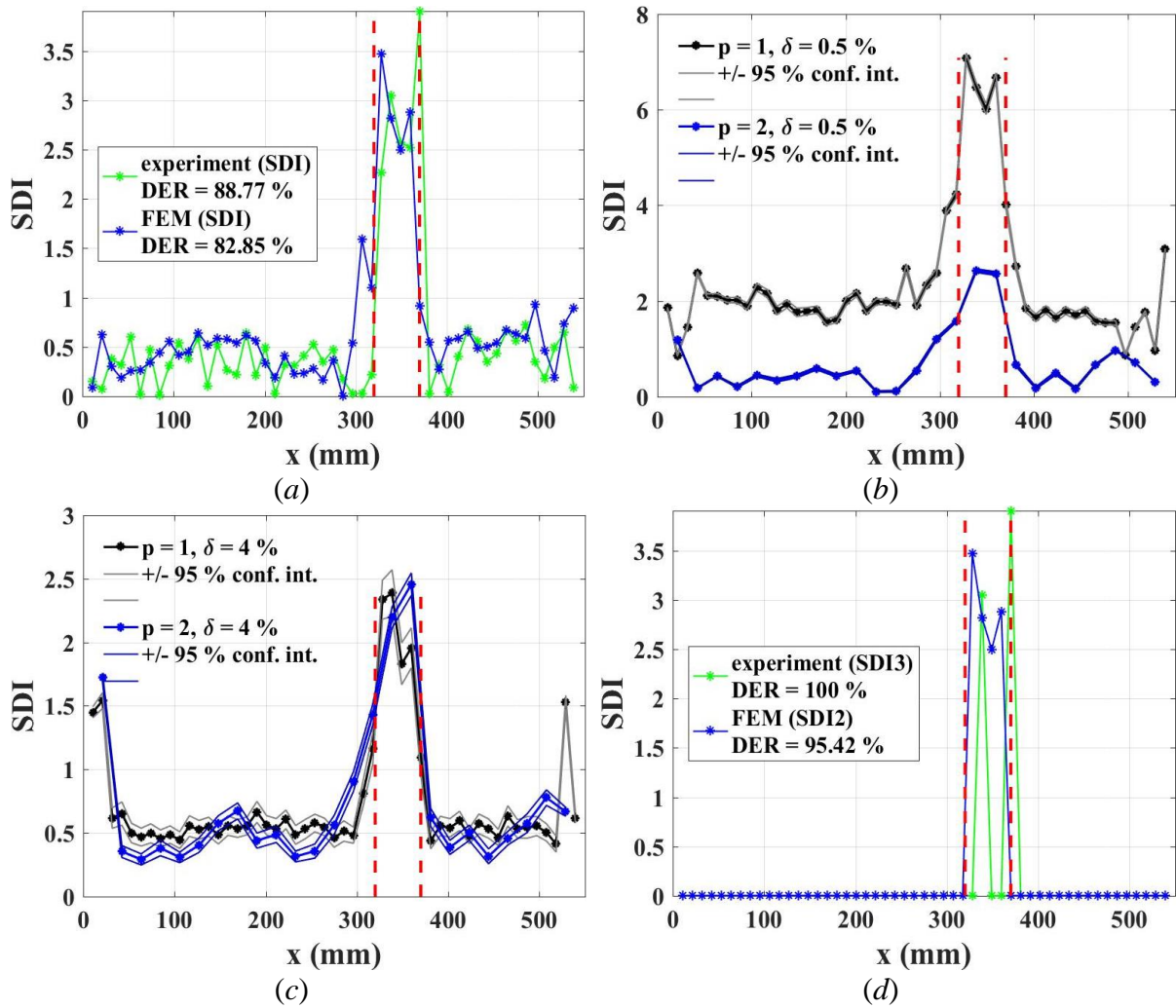
Fig. 3.34. Standardized damage indices for MSCS method: (*a*) experiment and FEM (no threshold); (*b*) FEM with $\delta = 0.5$ %; (*c*) FEM with $\delta = 4$ %; (*d*) experiment and FEM (thresholded).

The scalograms and normalized wavelet scalograms in the same manner as in Fig. 3.16 and Fig. 3.18 are shown in Fig. 3.35. Significant amplitudes are in the zones where damage is not present. The normalization of the wavelet scalograms provides a remedy for the smearing out of amplitudes over the coordinate of the beam.

Damage has been localized also using TVNWS method with noise levels of $\delta = 0.5$ % and $\delta = 4$ % as shown in Fig. 3.36, although the method suffers from the sensitivity to sensor density with considerable peaks outside the true zone of damage. The DER value of the filtered variance of normalized wavelet scalogram for $p = 1$, $\delta = 0$ % is about 61.4 % which is around 19 % lower than DER for the CWT method and 21 % less than in the case of the MSCS method. On the other hand, the experimental results (shown in green) demonstrate the success of the algorithm with DER equal to 95. 29 %.
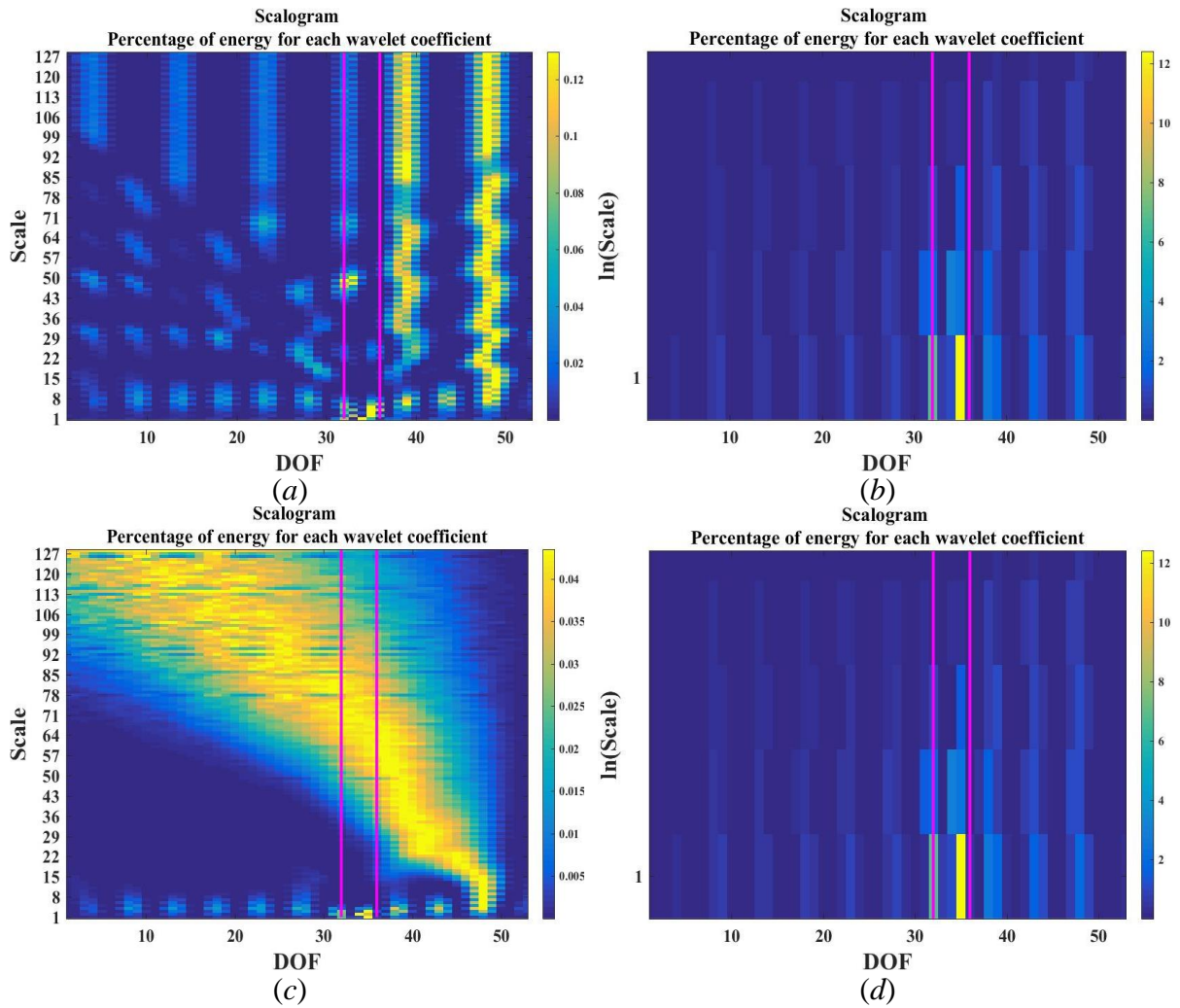
Fig. 3.35. Wavelet scalograms for CFRP beam at $p = 1$ (experiment): (*a*) scalogram for Haar wavelet; (*b*) normalized scalogram for Haar wavelet; (*c*) best performance scalogram for complex morlet 1-1 wavelet; (*d*) best performance normalized scalogram for complex morlet 1-1 wavelet.

(*a*)
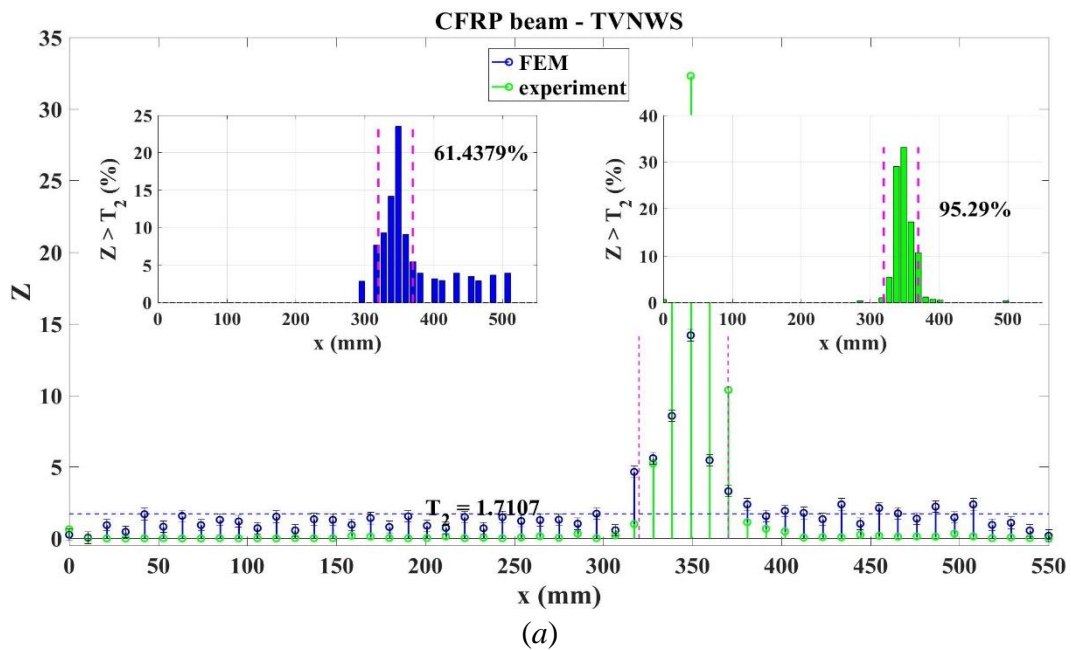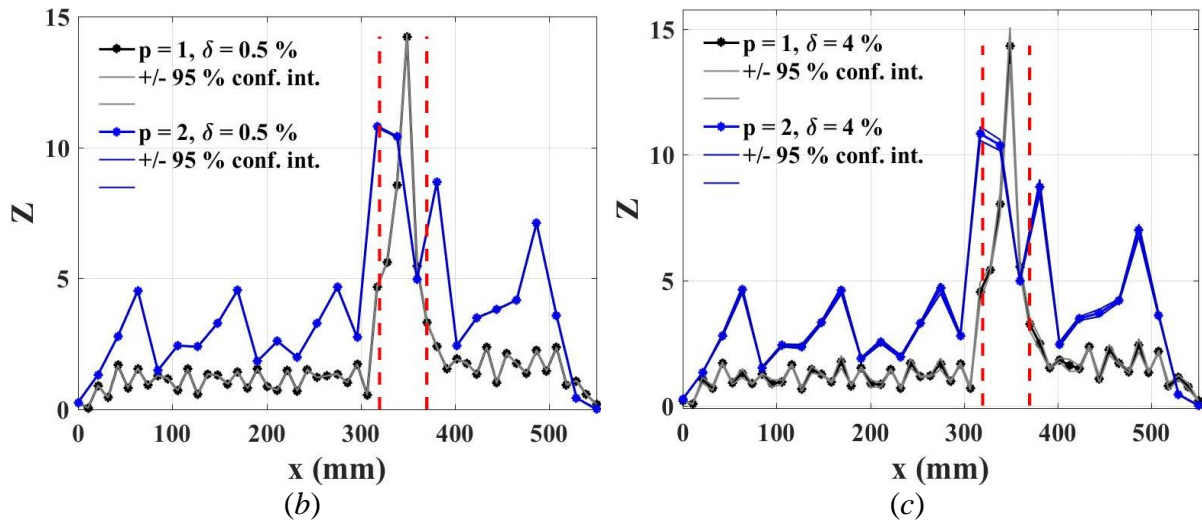
Fig. 3.36. Damage indices for TVNWS method for CFRP beam with an impact damage: (*a*) fractional wavelet scalogram with second threshold and filtered values; (*b*) FEM with $\delta = 0.5$ %; (*c*) FEM with $\delta = 4$ %.

The performance of methods in terms of DER parametric check is assessed in a similar manner to aluminium beams by constructing the damage estimate reliability diagrams for all 3 methods (Fig. 3.37).

A relatively large drop in DER values is associated with introducing noise for both sensor densities $p = 1$ and $p = 2$ for the CWT method, however DER values remain stable with increasing noise levels with slightly lower DER for $p = 2$. As with aluminium beams, non-significant decrease in DER is observed with decreasing sensor density for the MSCS method. On the other hand, noise is a more considerable issue comparing to the CWT method. Again, as with aluminium beams, the TVNWS method's performance is the worst in terms of DER values, however the increasing noise levels and decreasing sensor density do not have a significant impact on DER.

CFRP beam - F4

(b)

CFRP beam - TVNWS

(c)
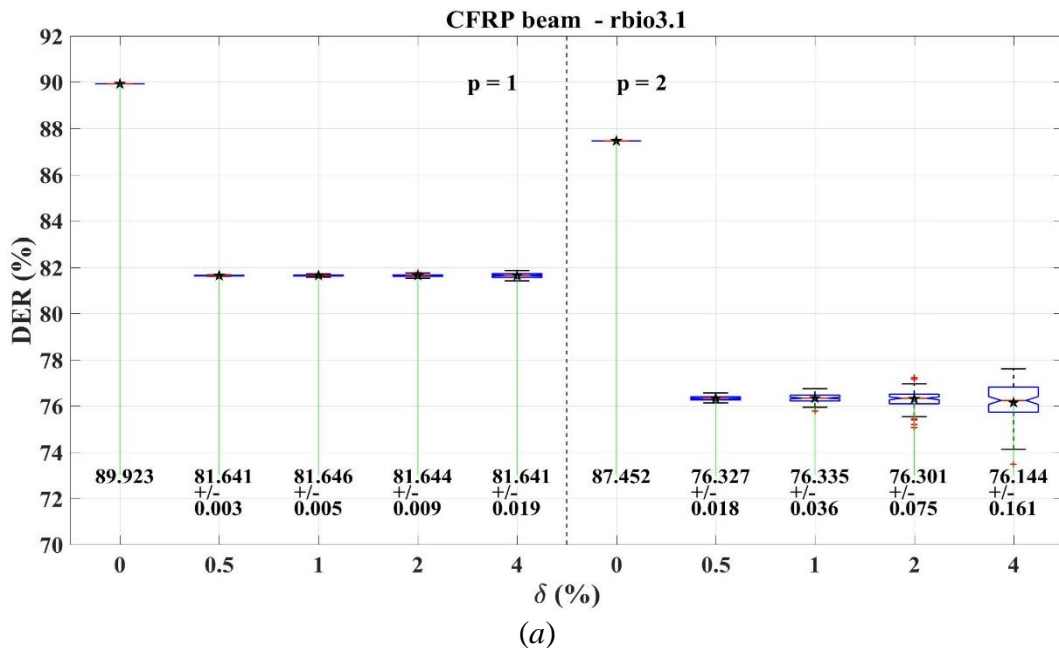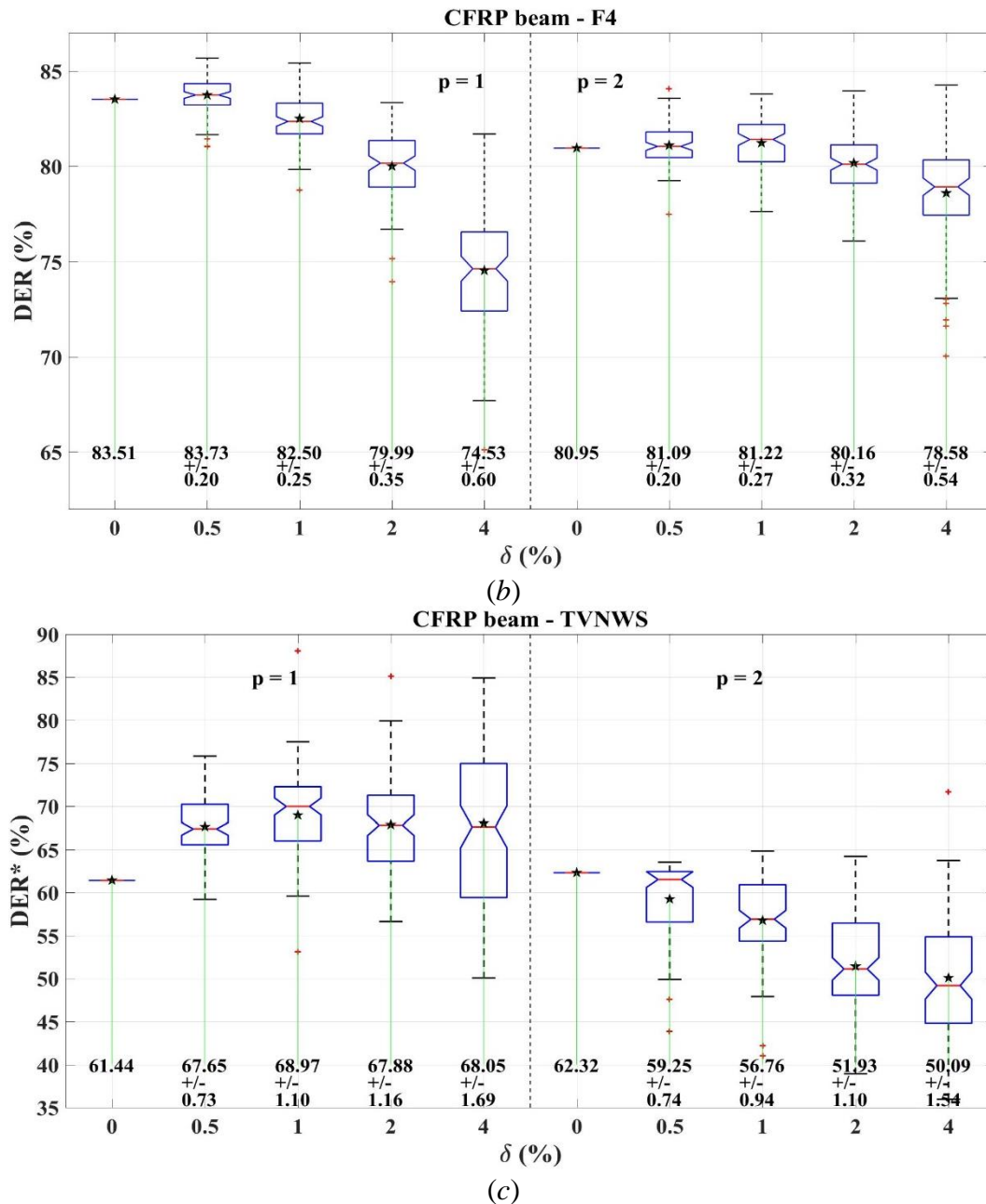
Fig. 3.37. Effect of sensor density and noise on DER variability for CFRP beam with an impact damage: (a) CWT; (b) MSCS; (c) TVNWS.

Damage is successfully localized by applying an algorithm involving standardization of damage indices and a subsequent decision making based on results from statistical hypothesis testing. The methods provide reliable information about the location of damage in two aluminium beams with single and multiple mill-cut damage sites and also in CFRP beam containing impact damage with all beams at clamped-clamped boundary conditions. The following findings for this chapter are reported:

- While, in general, the data of a healthy structure is a necessity in order for Mode Shape Curvature Square methods to work, it is demonstrated that this is not necessary – mode shape curvatures of a healthy structure are obtained through interpolation of damaged mode shape curvature with Fourier series functions.

- It is necessary to test all available wavelet functions and Fourier series functions of all orders to identify the best function for damage identification algorithm. There are a lot more wavelet functions than Fourier series orders; therefore, proposed Mode Shape Curvature-based method is more robust.

- A likelihood of damage localization for both methods is described with a Damage Estimate Reliability parameter. Analysis of this parameter versus wavelet scale is necessary to determine the scale that yields the best damage identification results. It is observed that Damage Estimate Reliability curves are overall smoother for larger sensor densities and for smaller scales.

- Both methods show reliable damage identification performance in terms of Damage Estimate Reliability parameter, although for Mode Shape Curvature Square method these results are, in general, better and more stable with varying sensor density.

- It is a well-known fact, that wavelet scales are inversely proportional to their pseudo frequency. These pseudo frequencies are needed for comparison between different wavelets in a characterization of particular phenomenon. It is observed that pseudo frequencies corresponding to maximum Damage Estimate Reliability parameter exhibit a shift towards higher values with increasing sensor density.

- A statistical hypothesis approach is exploited to classify whether the element of structure is damaged or not. Standardized Damage Indices are then thresholded to ascertain for damage localization confidence. Threshold value of 3, corresponding to 99 % confidence is chosen for both methods. It is found, that Mode Shape Curvature Squares method yields better results also considering the application of thresholds with damage estimate reliability parameter exceeding 98 %, although large amplitude Standardized Damage Index values are still present at the edges of both beams.

4. DAMAGE LOCALIZATION IN 2-D STRUCTURES

Robustness and effectiveness of the proposed damage detection method in combination with SLV system is demonstrated experimentally on an aluminium plate containing mill-cut damage and CFRP beam with impact damage from previous chapter whose deflection shapes are measured in two dimensions. Validity of the proposed damage detection method is assessed by comparing the damage detection results of the experimental test case to the results obtained from the simulated test case.

4.1. Case study 1: Aluminium plate with a mill-cut damage

A research effort aimed at detecting and localizing damage in plate-like structures by using a mode shape curvature based method is described. The basic idea of the method is that the mode shape curvature of a healthy structure has a smooth surface, and it can be approximated by a polynomial. Using a mode shape curvature data of the damaged structure and a regression analysis with a polynomial approximation, smooth mode shape curvature surfaces of the healthy structure are estimated. The damage index is defined as the absolute difference between the measured curvature of the damage structure and the smoothed polynomial representing the healthy structure and the maximum value indicates the location and size of the damage. To examine the advantages and limitations of the proposed method, several sets of numerical simulations considering different levels of damage severity, measurement noise and sensor sparsity are carried out. Applicability and effectiveness of the proposed damage detection method is further demonstrated experimentally on an aluminium plate containing mill-cut damage.

4.1.1. Finite element model and modal analysis

Square plate

To evaluate the applicability and effectiveness of the proposed damage detection algorithm, a square aluminium plate with characteristics described in subsection 4.1.2. is considered. Numerical modal analysis is carried out by using the commercial FE software $ANSYS^{\mathrm{TM}}$. The finite element model of the plate consists of 8-node shear-deformable shell elements. For the healthy plate, constant flexural stiffness is assumed for all elements, while the damaged plate is modelled by reducing the flexural stiffness of the selected elements. Reduction of flexural stiffness is achieved by decreasing the thickness of elements in the damaged region of the plate, thus simulating a cut on one side of the plate. In order to correctly compare the damage detection results, the numerical model is built according to the experimental set-up. The plate is divided into 52×52 elements and the clamped boundary conditions are applied at all four edges of the plate. The mode shapes are extracted from 51×51 nodes in the region $20 \text{ mm} \leq x \leq 980 \text{ mm}$ and $20 \text{ mm} \leq y \leq 980 \text{ mm}$ of the plate, thus boundary nodes at all four edges of the plate are excluded from the damage detection analysis. The modal frequencies and corresponding mode shapes for 12 modes are extracted from all from 51×51 nodes in the damaged plate model.

Several sets of simulated data are used to investigate the effectiveness of the proposed algorithm for damage detection in plate-like structures. Five different levels of damage severity (cut depth) are introduced in the region $270 \text{ mm} \leq x \leq 350 \text{ mm}$ and $640 \text{ mm} \leq y \leq 700 \text{ mm}$ representing 0.48 % of the plate area (Fig. 4.1). Cut depths of $h_1 = 0.5, 1, 1.5, 2, 2.5$ mm are assumed.

To ascertain the sensitivity of the proposed algorithm to noisy experimental data, a series of uniformly distributed random variables is added to the numerical mode shapes to generate the noise-contaminated mode shapes according to Eq. (3.1). In this study four different noise levels $\delta = 1 \times 10^{-2}, 5 \times 10^{-3}, 1 \times 10^{-3}, 5 \times 10^{-4}$ are examined. Combination of different noise levels and cut depths results in 20 simulated test cases, which are given in Table 4.1.

Although the latest measurement systems such as SLV allow obtaining high-density mode shape data, in practice mode shapes often can be only measured using relatively sparse distribution of sensors and thus the robustness of the proposed method under limited data points is of interest. In order to evaluate the effect of different number of measured mode shape data points on the performance of the method, it is proposed to divide the initial matrix of 51×51 data points by integer values of $p = 1, 2, 3, 4, 5$. In these five cases, the extracted mode shape data form matrices with the following sizes: 51×51, 26×26, 17×17, 13×13, 11×11. For comparison purposes the cut depth of 2 mm and the noise level $\delta = 2 \times 10^{-3}$ is assumed.

Rectangular plate

In order to evaluate the robustness of the proposed algorithm to different aspect ratios of the plate, a rectangular aluminium plate 1000×400 mm of $h = 5$ mm thickness with the same physical properties as for the square plate is also examined. The plate is divided into 52×22 elements and the clamped boundary conditions are applied at all four edges of the plate. The mode shapes are extracted from 51×21 nodes in the region $20 \text{ mm} \leq x \leq 980 \text{ mm}$ and $20 \text{ mm} \leq y \leq 380 \text{ mm}$ of the plate. Mill-cut damage with a depth of 2 mm is introduced in the region $270 \text{ mm} \leq x \leq 350 \text{ mm}$ and $240 \text{ mm} \leq y \leq 270 \text{ mm}$ of the plate. In total, 12 modal frequencies and corresponding mode shapes are calculated. The noise level $\delta = 2 \times 10^{-3}$ is added to the calculated mode shapes to generate the noise-contaminated mode shapes.

Elements with reduced thickness
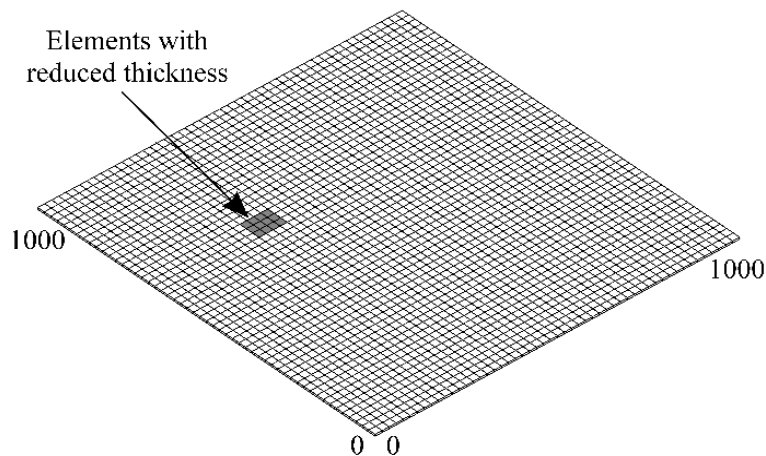
Fig. 4.1. FE model of an aluminium plate with damage.

4.1.2. Aluminium plate specimen

A square aluminium plate 1000×1000 mm of 5 mm thickness is considered. The elastic material properties are taken as follows: Young's modulus $E = 69$ GPa, Poisson's ratio $\nu = 0.31$, and the mass density $\rho = 2708$ kg/m³. Mill-cut damage with a depth of 2 mm is introduced in the region 270 mm $\leq x \leq$ 350 mm and 640 mm $\leq y \leq$ 700 mm of the plate.

The clamped boundary conditions are also realized for an aluminium plate by fixing the plate into a specially designed aluminium frame (Fig. 4.2). The distance of 18 mm of each edge of the plate is fixed between the frame and solid aluminium bar and tied together by means of bolts with the spacing distance of 100 mm. The clamping strength is realized by applying 20 N · m of fastening torque onto the bolts. To ensure uniform pressure through the whole contact surface, an aluminium beam with the same thickness and physical properties as the test plate is inserted between the frame and the bar on the other side of the bolts.

The extracted resonant frequencies for the aluminium plate with the damage are depicted in Table 4.1. As one can see, the experimentally measured resonant frequencies are slightly higher than those calculated in a simulation. This is probably due to the boundary conditions.

(*a*)   (*b*)
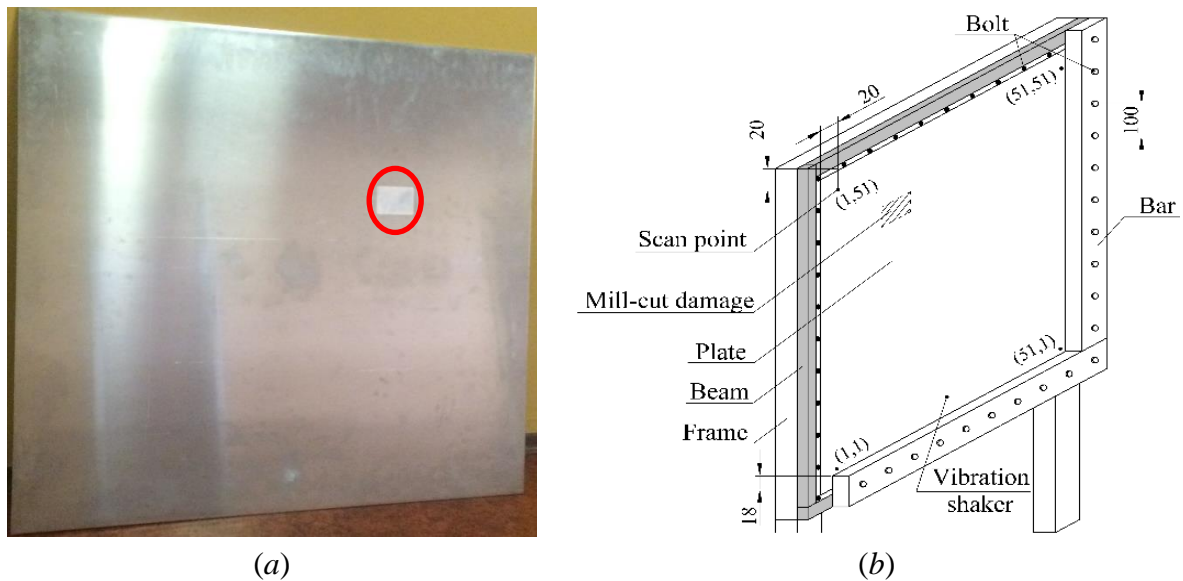
Fig. 4.2. Tested aluminium plate: (*a*) specimen with a mill-cut damage; (*b*) clamping boundary conditions for the vibration test.

Table 4.1

Resonant frequencies (Hz), extracted for damaged clamped-clamped aluminium plate from a vibration test and finite element simulation

No.	Experiment	FEM
1	41.00	43.90
2	85.00	89.43
3	-	89.58
4	128.00	131.91
5	152.00	161.05
6	-	161.73
7	192.00	201.65
8	-	201.82
9	248.00	258.08
10	-	258.37
11	262.50	268.74
12	287.50	296.71
13	-	297.70
14	360.00	362.40
15	-	363.19

4.1.3. Damage localization results

For the illustration of the proposed damage detection algorithm, the general workflow implemented in *Matlab*™ is given below:

- For the numerical test case, a finite element model with the selected cut depth is built and the modal frequencies and corresponding mode shapes are extracted from all 51×51 nodes. For each of $n = 1, ..., N$ modes, a two-dimensional array of transverse displacements $\widetilde{w}_{i,j}^n = \widetilde{w}^n(x_i, y_j)$, $(1 \leq i, j \leq I)$, $I = 51$ is formed. For the experimental test case, transverse displacements $w_{i,j}^n = w^n(x_i, y_j)$, $(1 \leq i, j \leq 51)$ are recorded by means of laser vibrometer and, similarly, a two-dimensional array is formed.

- In the next step for each mode, the noise level δ is assigned to calculated mode shapes to generate noise-contaminated mode shapes $w_{i,j}^n$ according to Eq. (3.1).

- From the recorded quantities $w_{i,j}^n$ second order derivatives are calculated by the central difference approximation (Eq. (2.27)) for each $i, j = 2, ..., I - 1$.

- The smoothed mode shape curvature surfaces κ_x^n, κ_y^n are estimated by using the calculated second order derivatives and the weighted linear least-squares regression with a second degree polynomial approximation. It should be noted that the smoothing process is considered local because each smoothed value is determined by neighbouring data points defined within the span. In this study, the span is defined by 10 % of the total number of data points in order to fit the original surface as close as possible and not to smooth out too much information. The selection of the span is especially important due to possible quick changes of sign of neighbouring mode shape curvature values when the higher modes and a sparse distribution of sensors are considered (see Fig. 4.3).

- Damage indices $D_{i,j}^n$ are calculated according to Eq. (2.26). The absolute difference between the measured curvature and the smoothed polynomial in *x* and *y* directions is normalized with respect to the largest value of the respective component so that both components have equal weight in calculating damage index.
- Finally, damage indices $D_{i,j}$ for all modes are estimated by Eq. (2.8).

Smoothing process of the mode shape curvature of the damaged structure is the most important part of the proposed method for its successful application; therefore, illustration of the process is given in Fig. 4.4. Mode shape of the highest experimentally measured mode (in terms of both resonant frequency and nodal lines [4, 4]) of the plate and the corresponding second order derivatives in x direction are presented in Fig. 4.3. In this case a matrix of 17×17 measured data points is employed to build the mode shape and calculate the derivatives. The importance of the span selection for the surface smoothing is illustrated by two examples (see Fig. 4.4): in the first case the span is defined by 10 % of the total number of data points; in the second one – by 25 %.

It can be noticed that in the first case the smoothed surface (surface plot) fits most of the initial data points (blue standalone points) and therefore the largest absolute differences (used for calculation of damage indices) in measured curvature and smoothed surface are to be expected due to damage and subsequently could point at the damage location. On the other hand, when 25 % of data points are used for span definition, the smoothed surface still represents the pattern of the curvature like for the 10 % case, but most of the initial data points fall off the surface. In this case the absolute difference between the calculated and smoothed surfaces will result in noisier damage index plot and thus is much less useful for damage detection.
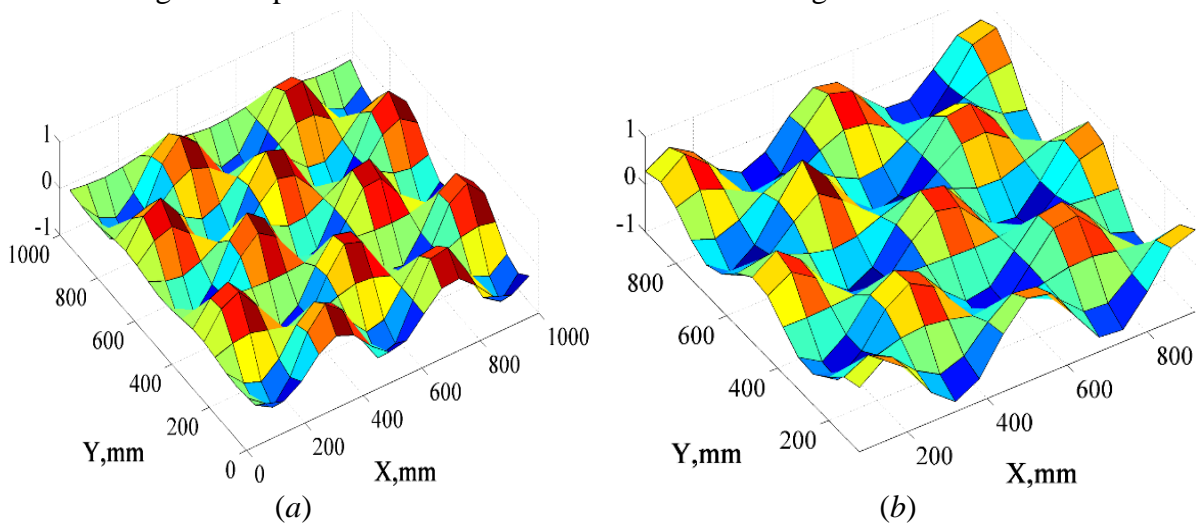
Fig. 4.3. The 12th mode of the aluminium plate: (*a*) mode shape; (*b*) κ_x^n.
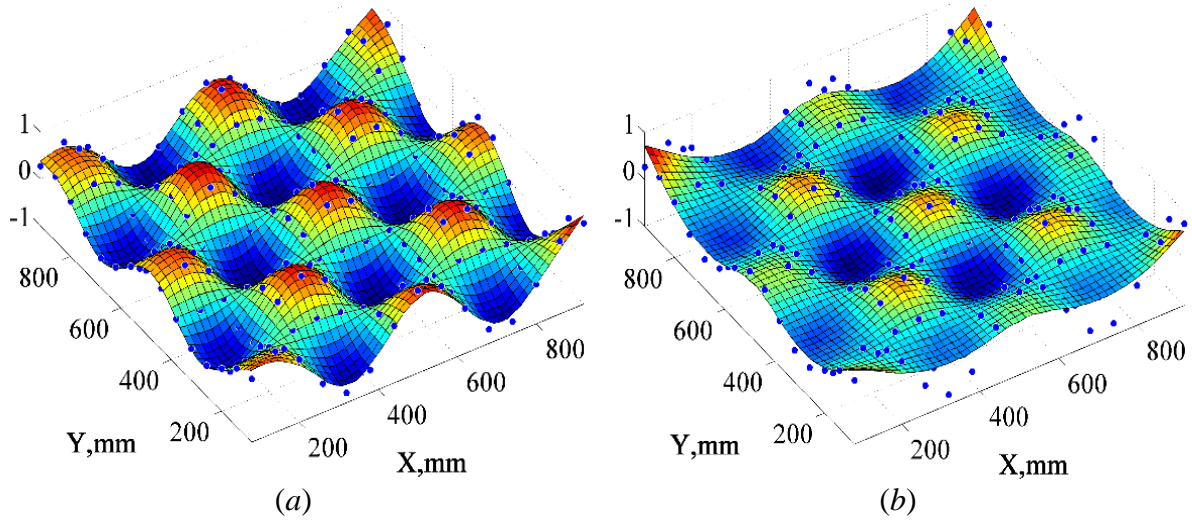
Fig. 4.4. The smoothed surface of the κ_x^n for 12th mode of the aluminium plate: (*a*) span is 10 % of the total number of data points; (*b*) span is 25 %.

Damage detection results for the experimental test case and the corresponding simulated test case (cut depth – 2 mm, noise level $\delta = 2 \times 10^{-3}$) using original matrix of 51×51 data points are given in Fig. 4.5 (*a*). Although in both cases the peak values occur at the pre-determined damage location, it can be seen that large values also emerge at the boundaries of the plate and some smaller peaks are present at other areas of the plate where no damage has been introduced. To classify the damaged elements, it is proposed to truncate the values of standardized damage indices (Eq. (2.10)) smaller than three units according to the standardized damage index threshold value for the 99 % confidence level for the presence of damage. Now the damage detection results for both cases clearly reveal the pre-determined damage location as shown in Fig. 4.6 (*d*). Similarly, the damaged elements are classified for the other two confidence levels. It can be seen that in general for both cases damage indices clearly point at the pre-determined damage location, however other insignificant peaks have passed the pre-assigned damage index threshold for both the 90 % and 95 % confidence levels and can be classified as damage. On the other hand, it must be noted that only 5 out of 12 employed mode shapes for the experimental test case and 6 out of 12 for the simulated test case are affected by the introduced damage and their corresponding damage indices could individually point the damage location.
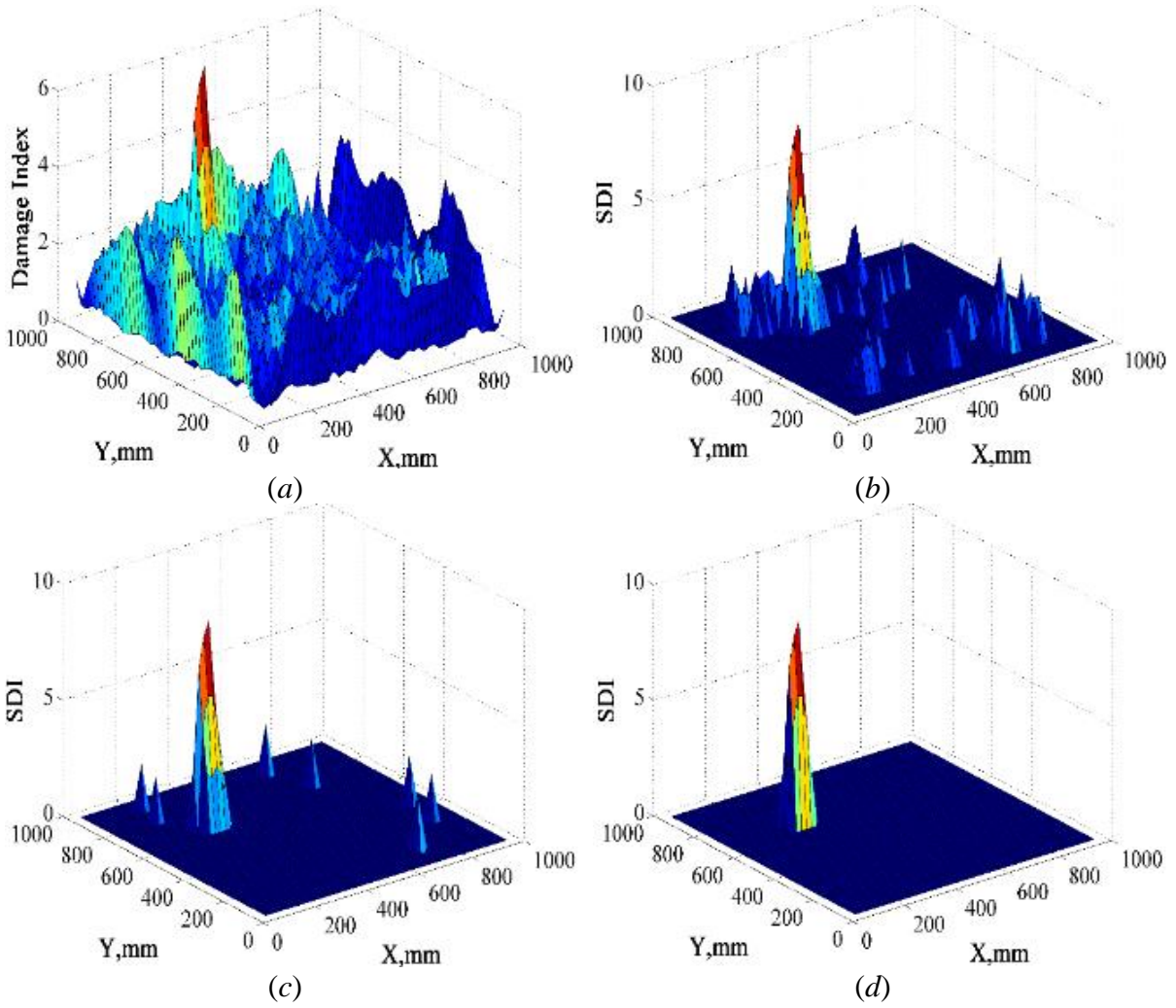
Fig. 4.5. Damage indices for aluminium plate (experiment): (*a*) without standardization; (*b*) standardized indices with 90 % confidence; (*c*) standardized indices with 95 % confidence; (*d*) standardized indices with 99 % confidence.
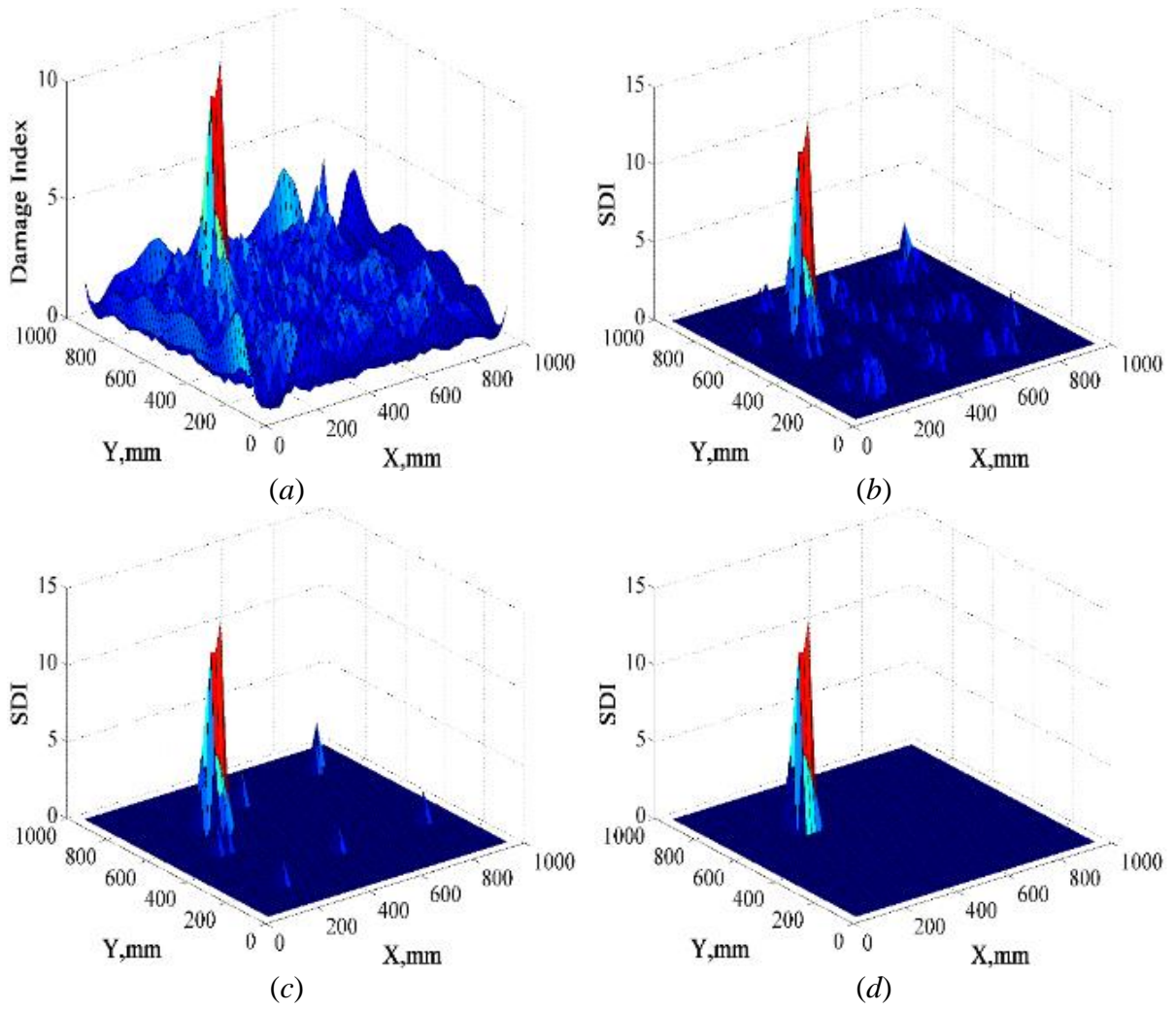
Fig. 4.6. Damage indices for aluminium plate (FEM): (*a*) without standardization; (*b*) standardized indices with 90 % confidence; (*c*) standardized indices with 95 % confidence; (*d*) standardized indices with 99 % confidence.

To analyse the influence of the noise level and damage severity on the effectiveness of the proposed method, a false-positive damage indication ratio FP is introduced. False-positive indication of damage means that standardized damage indices outside the pre-determined damage location have passed the pre-assigned damage classification criterion and indicate the presence of damage although no damage is present there. The ratio represents the relationship between a number of nodes with a false-positive damage indication and the total number of nodes for the plate:

$$FP = \frac{\sum_{i,j=2}^{A-1} n(SDI_{i,j} \geq 3)}{\sum_{i,j=2}^{A-1} 1} \times 100\ \% = \frac{\sum_{i,j=2}^{A-1} n(SDI_{i,j} \geq 3)}{(A-2) \times (A-2)} \times 100\ \%$$

$$n(SDI_{i,j} \geq 3) = \begin{cases} 1 \text{ if } SDI_{i,j} \geq 3 \\ 0 \text{ if } SDI_{i,j} < 3 \end{cases} \tag{4.1}$$

where $n(SDI_{i,j} \geq 3)$ is related to those nodes, for which the standardized damage index value has passed the threshold value for the 99 % confidence level for the presence of damage.

Similarly, false-positive damage indication ratios are calculated for the other two confidence levels. Calculated false-positive damage indication ratios for the simulated test cases are summarized in Table 4.2. It must be noted that false-positive damage indication ratios are included in the table only for those simulated test cases where standardized damage indices at the pre-determined damage location passed the standardized damage index threshold value for the corresponding confidence level. In general, the capability of the proposed damage detection algorithm is found to be dependent on both the introduced noise level and damage severity. As expected, the false-positive damage indication ratio FP increases as the damage severity decreases and increases as the noise level is increased.

Standardized damage indices presented in Fig. 4.7 illustrate the effectiveness of the proposed method when different numbers of measured mode shape data points are available for the damage detection. As seen from these figures, the method is able to correctly detect damage in all 5 simulated test cases and in 4 out of 5 times for the experimental test cases if the standardized damage index threshold value 3 for the 99 % confidence level for the presence of damage is applied. However, its ability to accurately indicate the pre-determined damage location and to illustrate the approximate shape of the damage gradually decreases as the sensor spacing increases. The method is still able to detect the damage when the lowest number of measurement points 11×11 is considered for the simulated test case, but it fails to accurately determine the pre-determined location and size of the damage. The results show that robustness of the proposed damage detection algorithm under the limited measured data points is relatively good and the method can be applied for practical structural tests.

Table 4.2

Calculated false-positive damage ratios for the simulated test cases for aluminium plate

Confidence level	Noise level $\delta = 1 \times 10^{-2}$			Noise level $\delta = 5 \times 10^{-3}$			Noise level $\delta = 1 \times 10^{-3}$			Noise level $\delta = 5 \times 10^{-4}$		
Cut depth [mm]	90%	95%	99%	90%	95%	99%	90%	95%	99%	90%	95%	99%
0.5	-	-	-	-	-	-	1.42	0.12	0	0.66	0.04	0
1.0	-	-	-	7.83	1.79	0.08	1.33	0.21	0	0.25	0	0
1.5	-	-	-	7.08	1.67	0.04	0.96	0.08	0	0	0	0
2.0	8.29	1.58	0.04	6.50	1.25	0.04	0.62	0.04	0	0	0	0
2.5	7.91	2.17	0.21	5.66	0.87	0.04	0.12	0	0	0	0	0

(a)

(b)

(c)

94

(d)

(e)
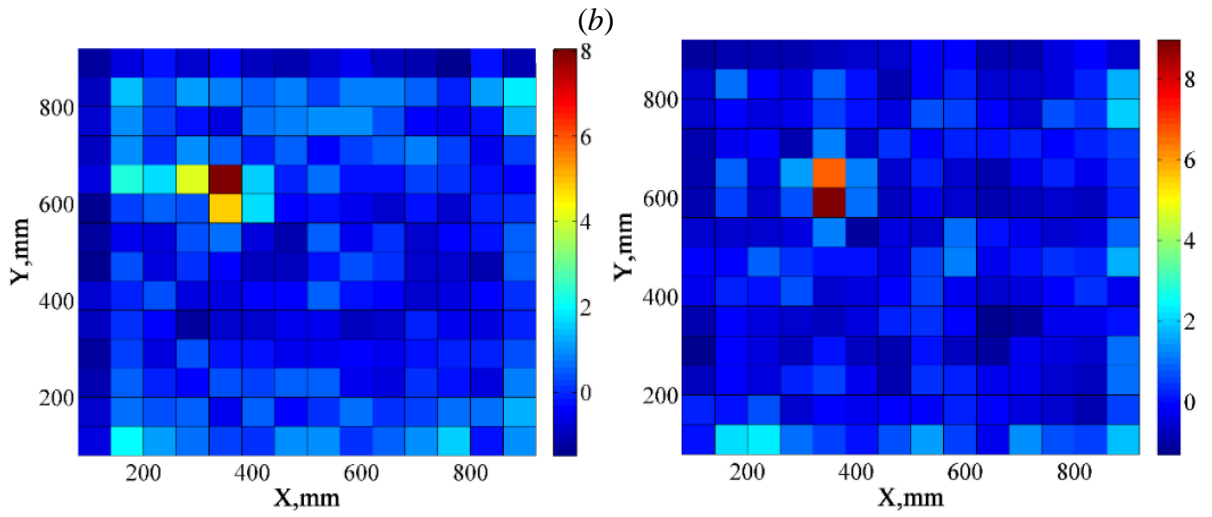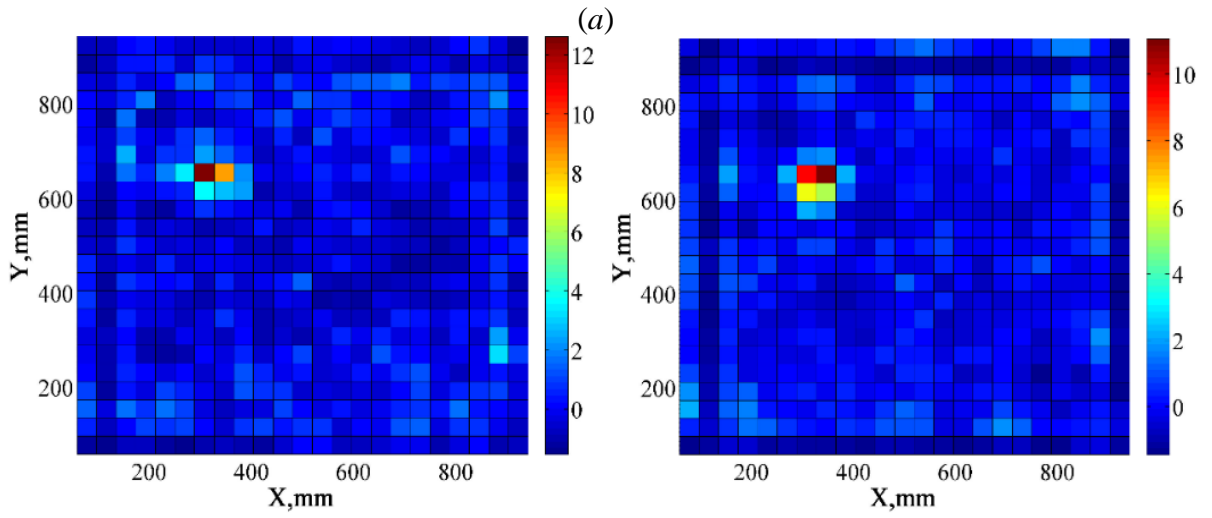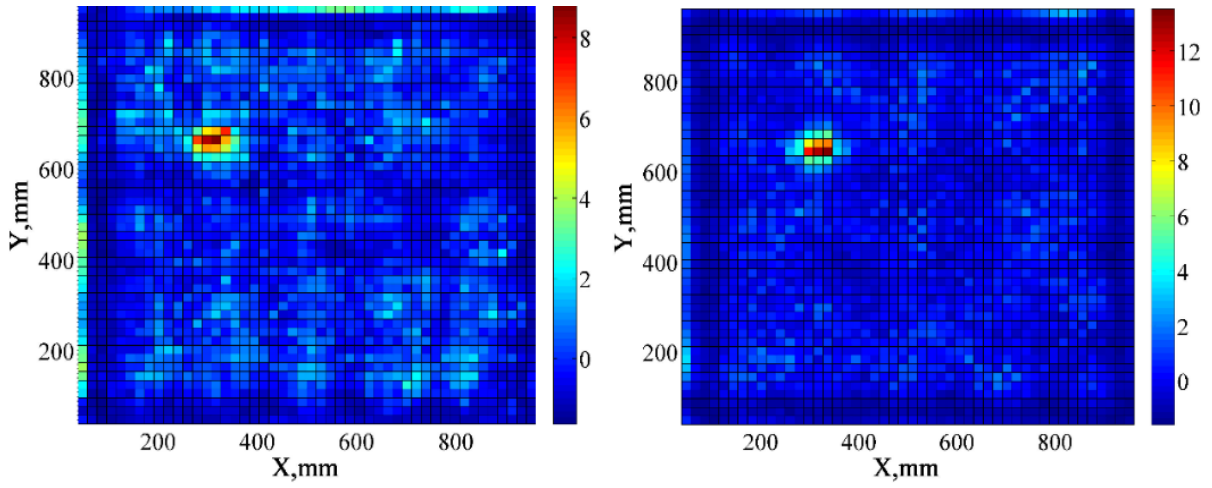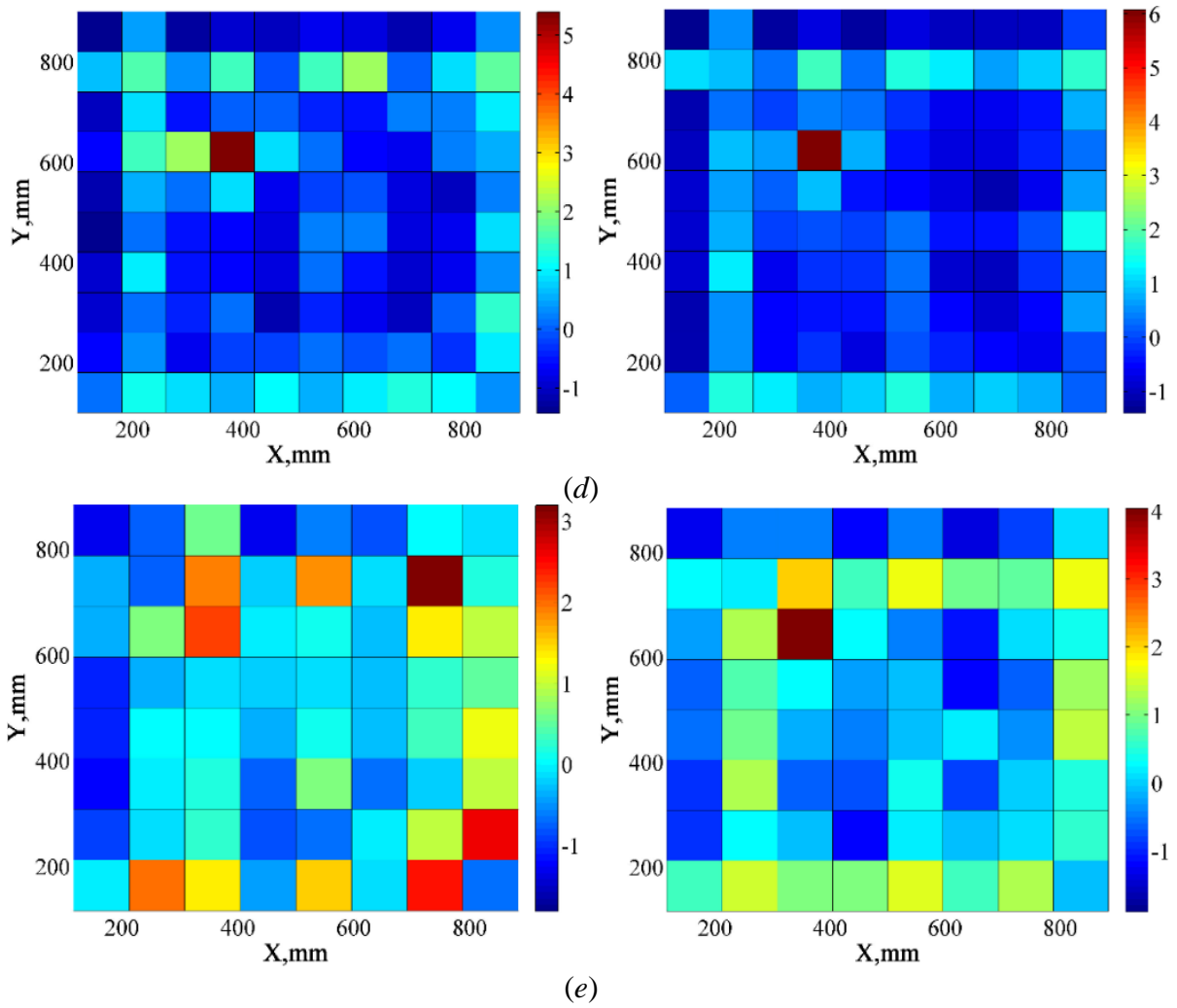
Fig. 4.7. Standardized damage indices for aluminium plate using various sizes of mode shape data: (*a*) 51×51; (*b*) 26×26; (*c*) 17×17; (*d*) 13×13; (*e*) 11×11. Left: experiment, right: FEM.

Standardized damage indices for the rectangular plate are given in Fig. 4.8. Five different data sets, namely, original matrix of 51×21 calculated mode shape data points and the following reduced matrices of 26×11, 17×7, 13×6 and 11×5 data points are considered for the damage detection. Fig. 4.8 (*d*) shows that the damage can reliably be detected by using just 13×6 measurement points. Similarly, as for the square plate, the ability of the method to accurately determine the pre-determined location and size of the damage gradually decreases as the sensor spacing increases. The results of this numerical experiment suggest that the proposed method can be successfully applied for damage detection in different aspect ratio plates under the limited measurement points.
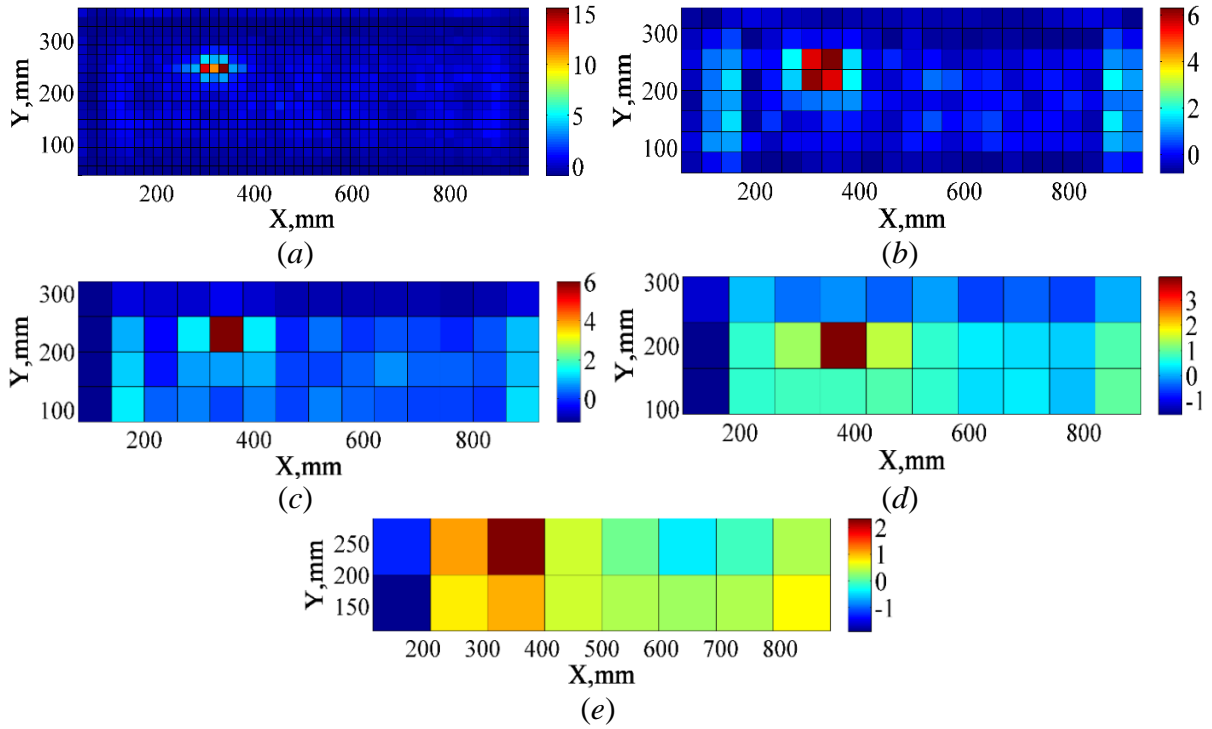
Fig. 4.8. Standardized damage indices for rectangular aluminium plate using (*a*) 51 × 21; (*b*) 26 × 11; (*c*) 17 × 7; (*d*) 13 × 6 and (*e*) 11 × 5 data points.

4.2. Case study 2: CFRP beam with an impact damage

4.2.1. Dynamic vibration test

Scanning grid set up for the composite beam clamped at both ends (analysed in subsection 3.2) is shown in Fig. 4.9. It contains 5 rows with 56 columns of points, thus the size of measured deflection shape signal is 5×56.
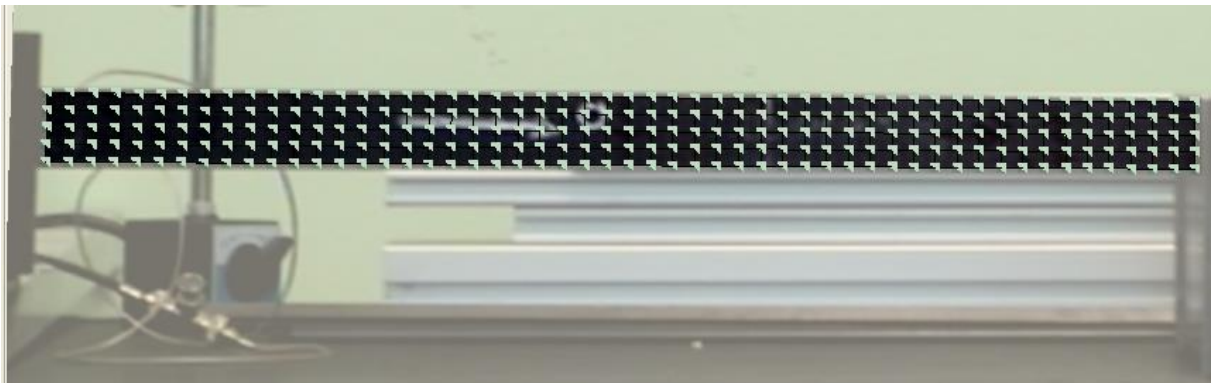
Fig. 4.9. Laser vibrometer scanning grid for CFRP beam.

Bending deflection shapes of the composite beam with mode shape curvatures in x and y dimensions along with corresponding polynomial fitting of these curvatures are depicted in Fig. 4.10, while the respective resonance frequencies are shown in Table 4.3.

Table 4.3

96

Resonance frequencies (Hz) for the CFRP beam

Shape No.	2	3	4	5	6	7	8	9	10	11
	136.5	263.0	408.5	654.0	890.5	1220.5	1398.5	1813.5	2162.0	2417.0

$\rho_{xy} = 0.9110$

$\rho_{xy} = 0.9456$
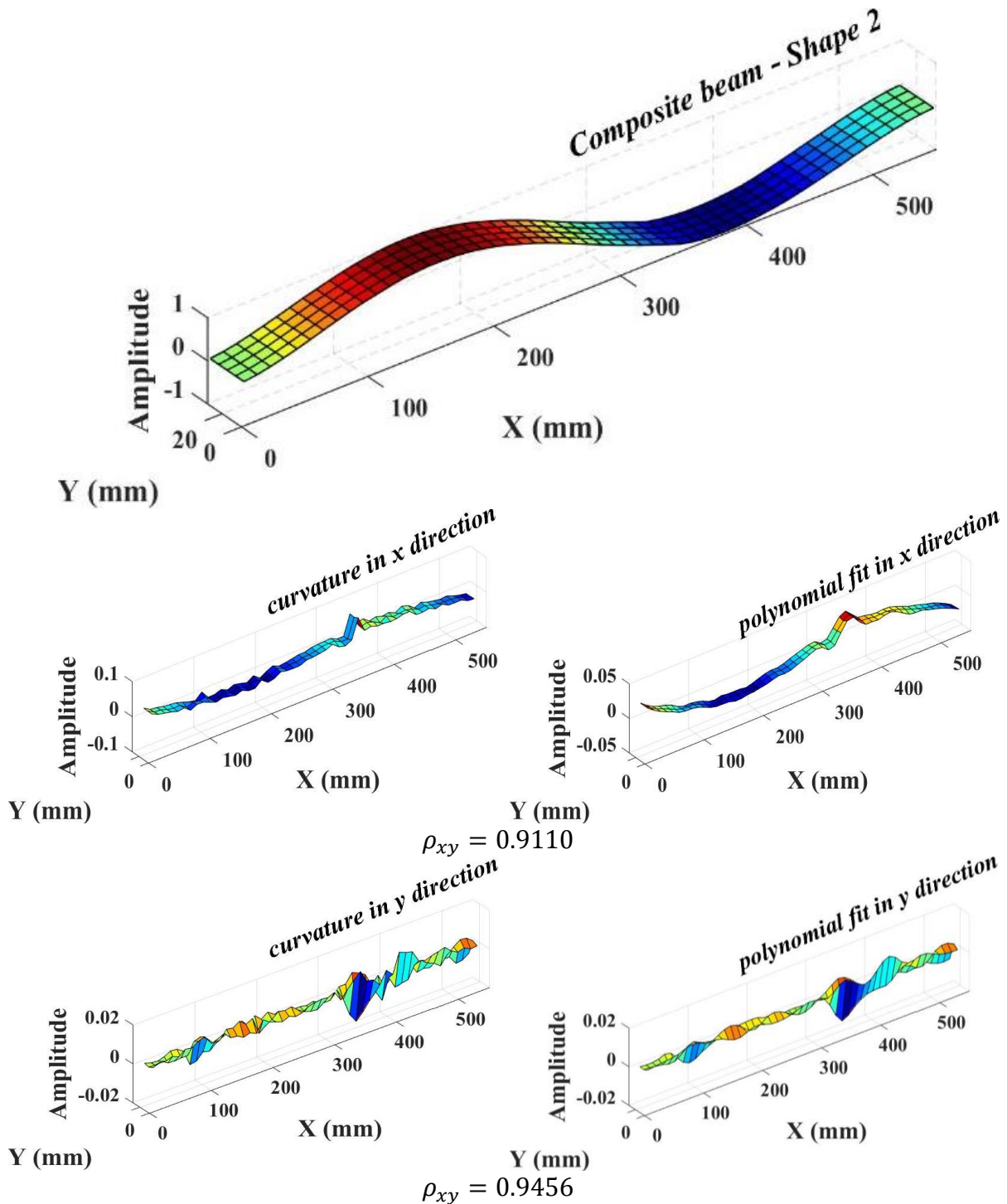
Fig. 4.10. Bending deflection shape 2 for CFRP beam at damaged state with mode shape curvatures in x and y directions and polynomial fitting of these curvatures with a correlation coefficient.

To evaluate the correspondence between calculated mode shape curvatures and polynomial least squares fitting of these curvatures, a correlation coefficient of a mode shape curvature-

polynomial fit pair in each direction is calculated for both beams. These pairs are highly correlated with correlation coefficient ranging from 91 % to 94 %, suggesting an appropriate representation of a smoothed surface to obtain data of a healthy structure.

4.2.2. Damage detection performance assessment

DER values for the composite beam are calculated according to the procedure described in subsection 2.1.1. The range for scale parameters is chosen to be from 1 till 16 as it is observed than the increase of this range does not significantly contribute to wavelet performance enhancement. In total, 16 wavelet functions, found in *Matlab*^{TM} *Wavelet Toolbox* under the section of 2D Continuous Wavelet Transform, are used. These wavelets include families such as Dog (Derivative of Gaussian), Morlet, Mexican hat and single wavelets Pet Hat, Wheel, Fan, Sinc. The results are shown in Table 4.4 for all wavelets.

Table 4.4

Maximum DER values and corresponding scales for all wavelets for CFRP beam. Best and worst performances are marked with green and red, respectively

Wavelet	max DER (%)	Scale
Dog	89.18	1
Dog 2	88.57	1
Es Mexican Hat	81.30	1
Es Morlet	82.17	2
Fan	88.45	3
Gab Mexican Hat	60.40	14
Gaus 2	86.06	1
Gaus 3	86.06	1
Iso Dog	74.94	11
Iso Morlet	86.66	6
Mexican Hat	90.07	1
Morlet	89.58	4
Pet Hat	88.81	7
R Morlet	88.91	4
Sinc	80.40	16
Wheel	88.67	1

Mexican Hat wavelet at scale 1 is selected for SDI calculations in further steps as the performance of this wavelet is the best (marked with green colour in Table 4.4).

The optimum size of span for the least-squares fitting for is determined based on goodness-of-fit metrics, namely, adjusted R^2 value where the number of degrees of freedom of the data is taken into account as opposed to ordinary R^2. Sizes of span, ranging from 1 % to 20 % are tested to obtain the best approximation. The results are shown in Fig. 4.11.
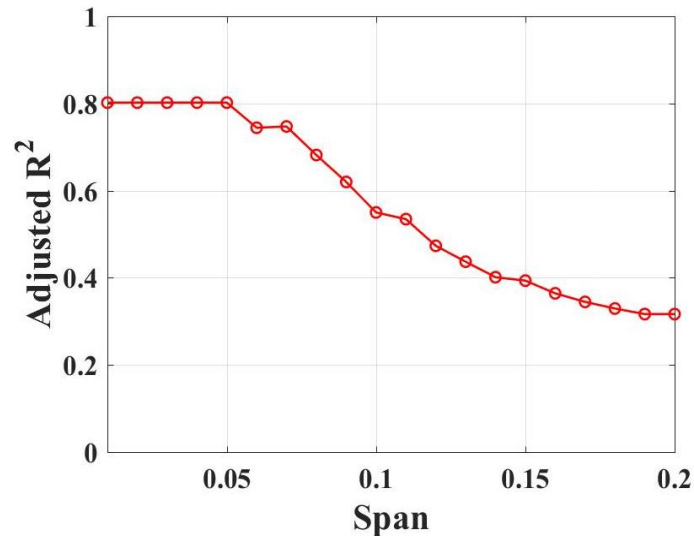
Fig. 4.11. Performance of least-squares fitting versus size of span for CFRP beam.

The values of adjusted R^2 are about 80 % and decrease with increasing size of span. Therefore, a value of 0.05 is chosen for the span size.

4.2.3. Damage localization

SDI distributions over the whole area of the composite beam are shown in Fig. 4.12. Only the SDI distributions corresponding to highest confidence of damage localization are shown.
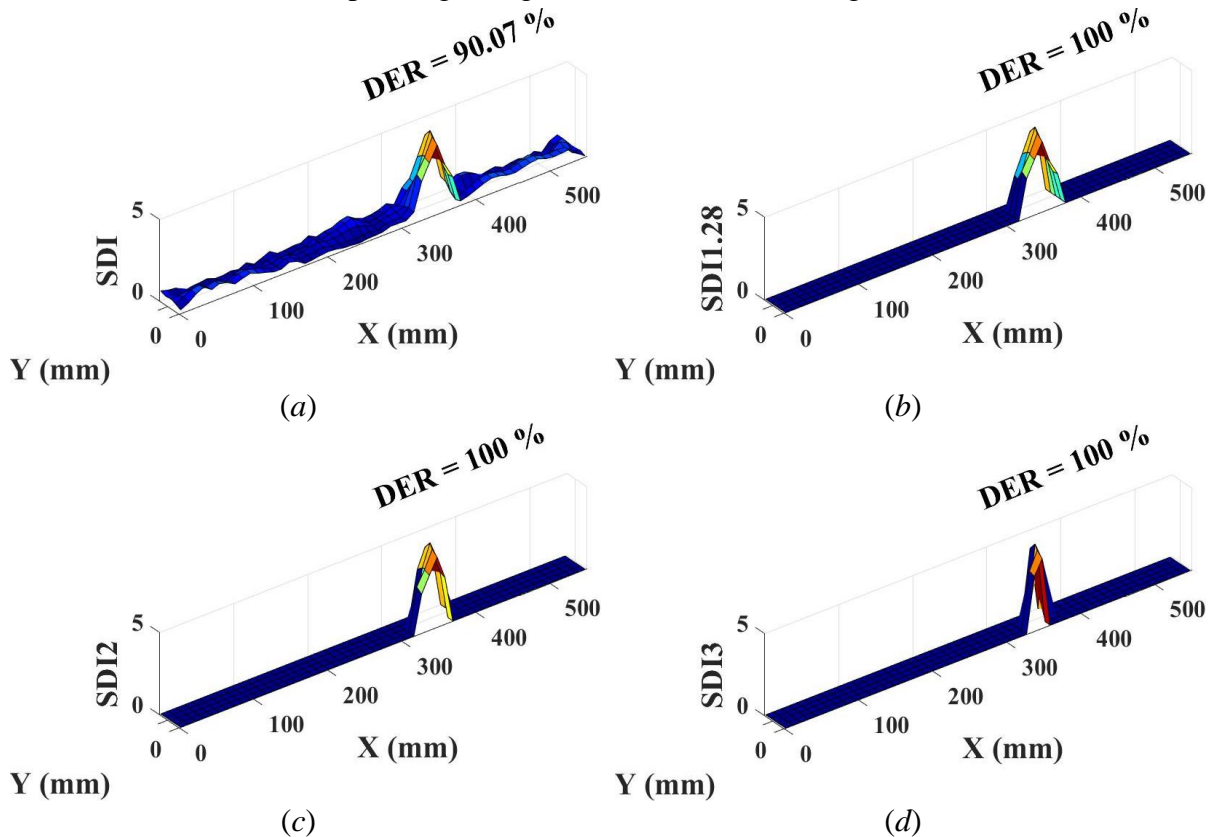
Fig. 4.12. Standardized damage index distributions (2D CWT): (*a*) no threshold; (*b*) threshold of 1.28 (confidence of 90 %); (*c*) threshold of 2 (confidence of 95 %); (*d*) threshold of 3 (confidence of 99 %).

The location of impact damage is clearly revealed through SDI in an actual zone of impact.

Distributions of Standardized Damage Index for the MSCS method are presented in Fig. 4.13. It can be seen that the location of an impact damage is found. By application of MSCS method, one can locate the damage with as much as 99 % confidence.
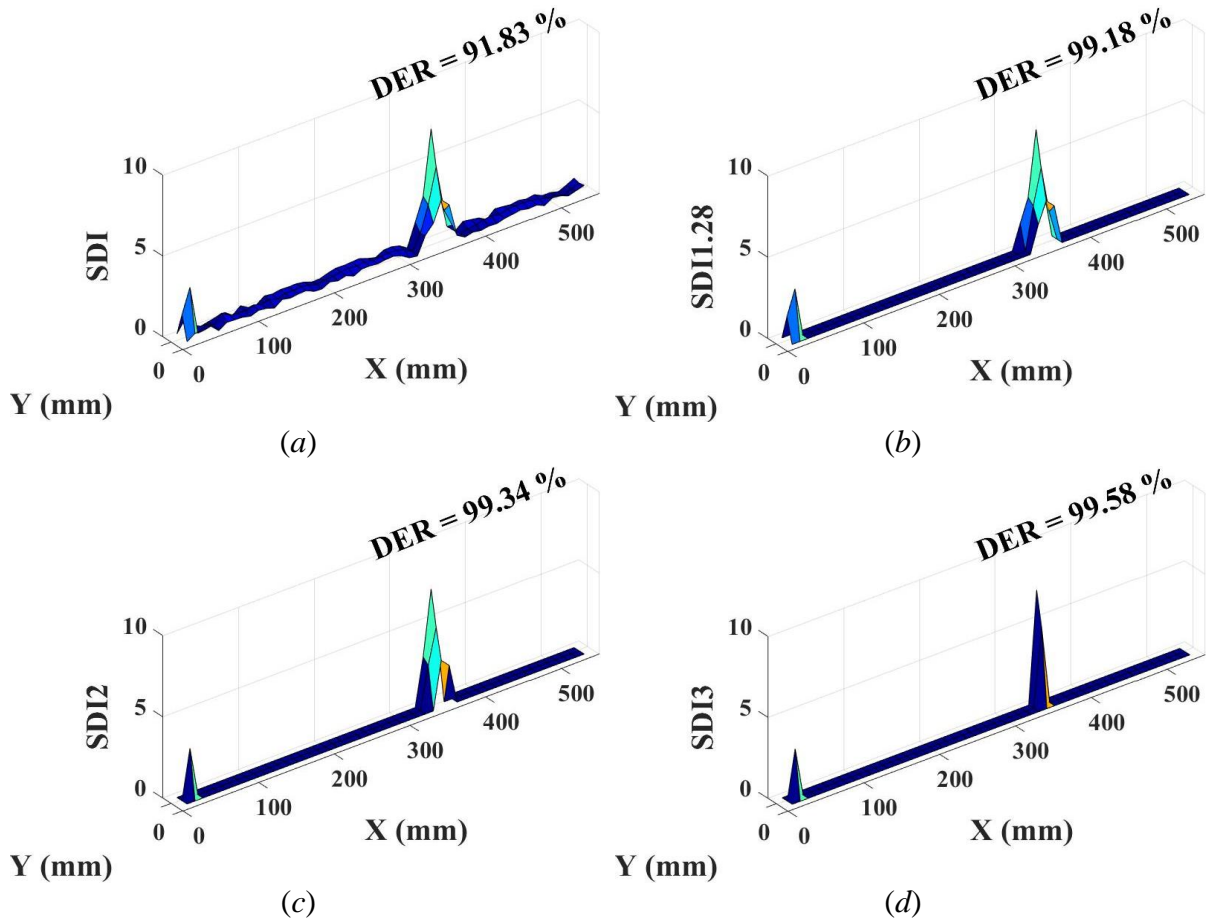
Fig. 4.13. Standardized damage index distributions (2D MSCS): (*a*) no threshold; (*b*) threshold of 1.28 (confidence of 90 %); (*c*) threshold of 2 (confidence of 95 %); (*d*) threshold of 3 (confidence of 99 %).

The respective DER values, including various levels of confidence for the presence of damage, are also shown in Fig. 4.13. Thus one can conclude that MSCS method is not only simpler, but also involves less tedious analysis than CWT method.

The obtained results show that the proposed damage index provides reliable information about the location and size of the damage in case of the presence of medium severe damage, relatively accurate measurement data and relatively dense distribution of sensors. Last two drawbacks of the method can be overcome by using the latest scanning laser vibrometer systems which allow high-density transverse displacement measurements with a low degree of measurement noise ($\delta = 0.1$ % ... 1 %). In this case, the major drawback of the method is that the severity of damage has to be relatively high for successful damage detection. The obtained results suggest that the proposed method can be applicable not only for laboratory tests, but also for practical structural applications.

PART II – CLASSIFICATION OF DAMAGE SENSITIVE FEATURES

5. CONDITION MONITORING WITH DEFECT LOCALIZATION IN A TWO-DIMENSIONAL STRUCTURE BASED ON SUPERVISED MULTICLASS CLASSIFICATION OF STRAIN FEATURES

Cantilevered carbon fibre reinforced polymer (CFRP) composite plate is selected as an example for the prosposed Condition Monitoring method as many structures of high importance, such as wind turbine blades, offshore platforms and aircraft wings, among others, are seen as plate-type structures [203]. The idea of the method is based on compilation of different damage scenarios in a sort of damage catalogue using finite element modelling. By simulating damage of varying severity and different coordinates, different damage cases from the compiled catalogue can be compared with real structural damage. Comparison of sensor measurement data of real damage and data values from catalogue would reveal the necessary damage information – severity and position. Rather than actually damaging the plate, authors propose to introduce a pseudo-defect. The pseudo-defect is added mass that serves the purpose to locally modify structural response of the object as in the case with real damage. Numerical simulations are carried out and the proposed methodology is validated with an experimental study.

5.1. Numerical model

5.1.1. Model of a composite plate

The finite element model of a cantilevered composite plate is created with commercial finite element package *Ansys*^TM version 16.2. The material model is a prepreg carbon fibre laminate consisting of 32 layers of lamina with layer thickness of $90\,\mu$m and stacking sequence is $(90/0)_{8s}$. The material properties are shown in Table 5.1.

Table 5.1

Material properties of the modelled cantilevered composite plate

E_x (GPa)	E_y (GPa)	E_z (GPa)	G_{xy} (GPa)	G_{yz} (GPa)	G_{xz} (GPa)	ν_{xy}	ν_{yz}	ν_{xz}	ρ (kg/m^3)
110	7	7	4.5	4.5	4.5	0.33	0.33	0.33	1560

The dimensions of the plate are $(366 \times 130 \times 2.88)$ mm and it is partitioned into 183×65 finite elements. The element types used to create the model are displayed in Table 5.2.

Table 5.2

Types of finite elements used in the creation of model of dynamically excited composite plate

Plate	SHELL181
	4 nodes with 6 DOFs in each node, namely UX, UY, UZ, ROTX, ROTY, ROTZ
Point mass	MASS21
	concentrates on a single node, without rotary inertia in this case with DOFs UX, UY, UZ
Actuator	SOLID226
	3D element with 20 nodes and brick geometry and 14 integration points. Used for piezoelectric analysis with DOFs UX, UY, UZ, VOLT

The mass element with a magnitude of mass equal to 0.02 kg (9.43 % of plate's mass) is put on every zone of the plate and a harmonic analysis is conducted to extract the resonant frequencies of the plate. In the first step of the analysis, the frequency response is obtained in the frequency range of 0 Hz to 800 Hz with a resolution of 5 Hz (Fig. 5.1). The second phase of the harmonic analysis involves narrowing of the frequency region of interest around each peak. The identified frequency values are marked in Fig. 5.1. Density of the actuator is taken as $\rho_{act} = 5440$ kg/m^3. Dimensions of the actuator – (32×8) mm. For excitation purposes, a voltage of 10 volts is passed to the plate. As proved in [198], only two strain sensors with optimal position are enough for an effective strain feature classification. Strain gauge #1 is the farthest from MFC, perpendicular to fibre orientation, while strain gauge #2, in the direction of fibres, is the closest of the two to the MFC element. The model of the plate is shown in Fig. 5.2.
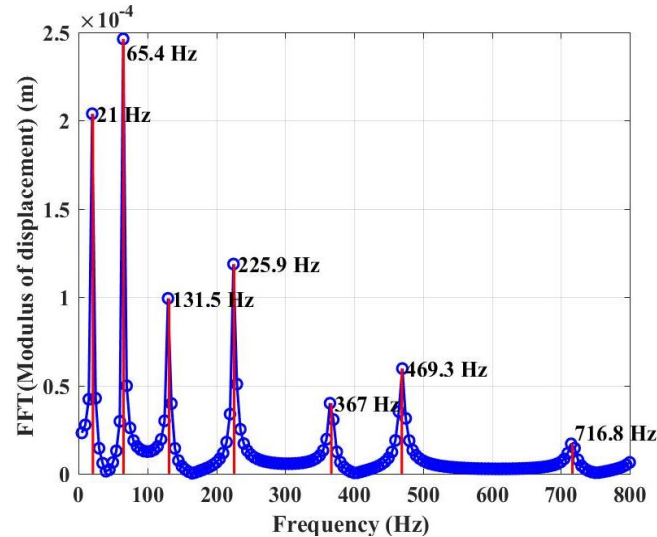
Fig. 5.1. Harmonic analysis– magnitude of displacement normal to the plate's surface (healthy plate).
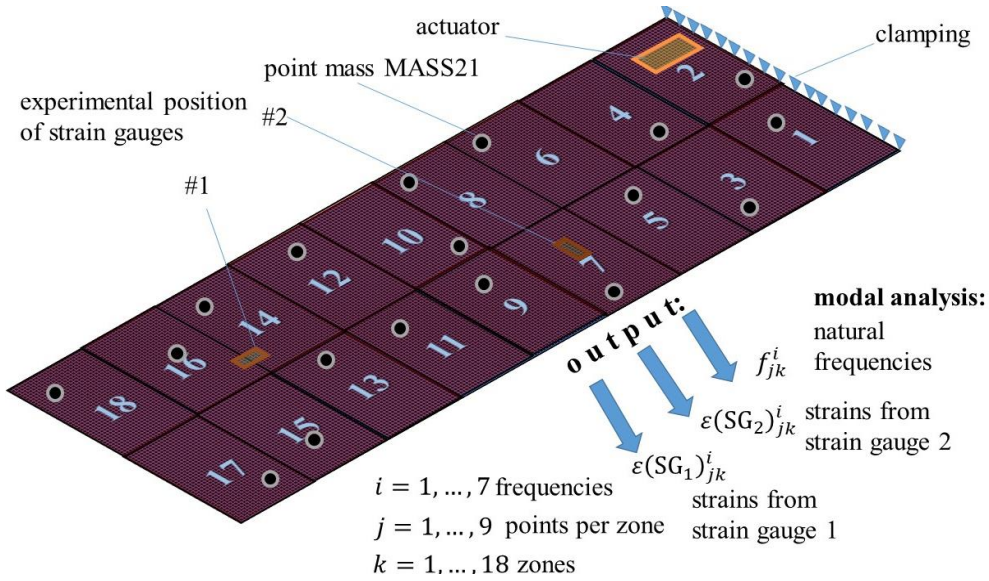
Fig. 5.2. Numerical model of the plate with partition zones, point mass and recording of output features.

5.1.2. Linear versus non-linear classification performance

The strain data set is partitioned into 9 folds because a total of 18 zones are used as class labels and different scenarios by setting 2, 3, 4, 5, 6, 7, 8 and 9 points per class are considered. This gives rise to data sets of size 2×18, 3×18, 4×18, 5×18, 6×18, 7×18, 8×18 and 9×18. Hence, 9 is a common denominator for each of these data sets. At each trial, 9-fold cross-validation loss is calculated (denoted by L_i in Fig. 5.3) and an average values along with a standard deviation of these values are computed.

Cross-validation errors are computed by considering varying numbers of data points per class (zone) for all 7 extracted resonant frequencies. These results for both algorithms are shown in Fig. 5.4. The overall lowest errors are associated with the first frequency of 21 Hz for both linear discriminant and k-NN. Also, cross-validation loss tends to increase with increasing numbers per zone, especially at lower frequencies. As for higher frequencies, the classification error remains more stable with respect to varying size of data. However, only the first resonant frequency is used in further calculations due to lower error values.
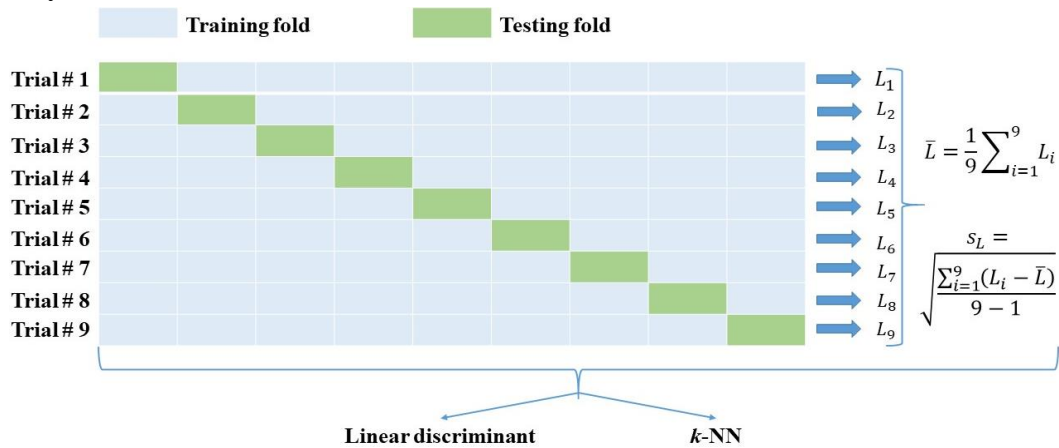
Fig. 5.3. 9-fold cross-validation scheme and calculation of classification losses.
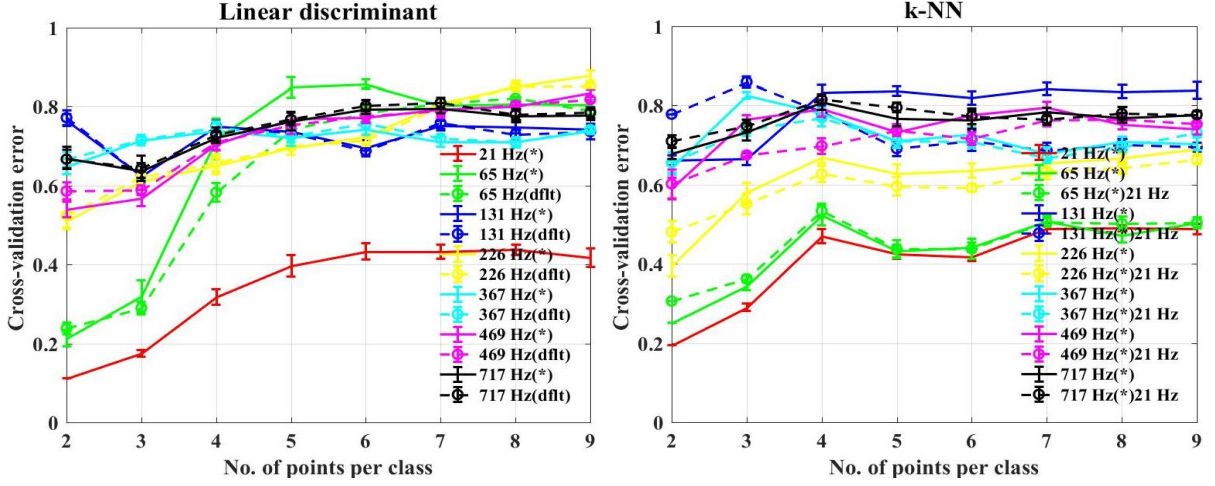
Fig. 5.4. Cross-validation errors for extracted frequencies versus number of points per class.

The default hyperparameter settings in *Matlab*[TM] for the *k*-NN algorithm is the number of neighbours $k = 1$, *Euclidean distance* between vectors x_s and y_t

$$d_{st}^{Eucl} = \sqrt{(x_s - y_t)(x_s - y_t)^T}$$ (5.1)

and equal distance weighting implying that no weighting is applied to the data points and all nearest neighbours that fall within a circle around some query point to be classified are treated equally. In this study, however, an optimized set of hyperparameters are used. By conducting a hyperparameter optimization routine, it is found that the optimum set of hyperparameters for the 1st frequency (21 Hz) is $k = 3$, distance equal to *Mahalanobis distance*

$$d_{st}^{Mah} = \sqrt{(x_s - y_t)\mathbf{\Sigma}^{-1}(x_s - y_t)^T}$$ (5.2)

where $\mathbf{\Sigma}$ – covariance matrix.

Inverse distance weighting (inversely proportional to the distance measure) is used. It is a common practice to set the number of nearest neighbours as an odd number to prevent ties in voting for class membership of the particular query point [182]. Standardization may be desirable to scale the data so that it is possible to compare this scaled data obtained from different sources, for example, sensors. The standardization of data vector x_i is achieved by subtracting it's mean and dividing by standard deviation according to [155]

$$Z_i = \frac{x_i - \bar{x}_i}{s_x}$$ (5.3)

No standardization for the data in this case was used. Default settings for linear discriminant are no regularization applied $- \gamma = 0, \delta = 0$.

Hyperparameter optimization results (dashed lines) are also displayed (marked with an asterisk * in Fig. 5.3, while the default or un-optimized linear discriminant classifier is denoted with "dflt" and the same optimization parameters as for 21 Hz used for higher resonant frequencies marked with (*)21 Hz for *k*-NN algorithm). The optimization of hyperparameters (γ and δ for linear discriminant and number of nearest neighbours, distance and distance weight for *k*-NN) have minor effect on cross-validation loss, although, by definition, the optimization of classifier hyperparameters seeks to minimize the cross-validation loss (objective function).

After the classifier models are trained, the next step is to construct the confusion matrices to check for misclassified class labels [204]. These results for 2 and 9 points per class for linear discriminant algorithm are displayed in Fig. 5.5. *k*-NN algorithm proves to be superior – a perfect classification is achieved with a classification accuracy of 100 % for all data set sizes. That is why only cases with 9 points per class are shown. The maximum *SR* achieved with linear discriminant method is as high as 94.4 % for the 1st resonant frequency and 2 points per class. The slight misclassification is associated with the first and last zones of the plate (2 points per class), while a lot more zones are misclassified for 9 points per class. Hence, only few data points are enough for data classification in this case.
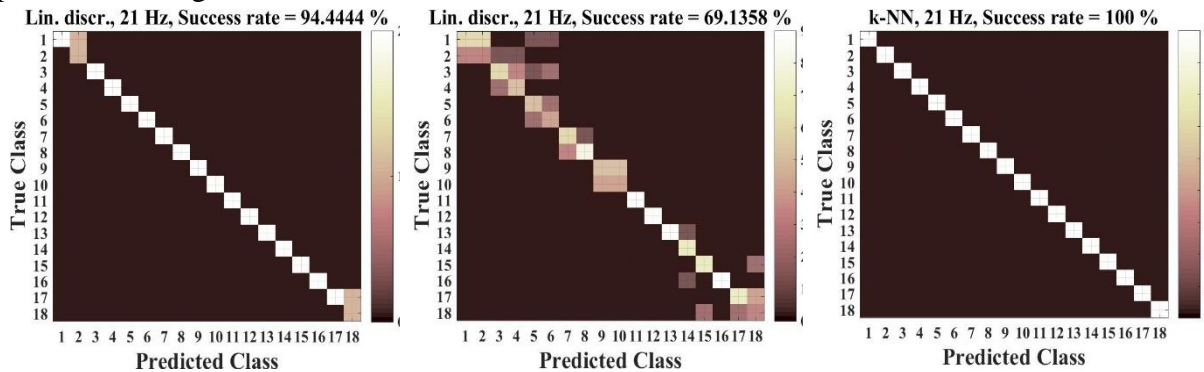
Fig. 5.5. Confusion matrices of classification for the numerical study.

5.1.3. Localization of query points

A total of five query points are simulated in random locations of the plate. Their coordinates are depicted in Table 5.3, whereas a visual representation is shown in Fig. 5.6. Query point #1 is in zone 18, query point #2 in the intersection of 4 zones – 9, 10, 11 and 12, query point #3 in zone 5, query point #4 in zone 1 and query point #5 in zone 8.
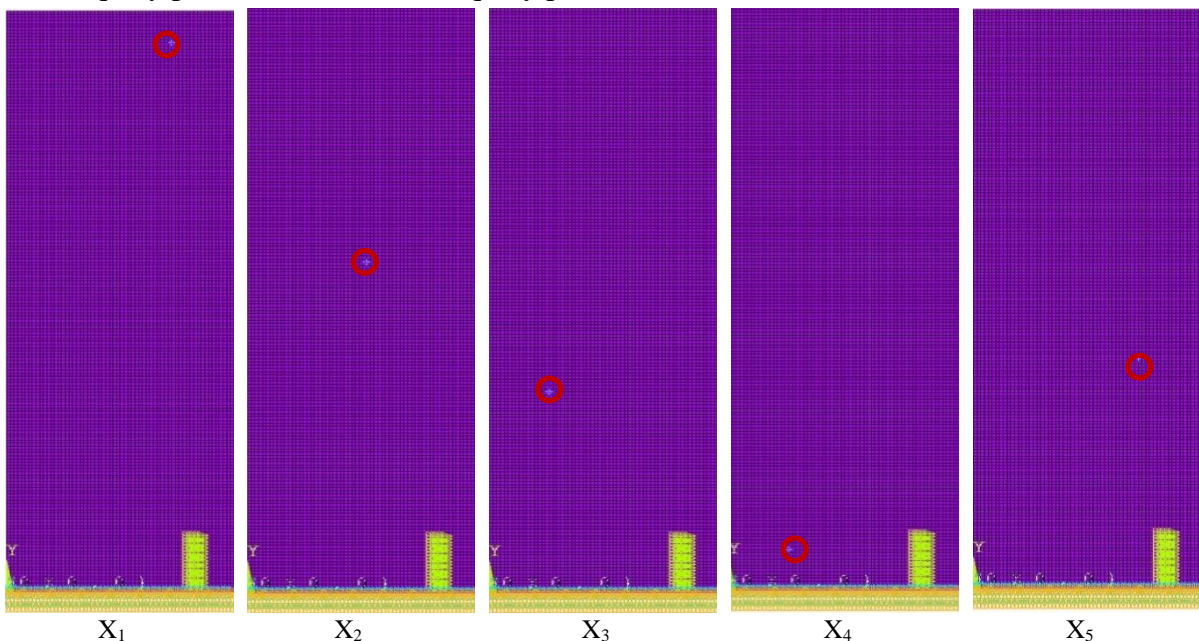
Fig. 5.6. Locations of five simulated query points.

Table 5.3

Coordinates of the simulated query points and their locations in terms of plate zones

Query point	X_1	X_2	X_3	X_4	X_5
x (m)	0.09	0.064	0.032	0.032	0.088
y (m)	0.346	0.206	0.126	0.026	0.146
Zone	18	between 9, 10, 11 and 12	5	1	8

Distributions of prediction probabilities of the unknown query points for both classifiers are depicted in Fig. 5.7. Only the results for 2 and 9 data points per class are shown.
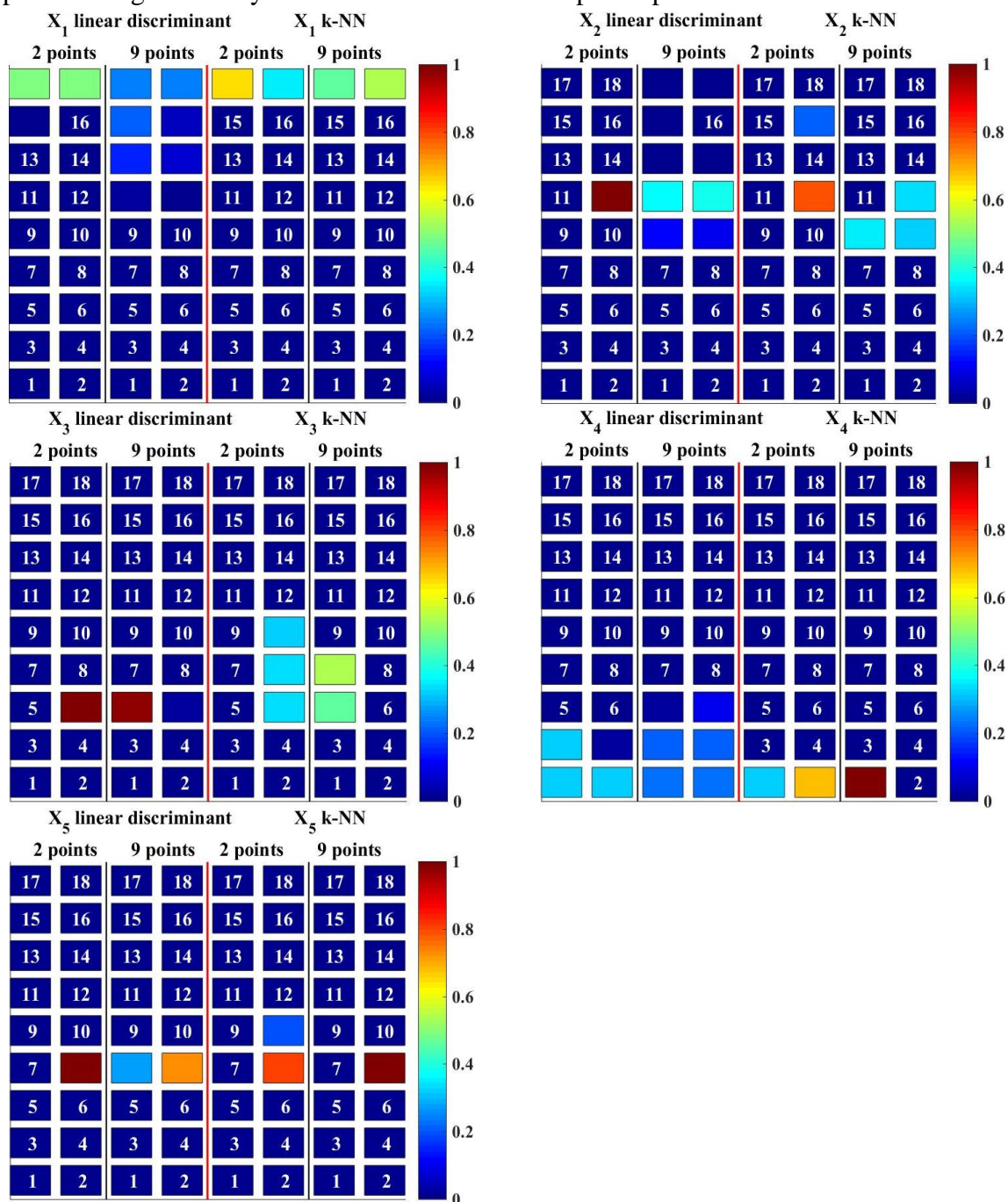
Fig. 5.7. Distributions of prediction probability of 5 query points.

Notable differences for most prediction cases are observed. The first query point X_1 lies in zone 18 (refer to Table 5.3) and is predicted to lie either in zone 17 or 18 with both classifiers and just 2 points per class. More points per class give inaccurate prediction, except for k-NN. The correct prediction for query point X_2 would be any of zones 9, 10, 11 or 12 as this point lies in the intersection of these zones and there is an equal probability for it to be attributed to any of these zones. Both classifiers assigned a class 12 to this point which is correct (2 points per zone). In this case, even for 9 points per class the prediction is correct for both algorithms. The query point X_3 lies in zone 5, but is classified to belong to zone 6 (linear discriminant) which is not correct, but close, considering that the strain values do not vary much in neighboring zones. k-NN algorithm classifies this point to belong either to zone 6, 8 or 9, which is larger misclassification as compared to linear discriminant. The only conclusive predictions for query point X_4 are obtained with k-NN with 9 points per class – this point is correctly classified to lie in zone 1. Linear discriminant also gives a correct classification, but again the probabilities are much more spread out over other zones with only slightly larger values in the correct zone. This effect is less pronounced for 2 points per class, though. The fifth query point X_5 is correctly classified by both algorithms to belong to zone 8. This time, both 2 points and 9 points per class yield the correct prediction.

5.2. Experimental procedure

5.2.1. Experimental damage localization scheme

A non-destructive approach is applied to localize the local changes of mass on the composite plate. The plate is by no means damaged – a pseudo-defect is introduced using a small weight of 20 g, comprising 9.43 % of plate's mass. The essential steps of damage localization are depicted in Fig. 5.8 and are as follows:
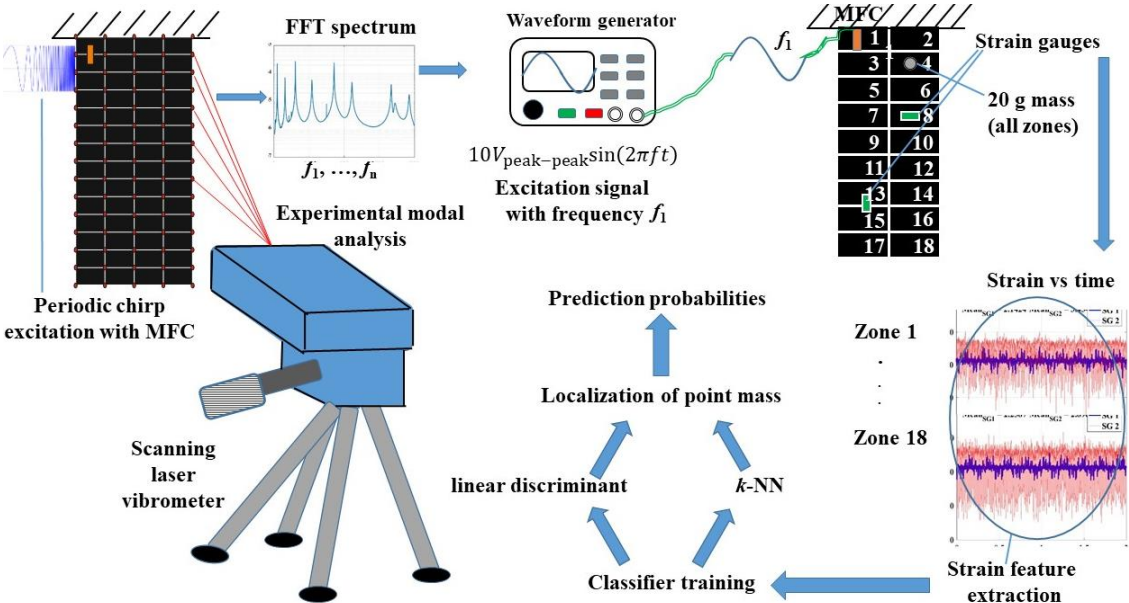
Fig. 5.8. Damage localization scheme based on strain feature classification.

1. The plate is clamped at one end yielding a cantilever configuration. A piezoelectric actuator from MFC (macro-fibre composites) is mounted close to the clamping. This system is placed on a rigid floor.
2. The MFC element is used to excite the structural vibration in the plate and an experimental modal analysis is carried out with an aid of scanning laser vibrometer. Vibration velocity is measured and FFT of the velocity is calculated to obtain the vibration spectrum. The first resonant frequency (peak picking method) and mode shape of the plate is extracted using *Polytec*^{TM} software.
3. The plate is instrumented with 2 strain gauges – one in the longitudinal direction with respect to the fibre orientation and one in transversal. The strain gauges are mounted in the same locations as strains read from a numerical model. Wave generator, signal amplifier and dynamic strain measurement system *Spider 8* are connected to the strain gauges and the MFC element.
4. The plate is partitioned into 18 zones and a small weight of 20 g is consequently placed in each of these zones. During this act, the plate is harmonically excited through the MFC element with amplitude of 10 volts peak-to-peak and a driving frequency equal to that identified from modal analysis (step 2). Time series of mechanical strain from both strain gauges is recorded. A total of 3 such measurements are made by placing the mass at each of 18 zones and a mean signal over an ensemble of these 3 measurements is computed.
5. The strain data is collected and divided into 2 equal parts as referring to numerical study, the best classification results are obtained by considering just 2 points per class.
6. A feature sensitive to the position of the added mass is extracted from this data by first considering the driving frequency of actuation. As this is the forced vibration problem, the response of the structure is expected to contain a strong component of the same frequency as the actuating signal. Therefore, the period of oscillation of the strain response T_r and the sampling period T_s are calculated

$$T_r = f_r^{-1} \tag{5.4}$$
$$T_s = f_s^{-1} \tag{5.5}$$

where f_r – dominating frequency of strain response, Hz;
$\quad\quad f_s$ – sampling frequency, Hz.

7. Each of both strain time series parts is divided into portions in which a maximum of absolute values is calculated. The size of each portion depends on the ratio of response and sampling periods.

$$B = \text{length}\left(\frac{y(t)}{b}\right) = \frac{T_r}{T_s} \tag{5.6}$$

where b – number of strain portions in the time series (refer to Fig. 5.9 where green dotted vertical lines show the division).
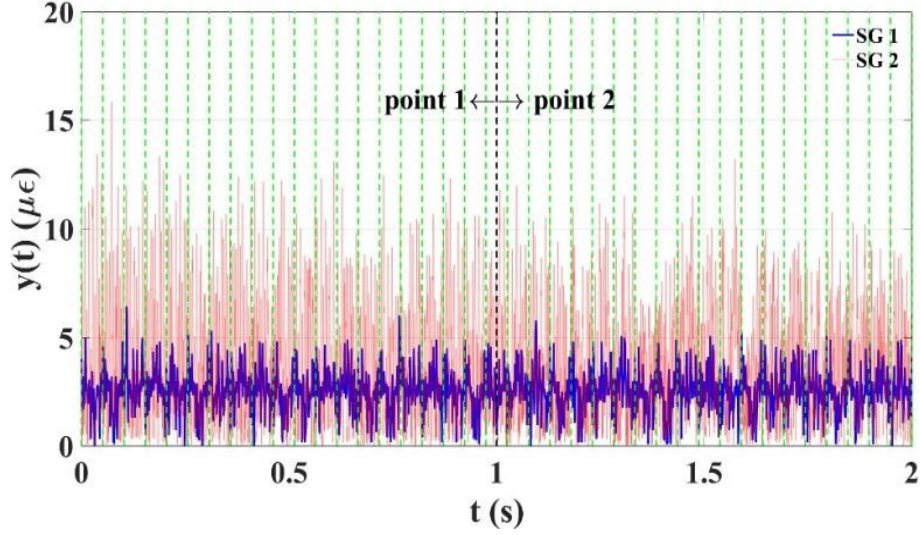
Fig. 5.9. Division of the strain signal into b portions.

The following command is initiated to compute the maximum of absolute value in each of the b portions:

$$\begin{cases} \text{for } b = 1: B: \dfrac{\text{length}(y(t))}{2} - B + 1 \\ \qquad \{\varepsilon\}_{1 \times b} = \max_{t=1:T_S} |y(t)| \\ \text{end} \end{cases} \tag{5.7}$$

8. The mean value of strains over all portions b is calculated.
9. Steps 6 through 8 are repeated for both strain gauges and all 18 zones of the plate. These calculated values of strain are assembled into matrix $(\varepsilon)_{2i \times j}$ where the number of rows $i = 1: 18$ represents the zones of the plate and multiplier of 2 is used to denote 2 points per class; the number of columns $j = 1: 2$ represents 2 strain gauges.
10. Linear discriminant and k-NN classifiers with a set of optimized hyperparameters obtained in numerical study are employed to classify the location of mass based on the extracted strain features.
11. The model is validated using 5 points of mass application in the process of classifier training. The points are picked such to belong not only to one particular zone, but also to lie on the boundary between two or more zones.

5.2.2. Composite plate with sensors

The proposed method is experimentally validated on a carbon prepreg cantilevered composite plate (Fig. 5.10 (a)). Positions of sensors and actuator correspond to the ones in the numerical model as is shown schematically in Fig. 5.10 (b). Thin copper tracks are glued on the surface of the plate in order to ensure the proper electrical conductivity.
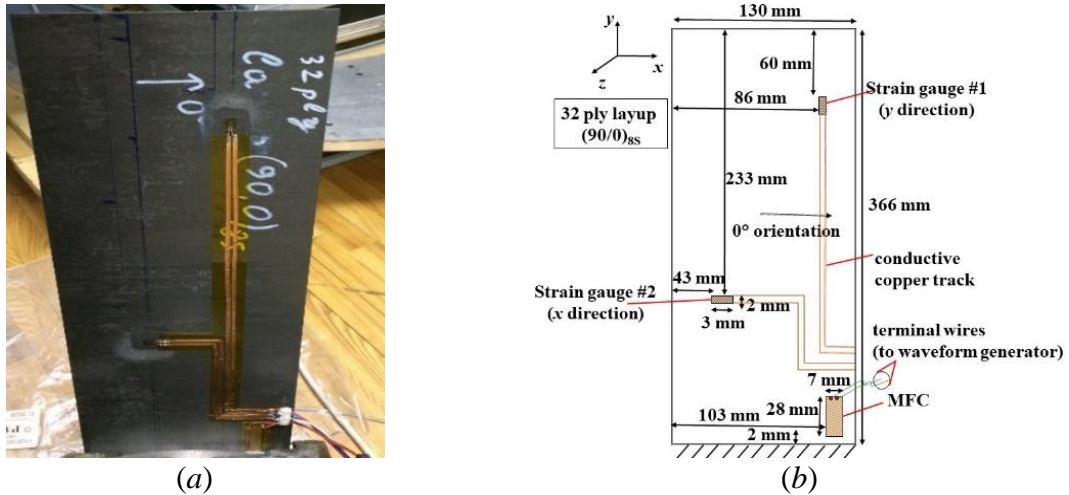
Fig. 5.10. Cantilevered composite plate: (*a*) photo; (*b*) positions of sensors with active dimensions.

The dynamic strain measurement system shown in Fig. 5.11 (*a*) consists of a waveform generator (Agilent 3322A 20 MHz Function/Arbitrary Waveform Generator) which is connected to the MFC actuator for harmonic excitation of the plate, signal amplifier (LE 150/025 Piezomechanik GmbH signal amplifier (230 V AC, serial number: 10902/936), strain measurement acquisition box (Spider 8 600 Hz/ DC HBM with USB adapter USBHBM2903) which is connected to both strain gauges using two channels and the waveform generator. *Spider 8* system is connected to personal computer through a USB port. The recorded strain signals are visualized in *Catman* software. In the software, the required measurement channels are activated and sensor parameters are set in accordance with Table 5.4. The sensors are initially zero-balanced to start measurements from zero strain. The time series of strain from both strain gauges are measured simultaneously with a duration of 2 seconds and sampling frequency of 2400 Hz giving 4800 samples plus 1 sample at time $t = 0$ s. A total of 3 measurements are recorded for each zone of the plate. The positions 5 selected query points for validation of classification model are shown in Fig. 5.11 (*b*). The event of application of actual mass on one of the zones is shown in Fig. 5.11 (*c*).
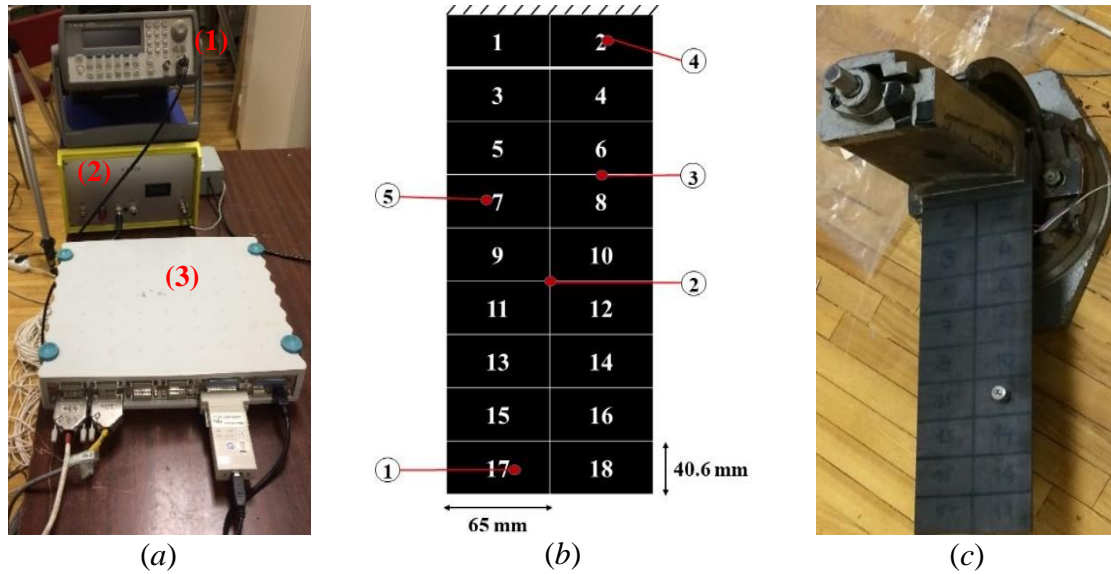
Fig. 5.11. Preparation for dynamic strain measurement: (*a*) strain measurement equipment with (1) waveform generator, (2) signal amplifier, (3) strain acquisition system *Spider 8*; (*b*) partition of the plate into zones and application of 5 query point masses; (*c*) photo showing application of mass on the cantilevered composite plate.

Table 5.4

Strain measurement parameters

Sampling rate	Sensor	Sensor amplifier	Transducer type	Measuring range	Gage factor	Filter	Filter frequency	Bridge factor
2400 Hz (0.42 ms)	SG 3 wire, 350 Ω	SR30 600 Hz (base)	Quarter bridge	3mV/V (4000 με)	1.99	Bessel lowpass	300 Hz	1

5.2.3. Experimental modal analysis

The procedure is carried out by employing a *Polytec*™ PSV-400-B scanning laser vibrometer system described in subsubsection 3.1.2. The size of the scanning grid is taken as 5×15 points. The plate is excited with a piezoelectric MFC (macro-fiber composite) element (model M2807-P1 smart material) glued on the surface of the plate. The excitation signal is 7 V amplitude periodic chirp with a bandwidth of 5-800 Hz, resolution of 0.25 Hz and sampling frequency of 2048 Hz. The number of FFT lines for this experiment is set to 3200.

The measured spectrum of vibration velocity averaged over all scanning grid of the plate is shown in Fig. 5.12. In the bandwidth of 800 Hz a total of 8 peaks are identified. Peak picking method is applied to extract the first resonant frequency from the spectrum (marked with red colour). The extracted mode shape along with respective resonant frequency value is shown in Fig. 5.12. Mode shape is shown with an amplitude normalized to the maximum value.
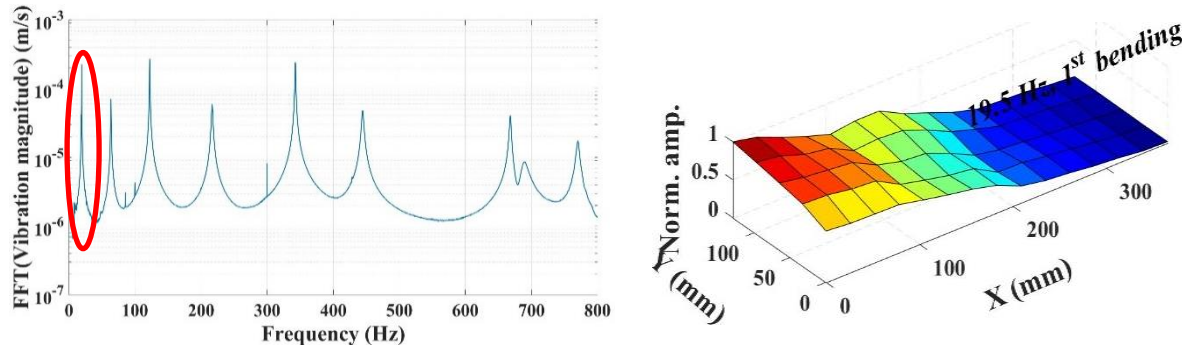
Fig. 5.12. Results of experimental modal analysis including response spectrum and identified deflection shape.

5.2.4. Strain features

The recorded time series of strain response averaged over an ensemble of 3 realizations for the 1st, 6th, 12th and 18th zone along with the maximum values of strain magnitude for both sensors is shown in Fig. 5.13. Significant increase of strain values is registered in the middle of the plate (zones 6 and 12) for both sensors. The difference between strain readings in these zones is also smaller than at the edges of the plate (zones 1 and 18). The final stage of the experiment involves the formation of classification matrix (refer to step 9 in subsection 2.3).
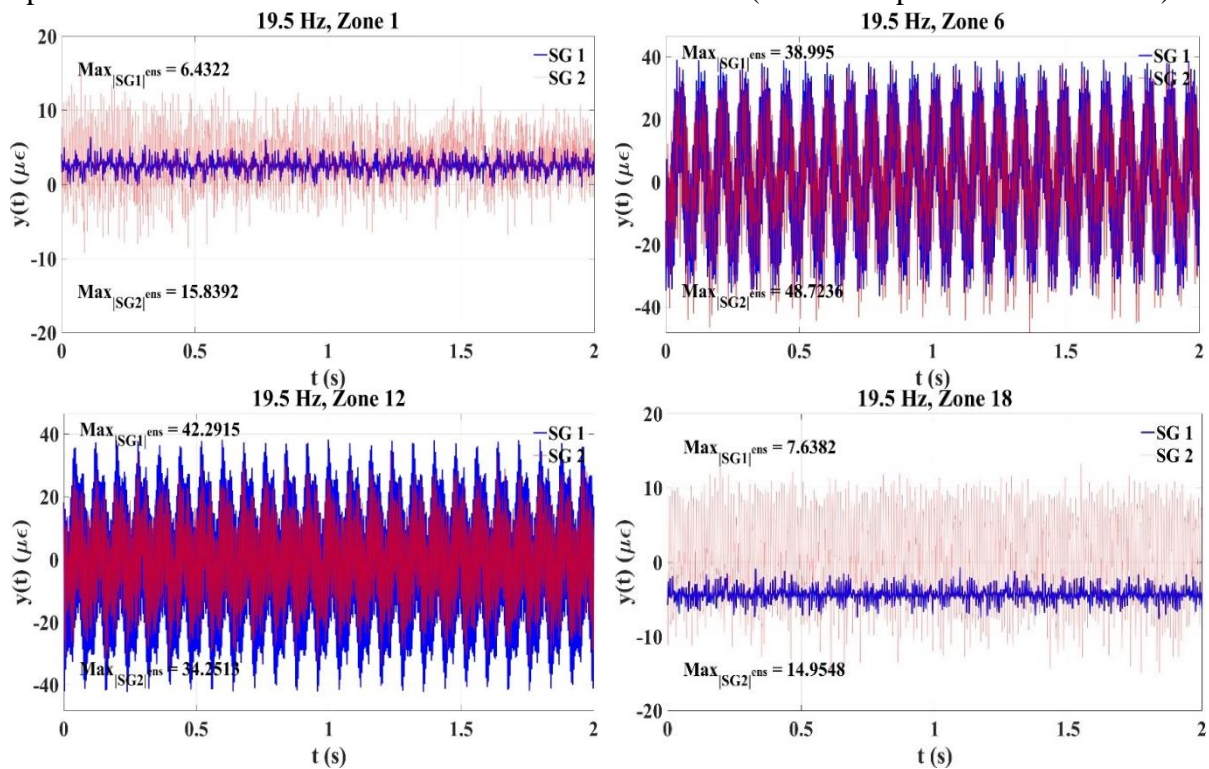
Fig. 5.13. Dynamic strain signals for an excitation sine wave with an amplitude of 10 V peak-to-peak for zones 1, 6, 12 and 18.

5.2.5. Localization of a pseudo-defect

The steps described in subsection 2.3 are followed to localize the 5 cases of added mass (Fig. 5.11 (*b*)). The 9-fold cross-validation scheme introduced in validating the numerical

113

simulations is adopted in this experimental study. The cross-validation error for both classifiers along with a standard deviation is shown in Table 5.5. This error is larger for k-NN algorithm.

The distributions of prediction probability across the zones of the plate calculated for 5 points of added mass are depicted in Fig. 5.14. Point X_1 is consistently classified to lie in zone 17. In general, the performance of linear discriminant is better than the one of k-NN as higher probabilities of prediction are associated with the correct zone. The point X_2 lies in the intersection of zones 9, 10, 11 and 12 and thus has an equal probability to belong to each of these zones. No convincing results are obtained by localizing this point. Point X_3 lies in the intersection between zones 6 and 8. The correct classification with linear discriminant is obtained showing zone 6. k-NN classifier also performs satisfactory. Points X_4 is slightly misclassified and X_5, on the other hand, is classified correctly to belong to zone 7.

From the above results, such as cross-validation losses, confusion matrices and prediction probabilities, it can be deduced that, contrary to the most cases, the classification performance to localize the added mass is better considering less points per class (2 versus 9). This fact is surprising, since the initial sample sizes are scarce (maximum of 9 points per class).

The results are probably related to initial positioning of strain sensors, their orientation (in angle with respect to fibre orientation of the composite structure) and, possibly, the number of such sensors. This as a matter of optimization of strain sensor placement which is a part of future studies regarding damage localization utilizing classifier algorithms.

Both linear and non-linear classifiers show stable performance involving simple classification cases when the unknown point lies in just one zone. This result is demonstrated by numerical simulations and validated experimentally. The situation with point lying in the intersection of 4 zones is passed to both classifiers and the numerical results are satisfactory – both classifiers demonstrate the largest fraction of prediction probability for at least one of these zones. The performance of a simple linear classifier, such as the linear discriminant is superior to the non-linear classifier, such as k-NN despite its inherent simplicity. Larger prediction probabilities are concentrated in the correct zones with a small scatter of remaining probability over other zones. The k-NN performs satisfactory with a bulk of the probability in the correct zone, although larger prediction probabilities are associated with misclassifications. Although both classifiers could not reliably manage the more difficult cases with points belonging to several zones simultaneously in the experimental validation phase, the linear discriminant still yields higher prediction probabilities associated with the correct predictions for the simpler cases (points lying in one zone only).

The numerical results of defect localization demonstrate the promising potential of the methodology – simulated query points lying in either just one or in the intersection of several zones are localized by both classifiers with the best results in terms of prediction probability acquired using the smallest data size of just 2 points per class (zone) and the fundamental resonant frequency. The experimental validation demonstrates that both classifiers are capable of capturing the zone of damage in the easiest cases when the mass lies in only one zone. By using this approach, no baseline data is necessary for successful localization of defect. Also, the defect does not necessary have to be near sensor to be localized as is the case with other methods. However, the limitation, as shown by results, is when mass is lying in the intersection

between several zones. Also, close lying pseudo-defects are likely to not be successfully distinguished as they will possess similar strain response.

The proposed methodology for defect localization in flat structural members is applicable for field tests and can be further enhanced with an optimization study regarding the optimum number of sensors and their placement.

Cross-validation error for both classifiers

Linear discriminant	0.250 ± 0.031
k-NN	0.349 ± 0.020
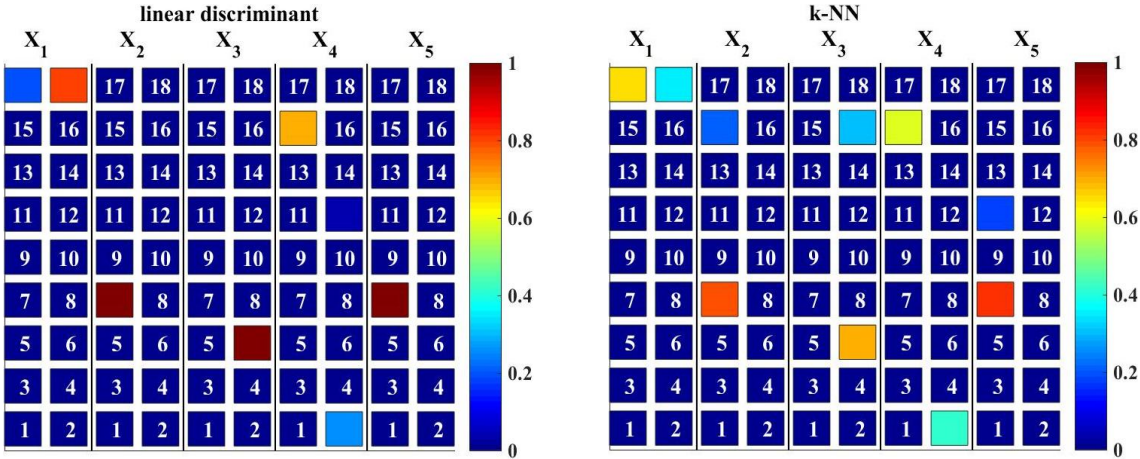
Fig. 5.14. Prediction probability for an experimental study using 2 points per class.

6. A NOVEL SEPARATION TECHNIQUE AND PEAK FREQUENCY SHIFT OF FLEXURAL LOADING-INDUCED ACOUSTIC EMISSION SOURCES IN RAILWAY PRE-STRESSED CONCRETE SLEEPERS

In this chapter, acoustic emission monitoring is employed for cracking characterization in railway pre-stressed concrete sleepers subjected to flexural loading, delivering an engineering assessment for future applications especially at railway switches and crossings. A set of full-scale concrete sleepers is loaded until failure, while the other set is used to identify cracking progression. The objectives of the study are to, firstly, identify flexural cracking damage in sleepers using AE sensing under various load testing regimes, namely, positive and negative bending moment. Secondly, by using a novel approach different from the most studies to focus on classification of damage modes, the uncorrelated acoustic emission features can be used to construct a classifier to separate acoustic emission sources in the sleepers and to examine the feasibility to use reduced set of AE parameters.

This study also proposes to filter non-significant peak frequencies of emissions due to noise by applying a modified universal threshold, a technique inspired by the research field of image analysis (subsection 2.2). This novel procedure allows for compression of the acquired acoustic emission data considerably leaving only the signatures due to cracking and failure. Then, the relationship can be established between peak frequencies acquired from three emission sensors and the distance from these sensors to the main emission source at the mid-span of sleepers.

6.1. Experimental procedure

The technical standard for testing of sleepers and bearers is specified by European Standard BS EN 13230 [205]. It provides material specifications, support conditions, loading procedures and some specific requirements for positive and negative bending tests on sleepers of which the test procedures must adhere to in order to verify the experimental data.

6.1.1. Sleeper specimens

Four full-scale pre-stressed railway concrete sleepers supplied by CEMEX are shown in Fig. 6.1. The length of sleepers is 2500 mm, height at mid-span is 175 mm, height at rail seat is 200 mm and width is 200 mm. A single sleeper has a mass of 309 kg $\pm$ 3 kg for loose fastening components. This is in good agreement with other studies [206-208]. A total of 6 pre-stressed steel tendons are embedded in each sleeper in the configuration shown in Fig. 6.1 (*c*).
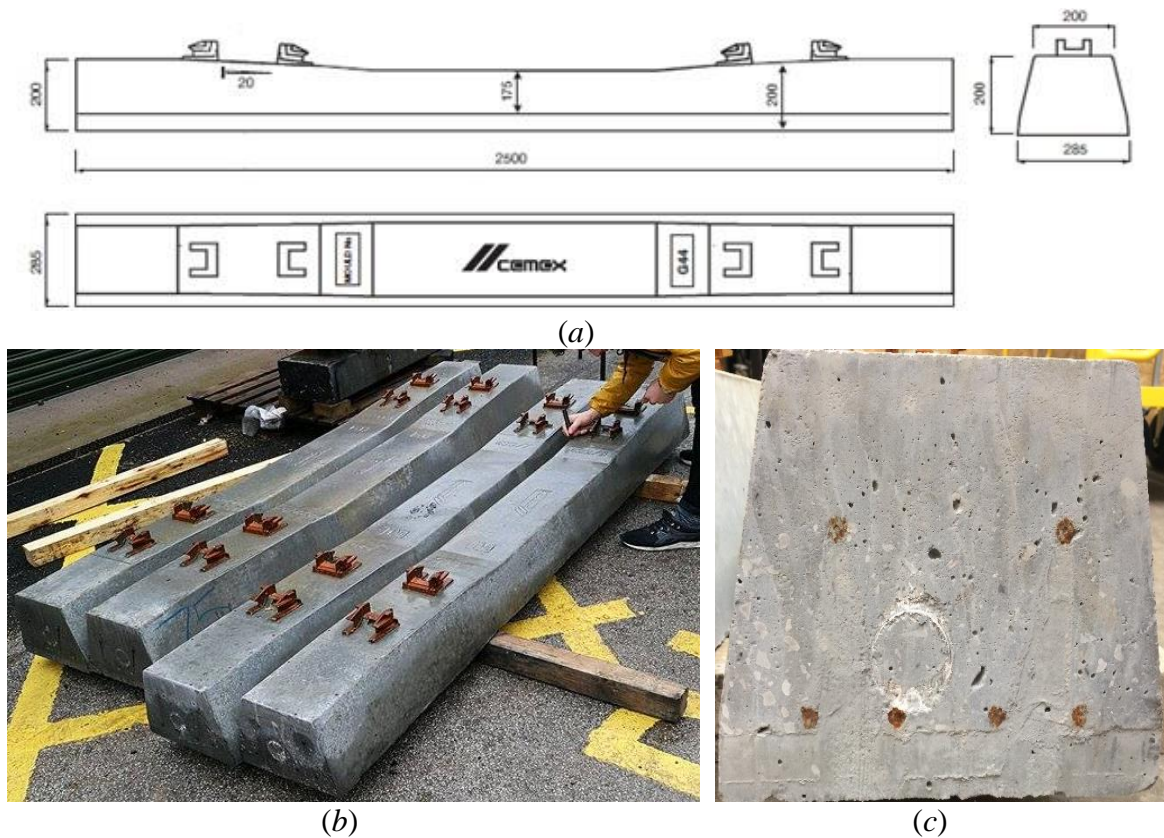
Fig. 6.1. Railway concrete sleepers with dimensions (in mm) in (*a*); photo of the sleeper specimens in (*b*); cross-section of the sleeper showing 6 steel tendons in (*c*).

6.1.2. Static loading

European Standard BS EN 13230 [205] specifies the support conditions required for the three-point bending test, instructing point supports at the railheads for both positive and negative bending tests. The support must be 100 mm wide and made from steel with a hardness Brinell: HBW > 240. The loading procedure is shown in Fig. 6.2.

For this study, a static load is applied at the mid span of the sleepers for both positive and negative bending. In practice, 3-point bending usually assesses cracking problems associated with railway sleepers. Fig. 6.3 (*a*) and (*b*) illustrate the layout of the loading procedure for positive and negative bending respectively. Additionally, the figure illustrates the location of the various NDT sensors. A photograph showing locations of mounted AE sensors for positive bending configuration is shown in Fig. 6.3 (*c*). Deflection was recorded using a linear variable differential transformer (LVDT) under the sleeper soffit (bottom) at mid span.
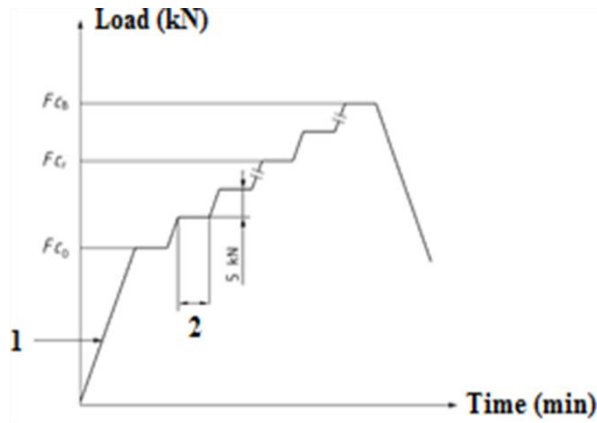
Fig. 6.2. Static procedure at the centre section for positive and negative design approval test [205].

Key labels: (1) 120 kN/min maximum; (2) from 10 s minimum to 5 min maximum.
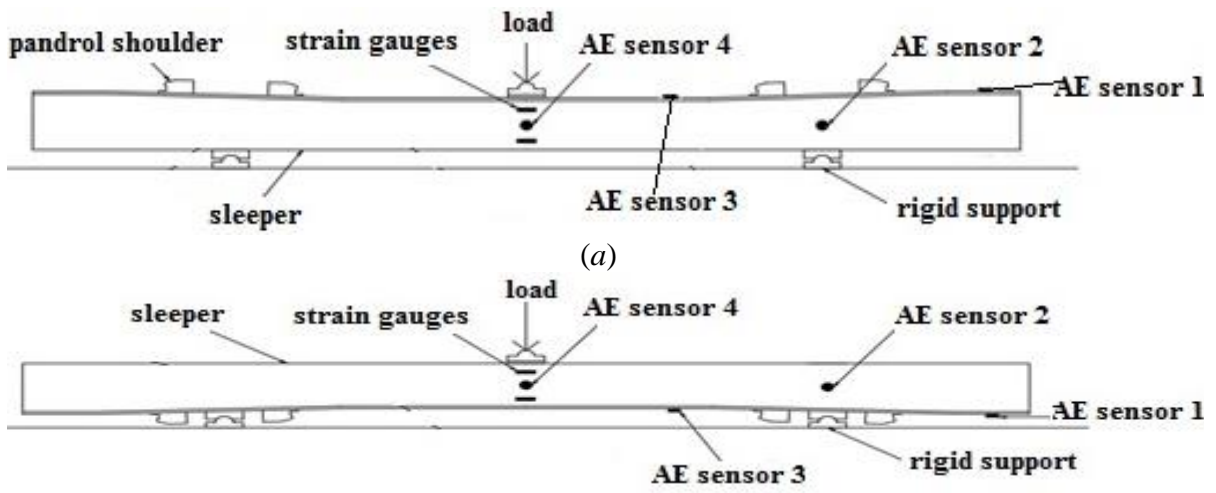
(a)

(b)
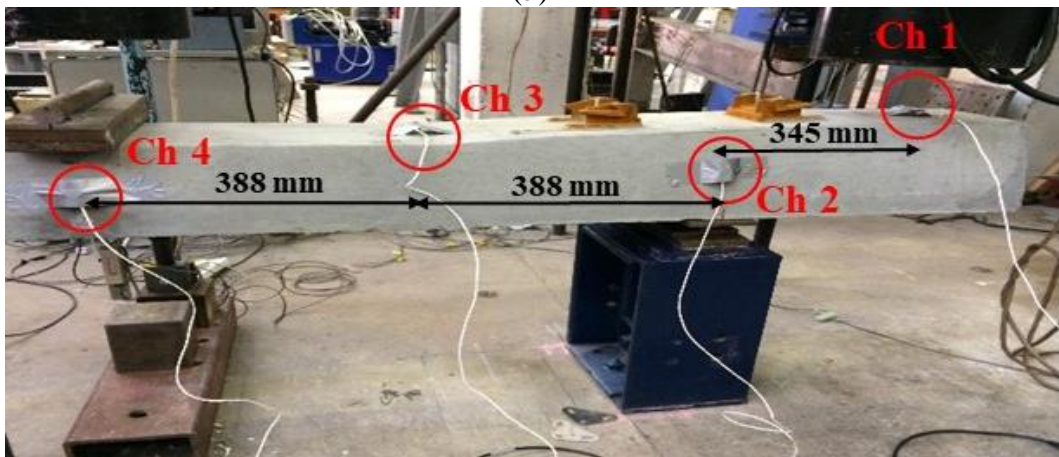
(c)

Fig. 6.3. Static loading layout for railway concrete sleepers in (a) negative and (b) positive bending configuration and (c) location of AE sensors (positive bending configuration).

6.1.3. Acoustic emission acquisition

AE measurements were carried out during all of the mechanical tests of the full-scale specimens to monitor and evaluate damage evolution during loading. The AE signals were detected and recorded using a 4-channel DAQ AE system procured from Physical Acoustics Corporation (PAC, now Mistras). The data acquisition was performed using "AE-Win" software. The AE signals were detected using wideband PAC-WD piezoelectric acoustic emission transducers operating at frequency range of 20-1000 kHz. The frequency response of these sensors allows the detection of AE signals over a wide frequency range. By this means, the AE signal characteristics associated with the different failure modes can be assessed. In addition, each sensor is connected to PAC 2/4/6 preamplifier operating in the frequency bandwidth of 20-1200 kHz. The amplification level of the pre-amplifiers (acoustic emission signal capturing threshold) was set to 50 dB prior to testing. A higher amplification level would increase the noise content as well as the amplitude of the unwanted AE signals. In contrast, a lower amplification level would result in lower noise levels, but the damage related signals would not be sufficiently amplified. The AE sensors were coupled on the samples using Vaseline petroleum jelly and held in place with duct tape. The use of coupling agent removes the air between the sensor and the surface of the sample, ensuring effective transmission of the AE signals with limited signal loss. In contrast, poor coupling quality has an adverse effect on the transmission of the AE signals and leads to increased signal loss during the tests.

The data acquisition system used was a custom-built AE and vibration acquisition system capable of continuously recording the complete waveform for periods of few seconds. The sampling rate for recording AE signals was set to 1 MSample/s, peak definition time (PDT), hit definition time (HDT) and hit lockout time (HLT) were set to 600 μs, 600 μs and 1000 μs, respectively. The pre-trigger time was set to 256 μs. The custom-built acquisition system consisted of the following components:

- A computer with a customised data logging software;
- An Agilent U2531A 4 channel data acquisition card;
- A 4 channel decoupling hub;
- A MISTRAS Wide bandwidth AE amplifier provided by PAC;
- A PAC model 2/4/6 preamplifier operating in the frequency range of 20-1200 kHz;
- Wideband PAC-WD piezoelectric AE sensors operating in the frequency range of 20-1000 kHz.

6.2. Methodology of acoustic emission source classification

The AE method detects stress changes in a specimen, relaying information by transient elastic waves that propagate and are identified by a piezoelectric sensor. Stress stimulation can be the result of crack initiation and growth, temperature variations or external sources. There are three main components in most AE systems; data acquisition, piezoelectric sensors and the pre-amplifiers/amplifiers. An AE signal must surpass a threshold magnitude to filter out unwanted noise. By accounting for the anticipated extraneous noise, the lower bound may

be established. Numerous parameters can be observed using AE, including rise time, counts, hits, energy, duration, amplitude, signal strength and others.

The flowchart of acoustic emission source separation methodology is shown in Fig. 6.4. Two out of four sleepers are statically loaded in negative bending configuration, while other two – in positive. Note that the centre-bound cracks of sleepers reflect one of the most common failure modes of sleepers [206]. In these tests, two sleepers are loaded until failure. The other two sleepers (no. 2 and 4) are first loaded until the first crack. Then the load is further increased until it reaches 1.5 times the load corresponding to the first crack. Four acoustic emission channels record the emission signatures during the tests.

Eight acoustic emission features are selected from the whole set of registered features (their explanation is provided):

- Rise (R) – time from start of the emission to maximum amplitude (μs);
- Counts (C) – cycles from start to end of the emission (non-dimensional);
- Energy (E) – energy counts (non-dimensional);
- Duration (D) – duration of emission (μs);
- Counts/Duration (C/D) or average frequency (MHz);
- Amplitude (A) – maximum amplitude of the signal (dB);
- Rise/Peak amplitude or RA value (μs/dB);
- Signal strength (SS)– area under signal envelope (pVs)

Besides the more traditional AE parameters mentioned above, the derived parameters RA value and average frequency are chosen because these two parameters are used to distinguish between different fracture modes, such as tensile and shear cracks – small RA value and large average frequency are usually due to flexural loading with initiation of tensile cracking, while the vice versa holds for shear loading [169]. It is known that sleepers (or any other structure) under different loading configuration undergo different failure mechanisms.

Data of different parameters varies in magnitude; therefore, it is imperative to rescale the data. This scaling scheme is based on data standardization [154] which involves the calculation of mean value and standard deviation of the data set for every parameter. Referring to [209], the correlation analysis was conducted to study the linear relationship between these signatures. The features that showed the most correlation were discarded from the further calculations to avoid the multi-collinearity between AE features. Cases studies are conducted where each case corresponds to a set number of uncorrelated features. At first, only the feature with the most mutual correlation is removed (7 out of 8 features). One feature is further removed in every consecutive case study with a total of 7 case studies – 8 out of 8 features, 7 out of 8 features, etc. with the last study of 2 out of 8 features. At least two features have to be included so that it is possible to assess their mutual relationship (see Fig. 6.4). The features from each case are input in a decision trees classifier, since it is the only classifier with a reasonable computation time with about 98,609 samples to process. Hyperparameters of decision trees are optimized over a course of 10 runs because of the 10-fold cross validation used in the process. The average values of hyperparameters are calculated and a final decision trees model is built for every case.

The classification performance of classifiers is evaluated via confusion matrices and classification/resubstitution errors.
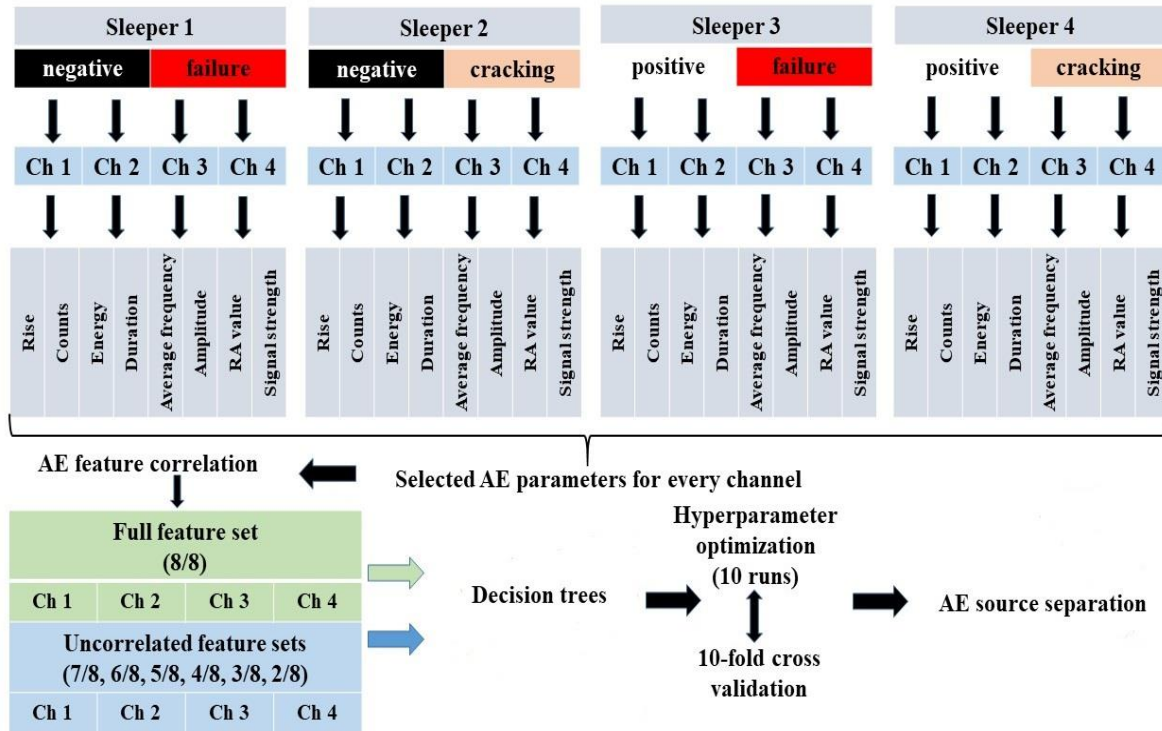
Fig. 6.4. Flowchart of acoustic emission source classification procedure.

6.2.1. Data classification with decision trees

Nodes in a decision tree involve testing a particular attribute; usually this attribute is compared with a constant. Leaf nodes give a classification that applies to all instances that reach the leaf. To classify an unknown instance, it is routed down the tree according to the values of the attributes tested in successive nodes and when a leaf is reached the instance is classified according to the class of a leaf.

If the tested attribute at the node is numeric, this test determines whether its value is greater or less than some constant, giving a two-way split (binary trees) [181] as shown in Fig. 6.5.

The cross-validation scheme is adopted in order to improve the performance of the classifier. In cross-validation, one could decide on a fixed number of folds to partition the data in. For K number of folds, the data is split into K approximately equal partitions and each in turn is used for testing while the remainder is used for training. The whole procedure is repeated K times so that every instance has been used exactly once for testing. It is K-fold cross-validation [181]. The standard approach is to apply 10 folds. Hence, this number of folds is also used in this study. In this work, the cross-validation is used to obtain a more objective representation of a classifier model and to avoid overfitting.

Classification performance of a classifier can be evaluated by considering a loss function which can be viewed as two types of errors: resubstitution loss which is a fraction of misclassifications over all set of instances on the training data from the predictors of classification model and cross-validation loss, which is an average loss of each cross-validation

121

model when predicting on data that is not used in training. The loss function is calculated in *Matlab*[TM] environment according to Eq. (1.12) and Eq. (1.13). The cross-validation framework adopted in this work is depicted in Fig. 6.6.

In the case of decision trees, resubstitution loss is influenced by number of maximum node splits, while cross-validation loss is affected by number of data partitioning folds. Optimization of these parameters is imperative for successful classification of data.
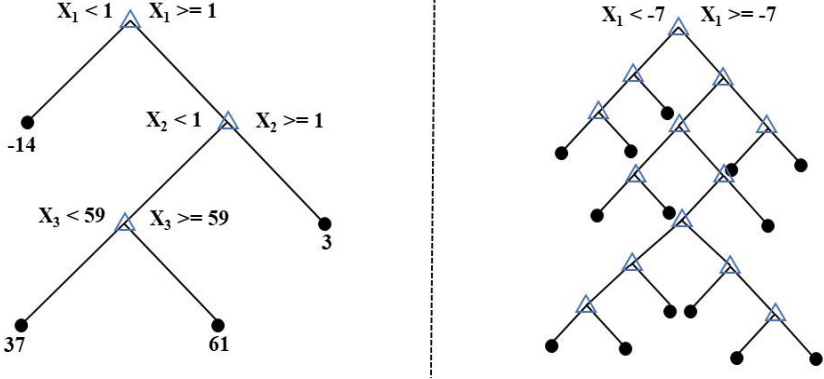
Fig. 6.5. New decision trees. Left: shallow tree with 3 splits; right: deeper tree with 13 splits.
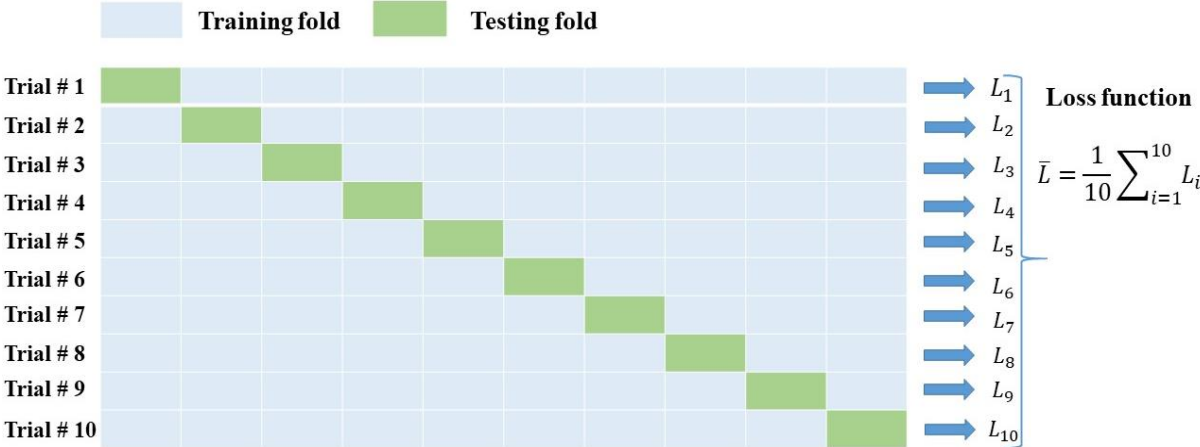
Fig. 6.6. 10-fold cross-validation scheme.

6.3. Peak frequency filtering and shift assessment

The generation of acoustic emission events due to breakage of bonds between particles of material occurs at specific frequency regions or bands. At increased loading, defects (cracks in concrete) propagate, increasing the range of emitted frequencies (frequency shifting). This ideology of characteristic frequencies of defect formation in the structure can be compared to inherent resonant frequencies of the structure in terms of resonant frequency changes due to damage. For example, by conducting modal analysis for some structure, resonant frequencies are obtained. These frequencies shift if some sort of damage is present and the magnitude of shift is dependent on damage severity and size.

Acoustic emissions with a wide array of different peak frequency values are recorded during the loading process. Some of these frequencies are characteristic of noise. However, the events of formation of damage usually emit waves characterized with a relatively massive amount of

122

emission counts. As the number of broken atomic bonds increases, the number of hits and counts that represent the emitted elastic waves also increases. Peak frequency of an acoustic emission waveform is chosen as a damage-sensitive parameter. Peak frequency is a frequency that corresponds to a maximum amplitude of Fourier Transform of acoustic emission waveform. Peak frequency is a reliable indicator of different acoustic emission sources [210], including corrosion of concrete reinforcement and load-induced cracking.

The purpose of this study is to filter out insignificant peak frequencies of acoustic emissions – the ones that are, most likely, not associated with the events of cracking in pre-stressed railway concrete sleepers. As a tool for such a filtering, the universal threshold T, introduced by Donoho is adopted for modification (Eq. (2.16)).

The modification procedure is as follows:

1. A total number of counts is summed for every value of peak frequency recorded throughout the whole acoustic emission interrogation process for every channel of every sleeper.
2. The universal threshold from Eq. (2.16) is applied to all count values and only the ones that exceed the threshold are retained. Others are discarded.
3. A new set of peak frequency and corresponding count pairs is formed based on the filtering in the previous step. From this set, the peak frequency corresponding to maximum number of counts is registered.
4. Using the filtered peak frequency-counts sets, the centroid value of peak frequency PFC is computed using the formula in analogy to centre of mass for a body

$$PFC = \frac{\sum_i^N C_i \times PF_i}{\sum_i^N C_i} \tag{6.1}$$

where C – counts;
PF – peak frequency.

For every sample i the number of counts is multiplied by the corresponding peak frequency and all such multiplications are summed up for all samples N. This summation is then divided by the sum of all counts. The calculation is done in order to evaluate the location of largest proportion of counts in terms of peak frequency and compare this to the one corresponding to maximum counts.

5. A linear regression model of peak frequency shifts with distance from the main acoustic emission source at the mid-span of the sleepers is made for both approaches – peak frequencies corresponding to maximum number of counts (step 3) and centroid values of peak frequencies obtained from step 4.

6.4. Response to loading and peak frequency analysis

Generally, a load-deflection curve shows the elastic and plastic behaviour of the sleeper, with the initial linear portion representing the elastic zone. When the curve reaches the ultimate load, substantial loss of flexural strength will occur. By overlaying the AE data, the damage events recorded by the sensors can be correlated with the transition into the plastic zone and its post-failure behaviour thereafter. It is expected that the most substantial AE energy hits will

occur at the ultimate load, provided that the sleepers still have residual flexural capacity [211-212], significant activity may continue after failure. By controlling the loading rate, deflection can be plotted against time to give meaningful results.

6.4.1 Negative bending to ultimate load

A typical failed specimen is shown in Fig. 6.7 (*a*). The failure mode is mixed (flexural + shear), which confirms the results of previous studies [213]. Load-deflection plot in Fig. 6.7 (*b*) shows the elastic zone extends to approximately 60 kN at which point of the first crack occurs, a lower value than visual observations of 70 kN. Energy from the first crack event is negligible, thus it cannot be seen due to the magnitude of later events. The marking of crack progression was ceased above the load of 98 kN (when concrete crushing starts) for the safety of testing personnel since severe cracking and possible failure was imminent at any moment. The highest energy signal of 31,600 atto-joules takes place at the ultimate load of the specimen, 102 kN. At the moment of failure, a deflection of 17 mm is registered at the mid-span. Beyond this point, the steel tendons assume the tensile load, allowing further deformation to take place, hence AE activity continues. At 78 kN post failure, another substantial event leads to a dense concentration of high energy hits up to 16,500 atto-joules. There is a significant loss of tendon pre-stressed force and concrete disintegration here. The CEMEX G44 sleeper is a relatively brittle design with just six tendons making its behaviour less ductile.
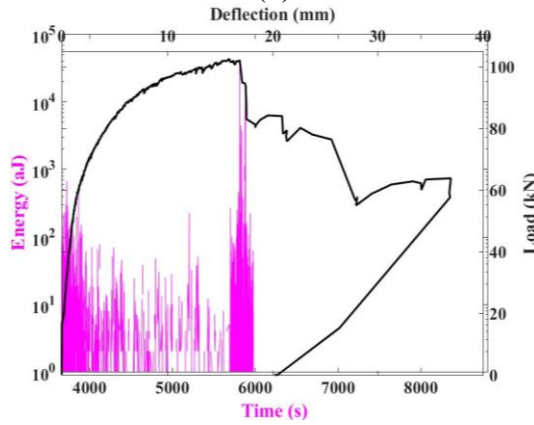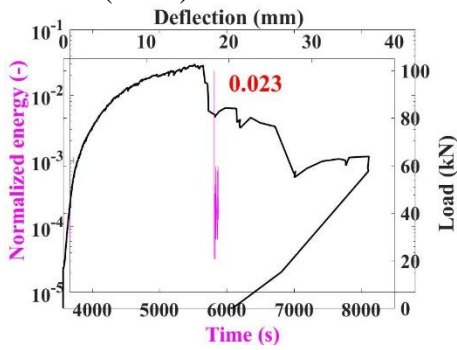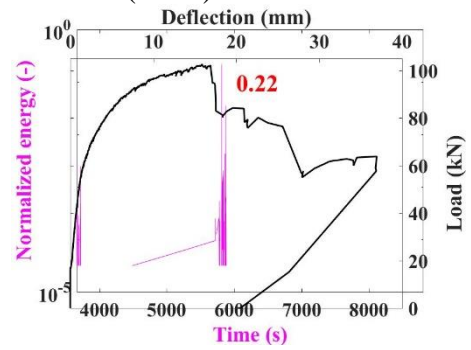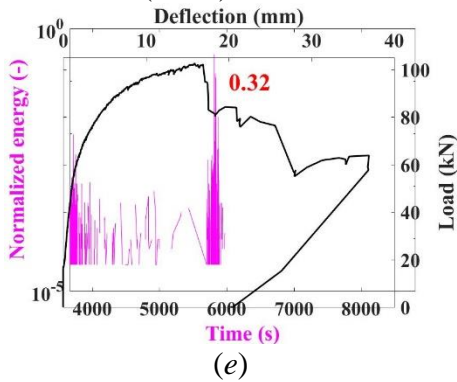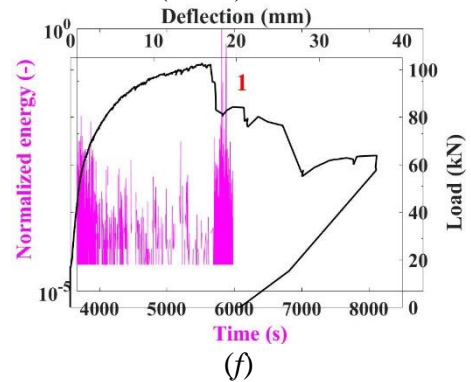
Fig. 6.7. Failure pattern for sleeper no. 1 (*a*); acoustic energy for all channels superimposed with load vs deflection (*b*); normalized acoustic energy channel 1 (*c*); channel 2 (*d*); channel 3 (*e*); channel 4 (*f*).

125

Normalized energy of AE events for every channel separately is shown in Fig. 6.7 (*c*)-(*f*). The largest values are depicted with red numbers. The largest fraction of magnitude of total energy corresponds to channel no. 4, which is at mid-span where the emitted energy due to cracking is overwhelmingly larger compared to other channels (sources). By increasing the distance from mid-span, the absolute AE energy values decrease with only about 2 % of the maximum energy at channel no. 1.

The evolution of peak frequencies corresponding with loading, along with load-deflection curves, is shown in Fig. 6.8. No distinct emission burst is observed at the event of the first crack. However, the most intense emissions correspond to the event of failure and even after that. According to [214], a somewhat similar phenomenon was observed – the amount of acoustic emission energy released before peak load was less than 10 % of the total emitted energy. Farnam et al. [214] explained that the reason of small fraction of acoustic emissions at the initial cracking may be due to the formation of small micro cracks with relatively small surface areas. In this study, emission events are clearly dominated by the ones coming from mid-span (channel no. 4) with a range of peak frequencies from 150 kHz to about 600 kHz. Three distinctive bands of peak frequencies are registered – [150-300] kHz, [385-460] kHz and [498-496] kHz as indicated from Fig. 6.8. Emissions from channels no. 1 and 2 occur at the lowest frequency band [150-300] kHz.

The results of peak frequency filtering are shown in Fig. 6.9. Apparently, the maximum number of counts greatly exceeds the threshold value. For channel no. 1, this difference is 19 times. The differences of 20 times, 48 times and 266 times for channels no. 2, 3 an 4, respectively, are registered. The peak frequency filtering technique allows to significantly reduce the number of peak frequencies for further analysis. In the case of sleeper 1, only 20 %, 18 %, 22 % and 28 % of peak frequency values are retained for channels no. 1, 2, 3 and 4, respectively. Bar plots of retained peak frequency-count pairs are shown as inlet plots in Fig. 6, 10, 13, 16. After the filtering, the effective peak frequency range is decreased and this effect is more pronounced for channel no. 4 with the largest proportion of emissions. For channel no. 1 the peak frequency range [111-271] kHz is filtered to [119-265] kHz, whereas for channel no. 4 – from [111-837] kHz to [160-529] kHz.
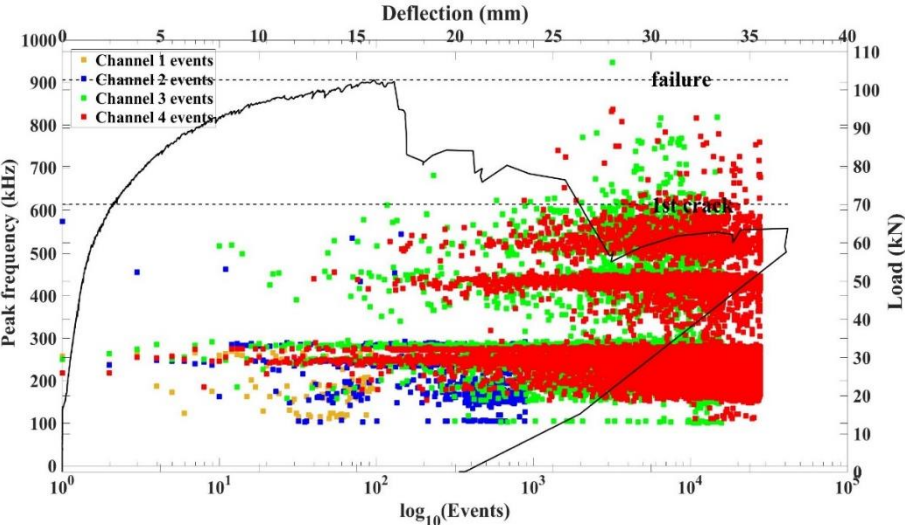
Fig. 6.8. Peak frequency evolution for sleeper no. 1.

126
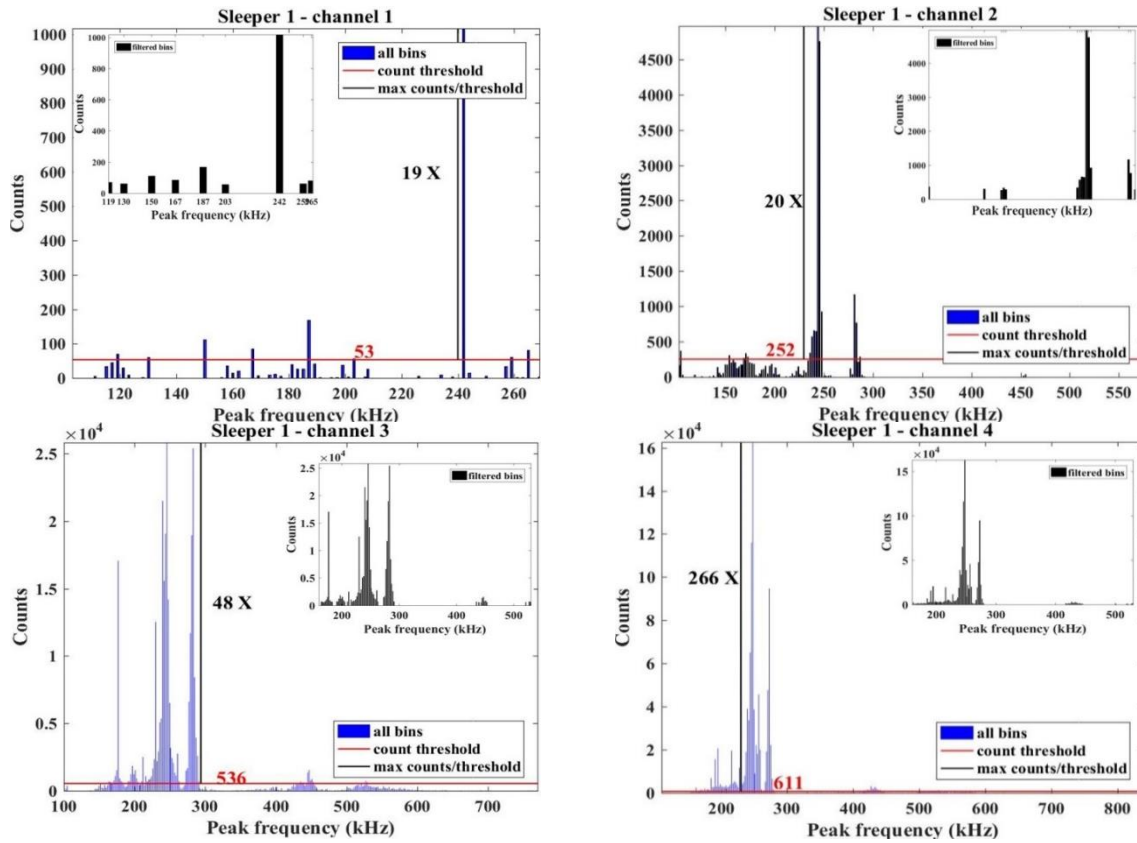
Fig. 6.9. Peak frequency filtering for sleeper no. 1.

6.4.2 Negative bending crack progression

The sleeper no. 2 and similarly sleeper no. 4 are loaded until the first crack and unloaded. Then, the applied load is again increased from 0 kN to a load roughly corresponding to 1.5 times the load of the first crack. During both loading phases, acoustic emissions are recorded. The load-deflection curve (in Fig. 6.10 (*c*)) shows the incremental loading pattern from the crack progression in Fig. 6.10 (*b*). In comparison to the failure curve, the energy hits are very low, but it does confirm the observed initial cracking in Fig. 6.10 (*a*) at 53 kN. The concrete activity prior to the initial surface cracks corresponds to minor internal cracks and extraneous noise. Due to the Kaiser effect, when the sleeper is unloaded then reloaded back to the force required for the initial crack, there is no AE activity, so it is possible to put these AE signatures (from the first crack and 1.5*first crack load phases) in a single time sequence. Cracking alters the flexibility of the sleeper, hence why for 1 mm deflection the load in a reloading phase is 6 kN greater. Beyond the first crack, the slope of the curve indicates the transition into the plastic zone, where regular AE activity is maintained. Comparing the crack progression in Fig. 6.10 (*b*) to the AE energy hits, there is a strong correlation between them, supporting the competence of using AE in damage detection. There are clearly peaks and troughs in the energy sequence that display when any major cracking events that are taking place.

(*a*)   (*b*)

(*c*)

6/8 (75 %) nonzero AE events   491/763 (64 %) nonzero AE events

(*d*)   (*e*)

6857/10888 (63 %) nonzero AE events   482/660 (73 %) nonzero AE events
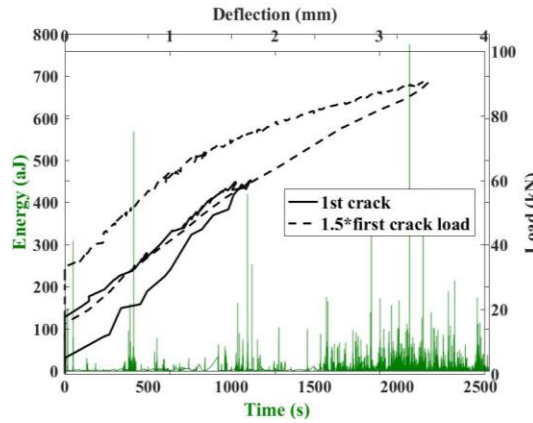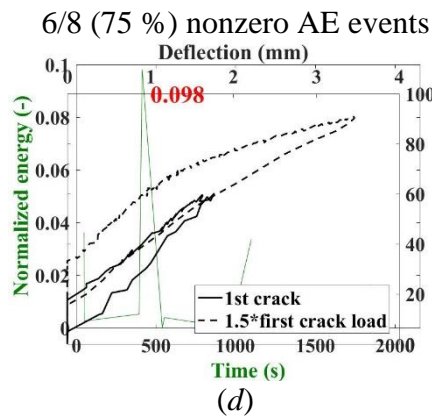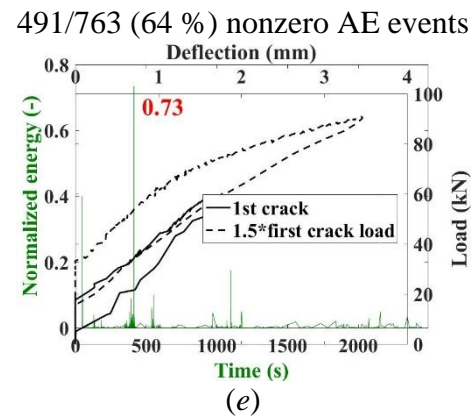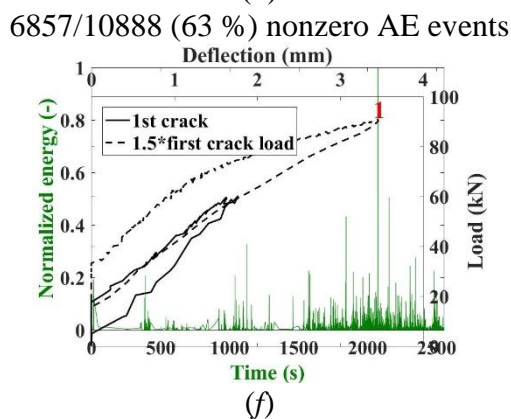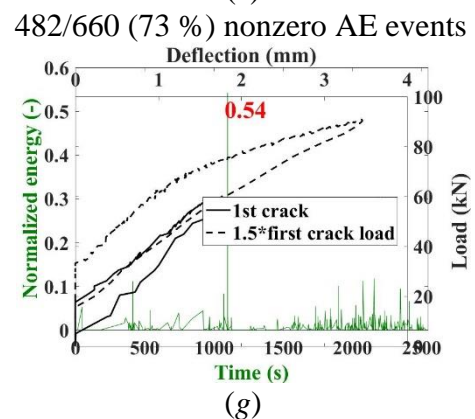
(*f*)   (*g*)

Fig. 6.10. The first crack of sleeper no. 2 (*a*); cracking pattern at load of 1.5 times the first crack load (*b*); acoustic energy for all channels superimposed with load vs deflection (*c*); normalized acoustic energy channel 1 (*d*); channel 2 (*e*); channel 3 (*f*); channel 4 (*g*).

Relative energies of acoustic emission for every channel in Fig. 6.10 (*d*)-(*g*) show that the largest proportion of emitted energy concentrates in the vicinity of channel no. 3 which is

128

roughly one sixth of a sleeper`s length apart from the mid-span. The smallest fraction of emitted energy is again in the vicinity of channel no. 1. This proportion comprises only about 10 % of the total energy emitted in the process of cracking. In this case, there is no monotonic trend for decrease of energy of emission events with increasing distance from mid-span.

The load-deflection curves overlaid with peak frequency evolution with loading are depicted in Fig. 6.11. The total deflection at the highest load is about 3.5 mm. Again, three distinct peak frequency bands are present with the most contribution from channel no. 4. The bands are [140-290] kHz, [360-440] kHz and [500-600] kHz. The emissions from other channels are barely visible with an exception of channel no. 3. Emissions from channels no. 1 and 2 are mostly associated with lower frequency band of [140-290] kHz.

Peak frequency filtering results are shown in Fig. 6.12. Only 4 out of 23 peak frequencies are significant for channel no. 1, while 65 out of 256 for channel no. 4. The count information retained is 67 % and 91 %, respectively. This result indicates the possibility of significant data compression for analysis of acoustic emission phenomena. As with the cases for other sleepers, large difference between threshold value and maximum number of counts can be observed – ranging from 5 times for channel no. 1 to 57 times for channel no. 4.
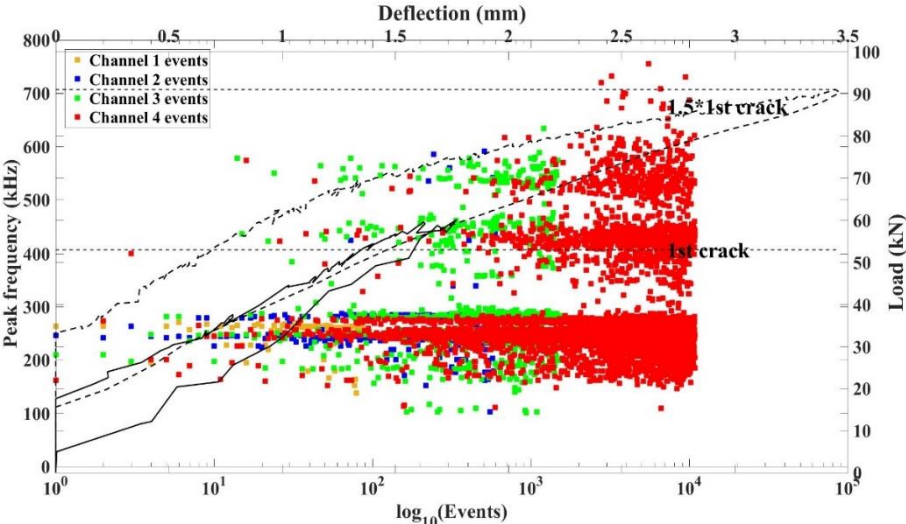
Fig. 6.11. Peak frequency evolution for sleeper no. 2.
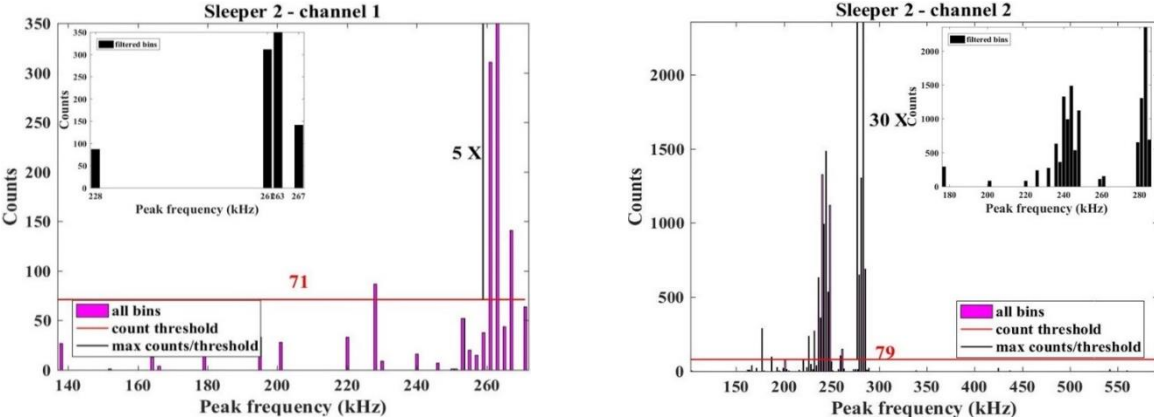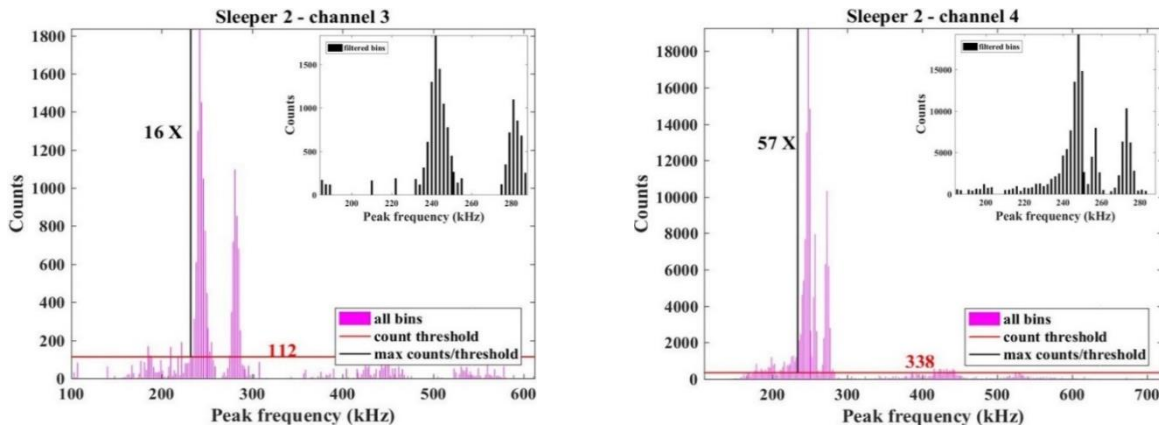
Fig. 6.12. Peak frequency filtering for sleeper no. 2.

6.4.3. Positive bending to ultimate load

The failure pattern if a test specimen is shown in Fig. 6.13 (*a*). The failure mode is pure shear with pre-stressing tendons clearly exposed near the mid-span. The failure is characterized with substantial loss of concrete mass as can be seen in Fig. 6.13 (*a*). The total deflection of sleeper at mid-span at the moment of failure is about 7.7 mm. Load/deflection curves are shown in Fig. 6.13 (*b*). The initial cracking for sleeper no. 3 occurs at 53 kN while the failure of the sleeper is registered at load of 113 kN. The ultimate load for positive bending is over 11% higher than for negative bending, this is unsurprising since sleepers are designed to have higher strength in this orientation. The AE energy data shows reasonably strong correlation with the load-deflection curve so that the first crack and ultimate load events can be distinguished. In comparison to the negative bending test, the values of energy are relatively low at ultimate load. It is possible, that the aggressive brittle failure that took place prevented the sensors from recording high energy data. Beyond the ultimate load, the sleeper's tensile capacity diminishes and no further activity proceeds. Although it is not documented in this report, the exact location of damage can be found based on the time taken for a signal to arrive at each sensor, this method is called linear localisation. Separating the sensors into individual channels means that by identifying the sensor corresponding to an energy event, the damage location can be spatially approximated. The first crack is identified by sensor 4 at the mid-span; this can be anticipated since the first crack is flexural. It matches well with the load deflection curve as it marks the transition in the plastic zone. Sensor 2 – located at the rail seat, records a high energy hit just after the initial cracking, which represents spalling of the concrete at the supports. At the ultimate load, sensors 3 and 4 record high energy hits, as expected, since they are located nearest the mid span.

(*a*)
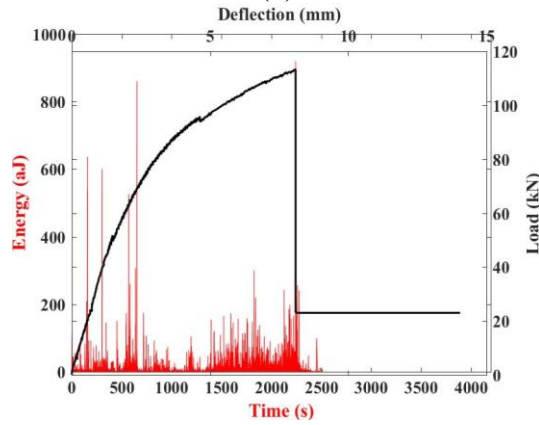
(*b*)

38/59 (64 %) nonzero AE events
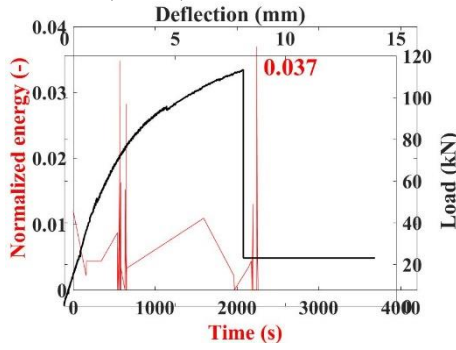
(*c*)

1988/2963 (67 %) nonzero AE events
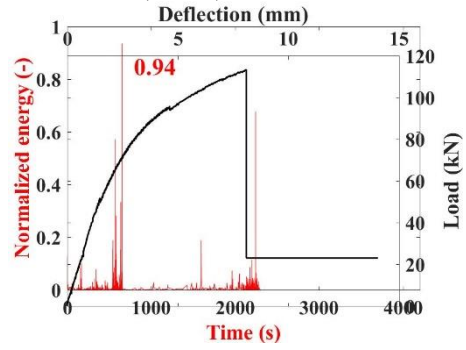
(*d*)

3122/5010 (62 %) nonzero AE events
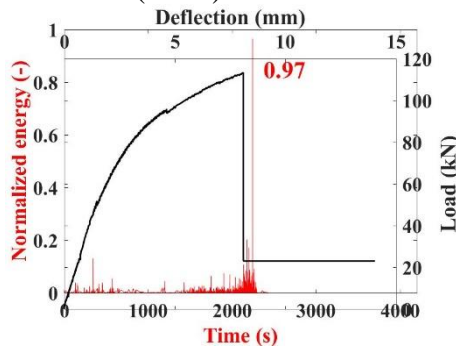
(*e*)

11501/18835 (61 %) nonzero AE events
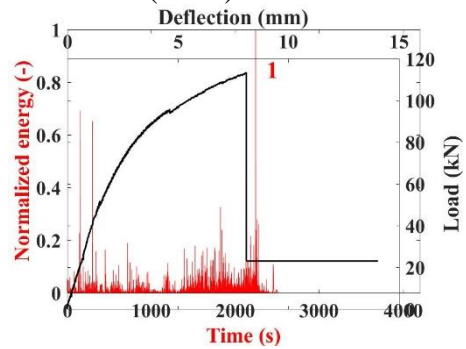
(*f*)

Fig. 6.13. Failure pattern for sleeper no. 3 (*a*); acoustic energy for all channels superimposed with load vs deflection (*b*); normalized acoustic energy channel 1 (*c*); channel 2 (*d*); channel 3 (*e*); channel 4 (*f*).

The trend for relative energy proportions for every AE channel in Fig. 6.13 (*c*)-(*f*) is similar to that observed for sleeper 1. The largest fraction of energy concentrates at mid-span with comparable energies farther from this area and the smallest proportion– at the remote end of a sleeper near channel no. 1.

Three bands of peak frequency values are clearly seen in Fig. 6.14. The widest band is [150-300] kHz, the second band is [350-450] kHz and the third band is [500-600] kHz. Acoustic emission events are clearly dominated by channel no. 4 characterized by highest density of cracks. As with sleepers no. 1 and 2, acoustic emissions from channels no. 1 and 2 mostly occur at the lowest frequency band of [150-300] kHz. Significant emission bursts correspond to the stage of failure. Emissions from other channels are much less pronounced. Different emisison frequencies correspond to different failure mechanisms – at the loading stage near failure the acoustic emisison events are due to tensile matrix micro-cracking, while fiber pull-out takes place after the formation of main cracks, in accordance with [215].

Peak frequency distributions and filtering results for sleeper no. 3 are shown in Fig. 6.15. Atypical data compared to other channels and channels of other sleepers is the result for channel no. 1. It shows that maximum number of counts corresponds to peak frequency of 140 kHz, while in all ather cases this value is about (250 ± 10) kHz. Large differences between established threshold values and maximum bumber of counts can be observed for this sleeper. Also, there is a trend for increasing threshold with decreasing distance to mid-span (from channel no. 1 to channel no. 4). The most prominent reduction in peak frequency range after filtering is observed for channel no. 3 and 4 – from [103-759] kHz to [142-447] kHz for channel no. 3 and from [107-998] kHz to [169-527] kHz for channel no. 4.
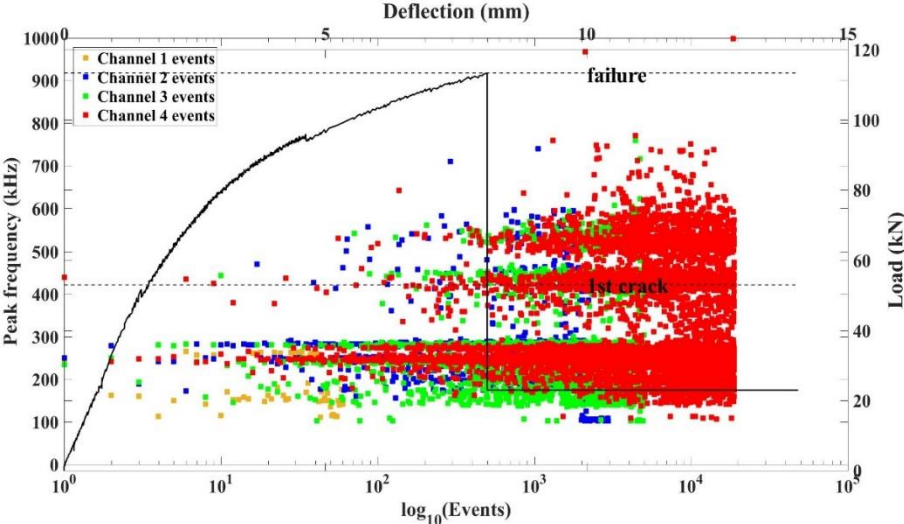

Fig. 6.14. Peak frequency evolution for sleeper no. 3.
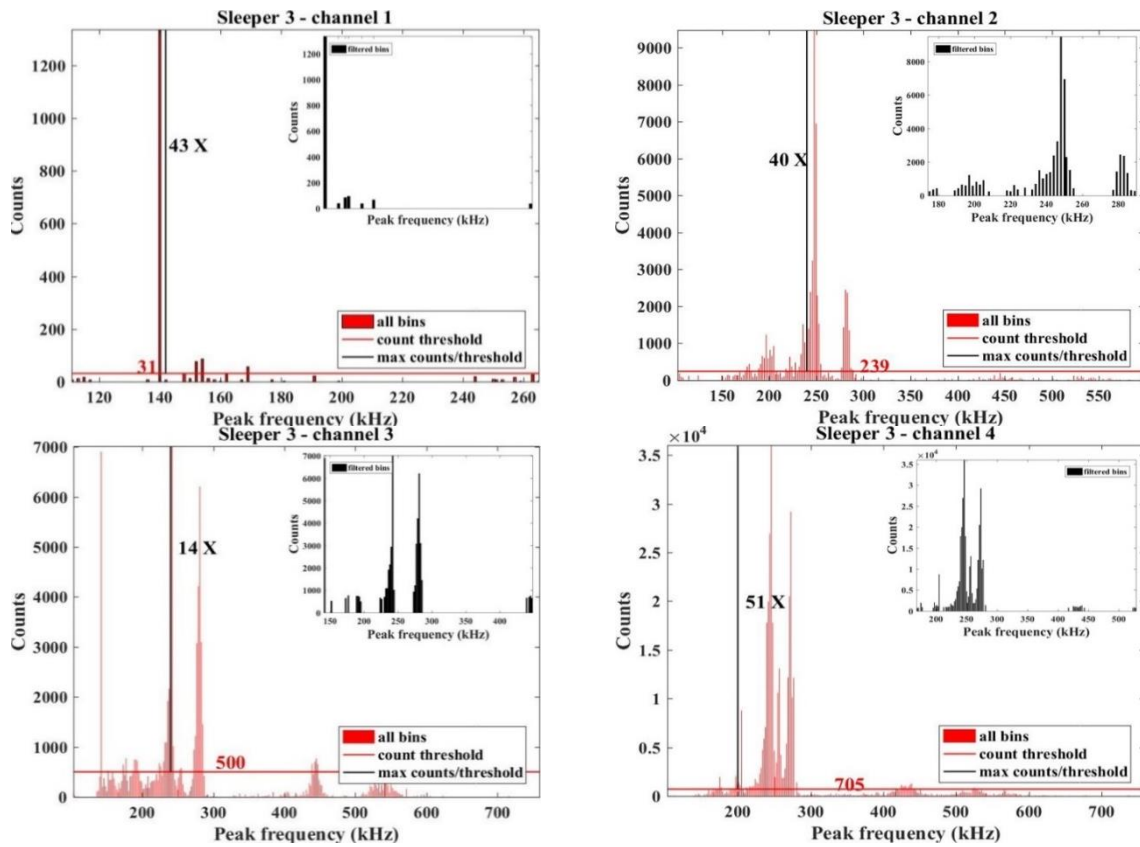
Fig. 6.15. Peak frequency filtering for sleeper no. 3.

6.4.4. Positive bending crack progression

As seen in Fig. 6.16 (*a*), the first crack load is at 60 kN. AE does not correlate perfectly with the load-deflection curve, but the energy hit that caused the first crack can clearly be noticeable. There are some inconsistencies in the data, with some energy jumps prior to the first crack; this may correspond to concrete spalling or extraneous noise. Beyond the first crack, AE energy stays low with exception to a hit at 79 kN. This magnitude of load is approaching the severe condition; therefore, damage events will produce greater energy. The loading is proceeded until the load of approximately 83 kN. During the initial loading phase the deflection of the sleeper is only 1 mm, while the total deflection is about 4 mm as recorded by LVDT.
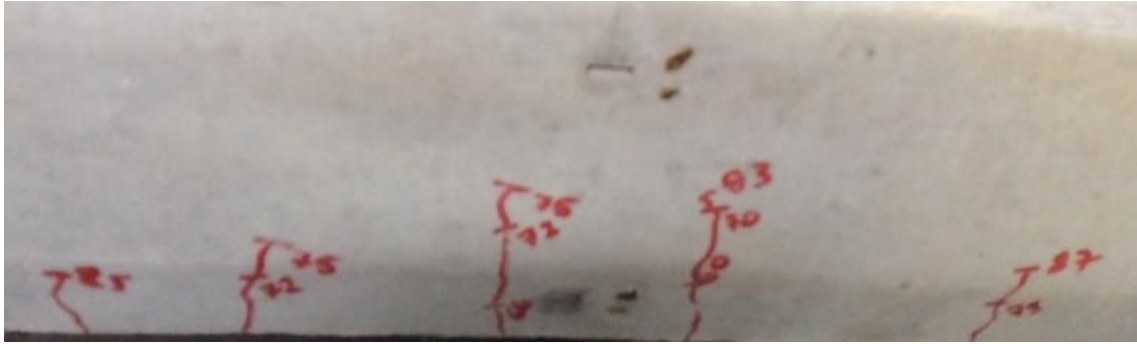
(*a*)
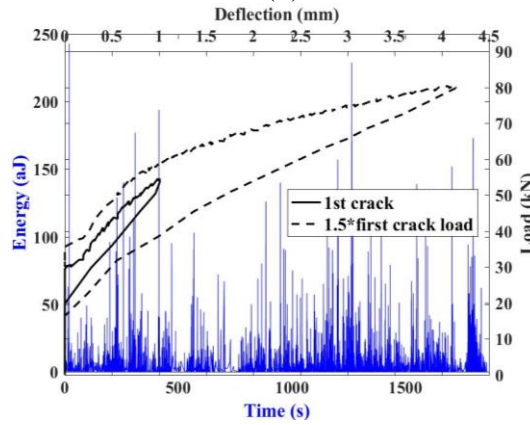
(*b*)

56/86 (65 %) nonzero AE events
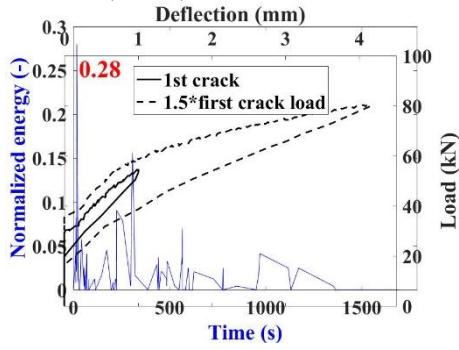
(*c*)

434/596 (73 %) nonzero AE events
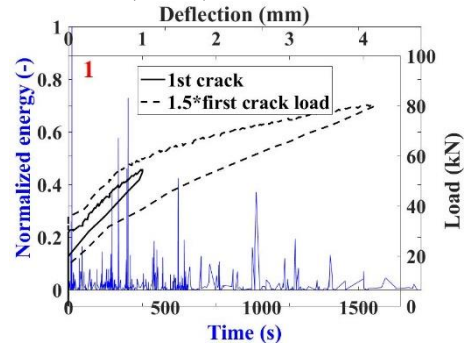
(*d*)

834/1543 (54 %) nonzero AE events
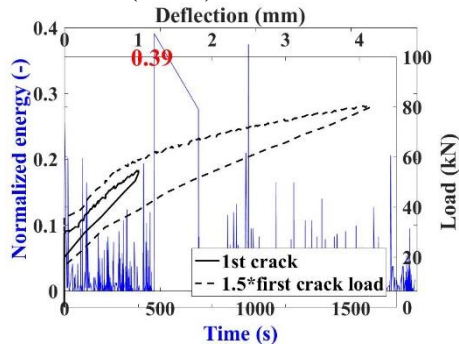
(*e*)

6540/10843 (60 %) nonzero AE events
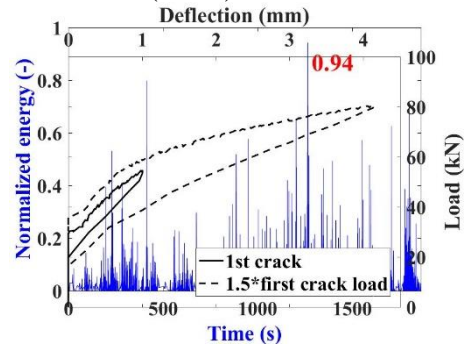
(*f*)

Fig. 6.16. Cracking pattern at load of 1.5 times the first crack load for sleeper no. 4 (*a*); acoustic energy for all channels superimposed with load vs deflection (*b*); normalized acoustic energy channel 1 (*c*); channel 2 (*d*); channel 3 (*e*); channel 4 (*f*).

134

It can be observed that, for sleepers not loaded until failure, the trend of relative energy magnitudes with increasing distance from midspan is not monotonic – as in the case with sleeper 2, considerable fraction of total energy is emitted at midspan, however, in Fig. 6.16 (*c*)-(*f*) one can see that channel no. 2 shows even greater release of energy. As always, the least energy is emitted at the remote end of sleepers farther from largest concentration of cracks.

The load-deflection curves along with peak frequency evolution during loading are shown in Fig. 6.17. Surprisingly, the increase of peak frequency values of channel no. 2 is the most pronounced with increasing load with the ladder-like signature and comparatively few emission events. Relatively lower peak frequencies are emitted in the vicinity of channel no. 4 – the band is [100-300] kHz and there are relatively few events in this channel, although the emissions have lasted through out the whole test. The dominating proportion of events are emitted near channel no. 3 where a range of frequencies is wide with 3 distinct bands [150-300] kHz, [300-460] kHz and [500-700+] kHz. Very few emisisons from channel no. 1 are registered and mostly attributed to the lowest frequency band [150-300] kHz.

The results of peak frequency filtering for all 4 channels are shown in Fig. 6.18. Only 6 peak frequency values are detected in channel no. 1. The largest number of counts is 2 times larger than threshold value of 79, thus only 1 significant value of 259 kHz peak frequency is retained. For channel no. 2, only 14 % of all values remain after filtering with largest number of counts at 287 kHz peak frequency. The largest difference of 36 times between threshold value and the largest count peak is for channel no. 3. Peak frquency corresponding to the most counts is at 248 kHz and only 18 % of all peak frequency values are significant in this case. Acoustic emisisons with a peak frequency of 240 kHz have generated the most counts at the mid-span. Only 14 out of 87 different peak frequency values are significant.
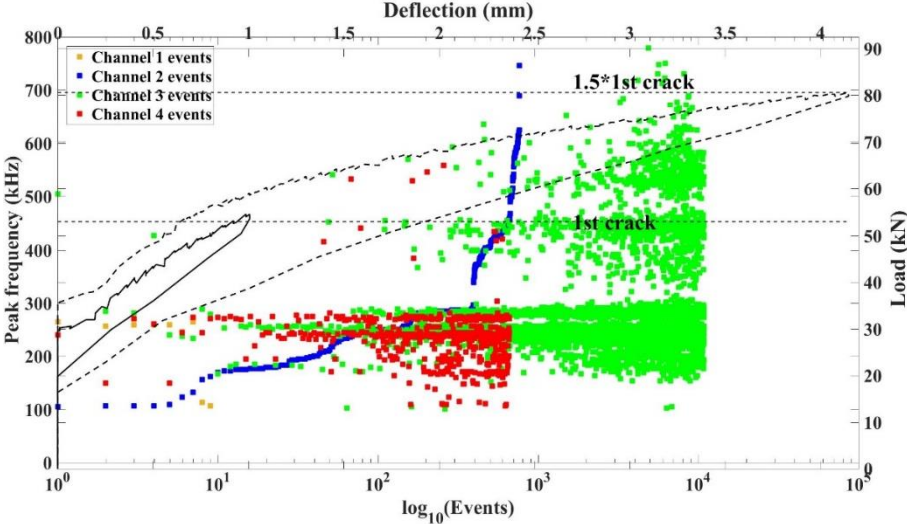
Fig. 6.17. Peak frequency evolution for sleeper no. 4.
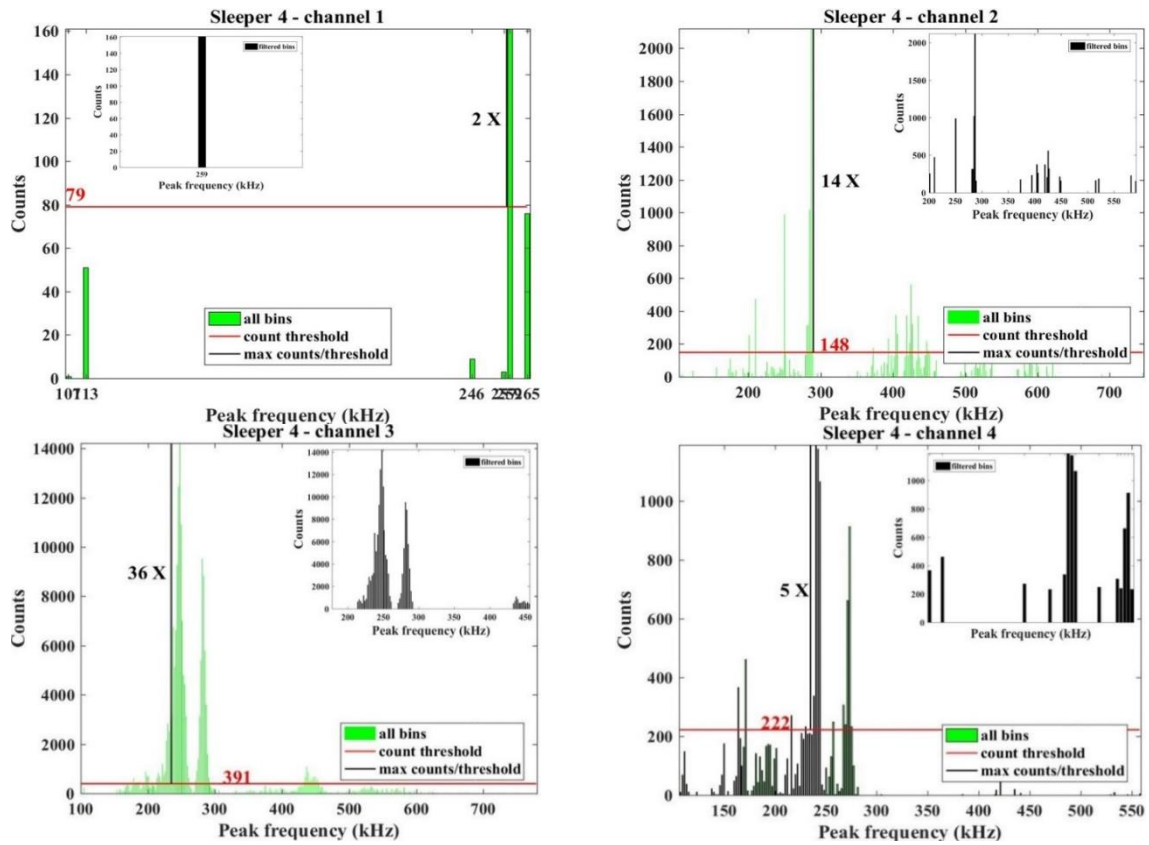
Fig. 6.18. Peak frequency filtering for sleeper no. 4.

The results summarizing the raw peak frequency/counts data and the information retained after the filtering are shown in Table 6.1. It is clear that the universal threshold value increases by decreasing the distance from channel no. 1 to channel no. 4. In short, the intensity of acoustic emissions had increased in the direction towards the mid-span of the sleepers. The only exception is sleeper no. 4. For all of the channels, the proportion of significant peak frequencies constitute only 14 % to 34 % of the initial data with 53 % to 98 % count information retained. This insight is critical for modified universal thresholds that are suitable for local placement of sensors. Overall, the total range of peak frequencies recorded in the events of acoustic emissions is from 101 kHz to 998 kHz. This is an ultrasound range. The largest variety of different peak frequencies is emitted mostly at mid-span. After the application of modified threshold, the peak frequency range, so-called 'effective peak frequency', has decreased – 105 kHz to 591 kHz. In addition, the farthest end of recorded peak frequency spectrum has insignificant number of counts and thus 592 kHz to 998 kHz values are discarded.

136

Table 6.1

Results of remaining information after counts filtering using universal threshold

Sleeper 1								
Channel no.	Full			Filtered			Remaining (%)		Threshold
	Bins	Counts	Range (Hz)	Bins	Counts	Range (Hz)	Bins	Counts	
1	44	2228	111-271	9	1709	119-265	20	77	53
2	85	21767	103-574	15	16667	105-287	18	77	252
3	302	307246	101-947	67	280512	164-529	22	91	536
4	289	1012949	111-837	82	988526	160-529	28	98	611

Sleeper 2								
Channel no.	Full			Filtered			Remaining (%)		Threshold
	Bins	Counts	Range (Hz)	Bins	Counts	Range (Hz)	Bins	Counts	
1	23	1328	138-271	4	889	228-267	17	67	71
2	53	13257	103-591	18	12674	177-285	34	96	79
3	170	17918	101-634	25	13499	185-287	15	75	112
4	256	160494	109-755	65	146324	169-529	25	91	338

Sleeper 3								
Channel no.	Full			Filtered			Remaining (%)		Threshold
	Bins	Counts	Range (Hz)	Bins	Counts	Range (Hz)	Bins	Counts	
1	31	1965	111-265	7	1706	140-263	23	87	31
2	178	58226	103-740	38	50736	175-289	21	87	239
3	204	77305	103-759	29	53777	142-447	14	70	500
4	293	358301	107-998	57	318029	169-527	19	89	705

Sleeper 4								
Channel no.	Full			Filtered			Remaining (%)		Threshold
	Bins	Counts	Range (Hz)	Bins	Counts	Range (Hz)	Bins	Counts	
1	6	301	107-265	1	161	259	17	53	79
2	156	14614	105-746	22	9261	201-591	14	63	148
3	263	177646	101-779	48	154327	214-455	18	87	391
4	87	12370	107-558	14	7714	164-275	16	62	222

6.5. Classification of acoustic emission sources

Positions of data points corresponding to one variable with respect to another can be illustrated using scatter plots. Such scatter plot is shown in Fig. 6.19 where two AE features (counts and rise time) are displayed relative to one another. These features are taken from a predictor set of features, comprising of either 8 features (full set) or reduced number of features (see Table 6.3). In our case, class names are sleeper channels (AE sources) and are marked with different colours. A total of 16 classes have to be separated (4 classes per sleeper) with a total number of observations or samples equal to 98,609. The largest scatter of predictor values corresponds to sleeper 1, while the smallest – to sleeper 2. The largest proportion of features is

attributed to AE channel 4 (at the mid-span of sleepers) for almost all cases, which is not surprising considering that the largest bending moment is at the mid-span.
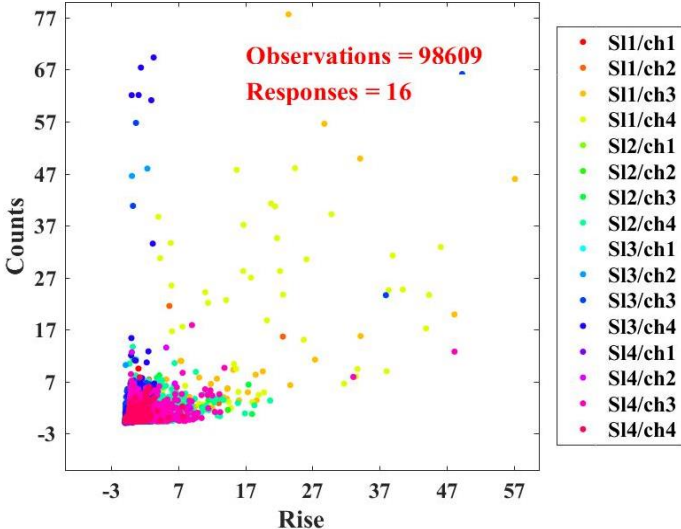
Fig. 6.19. Scatter plots of relationship between acoustic emission counts and rise time for channels of all sleepers combined.

6.5.1. Correlation between acoustic emission features

The results of mutual correlation of AE features are shown in Table 6.2 (refer to subsection 6.2 for the meaning of symbols). Only the results with a significant correlation (above 60 %) are shown. The number of samples recorded for every feature is shown for every AE channel (source). At the bottom of Table 6.2 the correlations for every feature are summed and displayed for every sleeper. The largest correlation throughout all sleepers is consistently exhibited by counts (C) feature, followed by duration (D), signal strength (SS), energy (E), amplitude and RA value (RA).

Based on these results, the case study involving the building of a novel decision trees classification model is conducted by incrementally removing the most correlated features in the order starting from the one with the largest correlation. This organization is shown in Table 6.3. A total of seven case studies is defined where the 1st case corresponds to a full feature set (all 8 features considered), the 2nd case corresponds to 7/8 features with counts feature removed and so on.

Table 6.2

Correlation (expressed in %) between acoustic emission features for every emission channel and number of recorded samples per feature

	Sleeper 1	Sleeper 2	Sleeper 3	Sleeper 4
Channel 1	**95 samples/feature**	**90 samples/feature**	**61 samples/feature**	**10 samples/feature**
	Rise time	Rise time	Rise time	Rise time
	R-RA = 100 %	R-D = 63.3 %	R-RA = 100 %	R-D=77.1 %
	Counts	R-RA = 100 %	Counts	R-RA=100 %
	C-E = 99.8 %	Counts	C-D = 99.2 %	Counts
	C-D = 95.4 %	C-E = 95.5 %	C-A = 89.7 %	C-E = 99.1 %
	C-A = 74.4 %	C-D = 91.5 %	C-SS = 99.8 %	C-D = 88.8 %
	C-SS = 99.8 %	C-A = 90.2 %	Energy	C-C/D = 79 %
	Energy	C-SS = 95.5 %	E-D = 61.7 %	C-A= 99.1 %
	E-D = 94.2 %	Energy	E-A = 81.1 %	C-SS = 99.1 %
	E-A = 70.2 %	E-D = 88.3 %	Duration	Energy
	E-SS = 100 %	E-A = 85.0 %	D-A = 90.5 %	E-D = 84.6 %
	Duration	E-SS = 99.9 %	D-SS = 98.9 %	E-C/D = 78.7 %
	D-A = 79.9 %	Duration	Amplitude	E-A = 97.7 %
	D-SS = 94.2 %	D-A = 88.4 %	A-SS = 86.9 %	E-SS = 100 %
	Amplitude	D-RA = 63.3 %		Duration
	A-SS = 70.3 %	D-SS = 88.7 %		D-C/D = 64.7 %
		Amplitude		D-A = 90.8 %
		A-SS = 85.0 %		D-RA = 77.1 %
				D-SS = 85 %
				Counts/duration
				C/D-A=84.4 %
				C/D-SS = 78.6 %
				Amplitude
				A-SS = 97.7 %
Channel 2	**890 samples/feature**	**639 samples/feature**	**3052 samples/feature**	**810 samples/feature**
	Rise time	Rise time	Rise time	Rise time
	R-C = 66.2 %	R-RA = 100 %	R-RA = 100 %	R-RA = 100 %
	R-D = 77.4 %	Counts	Counts	Counts
	R-RA = 100 %	C-E = 91.7 %	C-E = 83.5 %	C-E = 81.3 %
	Counts	C-D = 90.4 %	C-D = 91.9 %	C-D = 81.9 %
	C-E = 83.3 %	C-A = 86.4 %	C-SS = 89.7 %	C-A = 83.4 %
	C-D = 93.9 %	C-SS = 91.9 %	Energy	C-SS = 81.5 %
	C-RA = 66.2 %	Energy	E-D = 65.7 %	Energy
	C-SS = 83.3 %	E-D = 94.8 %	E-SS = 62.3 %	E-D = 78.7 %
	Energy	E-A = 72.3 %	Duration	E-SS = 100 %
	E-D = 73.1 %	E-SS = 100 %	D-SS = 99.6 %	Duration
	E-SS = 100 %	Duration		D-SS = 78.8 %
	Duration	D-A = 68.7 %		
	D-RA = 77.4 %	D-SS = 94.9 %		
	D-SS = 73.1 %	Amplitude		
		A-SS = 72.6 %		

	15941 samples/feature	1643 samples/feature	5020 samples/feature	10909 samples/feature
Channel 3	Rise time R-C = 73.7 % R-E = 63.8 % R-D = 85.5 % R-RA = 100 % R-SS = 63.8 % Counts C-E = 97.1 % C-D = 94.2 % C-RA = 73.7 % C-SS = 97.1 % Energy E-D = 87.6 % E-RA = 63.8 % E-SS = 100 % Duration D-RA = 85.5 % D-SS = 87.6 % RA RA-SS = 63.8 %	Rise time R-D = 74.3 % R-RA = 100 % Counts C-E = 88.9 % C-D = 79.5 % C-A = 79.3 % C-SS = 89.2 % Energy E-D = 76.7 % E-A = 69.6 % E-SS = 99.9 % Duration D-RA = 74.3 % D-SS = 77.2 % Amplitude A-SS = 70.4 %	Rise time R-RA = 100 % Counts C-E = 85.2 % C-D = 73.9 % C-A = 88.2 % C-SS = 85.4 % Energy E-D = 87.2 % E-SS = 84.1 % Duration D-SS = 99.0 %	Rise time R-D = 71.9 % R-RA = 100 % Counts C-E = 75.1 % C-D = 69.2 % C-A = 87.9 % C-SS = 75.2 % Energy E-A = 63.1 % E-SS = 100 % Duration D-RA = 71.9 % Amplitude A-SS = 63.5 %

	27960 samples/feature	11794 samples/feature	19033 samples/feature	662 samples/feature
Channel 4	Rise time R-C = 73.9 % R-E = 64.1 % R-D = 82.8 % R-RA = 100 % R-SS = 64.1 % Counts C-E = 92.7 % C-D = 95.3 % C-RA = 73.9 % C-SS = 92.7 % Energy E-D = 83.2 % E-RA = 64.1 % E-SS = 100 % Duration D-RA = 82.8 % D-SS = 83.2 % RA RA-SS = 64.1 %	Rise time R-RA = 100 % Counts C-E = 84.3 % C-D = 62.8 % C-A = 86.6 % C-SS = 84.6 % Energy E-A = 70.1 % E-SS = 100 % Duration D-RA = 70.1 % Amplitude A-SS = 70.7 %	Rise time R-RA = 100 % Counts C-D = 92.7 % C-SS = 62 % Duration D-SS = 61 %	Rise time R-D = 65.7 % R-RA = 100 % Counts C-E = 73.8 % C-D = 91.2 % C-A = 92.7 % C-SS = 73.9 % Energy E-D = 70.8 % E-A = 65 % E-SS = 100 % Duration D-A = 85.6 % D-RA = 65.7 % D-SS = 71.1 % Amplitude A-SS = 65.3 %

| **Sum of correlation coefficients** | $\Sigma_i R_i = 1115.3$ %
$\Sigma_i C_i = 1626.6$ %
$\Sigma_i E_i = 1437.0$ % | $\Sigma_i R_i = 537.6$ %
$\Sigma_i C_i = 1388.3$ %
$\Sigma_i E_i = 1317.0$ %
$\Sigma_i D_i = 1347.2$ %
$\Sigma_i C/D_i = 0.0$ % | $\Sigma_i R_i = 400.0$ %
$\Sigma_i C_i = 1041.2$ %
$\Sigma_i E_i = 610.8$ % | $\Sigma_i R_i = 614.7$ %
$\Sigma_i C_i = 1761.5$ %
$\Sigma_i E_i = 1267.9$ % |

$\Sigma_i D_i = 1626.3$ %	$\Sigma_i A_i = 1095.3$ %	$\Sigma_i D_i = 1021.3$ %	$\Sigma_i D_i = 1470.6$ %
$\Sigma_i C/D_i = 0.0$ %	$\Sigma_i RA_i = 607.3$ %	$\Sigma_i C/D_i = 0.0$ %	$\Sigma_i C/D_i = 385.4$ %
$\Sigma_i A_i = 294.8$ %	$\Sigma_i SS_i = 1320.5$ %	$\Sigma_i A_i = 436.4$ %	$\Sigma_i A_i = 1076.2$ %
$\Sigma_i RA_i = 1115.3$ %		$\Sigma_i RA_i = 400.0$ %	$\Sigma_i RA_i = 614.7$ %
$\Sigma_i SS_i = 1437.1$ %		$\Sigma_i SS_i = 928.7$ %	$\Sigma_i SS_i = 1269.7$ %

Table 6.3

Feature selection strategy for AE source classification

Case No.	Number of features	Features to exclude
1	8/8	None
2	7/8	C
3	6/8	C, D
4	5/8	C, D, SS
5	4/8	C, D, SS, E
6	3/8	C, D, SS, E, A
7	2/8	C, D, SS, E, A, RA

6.5.2. Assessment of AE source classification performance

Classification of AE sources is conducted using the new decision trees method. The procedure is as follows:

- Hyperparameter optimization of all parameters is carried out using Bayes optimization method. Hyperparameters include minimum leaf size − minimum number of leaf node observations, maximum number of splits − maximum number of decision splits (or branch nodes), splitting criterion − either Gini's diversity index, twoing rule or deviance for reduction of maximum deviance (cross-entropy).
- Optimization runs are conducted 10 times due to the 10-fold cross validation used in this study. In each optimization run, 10 % of data is randomly taken from the whole set of data and the parameters of the classifier to classify this data are optimized. This is repeated 10 times, so that 100 % of data is taken into account.
- In each optimization run all hyperparameters are recorded. These results are shown in Table 6.4.
- The averaged hyperparameters are input into decision trees classification model and a classifier with optimum parameters is built. Cross validation (classification) and resubstitution errors are recorded.
- The confusion matrices for each of these cases are calculated and an average classification accuracy is computed considering an average values over all 16 classes.

As one can see in Table 6.4, minimum leaf size is 1 for all cases (the majority out of 10 runs), while the splitting criterion is either deviance or Gini's diversity index. The average number of maximum number of splits or branch nodes is quite high – reaching 46,222 in the case of only 2 AE features considered. The general trend of the maximum number of decision splits is to decrease initially and increase starting from case 4 (5/8 features). With only 2 features this parameter doubles with respect to the initial case.

Table 6.4

Optimized hyperparameters in a course of 10 runs for all cases of AE feature reduction
(MinLS – minimum leaf size, MaxNS – maximum number of splits, SC – split criterion)

Case	Run no.	1	2	3	4	5	6	7	8	9	10	Average
1	MinLS	1	1	1	2	1	1	1	1	2	1	1
	MaxNS	35321	7024	7133	2210	16137	98469	25431	5672	27137	3277	22781
	SC	gdi	dev	gdi	dev	gdi	gdi	dev	gdi	gdi	gdi	gdi
2	MinLS	1	2	1	1	2	2	1	2	1	1	1
	MaxNS	38855	2292	7058	2289	20226	40904	2393	33567	51830	21185	22060
	SC	dev	dev	dev	gdi	dev	dev	dev	dev	gdi	dev	dev
3	MinLS	1	1	1	1	1	1	2	1	1	1	1
	MaxNS	98266	6805	11720	13744	2306	2854	1213	2480	32206	8309	17990
	SC	dev	gdi	gdi	gdi	gdi	gdi	dev	gdi	gdi	gdi	gdi
4	MinLS	1	1	2	2	2	1	1	1	1	1	1
	MaxNS	5988	9552	16852	32479	40687	48495	27821	18780	2596	3790	20704
	SC	dev	dev	dev	dev	dev	dev	dev	dev	dev	dev	dev
5	MinLS	2	1	1	1	1	1	1	1	1	2	1
	MaxNS	60298	59990	44345	44106	25599	8158	16182	9267	45389	92843	40618
	SC	gdi	gdi	gdi	gdi	gdi	gdi	gdi	gdi	gdi	gdi	gdi
6	MinLS	1	1	1	1	1	1	1	1	1	1	1
	MaxNS	35499	5380	34457	29470	54274	5417	67809	38501	59706	14436	34495
	SC	gdi	gdi	gdi	gdi	gdi	gdi	gdi	gdi	gdi	gdi	gdi
7	MinLS	1	1	1	1	1	1	1	1	1	1	1
	MaxNS	28887	98385	5571	73221	44270	63493	30425	76524	34641	6802	46222
	SC	gdi	gdi	gdi	gdi	gdi	gdi	gdi	gdi	gdi	gdi	gdi

Confusion matrices for every case and different content of feature sets taken as an average over all 10 runs are shown in Fig. 6.20. The vast majority of values lie on the main diagonal (green tiles), indicating excellent classification performance, which is shown in percentage. Only a small fraction of misclassifications is present (orange tiles). A reliable separation of acoustic emission sources is achieved for all cases of AE feature reduction with a total of 16 classes to separate. The position with the largest proportion of misclassification is marked with a red circle. For the first 3 cases it is the 1st channel of the sleeper 2. For cases 4 and 5, it is the 1st channel of sleeper 3. For cases 6 and 7, it is the 1st channel of sleeper 4. For these last 2 cases, the classification accuracy drops to 50 %. There is no considerable difference in the bending configuration of sleepers in terms of AE source separation since these sources are separated equally well. Also, the same degree of AE source separation (classification) is achieved by reducing AE feature set, meaning that it is possible to reduce the redundancy of

data analysis of acoustic emission by conducting a mutual correlation analysis of AE features first. However, as one can see in Fig. 6.21, there is a slight drop in the average classification accuracy by about 10 % with only 2 features as opposed to 94.52 % for full feature set. A surprising fact is that the efficiency of class separation increases by reducing feature set. By reducing 2 features, the classification accuracy increases by 2.06 %. Note that the classification and resubstitution errors increase with reduction of features, although even with the most extreme reduction these values are acceptable (5.35 % for classification error and 2.52 % for resubstitution error).

The detection rate and false alarm rate (TP_r and FP_r, respectively) are calculated as

$$TP_r = 100\ \% \times \frac{TP}{TP + FP} \tag{6.2}$$

$$FP_r = 100\ \% \times \frac{FP}{TN + FP} \tag{6.3}$$

These values are calculated for all of the feature sets and shown in Table 6.5. Although the largest detection rate value is obtained by removing just one feature, acceptable (over 93 %) detection rate is achieved by attaining just 2 features with less than 0.2 % of false alarm rate.

True Class	Sl1/ch1	Sl1/ch2	Sl1/ch3	Sl1/ch4	Sl2/ch1	Sl2/ch2	Sl2/ch3	Sl2/ch4	Sl3/ch1	Sl3/ch2	Sl3/ch3	Sl3/ch4	Sl4/ch1	Sl4/ch2	Sl4/ch3	Sl4/ch
Sl1/ch1	82 (86.3 %)	1	1	1	0	1	0	0	1	0	0	0	0	2	3	3
Sl1/ch2	1	866 (97.3 %)	1	4	0	2	0	1	0	2	1	1	0	4	7	0
Sl1/ch3	0	4	15881 (99.6 %)	32	0	0	3	7	0	0	0	3	0	0	10	1
Sl1/ch4	1	3	44	27897 (99.8 %)	0	4	0	4	0	0	0	2	0	0	3	2
Sl2/ch1	3	2	2	0	70 (77.8 %)	4	1	1	0	0	0	0	0	0	1	6
Sl2/ch2	0	2	3	1	5	594 (93 %)	3	5	1	1	0	0	0	5	10	9
Sl2/ch3	0	2	2	3	0	9	1566 (95.3 %)	39	0	0	0	1	0	0	21	0
Sl2/ch4	1	3	10	5	1	10	17	11692 (99.1 %)	0	0	1	0	0	1	53	0
Sl3/ch1	0	0	1	1	0	2	0	0	56 (91.8 %)	0	0	0	0	0	0	1
Sl3/ch2	0	0	0	0	0	1	2	0	0	3031 (99.3 %)	4	9	0	3	2	0
Sl3/ch3	0	1	0	1	0	1	4	2	0	15	4989 (99.4 %)	1	0	2	4	0
Sl3/ch4	0	3	2	1	0	0	0	2	0	15	4	19006 (99.9 %)	0	0	0	0
Sl4/ch1	0	0	0	0	0	0	0	0	0	0	1	0	9 (90 %)	0	0	0
Sl4/ch2	0	8	6	2	0	11	3	8	0	1	2	0	0	737 (91 %)	25	7
Sl4/ch3	1	7	5	7	2	13	18	46	0	1	4	0	0	1	10796 (99 %)	8
Sl4/ch4	4	2	0	2	4	7	3	3	0	2	1	0	0	9	5	620 (93.7 %)

Predicted Class

(a)

(b)

True Class \ Predicted Class	Sl1/ch1	Sl1/ch2	Sl1/ch3	Sl1/ch4	Sl2/ch1	Sl2/ch2	Sl2/ch3	Sl2/ch4	Sl3/ch1	Sl3/ch2	Sl3/ch3	Sl3/ch4	Sl4/ch1	Sl4/ch2	Sl4/ch3	Sl4/ch4
Sl1/ch1	85 (89.5 %)	3	0	1	0	0	0	1	0	0	0	0	0	1	2	2
Sl1/ch2	0	870 (97.8 %)	0	12	0	1	0	0	0	0	0	0	0	2	3	2
Sl1/ch3	0	0	15897 (99.7 %)	23	0	0	1	11	0	0	0	0	0	3	6	0
Sl1/ch4	0	12	58	27867 (99.7 %)	4	1	0	5	0	0	3	0	0	3	7	0
Sl2/ch1	0	1	1	0	78 (86.7 %)	1	0	3	0	0	0	0	0	0	1	5
Sl2/ch2	0	4	2	4	0	594 (93.0 %)	5	14	0	0	1	0	0	5	10	0
Sl2/ch3	0	2	9	1	0	4	1572 (95.7 %)	34	0	0	0	0	0	2	18	1
Sl2/ch4	0	1	14	1	1	5	19	11704 (99.2 %)	0	0	2	0	0	5	42	0
Sl3/ch1	0	1	0	0	1	0	0	0	59 (96.7 %)	0	0	0	0	0	0	0
Sl3/ch2	0	0	0	0	0	0	0	0	0	3042 (99.7 %)	6	4	0	0	0	0
Sl3/ch3	0	0	0	0	0	1	1	2	0	3	5007 (99.7 %)	3	2	1	0	0
Sl3/ch4	0	0	1	4	0	0	0	2	0	2	0	19024 (99.95 %)	0	0	0	0
Sl4/ch1	0	0	0	0	0	0	0	0	0	0	0	0	9 (90.0 %)	0	0	1
Sl4/ch2	0	1	2	1	1	7	5	5	0	0	0	0	0	773 (95.4 %)	13	2
Sl4/ch3	0	2	13	5	1	3	17	73	0	0	0	0	0	5	10779 (98.8 %)	11
Sl4/ch4	0	6	0	0	1	3	0	2	0	0	0	0	0	8	6	636 (96.1 %)

Predicted Class

(b)

(c)

True Class \ Predicted Class	Sl1/ch1	Sl1/ch2	Sl1/ch3	Sl1/ch4	Sl2/ch1	Sl2/ch2	Sl2/ch3	Sl2/ch4	Sl3/ch1	Sl3/ch2	Sl3/ch3	Sl3/ch4	Sl4/ch1	Sl4/ch2	Sl4/ch3	Sl4/ch4
Sl1/ch1	85 (89.5 %)	0	3	0	0	3	0	1	0	0	0	0	0	1	0	2
Sl1/ch2	1	853 (95.8 %)	3	15	0	0	3	0	0	0	2	0	0	5	2	6
Sl1/ch3	0	0	15863 (99.5 %)	47	0	0	0	12	0	0	0	0	0	6	11	2
Sl1/ch4	0	6	58	27880 (99.7 %)	4	2	0	3	0	0	1	0	0	3	2	1
Sl2/ch1	0	0	1	0	80 (88.9 %)	3	0	3	0	0	0	0	0	0	3	0
Sl2/ch2	0	2	1	1	1	592 (92.6 %)	5	2	0	0	0	3	0	11	11	10
Sl2/ch3	0	0	4	1	1	5	1597 (97.2 %)	17	0	0	0	0	0	1	16	1
Sl2/ch4	1	2	9	6	0	3	14	11730 (99.5 %)	0	0	0	0	0	1	28	0
Sl3/ch1	0	0	0	0	1	0	0	1	59 (96.7 %)	0	0	0	0	0	0	0
Sl3/ch2	0	0	0	0	0	0	0	0	0	3043 (99.7 %)	5	4	0	0	0	0
Sl3/ch3	0	0	0	1	0	0	2	0	0	3	5009 (99.8 %)	2	2	0	1	0
Sl3/ch4	0	0	1	0	0	0	0	0	0	2	0	19030 (99.98 %)	0	0	0	0
Sl4/ch1	0	0	0	0	0	0	0	0	0	0	0	0	10 (100 %)	0	0	0
Sl4/ch2	0	1	10	4	0	10	2	4	0	0	1	1	0	763 (94.2 %)	8	6
Sl4/ch3	0	1	8	9	0	6	5	44	0	0	3	2	0	6	10819 (99.2 %)	6
Sl4/ch4	1	3	3	0	0	16	2	8	0	0	0	0	0	6	8	615 (92.9 %)

Predicted Class

(c)

144

(d)

True Class \ Predicted Class	Sl1/ch1	Sl1/ch2	Sl1/ch3	Sl1/ch4	Sl2/ch1	Sl2/ch2	Sl2/ch3	Sl2/ch4	Sl3/ch1	Sl3/ch2	Sl3/ch3	Sl3/ch4	Sl4/ch1	Sl4/ch2	Sl4/ch3	Sl4/ch4
Sl1/ch1	89 (93.7 %)	1	1	1	0	0	0	0	0	3	0	0	0	0	0	0
Sl1/ch2	1	855 (96.1 %)	4	22	0	0	0	0	0	2	1	4	0	1	0	0
Sl1/ch3	0	0	15840 (99.4 %)	69	0	0	1	9	0	4	2	10	0	0	6	0
Sl1/ch4	0	6	56	27878 (99.7 %)	0	1	0	5	0	4	2	4	0	0	0	4
Sl2/ch1	0	0	0	0	76 (84.4 %)	4	0	3	0	2	2	1	0	0	1	1
Sl2/ch2	0	2	1	0	0	604 (94.5 %)	2	2	0	1	7	10	0	1	9	0
Sl2/ch3	0	0	1	1	1	7	1584 (96.4 %)	22	0	3	0	10	0	0	14	0
Sl2/ch4	0	0	5	4	0	2	13	11686 (99.1 %)	0	2	6	34	0	0	42	0
Sl3/ch1	0	2	1	0	3	0	0	2	42 (68.9 %)	1	3	0	0	0	7	0
Sl3/ch2	1	1	6	6	0	10	3	11	0	2913 (95.4 %)	34	39	0	7	16	5
Sl3/ch3	2	2	6	6	0	0	13	14	0	21	4894 (97.5 %)	52	2	1	5	2
Sl3/ch4	1	0	22	9	0	4	18	41	1	14	34	18856 (99.1 %)	0	2	28	3
Sl4/ch1	0	0	0	0	0	0	0	0	0	0	0	0	10 (100 %)	0	0	0
Sl4/ch2	0	3	1	6	0	10	1	4	0	9	0	11	0	762 (94.1 %)	3	0
Sl4/ch3	0	0	8	8	0	3	8	44	0	12	12	52	0	0	10760 (98.6 %)	2
Sl4/ch4	0	4	5	3	1	4	2	1	0	12	6	17	0	3	8	596 (90.0 %)

Predicted Class

(d)

(e)

True Class \ Predicted Class	Sl1/ch1	Sl1/ch2	Sl1/ch3	Sl1/ch4	Sl2/ch1	Sl2/ch2	Sl2/ch3	Sl2/ch4	Sl3/ch1	Sl3/ch2	Sl3/ch3	Sl3/ch4	Sl4/ch1	Sl4/ch2	Sl4/ch3	Sl4/ch4
Sl1/ch1	65 (68.4 %)	5	2	2	1	6	1	1	0	1	0	1	0	1	3	6
Sl1/ch2	2	783 (88.0 %)	11	41	1	10	6	3	0	2	3	3	0	3	9	13
Sl1/ch3	3	13	15700 (98.5 %)	168	0	1	4	18	0	0	3	8	0	3	14	6
Sl1/ch4	2	13	115	27709 (99.1 %)	0	4	22	19	0	6	9	19	0	10	19	13
Sl2/ch1	2	4	2	5	60 (66.7 %)	2	1	0	0	1	2	2	0	1	1	7
Sl2/ch2	1	8	5	15	1	570 (89.2 %)	1	5	0	9	1	1	0	12	5	5
Sl2/ch3	0	8	10	16	0	2	1552 (94.5 %)	9	0	5	6	5	0	7	20	3
Sl2/ch4	1	2	24	37	0	3	1	11670 (98.9 %)	0	1	3	14	0	2	35	1
Sl3/ch1	0	4	0	4	1	12	1	1	30 (49.2 %)	0	0	0	0	4	0	4
Sl3/ch2	1	5	2	8	0	3	9	7	0	2993 (98.1 %)	6	8	0	3	5	2
Sl3/ch3	0	5	9	4	0	0	3	1	0	3	4986 (99.3 %)	5	0	2	2	0
Sl3/ch4	0	0	39	40	0	1	1	11	0	4	7	18925 (99.4 %)	0	3	2	0
Sl4/ch1	0	1	1	1	1	0	1	0	0	0	0	0	5 (50.0 %)	0	0	0
Sl4/ch2	3	19	12	18	3	7	17	14	1	8	7	3	0	682 (84.2 %)	15	1
Sl4/ch3	1	1	29	35	4	0	4	62	0	9	3	9	0	5	10747 (98.5 %)	0
Sl4/ch4	0	10	7	18	0	14	8	5	3	7	3	3	0	4	7	573 (86.6 %)

Predicted Class

(e)

(f)

True Class \ Predicted Class	Sl1/ch1	Sl1/ch2	Sl1/ch3	Sl1/ch4	Sl2/ch1	Sl2/ch2	Sl2/ch3	Sl2/ch4	Sl3/ch1	Sl3/ch2	Sl3/ch3	Sl3/ch4	Sl4/ch1	Sl4/ch2	Sl4/ch3	Sl4/ch
Sl1/ch1	53 (55.8 %)	4	3	5	0	3	2	6	0	2	1	0	0	0	8	8
Sl1/ch2	2	750 (84.3 %)	20	73	0	6	11	6	0	1	2	2	0	3	4	10
Sl1/ch3	1	15	15514 (97.3 %)	248	0	3	12	43	0	9	2	45	0	4	35	10
Sl1/ch4	2	18	242	27488 (98.3 %)	3	5	25	38	0	15	5	37	0	12	51	19
Sl2/ch1	2	2	2	6	62 (68.9 %)	2	1	2	0	1	1	1	0	2	3	3
Sl2/ch2	0	1	19	27	1	562 (87.9 %)	1	10	0	1	0	2	0	2	8	5
Sl2/ch3	1	3	36	44	1	3	1494 (90.9 %)	24	0	1	1	7	0	0	28	0
Sl2/ch4	1	1	60	80	0	4	16	11523 (97.7 %)	0	10	3	30	0	0	60	6
Sl3/ch1	0	5	1	3	0	5	1	4	31 (50.8 %)	0	2	0	0	0	5	4
Sl3/ch2	0	3	18	14	3	0	1	10	0	2945 (96.5 %)	16	39	0	0	3	0
Sl3/ch3	0	1	6	6	3	0	1	6	0	12	4955 (98.7 %)	28	0	0	2	0
Sl3/ch4	0	1	36	27	0	0	1	15	0	15	12	18913 (99.4 %)	0	0	13	0
Sl4/ch1	0	1	1	1	0	1	0	0	0	0	0	0	5 (50.0 %)	0	1	0
Sl4/ch2	2	5	13	33	1	3	8	8	0	3	0	3	0	714 (88.1 %)	15	2
Sl4/ch3	4	2	58	84	2	6	12	77	0	16	8	25	0	1	10610 (97.3 %)	4
Sl4/ch4	0	8	20	30	0	13	4	15	2	7	6	9	0	6	33	509 (76.9 %)

(g)

True Class \ Predicted Class	Sl1/ch1	Sl1/ch2	Sl1/ch3	Sl1/ch4	Sl2/ch1	Sl2/ch2	Sl2/ch3	Sl2/ch4	Sl3/ch1	Sl3/ch2	Sl3/ch3	Sl3/ch4	Sl4/ch1	Sl4/ch2	Sl4/ch3	Sl4/ch
Sl1/ch1	53 (55.8 %)	4	3	5	0	3	2	6	0	2	1	0	0	0	8	8
Sl1/ch2	2	749 (84.2 %)	20	74	0	6	11	6	0	1	2	2	0	3	4	10
Sl1/ch3	1	15	15514 (97.3 %)	248	0	3	12	43	0	9	2	45	0	4	35	10
Sl1/ch4	2	18	242	27488 (98.3 %)	3	5	25	38	0	15	5	37	0	12	51	19
Sl2/ch1	2	2	2	6	62 (68.9 %)	2	1	2	0	1	1	1	0	2	3	3
Sl2/ch2	0	1	19	27	1	562 (87.9 %)	1	10	0	1	0	2	0	2	8	5
Sl2/ch3	1	3	36	44	1	3	1494 (90.9 %)	24	0	1	1	7	0	0	28	0
Sl2/ch4	1	1	60	80	0	4	16	11523 (97.7 %)	0	10	3	30	0	0	60	6
Sl3/ch1	0	5	1	3	0	5	1	4	31 (50.8 %)	0	2	0	0	0	5	4
Sl3/ch2	0	3	18	14	3	0	1	10	0	2945 (96.5 %)	16	39	0	0	3	0
Sl3/ch3	0	2	6	7	3	0	1	6	0	12	4953 (98.5 %)	28	0	0	2	0
Sl3/ch4	0	1	36	27	0	0	1	15	0	15	12	18913 (99.4 %)	0	0	13	0
Sl4/ch1	0	1	1	1	0	1	0	0	0	0	0	0	5 (50.0 %)	0	1	0
Sl4/ch2	2	5	13	33	1	3	8	8	0	3	0	3	0	714 (88.1 %)	15	2
Sl4/ch3	4	2	58	84	2	6	12	77	0	16	8	25	0	1	10610 (97.3 %)	4
Sl4/ch4	0	8	20	30	0	13	4	15	2	7	6	9	0	6	33	509 (76.9 %)

Fig. 6.20. Confusion matrices of acoustic emission features for all sleepers combined: (*a*) Case 1 with feature set (8/8); (*b*) Case 2 with feature set (7/8); (*c*) Case 3 with feature set (6/8); (*d*) Case 4 with feature set (5/8); (*e*) Case 5 with feature set (4/8); (*f*) Case 6 with feature set (3/8); (*g*) Case 7 with feature set (2/8).

Table 6.5

Detection rate and false alarm rate for different sizes of acoustic emission feature sets

Class	Feature 8/8		Feature 7/8		Feature 6/8		Feature 5/8		Feature 4/8		Feature 3/8		Feature 2/8	
	FP_r	TP_r	FP_r	TP_r	FP_r	TP_r	FP_r	TP_r	FP_r	TP_r	FP_r	TP_r	FP_r	TP_r
Sl1/ch1	0.01	88.17	0	100	0	96.59	0.01	94.68	0.02	80.25	0.02	77.94	0.02	77.94
Sl1/ch2	0.04	95.80	0.03	96.35	0.02	98.27	0.02	97.60	0.10	88.88	0.07	91.46	0.07	91.34
Sl1/ch3	0.09	99.52	0.12	99.37	0.12	99.37	0.14	99.27	0.33	98.32	0.65	96.67	0.65	96.67
Sl1/ch4	0.09	99.79	0.07	99.81	0.12	99.70	0.19	99.52	0.59	98.53	0.97	97.58	0.97	97.58
Sl2/ch1	0.01	85.37	0.01	89.66	0.01	91.95	0.01	93.83	0.01	83.33	0.01	81.58	0.01	81.58
Sl2/ch2	0.07	90.14	0.03	95.81	0.05	92.50	0.05	93.07	0.07	89.76	0.06	91.23	0.06	91.23
Sl2/ch3	0.06	96.67	0.05	97.04	0.03	97.98	0.06	96.29	0.08	95.10	0.10	93.96	0.10	93.96
Sl2/ch4	0.14	99	0.18	98.72	0.11	99.20	0.18	98.67	0.18	98.68	0.31	97.76	0.31	97.76
Sl3/ch1	0	96.55	0	100	0	100	0	97.67	0	88.24	0	93.94	0	93.94
Sl3/ch2	0.04	98.79	0.01	99.84	0.01	99.84	0.09	97.00	0.06	98.16	0.10	96.94	0.10	96.94
Sl3/ch3	0.02	99.64	0.01	99.76	0.01	99.76	0.12	97.82	0.06	98.95	0.06	98.82	0.06	98.82
Sl3/ch4	0.02	99.91	0.01	99.96	0.02	99.94	0.31	98.72	0.10	99.57	0.29	98.81	0.29	98.81
Sl4/ch1	0	100	0	81.82	0	83.33	0	83.33	0	100	0	100	0	100
Sl4/ch2	0.03	96.47	0.04	95.67	0.04	95.02	0.02	98.07	0.06	91.91	0.03	95.97	0.03	95.97
Sl4/ch3	0.16	98.68	0.12	99.01	0.10	99.17	0.16	98.72	0.16	98.74	0.31	97.53	0.31	97.53
Sl4/ch4	0.04	94.37	0.02	96.36	0.03	94.76	0.02	97.23	0.06	90.38	0.07	87.76	0.07	87.76
Mean	**0.05**	**96.18**	**0.04**	**96.82**	**0.04**	**96.71**	**0.09**	**96.34**	**0.12**	**93.68**	**0.19**	**93.62**	**0.19**	**93.61**

The largest average classification accuracy is obtained by removing 2 features and attaining 6 as shown in Fig. 6.21 (*a*). This is in close agreement with findings from detection rate data as values of performance metrics of excluding 1 and 2 features are close. A drop of around 12 % of average classification accuracy and just 3 % of detection rate is a penalty of excluding as many as 6 AE features.

The number of AE features obviously has an influence on data size that has to be processed and analysed. The aforementioned decrease in classification performance in compensated by a compression of data to be processed. By decreasing the number of AE features by one in each increment, the data size decreases linearly as shown in Fig. 6.21 (*b*). It is found that the average slope of data reduction is roughly 1.9 MB per AE feature, which has been removed from the classification model. It can thus be concluded that, by considering only a bare minimum of AE features (two, to be exact), the average classification accuracy decreases only by about 10 %, while the size of the data to be analysed decreases by about 70 %. This insight can form a strategy for placing AE sensors at the switches and crossings where it is difficult to locate the damage.
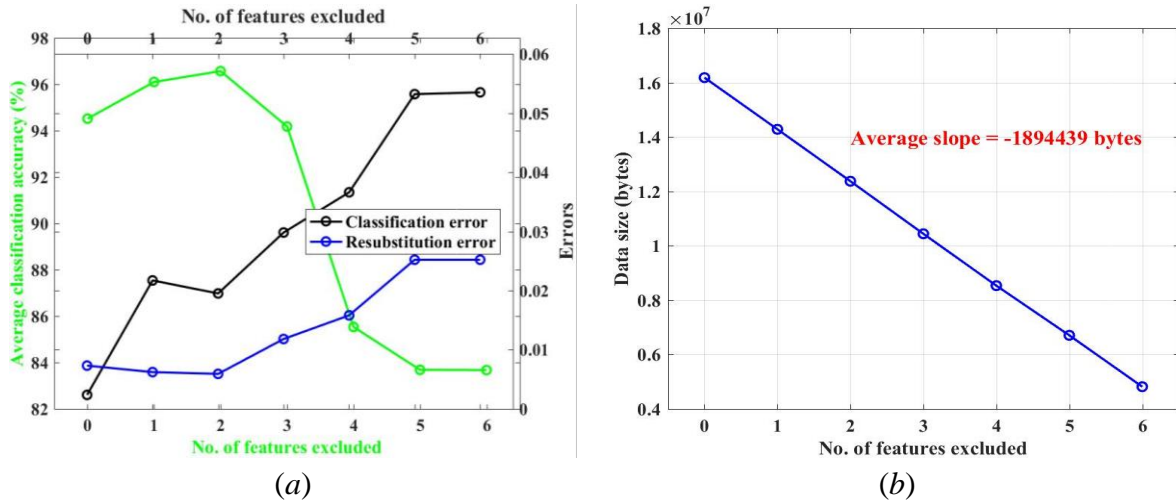
Fig. 6.21. Influence of the number of features on: (*a*) average classification accuracy and errors of a novel decision tree classifier with optimized hyperparameters; (*b*) the size of the analysed AE data.

6.6. Linear modeling of peak frequency shifts

The results of linear fitting of peak frequency values vs distance from the main source of acoustic emissions are presented in Fig. 6.23. A common least-squares fitting procedure is adopted. As one can see, the relationship is nearly linear. *MAD* value from Eq. (2.16) is shown (depicted by s), representing deviations from median value. Large deviations are present, in particular, for sleeper no. 4. This is due to the fact that, surprisingly, the highest density of acoustic emissions is registered not at mid-span, but at channel no. 3 instead (see Table 6.1). As for sleeper no. 3, one outlier point is detected – for channel no. 1 (Fig. 6.23 (*a*)) and channel no. 4 (Fig. 6.23 (*b*)). One also sees that both methods display somehow contradictory results in terms of increasing or decreasing shift with increasing distance. On Fig. 6.23 (*a*) the trend is increasing for sleepers no. 2 and 4, while it is decreasing for sleepers no. 1 and 3. On Fig. 6.23 (*b*) the results are opposite. This insight informs that predicted modes of failure should be consistent to the placement of sensors. It is clear that the results conform exceptionally well for the sleepers failing in bending and mixed bending shear modes. In contrast, the acoustic emission intensity will be directed to the nearest sensors as clearly evident in the cases of sleepers failing in brittle or pure shear modes.

148
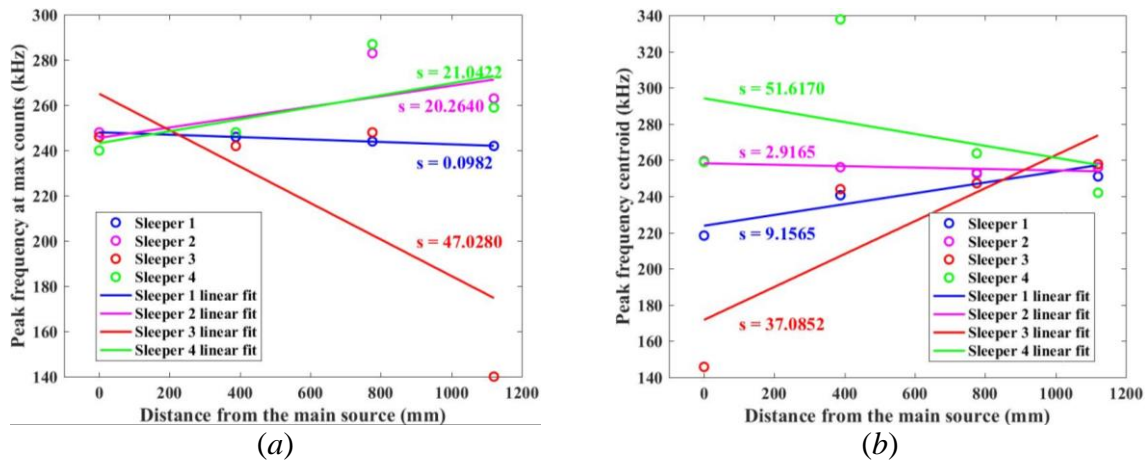
Fig. 6.23. Linear fits of relationship between peak frequency and distance from the main source of emissions at mid-span: (*a*) peak frequency corresponding to maximum counts; (*b*) centroid value of peak frequency.

The intercept and slope terms of a linear model fit from Fig. 6.23 are shown in Table 6.6. The sign of slopes is opposite using both methods. The intercept values do not differ significantly, except for sleepers no. 3 and 4. In general, it can be estimated that the trends are linear; however, relatively large outliers are present in most cases. Also, there is no consistency between both shift assessment methods in terms of increasing or decreasing relationship between peak frequencies and distance from the main emission source. The most reliable fit is obtained for sleeper no. 1 by considering peak frequencies at maximum number of counts. The trend is for peak frequencies to decrease slightly with increasing distance from the largest emission bursts.

One of the most important factors influencing the proposed methodology monitoring the crack propagation in railway sleepers is boundary conditions. The experiments were conducted in simply supported conditions adjusted for three-point bending tests. Of course, in a real railway track sleepers are embedded in a ballast bed which is free support condition. In this case, the distribution of mechanical stresses is also different influencing the formation of defects (cracks). However, most cracking in railway concrete sleepers occur at mid-span [29] anyway which is in accordance with our experimental results. Another factor influencing the results is maintenance of a railway track. If the AE system is to be set in a real railway track, AE sensors will record the AE signal coming from sleepers subjected to dynamic loading of the passing trains. A practical solution for real in situ applications is to employ wireless sensors which are already commercially available [216]. In this case, the complicated wiring issue and parasitic inductance stemming from the excessive wiring is avoided. Thus, monitoring of the crack propagation using the proposed method can be achieved. Nevertheless, if the railway track is not maintained properly, degradation of sleepers can occur due to environmental conditions (temperature changes, moisture, etc.) and make an undesirable impact on the monitoring results.

Table 6.6

Coefficients of linear fitting model

Shift assessment method	Sleeper 1		Sleeper 2		Sleeper 3		Sleeper 4	
	Slope	Intercept	Slope	Intercept	Slope	Intercept	Slope	Intercept
max counts	-0.0053	248	0.023	246	-0.081	265	0.024	243
centroid	0.030	224	-0.0039	258	0.091	172	-0.033	294

Based on the novel and different approach for classifying failure modes, this study shows that acoustic emission sources with different intensities and locations can be separated from one another or distinguished thus helping to pinpoint the most critical locations on the sleepers experiencing various loading conditions during their service life. These self-monitoring systems could distinguish between acoustic emission sources with different sets of signatures and intensities, hence enabling to pinpoint the most critical locations on the structure.

In an attempt to evaluate and analyse the changes of peak frequency of acoustic emission events in railway pre-stressed concrete sleepers subjected to static flexural loads a wide variety of peak frequency values is registered with over 5 million data points. The range is consistently within [101-998] kHz. However, not all af these peak frequencies are due to formation of cracks, crack propagation and failure – a fair proportion is due to noise. In this study, it is proposed to apply a modified filtering to filter out insignificant peak frequencies – those having low number of emission counts. A modified universal threshold technigue is established for filtering. All peak frequencies with corresponding counts lower than the threshold are rejected. Hence, most data can be rejected and the most important information pertinent to structural health of railway concrete sleepers still maintained. The new findings show that the modified universal treshold is suitable for monitoring structural integrity of railway sleepers. This is because general track inspections cannot precisely identify modes of failure and the use of modified threshold can be more adaptive to the actual modes of failure of the sleepers in the field.

The study also attempts to establish a linear relationship between maximum value of retained peak frequencies and distance from the main source of acoustic emissions, which happens to be at or adjacent to mid-span for almost all sleeper cases. Centroid of retained peak frequency ditributions is calculated to evaluate the location of largest proportion of counts in terms of peak frequency. This value is calculated for all four acoustic emission channels for every sleeper. A linear regression model is built where maximum values of retained peak frequencies and peak frequency centroids versus distance from mid-span are fitted to linear function. The results reasonably suggest that the relationship is fairly linear, however, strong outliers are present in some cases contributing to significant deviations from linearity. Perhaps, this scatter could be decreased by considering more sleeper specimens. Even though the variability of material properties of the sleepers does not exceed 3 %, the statistical confidence would benefit from increased sample size. This was, however, not done due to the nature of of specimens themselves (mass and size), as well as imposed limitations on sleeper shipment. Fitted linear models using both methods (maximum of retained peak frequency and peak

frequency centroid) do not match in terms of slopes – one method displays increasing trend, while the other shows decreasing relationship. This implies that the mode of failure in each case is different. Then, the best fit in terms of the smallest deviation from linearity can be achieved using maximum of retained peak frequency towards the nearest sensor.

CONCLUSIONS

This thesis deals with development of structural damage localization algorithms comprising of two parts. The first part describes algorithms based on mode shape transformation methods, namely continuous wavelet transform (CWT), mode shape curvature square magnitude (MSCS) and another method developed in the framework of this thesis. This method is based on normalized wavelet scalogram involving computation of variance with respect to scale parameter and summing the results for all wavelet functions considered in this work. Hence, the selection of two appropriate parameters (scale and wavelet function) is avoided in this method. These methods are designed for structural elements, such as beams and plates. Mode shapes of the damaged structures (aluminium beams with mill cut damage and carbon fibre reinforced plastic beam with an impact damage and aluminium plate with a mill cut damage) are experimentally measured with non-contact scanning laser vibrometer and numerically simulated using commercial finite element program $Ansys^{TM}$. These mode shapes are post-processed in $Matlab^{TM}$ environment with the aforementioned methods to reveal the location of damage. Also, a parametric study is conducted involving different noise levels ranging from 0 % to 4 % and sensor densities where original mode shape signal is divided by integer values from 1 to 6. The following conclusions can be drawn:

- All three methods are capable of localizing damage in all cases (mill-cut damage in aluminium beams with one and two sites of damage, impact damage in carbon fibre reinforced plastic composite beam and aluminium plate with a mill-cut damage) with varying estimate reliability. Moreover, mode shape information on damaged structures is sufficient – no baseline data of healthy structures is needed.

- The CWT is a promising method for structural damage detection and localization based on mode shape information. However, this is not a straightforward procedure as it involves selection of the appropriate wavelet function and scale parameter. Also, there is an issue on sensitivity to damage size as this thesis deals with a relatively appreciable reduction of stiffness due to damage, although a more rigorous treatment of this problem was not within a scope of this thesis.

- The MSCS method is an effective damage localization tool and, in it's nature, simpler than the wavelet transform involving fewer adjustable parameters. This thesis offers an approach to obtain mode shapes of healthy structures using exclusively mode shapes with structural damage. The mode shapes with damage information are subjected to the polynomial smoothing technique for plate structures and smoothing based on harmonic Fourier approximation functions. Compared to CWT, MSCS offers better overall performance, although it is more susceptible to noise.

- The performance of the methods is enhanced through the application of statistical hypothesis testing. Non-significant damage indices are filtered out thus highlighting the locations of the most significant damage index peaks which lie in the zone of damage.

- The performance of the methods is assessed through the parameter called damage estimate reliability (DER) expressed in percent. As expected, this performance deteriorates with decreasing sensor density. However, the best performance is not

achieved at the original mode shape signal length – in most cases fewer data points yield better performance and this case is more robust to noise.

- According to results of simulations on varying depths of damage for aluminium beam with one damage site, the proposed methods are a reliable tool for damage localization even in the case of relatively shallow damage (relative flexural stiffness reduction below 1 %), except for TVNWS which shows instability of performance with increasing damage depth and varying sensor density.

- A notable limitation to the proposed algorithms is the issue of edge effect – significant damage index values at edges of structures where, in fact, damage is not introduced. This is the case for experimental studies only with reason lying in the discontinuity of mode shapes at the edges of the structures. The possible remedy to this problem is application of padding methods that artificially extend the mode shape signal. For example, zero padding where zeros are added at the ends of mode shape signal. This issue, however was not addressed in the thesis.

The second part of the thesis explores the plausibility of acoustic emission source separation in full-scale pre-stressed railway concrete sleepers involving acoustic emission interrogation technique coupled with a classification framework. An effective Condition Monitoring method in two-dimensional structural elements is developed. The method is supplemented for damage localization by utilizing multiclass classification approach. These structural elements could be, for example, wind turbine blades or aircraft wings – parts that must undergo regular structural inspections. The method is demonstrated on a cantilevered carbon composite plate with a pseudo-defect (added mass). Added mass locally modifies the mass of the structure, thus providing local structural changes necessary for defect localization.

Four sleepers were tested – two sleepers to failure and two sleepers were subjected to two-phased loading (till the first crack and till 1.5 load of the first crack load). Static three-point bending tests of the concrete sleepers were carried out and acoustic emission signals were recorded with four sensors. The classic load/deflection curves are overlaid with acoustic emission signature to correlate the events of cracking. The classification scheme involving decision trees with optimized hyperparameters is adopted to separate the largest concentrations of acoustic emission sources and characterize peak frequency shifting from largest to smallest concentrations of cracking. Within the scope of existing research into this field, this study realises the potential of self-monitoring systems, providing a positive case for their implementation on track structures, such as pre-stressed concrete sleepers and bearers in remote locations such as switches and crossings, railway bridges, and transition zones. This insight will significantly help the development of an acoustic emisison sensor system that can accurately inform mode of failure and fragility tensors. It will revolutionise the SHM system of railway networks, particularly at discreet and remote locations such as swithes and crossings. The following conclusions are made:

- The acoustic emission sensing technology is effective in the detection of initial crack events. The energy jump induced by these cracks correlate well with other variable parameters.

- The data obtained through AE confirms the behaviour of concrete sleepers under flexural bending. The deflection curve provides a simple method of real-time damage detection, because vertical displacement recordings can identify changes in structural integrity. The most prominent cracking occurs at the mid-span, which is verified by the largest proportion of released acoustic energy. In general, the fraction of emitted acoustic energy decreases with increasing distance from mid-span. This fact is clearly observed for sleepers loaded till failure, while this trend is not completely true for sleepers loaded till 1.5 times the load of the first crack. The concentration of cracks and hence acoustic emission events greatly increases in the moment of fracture, which is why an overwhelmingly larger proportion of emitted acoustic energy corresponds to mid-span compared to other emission sources located farther.

- The acoustic emission sources, each with their unique set of emission signatures have been studied in terms of various emission parameters and their mutual correlations. Parameters experiencing the largest correlations have been incrementally removed from further analysis, resulting in several case studies.

- The acoustic emission sources have been separated to highlight their uniqueness with respect to one another. This unique and novel procedure is useful to assess the contribution of emission intensity from each source and to eventually detect the most critical ones. The source separation is based on a new classification method employing the novel decision trees classifier with optimized hyperparameters. A total of 16 classes comprising of four sleepers with four acoustic emission channels per sleeper have been separated from each other.

- It is shown that reduction of number of acoustic emission features from eight to two has a minor impact on acoustic emission source classification accuracy - the drop is only about 10 %, while the size of the data to be processed decreases by 70 %.

- In the cases for all four concrete sleepers, the recorded evolution of peak frequencies with increased loading suggests that most of the peak frequency values cluster around three bands with the following average values over all sleepers: [150-300] kHz, [300-460] kHz and [500-800] kHz.

- A modified universal threshold technique is established for filtering the peak frequencies due to noise. The filtering results suggest that it is possible to retain 14 % to 34 % of initially recorded peak frequencies, while retaining count information to the extent of 53 % to 98 % of the initial number of counts.

- Contrary to the most cases, the classification performance to localize the pseudo-defect on a carbon fibre reinforced plastic plate is better considering less points per class (2 versus 9).

- Although both classifiers could not reliably manage the more difficult cases with points belonging to several zones simultaneously in the experimental validation phase, the linear discriminant still yields higher prediction probabilities associated with the correct predictions for the simpler cases (points lying in one zone only) than *k*-nearest neighbors.

- By exploring the classifier performance based on strain responses obtained at different resonant frequencies, the first fundamental frequency in bending yields lower classification and resubstitution losses.
- A catalogue of all possible damage locations and severities can be built by conducting extensive finite element modelling campaign. The sensor readings obtained from a real damaged structure can be correlated with the data from this catalogue to deduce the case of damage in question.

APPROBATION OF THE THESIS

Book chapter

1) **R. Janeliukstis**, S. Rucevskis, M. A. Sumbatyan, A. Chate. Localization of Impact Damage in Thin-Walled Composite Structure Using Variance-Based Continuous Wavelet Transform In book: *Non-destructive Testing and Repair of Pipelines*, Chapter 2.5 (Editors - Evgeny N. Barkanov, Andrei Dumitrescu, Ivan A. Parinov), 2017, p. 73-89, Springer, DOI: 10.1007/978-3-319-56579-8_6. **WEB OF SCIENCE**

Journal papers

1) **R. Janeliukstis**, A. Clark, M. Papaelias, S. Kaewunruen. Flexural cracking-induced acoustic emission peak frequency shift in railway prestressed concrete sleepers. *Engineering Structures*, 178, 2019, p. 493-505. **SCOPUS**

2) **R. Janeliukstis**, S. Ruchevskis, A. Chate. Classification Model for Damage Localization in a Plate Structure. *Mechanics of Composite Materials*, 53(6), 2018, p. 725-736. **SCOPUS, WEB OF SCIENCE**

3) R. You, D. Li, C. Ngamkhanong, **R. Janeliukstis**, S. Kaewunruen. Fatigue Life Assessment Method for Prestressed Concrete Sleepers. *Frontiers in Built Environment* 3:68, 2017, p. 1-13.

4) **R. Janeliukstis**, S. Rucevskis, M. Wesolowski, A. Chate. Experimental structural damage localization in beam structure using spatial continuous wavelet transform and mode shape curvature methods. *Measurement: Journal of the International Measurement Confederation*, 102, 2017, p. 253-270. **SCOPUS, WEB OF SCIENCE**

5) S. Rucevskis, **R. Janeliukstis**, P. Akishin, A. Chate. Mode shape-based damage detection in plate structure without baseline data. *Structural Control and Health Monitoring*, 23(9), 2016, p. 1180-1193. **SCOPUS, WEB OF SCIENCE**

6) **R. Janeliukstis**, A. Clark, M. Papaelias, S. Kaewunruen. A novel separation technique of flexural loading-induced acoustic emission sources in railway prestressed concrete sleepers. *IEEE Access*. **Submitted.**

7) **R. Janeliukstis**, S. Rucevskis, S. Kaewunruen. Mode shape curvature squares method for crack detection in railway prestressed concrete sleepers. *Engineering Failure Analysis*. **Submitted**.

8) **R. Janeliukstis**, S. Rucevskis, A. Chate. Condition monitoring enhanced with pseudo-defect localization in a two-dimensional structural element based on supervised multiclass classification of strain features. *Nondestructive Testing and Evaluation*. **Submitted.**

Conference papers

1) **R. Janeliukstis**, S. Rucevskis, A Chate. Classification-based Damage Localization in Composite Plate using Strain Field Data, Journal of Physics: Conference Series, 1106, 012022, 2018. **SCOPUS**

2) S. Kaewunruen, **R. Janeliukstis**, A. Freimanis, K. Goto. Normalized curvature square ratio for detection of ballast voids and pockets under rail track sleepers, Journal of Physics: Conference Series, 1106, 012002, 2018. **SCOPUS**

3) P. Skels, **R. Janeliukstis**, V. Haritonovs. Review on structural health interrogation using fiber bragg grating sensors, *Engineering for Rural Development*, 2018. **SCOPUS**

4) S. Kaewunruen, C. Ngamkhanong, **R. Janeliukstis**, R. You. Dynamic amplification factors for railway turnout bearers in switches and crossings, COMPDYN 2017 - Proceedings of the 6th International Conference on Computational Methods in Structural Dynamics and Earthquake Engineering, 2017. **SCOPUS**

5) S. Kaewunruen, C. Ngamkhanong, **R. Janeliukstis**, R. You. Influences of surface abrasions on dynamic behaviours of railway concrete sleepers, 24th International Congress on Sound and Vibration, ICSV 2017, 2017. **SCOPUS**

6) **R. Janeliukstis**, S. Rucevskis, M. Wesolowski, A. Chate. Multiple Damage Identification in Beam Structure Based on Wavelet Transform, *Procedia Engineering*, 172, p. 426-432, 2017. **SCOPUS, WEB OF SCIENCE**

7) **R. Janeliukstis**, S. Rucevskis, M. Wesolowski, A. Chate. Damage identification in beam structure based on thresholded variance of normalized wavelet scalogram, *IOP Conference Series: Materials Science and Engineering*, 251, 012089, 2017. **SCOPUS, WEB OF SCIENCE**

8) A. Clark, S. Kaewunruen, **R. Janeliukstis**, M. Papaelias. Damage Detection in Railway Prestressed Concrete Sleepers using Acoustic Emission, *IOP Conference Series: Materials Science and Engineering*, 251, 012068, 2017. **SCOPUS, WEB OF SCIENCE**

9) **R. Janeliukstis**, S. Rucevskis, A. Kovaļovs, A. Chate. Numerical Investigation on Multiclass Probabilistic Classification of Damage Location in a Plate Structure. *International Conference on Structural Engineering Dynamics ICEDyn 2017: Technical Programme & Book of Abstracts*, Portugal, Ericeira, July 3-5, 2017, p. 57-58.

10) **R. Janeliukstis**, A. Clark, S. Rucevskis, S. Kaewunruen. Vibration-Based Damage Identification in Railway Concrete Sleepers. *Proceedings of SMAR 2017 Conference*, Switzerland, Zurich, September 13-15, 2017, p. 193-201.

11) **R. Janeliukstis**, S. Rucevskis, P. Akishin, A. Chate. Wavelet Transform Based Damage Detection in a Plate Structure, *Procedia Engineering*, 161, p. 127-132, 2016. **SCOPUS, WEB OF SCIENCE**

12) **R. Janeliukstis**, S. Rucevskis, M. Wesolowski, A. Kovalovs, A. Chate. Damage Identification in Polymer Composite Beams Based on Spatial Continuous Wavelet Transform, *IOP Conference Series: Materials Science and Engineering*, 111, 012005, 2016. **SCOPUS, WEB OF SCIENCE**

13) **R. Janeliukstis**, S. Rucevskis, M. Wesolowski, A. Chate. Damage Identification Dependence on Number of Vibration Modes Using Mode Shape Curvature Squares, *Journal of Physics: Conference Series*, 744, 012054, 2016. **SCOPUS**

14) S. Rucevskis, **R. Janeliukstis**, P. Akishin, A. Chate. Vibration-based approach for structural damage detection, ICSV 2016 - 23rd International Congress on Sound and Vibration: From Ancient to Modern Acoustics, 2016. **SCOPUS, WEB OF SCIENCE**

15) **R. Janeliukstis**, S. Rucevskis, M. Wesolowski, A. Kovalovs, A. Chate. Damage identification in beam structure using spatial continuous wavelet transform. *IOP Conference Series: Materials Science and Engineering*, 96, 012058, 2015. **SCOPUS, WEB OF SCIENCE**

16) M. Wesolowski, S. Rucevskis, **R. Janeliukstis**, M. Polanski. Damping properties of sandwich truss core structures by strain energy method. *IOP Conference Series: Materials Science and Engineering*, 96, 012022, 2015. **SCOPUS, WEB OF SCIENCE**

17) **R. Janeliukstis**, S. Rucevskis, M. Wesolowski, A. Chate, A. Kovalovs. Damage Identification in Beam Structure Using Mode Shape Data: from Spatial Continuous Wavelet Transform to Mode Shape Curvature Methods. *Proceedings of ICoEV 2015: International Conference on Engineering Vibration*, Slovenia, Ljubljana, September 7-10, 2015, p. 1-10.

18) **R. Janeliukstis**, S. Rucevskis, M. Wesolowski, A. Kovalovs, A. Chate. Damage Identification in Polymer Composite Beams based on Spatial Continuous Wavelet Transform and Mode Shape Curvature Squares. *Baltic Polymer Symposium 2015: Programme and Proceedings*, Latvia, Sigulda, September 16-18, 2015, p. 105-105.

REFERENCES

[1]   Airplane   crash.   Available   at   http://www.dailymail.co.uk/news/article-2020504/Caribbean-Airlines-crash-Guyana-I-dont-want-die-screamed-girl-plane-snapped-2.html

[2]   Collapse of a high-rise building. Available at http://www.haaretz.com/middle-east-news/iran/1.765999

[3]   Cai J, Qiu L, Yuan S, Shi L, Liu P, Liang D. Structural Health Monitoring for Composite Materials. Chapter 3 in *Composites and Their Applications*. InTech Publishing. 2012.

[4]   Kessler SS, Spearing SM, Soutis C. Damage detection in composite materials using Lamb wave methods. *Smart Mater Struct.* 2002;11: 269-278.

[5]   Park S, Park SK, Kim JW, Chang HJ. Debonding condition monitoring of a CFRP laminated concrete beam using piezoelectric impedance sensor nodes. *Proceedings of Fracture Mechanics of Concrete and Concrete Structures* FraMCoS-7. 2010.

[6]   Yan YJ, Yam LH. Online detection of crack damage in composite plates using embedded piezoelectric actuators/sensors and wavelet analysis. *Compos Struct*. 2002;58(1):29-38.

[7]   Failure   modes   in   composites.   Available   at   http://www.ltas-cm3.ulg.ac.be/FractureMechanics/overview_P3.html

[8]   Oskouei AR, Ahmadi M, Hajikhani M. Wavelet-based acoustic emission characterization of damage mechanism in composite materials under mode I delamination at different interfaces. *Express Polym Lett.* 2009;3(12):804-813.

[9]   Fotouhi M, Sadeghi S, Jalalvand M, Ahmadi M. Analysis of the damage mechanisms in mixed-mode delamination of laminated composites using acoustic emission data clustering. *J Thermoplast Compos.* 2017;30(3):318–340.

[10]   Qiao P, Lu K, Lestari W, Wang J. Curvature mode shape-based damage detection in composite laminated plates. *Compo. Struct.* 2007;80(3):409-428.

[11]   Ginzburg D, Pinto F, Iervolino O, Meo M. Damage tolerance of bio-inspired helicoidal composites under low velocity impact. *Compos Struct*. 2017;161:187-203.

[12]   Stelldinger E, Kühhorn A, Kober M. Experimental evaluation of the low-velocity impact damage resistance of CFRP tubes with integrated rubber layer. *Compos Struct*. 2016;139:30-35.

[13]   Topac TO, Gozluklu B, Gurses E, Coker D. Experimental and computational study of the damage process in CFRP composite beams under low-velocity impact. *Compos Part A – Appl S.* 2017;92:167-182.

[14]   Toivola R, Lai PN, Yang J, Jang SH, Jen AKY, Flinn BD. Mechanochromic fluorescence in epoxy as a detection method for barely visible impact damage in CFRP composites. *Compos Sci Tehnol.* 2017;139:74-82.

[15]   Li Y, Zhang W, Yang ZW, Zhang JJ, Tao SJ. Low-velocity impact damage characterization of carbon fiber reinforced polymer (CFRP) using infrared thermography. *Infrared Phys Techn.* 2016;76:91-102.

[16] Remennikov AM, Kaewunruen S. A review of loading conditions for railway track structures due to train and track vertical interaction. *Struct Control Hlth.* 2008;15(2):207-234.

[17] Kaewunruen S, Remennikov AM. Sensitivity analysis of free vibration characteristics of an in situ railway concrete sleeper to variations of rail pad parameters. *J Sound Vib.* 2006;298(1-2):453-461.

[18] Parvez A, Foster SJ. Fatigue of Steel-Fibre-Reinforced Concrete Prestressed Railway Sleepers. *Eng Struct.* 2017;141:241–250.

[19] Kaewunruen S, Remennikov AM. Progressive failure of prestressed concrete sleepers under multiple high-intensity impact loads. *Eng Struct.* 2009;31(10):2460-2473.

[20] Remennikov AM, Kaewunruen S. Experimental load rating of aged railway concrete sleepers. *Eng Struct.* 2014;76:147-162.

[21] Remennikov AM, Murray MH, Kaewunruen S. Conversion of AS1085. 14 for prestressed concrete sleepers to limit states design format, *AusRAIL PLUS Conference & Exhibition*. 2007: 1-19.

[22] Rezaie F, Farnam SM. Fracture mechanics analysis of pre-stressed concrete sleepers via investigating crack initiation length. *Eng Fail Anal.* 2015;58:267-280.

[23] Ferdous W, Manalo A. Failures of Mainline Railway Sleepers and Suggested Remedies – Review of Current Practice. *Eng Fail Anal.* 2014;44:17-35.

[24] Kaewunruen S. *Experimental and numerical studies for evaluating dynamic behaviour of prestressed concrete sleepers subject to severe impact loading*. *PhD thesis*. 2007. Available at: http://ro.uow.edu.au/theses/27 (accessed 12.03.2017.).

[25] Kaewunruen S, Remennikov A. Rotational capacity of railway prestressed concrete sleeper under static hogging moment, *The Tenth East Asia-Pacific Conference on Structural Engineering and Construction*. 2006: 399–404. Available at: http://ro.uow.edu.au/engpapers/318

[26] Wolf HE, Edwards JR, Dersch MS, Qian Y, Lange DA. Field Measurement of Bending Moments in Prestressed Concrete Monoblock Sleepers. *The Eleventh World Congress on Railway Research.* 2016. Available at: http://railtec.illinois.edu/articles/Files/Conference%20Proceedings/2016/WCRR2016_Wolf_et_al_Bending_Moments%5B1%5D.pdf (accessed 28.01.2017.).

[27] Mayville RA, Jiang L, Sherman M. *Performance Evaluation of Concrete Railroad Ties on the Northeast Corridor, U.S. Department of Transportation, Federal Railroad Administration, A Report*: 2014. Available at: https://trid.trb.org/view/1304992. (accessed on 19.03.2017.).

[28] Vlez W, Matta F, Ziehl P. Acoustic Emission Monitoring of Early Corrosion in Prestressed Concrete Piles. *Struct Control Health Monit.* 2015;22:873-887.

[29] Zakeri J, Rezvani FH. Failures of Railway Concrete Sleepers During Service Life. *Int. J Constr Eng Manag.* 2012;1(1):1-5.

[30] The relationship between SHM, CM and NDT. Available at http://www.bindt.org/forums/moodys-memoranda/the-relationship-between-shm-cm-and-ndt/

[31]   Güemes A. SHM Technologies and Applications in Aircraft Structures. *5th International Symposium on NDT in Aerospace*. 2013.

[32]   Sohn H, Park G, Wait JR, Limback NP, Farrar CR. Wavelet-based active sensing for delamination detection in composite structures. *IOP Conference Series: Smart Materials and Structures* 2003;13(1):153-160.

[33]   Barazanchy D, Martinez M, Rocha B, Yanishevsky M. A Hybrid Structural Health Monitoring System for the Detection and Localization of Damage in Composite Structures. *Journal of Sensors* 2014;Article ID 109403.

[34]   Liu X, Zhou C, Jiang Z. Damage localization in plate-like structure using built-in PZT sensor network. *Smart Struct. Syst.* 2012;9(1):21-33.

[35]   Baptista FG, Budoya DE, de Almeida VAD, Ulson JAC. An Experimental Study on the Effect of Temperature on Piezoelectric Sensors for Impedance-Based Structural Health Monitoring. *Sensors* 2014;14:1208-1227.

[36]   Yan W, Chen WQ. Structural Health Monitoring Using High-Frequency Electromechanical Impedance Signatures, a Review Article. *Adv Civ Eng.* 2010;Article ID 429148.

[37]   Giurgiutiu V, Zagrai A. Damage Detection in Simulated Aging-Aircraft Panels Using the Electro-Mechanical *Impedance Technique. Adaptive Structures and Material Systems Symposium, ASME Winter Annual Meeting*. 2000.

[38]   Carpinteri A, Lacidogna G, Accornero F, Mpalaskas AC, Matikas TE, Aggelis DG. Influence of damage in the acoustic emission parameters. *Cement Concrete Compos.* 2013;44:9-16.

[39]   Gholizadeh S. A review of non-destructuve testing methods of composite materials. *Procedia Struct Integrity* 2016;1:50-57.

[40]   Balageas D, Claus-Peter Fritzen CP, Güemes A. Structural Health Monitoring. London: ISTE. 2006: 496. Available at http://www.iste.co.uk/data/doc_xqjujdlhnfls.pdf

[41]   Hafizi ZM, Epaarachchi J, Lau KT. An Investigation of Acoustic Emission Signal Attenuation for Monitoring of Progressive Failure in Fiberglass Reinforced Composite Laminates. *IJAME* 2013;8:1442-1456.

[42]   Geng J, Sun Q, Zhang Y, Cao L, Zhang W. Studying the dynamic damage failure of concrete based on acoustic emission. *Const. Build Mater.* 2017;149:9-16.

[43]   Ramboll UK Ltd. Hammersmith Flyover - Phase 2 refurbishment and strengthening (HFO2) – Ramboll UK Limited. 2015. Available at: http://www.ramboll.co.uk/projects/ruk/hammersmith-flyover-phase-2#UHPFRC.

[44]   Webb GT, Vardanega PJ, Fidler PRA, Middleton CR. Analysis of Structural Health Monitoring Data from Hammersmith Flyover. *J Bridge Eng.* 2014;19(6):1–11.

[45]   Friswell MI. Damage identification using inverse methods. *Philos Trans Royal Soc. A* 2007;365(1851):393-410.

[46]   Fan W, Qiao P. Vibration-based damage identification methods: a review and comparative study. *Struct Health Monit*. 2011;10(1):83-111.

[47]   Wu D, Law SS. Damage Localization in Plate Structures from Uniform Load Surface Curvature. *J Sound Vib*. 2004;276(1-2):227-244.

[48] Fan W, Qiao P. A 2-D continuous wavelet transform of mode shape data for damage detection of plate structures. *Int J Solids Struct*. 2009;46(25-26):4379-4395.

[49] Khiem NT, Tran HT. A procedure for multiple crack identification in beam-like structures from natural vibration mode. *J Vib Control* 2014;20(9):417-1427.

[50] Hsu TY, Huang SK, Lu KC, Loh CH, Wang Y, Lynch JP. On-Line Structural Damage Localization and Quantification Using Wireless Sensors. *Smart Mater Struct*. 2011;20(10):art. no. 105025.

[51] Hong JC, Kim YY, Lee HC, Lee YW. Damage detection using the Lipschitz exponent estimated by the wavelet transform: applications to vibration modes of a beam. *Int J Solids Struct*. 2002;39:1803-1816.

[52] Ulriksen MD, Damkilde L. Structural damage localization by outlier analysis of signal-processed mode shapes – Analytical and experimental validation. *Mech Syst Signal Pr*. 2016;68-69:1-14.

[53] Rucevskis S, Sumbatyan MA, Akishin P, Chate A. Tikhonov's regularization approach in mode shape curvature analysis applied to damage detection. *Mech Res Commun*. 2015;65:9-16.

[54] Lestari W, Qiao P. Damage detection of fiber-reinforced polymer honeycomb sandwich Beams. *Compos Struct*. 2005;67(3):365-373.

[55] Chandrashekhar M, Ganguli R. Damage assessment of structures with uncertainty by using mode-shape curvatures and fuzzy logic. *J Sound Vib*. 2009;326(3-5):939-957.

[56] Dawari VB, Vesmawala GR. Modal curvature and modal flexibility methods for honeycomb damage identification in reinforced concrete beams. *Procedia Eng*. 2013;51:119-124.

[57] Dilena M, Morassi A. Dynamic testing of a damaged bridge. *Mech Syst Signal Pr*. 2011;25(5):1485-1507.

[58] Cao M, Ye L, Zhou L, Su Z, Bai R. Sensitivity of fundamental mode shape and static deflection for damage identification in cantilever beams. *Mech Syst Signal Pr*. 2011;25:630-643.

[59] Ndambi JM, Vantomme J, Harri K. Damage assessment in reinforced concrete beams using eigenfrequencies and mode shape derivatives. *Eng Struct*. 2002;24(4):501-515.

[60] Kim JT, Ryu YS, Cho HM, Stubbs N. Damage identification in beam-type structures: frequency-based method vs mode-shape-based method. *Eng Struct*. 2003;25(1):57-67.

[61] Amaravadi K, Rao V, Derriso M. Structural Integrity Monitoring of Bonded Composite Patch Repairs of Aging Airframes Using Wavelet Transforms. *Struct Health Monit*. 2002;1(2):161-184.

[62] Dessi D, Camerlengo G. Damage identification techniques via modal curvature analysis: Overview and comparison. *Mech Syst Signal Pr*. 2015;52-53:181-205.

[63] Kim JT, Stubbs N. Improved damage identification method based on modal information. *J Sound Vib*. 2002;252(2):223-238.

[64] Yuen MMF. A numerical study of the eigenparameters of a damaged cantilever. *J Sound Vib*. 1985;103:301-310.

[65] Pandey AK, Biswas M, Samman MM. Damage detection from changes in curvature

mode shapes. *J Sound Vib*. 1991;145:321-332.

[66]   Stubbs N, Kim JT. Damage localization in structures without baseline modal parameters. *AIAA J*. 1996;34:1644-1649.

[67]   Wahab A, Roeck G. Damage detection in bridges using modal curvatures: application to a real damage scenario. *J Sound Vib*. 1999;226:217-235.

[68]   Maia NMM, Silva JMM, Almas EAM, Sampaio RPC. Damage detection in structures: from mode shape to frequency response function methods. *Mech Syst Signal Pr*. 2003;17:489-498.

[69]   Rucevskis S, Wesolowski M, Chate A. Damage detection in laminated composite beam by using vibration data. *J Vibroeng*. 2009;11:363-373.

[70]   Fu YZ, Lu ZR, Liu JK. Damage identification in plates using finite element model updating in time domain. *J Sound Vib*. 2013;332:7018-7032.

[71]   Perez MA, Gil L, Oller S. Impact damage identification in composite laminates using vibration testing. *Compos Struct*. 2014;108:267-276.

[72]   Hamad WI, Owen JS, Hussein MFM. Modelling the degradation of vibration characteristics of reinforced concrete beams due to flexural damage. *Struct Control Health Monit* 2015;22(6):939-967.

[73]   Hsu TY, Liao WI, Shiao SY. A pseudo local flexibility method for damage detection in hyperstatic beams. *Struct Control Health Monit* 2015;22(4):682-693.

[74]   Shih HW, Thambiratnam DP, Chan THT. Damage detection in slab-on-girder bridges using vibration characteristics. *Struct Control Health Monit* 2013;20(10):1271-1290.

[75]   Beskhyroun S, Wegner LD, Sparling BF. New methodology for the application of vibration-based damage detection techniques. *Struct Control Health Monit* 2012;19(8): 632-649.

[76]   Ooijevaar TH, Warnet LL, Loendersloot R, Akkerman R, Tinga T. Impact damage identification in composite skin-stiffener structures based on modal curvatures. *Struct Control Health Monit* 2016;23(2):198-217.

[77]   Alves V, Cury A, Roitman N, Magluta C, Cremona C. Novelty detection for SHM using raw acceleration measurements. *Struct Control Health Monit* 2015;22(9):1193-1207.

[78]   Dworakowski Z, Kohut P, Gallina A, Holak K, Uhl T. Vision-based algorithms for damage detection and localization in structural health monitoring. *Struct Control Health Monit* 2016;23(1):35-50.

[79]   Mosalam KM, Takhirov SM, Park S. Applications of laser scanning to structures in laboratory tests and field surveys. *Struct Control Health Monit* 2014;21(1):115-134.

[80]   Dincal S, Stubbs N. Nondestructive damage detection in Euler-Bernoulli beams using nodal curvatures – Part II: Field measurements. *Struct Control Health Monit* 2014;21(3):331-341.

[81]   Dincal S, Stubbs N. Nondestructive damage detection in Euler-Bernoulli beams using nodal curvatures - Part I: Theory and numerical verification. *Struct Control Health Monit* 2014;21(3):303-316.

[82] Wavelets 4 Dummies: Signal Processing, Fourier Transforms and Heisenberg. Available at https://georgemdallas.wordpress.com/2014/05/14/wavelets-4-dummies-signal-processing-fourier-transforms-and-heisenberg/

[83] Introduction to wavelet transform with applications to dsp. Available at https://www.slideshare.net/jamalkhosti/introduction-to-wavelet-transform-with-applications-to-dsp-59131505

[84] Estrada RS. Damage detection in bridges through vibration monitoring: evaluation and application. Available at http://hdl.handle.net/1822/9023.

[85] Jerri AJ. *Introduction to Wavelets, 1st edition*. Potsdam, New York: Sampling Publishing: 2011.

[86] Alamdari MM, Li J, Samali B. Damage identification using 2-D discrete wavelet transform on extended operational mode shapes. *Arch Civ Mech Eng*. 2015;15:698-710.

[87] Moosavian A, Khazaee M, Najafi G, Khazaee M, Sakhaei B, Jafari SM. Wavelet denoising using different mother wavelets for fault diagnosis of engine spark plug. *P I Mech Eng E – J Pro*. 2017;231(3):359-370.

[88] Chiementin X, Kilundu B, Rasolofondraibe L, Crequy S, Pottier B. Performance of wavelet denoising in vibration analysis: highlighting. *J Vib. Control* 2011;18(6):850-858.

[89] Ruan C, Zhao D, Jia W, Chen C, Chen Y, Liu X, Shen T. Night Vision Image De-noising of Apple Harvesting Robots Based on the Wavelet Fuzzy Threshold. *Int J Adv Robot Syst*. 2015;12(169):1-16.

[90] Sowjanya V, Sasibhushana Rao G, Sarvani A. Investigation of Optimal Wavelet Techniques for De-noising of MRI Brain Abnormal Image. *Procedia Comput Sci.* 2016;85:669-675.

[91] Zhou XX, Yang JF, Sheng H, Wei L, Yan J, Sun P, Wang SH. Combination of stationary wavelet transform and kernel support vector machines for pathological brain detection. *Simul-Trans Soc M S.* 2016;92(9):827-837.

[92] Wu N, Wang Q. Experimental studies on damage detection of beam structures with wavelet transform. *Int J Eng Sci.* 2011;49(3):253-261.

[93] Kim H, Melhem H. Damage detection of structures by wavelet analysis. *Eng Struct*. 2004;26(3):347-362.

[94] Fei SW, He Y. Fault Diagnosis of Bearing Based on Cauchy Kernel Relevance Vector Machine Classifier with SIWPSO. *Shock Vib.* 2015;art. no. 129361.

[95] Yan R, Shan M, Cui J, Wu Y. Mutual Information-Assisted Wavelet Function Selection for Enhanced Rolling Bearing Fault Diagnosis. *Shock Vib.* 2015;art. no. 794921.

[96] Cao H, Fan F, Zhou K, He Z. Wheel-bearing fault diagnosis of trains using empirical wavelet transform. *Measurement* 2016;82:439-449.

[97] Fei SW. Fault Diagnosis of Bearing Based on Wavelet Packet Transform-Phase Space Reconstruction-Singular Value Decomposition and SVM Classifier. *Arab J Sci Eng.* 2017;42(5):1967-1975.

[98] Li F, Meng G, Ye L, Chen P. Wavelet Transform-based Higher-order Statistics for Fault Diagnosis in Rolling Element Bearings. *J Vib. Control* 2008;14(11):1691-1709.

[99] Konar P, Chattopadhyay P. Bearing fault detection of induction motor using wavelet and Support Vector Machines (SVMs). *Appl Soft Comput.* 2011;11(6):4203-4211.

[100] Combet F, Gelman L, LaPayne G. Novel detection of local tooth damage in gears by the wavelet bicoherence. *Mech Syst Signal Pr.* 2012;26:218-228.

[101] Bafroui HH, Ohadi A. Application of wavelet energy and Shannon entropy for feature extraction in gearbox fault detection under varying speed conditions. *Neurocomputing* 2014;133:437-445.

[102] Cao MS, Xu W, Ren WX, Ostachowicz W, Sha GG, Pan LX. A concept of complex-wavelet modal curvature for detecting multiple cracks in beams under noisy conditions. *Mech Syst Signal Pr.* 2016;76-77:555-575.

[103] Montanari L, Basu B, Spagnoli A, Broderick BM. A padding method to reduce edge effects for enhanced damage identification using wavelet analysis. *Mech Syst Signal Pr.* 2015;52-53:264-277.

[104] Wu N, Wang Q. Experimental studies on damage detection of beam structures with wavelet transform. *Int J Eng Sci.* 2011;49:253-261.

[105] Xu YF, Zhu WD, Liu J, Shao YM. Identification of embedded horizontal cracks in beams using measured mode shapes. *J Sound Vib.* 2014;333:6273-6294.

[106] Montanari L, Spagnoli A, Basu B, Broderick BM. On the effect of spatial sampling in damage detection of cracked beams by continuous wavelet transform. *J Sound Vib.* 2015;345:233-249.

[107] Gokdag H, Kopmaz O. A new damage detection approach for beam-type structures based on the combination of continuous and discrete wavelet transforms. *J Sound Vib.* 2009;324(3-5):1158-1180.

[108] Gentile A, Messina A. On the continuous wavelet transforms applied to discrete vibrational data for detecting open cracks in damaged beams. *Int J Solids Struct.* 2003;40(2):295-315.

[109] Solís M, Algaba M, Galvín P. Continuous wavelet analysis of mode shapes differences for damage detection. *Mech Syst Signal Pr.* 2013;40(2):645-666.

[110] Douka E, Loutridis S, Trochidis A. Crack identification in beams using wavelet analysis. *Int J Solids Struct.* 2003;40:3557-3569.

[111] Janeliukstis R, Rucevskis S, Wesolowski M, Kovalovs A, Chate A. Damage Identification in Beam Structure using Spatial Continuous Wavelet Transform. *IOP Conf Ser-Mat Sci.* 2015;96(1):art. no. 012058.

[112] Janeliukstis R, Rucevskis S, Wesolowski M, Kovalovs A, Chate A. Damage Identification in Polymer Composite Beams Based on Spatial Continuous Wavelet Transform. *IOP Conf Ser-Mat Sci.* 2016;111(1):art. no. 012005.

[113] Chang CC, Chen LW. Detection of the location and size of cracks in the multiple cracked beam by spatial wavelet based approach. *Mech Syst Signal Pr.* 2005;19(1):139-155.

[114] Loutridis S, Douka E, Trochidis A. Crack identification in double-cracked beams using wavelet analysis. *J Sound Vib.* 2004;277(4-5):1025-1039.

[115] Rucka M. Damage detection in beams using wavelet transform on higher vibration Modes. *J Theor Appl Mech.* 2011;49(2):399-17.

[116] Grabowska J, Palacz M, Krawczuk M. Damage identification by wavelet analysis. *Mech Syst Signal Pr*. 2008;22:1623-1635.

[117] Katunin A, Holewik F. Crack identification in composite elements with non-linear geometry using spatial wavelet transform. *Arch Civ Mech Eng*. 2013;13(3):287-296.

[118] Katunin A, Przystałka P. Damage assessment in composite plates using fractional wavelet transform of modal shapes with optimized selection of spatial wavelets. *Eng Appl Artif Intel*. 2014;30:73-85.

[119] Katunin A. Damage identification in composite plates using two-dimensional B-spline Wavelets. *Mech Syst Signal Pr*. 2011;25(8):3153-3167.

[120] Katunin A. Vibration-based spatial damage identification in honeycomb-core sandwich composite structures using wavelet analysis. *Compos Struct*. 2014;118(1):385-391.

[121] Katunin A. Stone impact damage identification in composite plates using modal data and quincunx wavelet analysis. *Arch Civ Mech. Eng*. 2015;15(1):251-261.

[122] Huang Y, Meyer D, Nemat-Nasser S. Damage detection with spatially distributed 2D Continuous Wavelet Transform. *Mech Mater*. 2009;41(10):1096-1107.

[123] Fan W, Qiao P. A 2-D continuous wavelet transform of mode shape data for damage detection of plate structures. *Int J Solids Struct*. 2009;46: 4379-4395.

[124] Xu W, Radzien´ski M, Ostachowicz W, Cao M. Damage detection in plates using two-dimensional directional Gaussian wavelets and laser scanned operating deflection shapes. *Struct Health Monit*. 2013;12(5-6):457-468.

[125] Ashory MR, Ghasemi-Ghalebahman A, Kokabi MJ. Damage detection in laminated composite plates via an optimal wavelet selection criterion. *J Reinf Plast Comp*. 2016;35(24):1761-1775.

[126] Ulriksen MD, Tcherniak D, Kirkegaard PH, Damkilde L. Operational modal analysis and wavelet transformation for damage identification in wind turbine blades. *Struct Health Monit*. 2016;15(4):381-388.

[127] Rucevskis S, Janeliukstis R, Akishin P, Chate A. Mode shape based damage detection in plate structure without baseline data. *Struct Control Health Monit* 2016;23(9):1180-1193.

[128] Choi YS, Jeong H, Lee JR. Laser Ultrasonic System for Surface Crack Visualization in Dissimilar Welds of Control Rod Drive Mechanism Assembly of Nuclear Power Plant. *Shock Vib*. 2014;art. no. 296426.

[129] Kaewunruen S, Remennikov AM. Dynamic Effect on Vibration Signatures of Cracks in Railway Prestressed Concrete Sleepers. *Adv Mat Res*. 2008;41-42:233-239.

[130] Kaewunruen S, Remennikov AM. Application of vibration measurements and finite element model updating for structural health monitoring of ballasted railtrack sleepers with voids and pockets. *Mechanical Vibrations: Measurement, Effects and Control*, Chapter 12, Nova Science Publishers: 2009.

[131] Ou G, Wang Y, Hao H, Zhu XQ. Identification of de-bonding between steel bars and concrete using wavelet techniques: Comparative study. *AJSE* 2013;14(1):43-56.

[132] Aguirre DA, Gaviria CA, Montejo L. Wavelet-Based Damage Detection in Reinforced Concrete Structures Subjected to Seismic Excitations. *J Earthq Eng.* 2013;17:1103-1125.

[133] Xu B, Zhang T, Song G, Gu H. Active interface debonding of a concrete-filled steel tube with piezoelectric technologies using wavelet packet analysis. *Mech Syst Signal Pr.* 2013;36:7-17.

[134] Silva CM, Castro LMSS. Damage analysis in concrete structures using polynomial wavelets. *Adv Eng Softw.* 2012;50:69-81.

[135] Melhem H, Kim H. Damage detection in concrete by Fourier and wavelet analyses. *J Eng Mech.* 2003;129(5):571-577.

[136] Ghaffar A, Rahman A, Noroozi S, et al. A hybrid approach for nondestructive assessment and design optimisation and testing of in-service machinery. *Nondestruct Test Eval.* 2013;28(1):44-57.

[137] Park B, Sohn H, Malinowski P, et al. Delamination localization in wind turbine blades based on adaptive time-of-flight analysis of noncontact laser ultrasonic signals. *Nondestruct Test Eval*. 2016;32(1):1-20.

[138] Harper MF, Thompson M. Health monitoring of a complex structure using a sparse array of modally selective transducers. *Nondestruct Test Eval*. 2005;20(3):159-173.

[139] Scala CM, Bowles SJ. Laser-generated Lamb waves to detect hidden interfacial corrosion in thin-skin aircraft components. *Nondestruct Test Eval*. 1994;11(6):357-367.

[140] Gordan M, Razak HA, Ismail Z, Ghaedi K. Recent Developments in Damage Identification of Structures Using Data Mining. *Lat Am J Solids Stru*. 2017;14:2373-24.

[141] Worden K, Manson G. The application of machine learning to structural health monitoring. *Phil Trans R Soc A* 2007;365:515–537.

[142] Jegadeeshwaran R, Sugumaran V. Comparative study of decision tree classifier and best first tree classifier for fault diagnosis of automobile hydraulic brake system using statistical features. *Measurement* 2013;46:3247-3260.

[143] Elangovan M, Babu Devasenapati S, Sakthivel NR, Ramachandran KI. Evaluation of expert system for condition monitoring of a single point cutting tool using principle component analysis and decision tree algorithm. *Expert Syst Appl.* 2011;38:4450-4459.

[144] Muralidharan V, Sugumaran V. Feature extraction using wavelets and classification through decision tree algorithm for fault diagnosis of mono-block centrifugal pump. *Measurement* 2013;46:353-359.

[145] Baraldi P, Cannarile F, Di Maio F, Zio E. Hierarchical k-nearest neighbours classification and binary differential evolution for fault diagnostics of automotive bearings operating under variable conditions. *Eng Appl Artif Intel.* 2016;56:1-13.

[146] Casimir R, Boutleux E, Clerc G, Yahoui A. The use of features selection and nearest neighbours rule for faults diagnostic in induction motors. *Eng Appl Artif Intel.* 2006;19(2):169-177.

[147] Pawar PM, Jung SN. Support Vector Machine based Online Composite Helicopter Rotor Blade Damage Detection System. *J Intel Mat Syst Str.* 2008;19:1217-1228.

[148] Das S, Srivastava AN. Classifying Induced Damage in Composite Plates Using One-Class Support Vector Machines. *AIAA J*. 2010;48(4):705-718.

[149] Balli S. A data mining approach to the diagnosis of failure modes for two serial fastened sandwich composite plates. *J Compos Mater*. 2017;51(20):2853-2862.

[150] Andrejiova M, Grincova A, Marasova D. Failure analysis of rubber composites under dynamic impact loading by logistic regression. *Eng Fail Anal*. 2018;84:311-319.

[151] Fasel TR, Todd MD. An adhesive bond state classification method for a composite skin-to-spar joint using chaotic insonification. *J Sound Vib*. 2010;329:3218-3232.

[152] de Lautour OR, Omenzetter P. Nearest neighbor and learning vector quantization classification for damage detection using time series analysis. *Struct Control Health Monit*. 2010;17:614-631.

[153] Loughalam A, Arwade SR. Prediction of Incipient Damage Sites in Composites using Classifiers. *Int J Damage Mech*. 2010;19:233-260.

[154] Vitola J, Pozo F, Tibaduiza DA, Anaya M. A sensor data fusion system based on k-nearest neighbor pattern classification for structural health monitoring applications. *Sensors* 2017;17:417-443.

[155] Vitola J, Pozo F, Tibaduiza DA, Anaya M. Distributed piezoelectric sensor system for damage identification in structures subjected to temperature changes. *Sensors* 2017;17:1252-1278.

[156] Jin J, Lin S, Ye X. FBG sensor network for pressure localization of spacecraft structure based on distance discriminant analysis. *Optik* 2014;125:404-408.

[157] Larrosa C, Lonkar K, Chang FK. In situ damage classification for composite laminates using Gaussian discriminant analysis. *Struct Control Health Monit*. 2014;13(2):190-204.

[158] Miller CA, Hinders MK. Classification of flaw severity using pattern recognition for guided wave-based structural health monitoring. *Ultrasonics* 2014;54:247-258,

[159] Gaudenzi P, Nardi D, Chiappetta I, Atek S, Lampani L, Pasquali M, Sarasini F, Tirilló J, Valente T. Sparse sensing detection of impact-induced delaminations in composite laminates. *Compos Struct*. 2015;133:1209-1219.

[160] Jiménez AA, Gómez Muñoz CQ, García Márquez FP. Machine Learning for Wind Turbine Blades Maintenance Management. *Energies* 2018;11(1):13.

[161] Marani R, Palumbo D, Renò V, Galietti U, Stella E, D'Orazio T. Modeling and classification of defects in CFRP laminates by thermal nondestructive testing, *Compos Part B-Eng*. 2018;135:129-141.

[162] Huang B, Koh BH, Kim HS. PCA-based damage classification of delaminated smart composite structures using improved layerwise theory. *Comput Struct*. 2014;141:26-35.

[163] Tibaduiza DA, Mujica LE, Rodellar J. Damage classification in structural health monitoring using principal component analysis and self-organizing maps. *Struct Control Health Monit*. 2013;20:1303–1316.

[164] Salehi H, Das S, Chakrabartty S, et al. Damage identification in aircraft structures with self-powered sensing technology: A machine learning approach. *Struct Control Health Monit*. 2018; e2262.

[165] Salehi H, Das S, Chakrabartty S, et al. Structural damage identification using image-based pattern recognition on event-based binary data generated from self-powered sensor networks. *Struct Control Health Monit* 2018; e2135.

[166] Agellis DG. Classification of cracking mode in concrete by acoustic emission parameters. *Mech Res Commun.* 2011;38:153-157.

[167] Behnia A, Chai HK, Yorikawa M, Momoki S, Terazawa M, Shiotani T. Integrated non-destructive assessment of concrete structures under flexure by acoustic emission and travel time tomography. *Constr Build Mater.* 2014;67:202-215.

[168] Ohno K, Ohtsu M. Crack classification in concrete based on acoustic emission. *Constr Build Mater.* 2010;24:2339-2346.

[169] Aldahdooh MAA, Bunnori NM. Crack classification in reinforced concrete beams with varying thicknesses by mean of acoustic emission signal features. *Constr Build Mater.* 2013;45:282-288.

[170] Elfergani HA, Pullin R, Holford KM. Damage assessment of corrosion in prestressed concrete by acoustic emission. *Constr Build Mater.* 2013;40:925-933.

[171] Shahidan S, Pullin R, Bunnori NM, Holford KM. Damage classification in reinforced concrete beam by acoustic emission signal analysis. *Constr Build Mater.* 2013;45:78-86.

[172] Omondi B, Aggelis DG, Sol H, Sitters C. Improved crack monitoring in structural concrete by combined acoustic emission and digital image correlation techniques. *Struct Health. Monit.* 2016;15(3):359-378.

[173] Prem PR, Murty AR. Acoustic emission monitoring of reinforced concrete beams subjected to four-point-bending. *Appl Acoust.* 2017;117:28–38.

[174] Sagar RV. Acoustic emission characteristics of reinforced concrete beams with varying percentage of tension steel reinforcement under flexural loading. *Case Stud Constr Mater.* 2017;6:162-176.

[175] Gross C, Reinhardt H, Dahm T. Localization and classification of fracture types in concrete with quantitative acoustic emission measurement techniques. *NDT&E Int.* 1997;30(4):223-230.

[176] Yella S, Dougherty M, Gupta NK. Condition monitoring of wooden railway sleepers. *Transport Res C*. 2009;17:38-55.

[177] Kocur GK, Vogel T. Classification of the damage condition of preloaded reinforced concrete slabs using parameter-based acoustic emission analysis. *Constr Build Mater.* 2010;24:2332-2338.

[178] Calabrese L, Campanella G, Proverbio E. Use of Cluster Analysis of Acoustic Emission Signals in Evaluationg Damage Severity in Concrete Structures. *JAE* 2010;28:129-144.

[179] Fotouhi M, Sadeghi S, Jalalvand M, Ahmadi M. Analysis of the damage mechanisms in mixed mode delamination of laminated composites using acoustic emission data clustering. *J Thermoplast Compos.* 2017;30(3):318–340.

[180] Morizet N, Godin N, Tang J, Maillet E, Fregonese M, Normand B. Classification of acoustic emission signals using wavelets and Random Forests: Application to localized corrosion. *Mech Syst Signal Pr.* 2016;70-71:1026-1037.

[181] Witten IH, Frank E, Hall MA. *Data Mining: Practical Machine Learning Tools and Techniques, Third edition*. Morgan Kaufman Publishers: 2011.

[182] Manning CD, Raghavan P, Schütze H. *An Introduction to Information Retrieval*. Cambridge University Press Cambridge, England: 2009.

[183] Karbassi A, Mohebi B, Rezaee S, Lestuzzi P. Damage prediction for regular reinforced concrete buildings using the decision tree algorithm. *Comput Struct*. 2014;130:46–56.

[184] Tesfamariam S, Liu Z. Earthquake induced damage classification for reinforced concrete buildings. *Struct Saf*. 2010;32:154–164.

[185] Mechbal N, Uribe JS, Rébillat M. A probabilistic multi-class classifier for structural health monitoring. *Mech Syst Signal Pr*. 2015;60-61:106–123.

[186] Vitola J, Vejar MA, Burgos DAT, Pozo F. *Data-Driven Methodologies for Structural Damage Detection Based on Machine Learning Applications, Pattern Recognition - Analysis and Applications*. InTech Publishing: 2016.

[187] Adeli H, Kim H. *Wavelet-Based Vibration Control of Smart Buildings and Bridges*. Boca Raton, London, New York: CRC Press, Taylor and Francis Group: 2009.

[188] Addison PS. *The Illustrated Wavelet Transform Handbook, Introductory Theory and Applications in Science, Engineering, Medicine and Finance*. New York, London: Taylor & Francis: 2002.

[189] Bayissa WL, Haritos N, Thelandersson S. Vibration-based structural damage identification using wavelet transform. *Mech Syst Signal Pr*. 2008;22(5):1194–1215.

[190] Goswami S, Bhattacharya P. 2015 Real-Time Damage Detection in Laminated Composite Beams Using Dynamic Strain Response and Modular Neural Arrays for Aerospace Applications. *IRJET*. 2015;2(3):2060-69.

[191] Reda Taha MM, Noureldin A, Lucero JL, Baca TJ. Wavelet Transform for Structural Health Monitoring: A Compendium of Uses and Features. *Struct Health Monitor*. 2006;5(3):267-95.

[192] Sowjanya V, Sasibhushana RG, Sarvani A. Investigation of Optimal Wavelet Techniques for De-noising of MRI Brain Abnormal Image *Procedia Comput. Sci.* 2016;85:669-75.

[193] Azzalini A, Farge M, Schenider K. Nonlinear wavelet thresholding: A recursive method to determine the optimal denoising threshold. *Appl Comput Harmon Anal*. 2005;18:177-85.

[194] Zhang X, Feng N, Wang Y, Shen Y. Acoustic emission detection of rail defect based on wavelet transform and Shannon entropy. *J Sound Vib*. 2015;339:419-32.

[195] Matlab R2014a surface smoothing. Available at http://se.mathworks.com

[196] Long J, Büyüköztürk O. Decentralised one-class kernel classification-based damage detection and localization. *Struct Control Health Monit*. 2017;24(6):e1930.

[197] Tibaduiza DA, Mujica LE, Rodellar J. Structural Health Monitoring Based on Principal Component Analysis: Damage Detection, Localization and Classification, *Workshop on Control, Dynamics, Monitoring, and Applications* 2011: 8-17.

170

[198] Janeliukstis R, Ruchevskis S, Chate A. Classification Model for Damage Localization in a Plate Structure. *Mech Compos Mater*. 2018;53(6):725-736.

[199] Singh MP, Elbadawy MZ, Bisht SS. Dynamic strain response measurement-based damage identification in structural frames. *Struct Control Health Monit*. 2018; e2181.

[200] Barkanov E, Wesolowski M, Hufenbach W, Dannemann M. An effectiveness improvement of the inverse technique based on vibration tests. *Comput Struct*. 2015;146:152-162.

[201] Auzins J, Skukis E. Robust Optimization approach for Mixed Numerical/Experimental Identification of Elastic Properties of Orthotropic Composite Plates. *Proceedings of the 6th International Conference on Coupled Problems in Science and Engineering: COUPLED PROBLEMS* 2015: 859-870.

[202] Wesolowski M, Barkanov E. Air damping influence on dynamic parameters of laminated composite plates. *Measurement* 2016;85:239-248.

[203] Tibaduiza DA, Mujica LE, Rodellar J. Structural Health Monitoring Based on Principal Component Analysis: Damage Detection, Localization and Classification. *Workshop on Control, Dynamics, Monitoring, and Applications* 2011:8-17.

[204] Rokach L, Maimon O. *Data Mining with Decision Trees: Theory and Applications, Second edition*, World Scientific: 2015.

[205] British Standards Institute (BSI), BS EN 13230:2016 Railway applications. Track. Concrete sleepers and bearers. London, UK. 2016.

[206] You R, Li D, Ngamkhanong C, Janeliukstis R, Kaewunruen S. Fatigue Life Assessment Method for Prestressed Concrete Sleepers. *Front Built Environ*. 2017;3:1-13.

[207] Kaewunruen S, Remennikov AM, Murray MH. Introducing a new limit states design concept to railway concrete sleepers: an Australian experience. *Front Mater*. 2014;1:1-8.

[208] Kaewunruen S, Remennikov AM. Impact capacity of railway prestressed concrete sleepers. *Eng Fail Anal.* 2009;16:1520–1532.

[209] Kim KB, Kang HY, Yoon DJ, Choi MY. Pattern Classification of Acoustic Emission Signals During Wood Drying by Principal Component Analysis and Artificial Neural Network. *Key Eng Mat.* 2005;297-300:1962-1967.

[210] Yoon DJ, Weiss WJ, Shah SP. Assessing damage in corroded reinforced concrete using acoustic emission. *J Eng Mech.* 2000;126(3):273–283.

[211] Kaewunruen S, Remennikov AM. Post-failure mechanism and residual load-carrying capacity of railway prestressed concrete sleeper under hogging moment. *Proceedings of the International Conference on Structural Integrity and Failure*. 2006: 331-336. Available at http://ro.uow.edu.au/engpapers/316/

[212] Kaewunruen S, Remennikov AM. On the residual energy toughness of prestressed concrete sleepers in railway track structures subjected to repeated impact loads. *EJSE* 2013;13(1):41–61.

[213] Kaewunruen S, Remennikov AM. Nonlinear finite element modeling of railway prestressed concrete sleeper, Real Structures: Bridges and Tall Buildings. *Proceedings*

of the 10th East Asia-Pacific Conference on Structural Engineering and Construction. 2006: 323-328.

[214] Farnam Y, Geiker MR, Bentz D, Weiss J. Acoustic emission waveform characterization of crack origin and mode in fractured and ASR damaged concrete. *Cement Concrete Comp.* 2015;60:135-145.

[215] Li W, Xu C, Ho SCM, Wang B, Song G. Monitoring Concrete Deterioration Due to Reinforcement Corrosion by Integrating Acoustic Emission and FBG Strain Measurements. *Sensors* 2017;17:657–668.

[216] Acoustic emission sensors. Available at https://www.physicalacoustics.com/wireless-systems/ (Accessed on 12.07.2018.).